The Pennsylvania State University

The Graduate School

Department of Materials Science and Engineering

DESIGN, FABRICATION, TEST, AND EVALUATION OF RF MEMS SERIES SWITCHES USING LEAD ZIRCONATE TITANATE (PZT) THIN FILM ACTUATORS

A Thesis in

Materials Science and Engineering

by

Ronald G. Polcawich

©2007 Ronald G. Polcawich

Submitted in Partial Fulfillment
of the Requirements
for the Degree of

Doctor of Philosophy

August 2007

The thesis of Ronald G. Polcawich was reviewed and approved* by the following:

Susan Trolier-McKinstry
Professor of Ceramic Science and Engineering
Thesis Advisor
Chair of Committee

Clive A. Randall
Professor of Materials Science and Engineering

Thomas R. Shrout
Professor of Materials

Srinivas Tadigadapa
Associate Professor of Electrical Engineering

Madan Dubey
Research Physicist, US Army Research Laboratory
Special Member

Gary Messing
Distinguished Professor of Ceramic Science and Engineering
Head of Department of Materials Science and Engineering

*Signatures are on file in the Graduate School.

Abstract

The aim of this thesis was to design and prototype a robust, low voltage RF MEMS switch for use in military phased arrays. The frequencies of interest for this work include very low frequencies down to DC operation with the upper limit extending to at least 40 GHz. This broad frequency requirement requires a robust high frequency design and simulation using microwave transmission lines. With the aid of researchers at the US Army Research Laboratory, co-planar waveguide (CPW) transmission lines were chosen and designed to provide a low loss, 50 ohm impedance transmission line for the switch. CPW designs allow for both series and shunt switch configuration with this work focusing on a series switch. Furthermore, a series switch an ohmic contact was chosen as opposed to capacitive contacts.

Piezoelectric actuation is chosen for the switch to enable operating voltages less than 10 volts while still maintaining a restoring force to prevent stiction. To meet these demands, lead zirconate titanate (PZT) thin films have been chosen for the piezoelectric actuator. Mechanical modeling of cantilevers comprised of an elastic layer and a Pt-PZT-Pt actuator were used to demonstrate feasibility of closing large gaps between switch contacts. Placement of the actuator to minimize perturbations to the RF transmission line is critical for broadband performance. Using fabrication design rules, electro-mechanical modeling, and high frequency design, the actuators were designed to fit with the RF gap between the RF conductor and ground planes of the CPW transmission line. Optimal performance was obtained with the actuators mechanically isolated from a majority of the RF transmission except for a small section that provides the contact pad to enable switch closure.

The resulting switch is the first demonstrated first surface micromachined RF MEMS switch operating from DC to 65 GHz. This switch has a median actuation voltage below 5 volts with operation as low as 2 volts. Isolation in the off state is better than -20 dB across the frequency band with values better than -60 dB observed for frequency below 1 GHz. The insertion loss in the on state is less than 1 dB below 40 GHz and remains below 2 dB up to 65 GHz. Switching time was demonstrated at 40 µs and was limited by bouncing between the contacts, with initial contact observed at less

than 10 μs. The cycle reliability of this switch has been tested with high contact resistance failures observed in the low 10^6 cycles range. The reliability appears to be limited by organic contamination between the contacting surfaces, possibly the result of resist residue and/or the development of a frictional polymer on the platinum coated contact surface.

Testing of CPW transmission lines pointed to the fact that the elastic layer used to stress engineer the PZT actuators significantly contributes to the transmission line loss and limits the insertion loss of the switch in the on state. The insertion loss was improved to better than 0.5 dB below 40 GHz by modifying the fabrication process to eliminate the silicon nitride layer within the elastic layer from underneath of the CPW. This process modification leaves the elastic layer intact beneath the PZT actuators, ensuring proper stress engineering of the actuators.

With one application of this RF MEMS switch targeted for military phased arrays, temperature sensitivity is an extremely important characteristic. The PZT SW5.1 design exhibited excellent off state performance with no change in the isolation characteristics from -25ºC to 100ºC. However, in the on state, the actuation voltage is required to increase to 20 volts to ensure operation at 100ºC. The temperature sensitivity was improved by redesigning the RF contact pad to enable co-linear contact between the RF input and output sides of the transmission. This redesign, PZT SW5.2, successfully enables operation of the PZT RF MEMS switch from -25ºC to 100ºC with an actuation voltage less than 10 volts. The isolation of the newer design remains similar to the earlier design with values better than -20 dB up through 50 GHz. The insertion loss of this design exhibited a slight improvement compared to the earlier design with values less than 0.3 dB below 40 GHz and rising to 0.5 dB up through 50 GHz.

The DC and RF power handling of the PZT SW5.2 design was evaluated with the goal of investigating the use of eutectic alloys in the contact dimple for improved RF performance at elevated power levels. The testing at DC highlighted the existence of a contamination layer on the switch contacts, evident by the significant reduction in contact resistance with increasing DC current. Subsequently analysis found these devices have residual resist remaining on the switch contacts possibly from carbonization of the resist during the fabrication process. This residue does not affect the power handling as it

breaks down at low currents. For RF power handling, the PZT SW5.2 switch demonstrated an average failure of 2 – 3 W_{RF}. A significant majority of the switch failures occurred along the RF contact pad from electromigration failures, as the contact pad has a contact resistance greater than that of the contact dimples.

Table of Contents

List of Figures ix
List of Tables xxi
Acknowledgements xxiii
Chapter 1 1
Introduction & Objectives 1
1.1 MEMS Switches 1
1.1.1 Historical Perspective 1
1.1.2 Contact in MEMS Switches 3
1.1.3 Actuation Mechanisms 4
1.1.4 Switch Performance Parameters 9
1.1.5 MEMS Switches for RF Applications 13
1.1.6 Existing Electrostatic RF MEMS Switches 13
1.1.7 Reducing the Actuation Voltage 17
1.2 Piezoelectricity 18
1.2.1 Ferroelectric Materials 19
1.2.2 Phenomenology 24
1.2.3 Lead Zirconate Titanate (PZT) 27
1.2.4 PZT Thin Film Technology 29
1.2.5 PZT Based MEMS Switches 30
1.3 MEMS Ohmic Switch Contacts 33
1.3.1 Contact Area and Resistance 33
1.3.2 Contact Materials 34
1.3.3 Failure Mechanisms with Ohmic Switches 35
1.4 Thesis Objectives 37
1.5 References 38

Chapter 2 42
Experimental Procedures 42
2.1 Residual Stress Measurement 42
2.2 Film Thickness Measurements 44
2.3 X-ray Diffraction 52
2.4 Ferroelectric & Dielectric Measurements 52
2.5 Static Deformation Measurements 53
2.6 Resonance Measurements 55
2.7 RF Switch Characterization 56
2.7.1 RF Performance as a Function of Frequency 56
2.7.2 Contact Resistance 58
2.7.3 Switching Time 59
2.7.4 Actuation Voltage 60
2.7.5 RF Power Handling 61
2.7.6 Lifetime Characterization 62
2.8 Thermal Sensitivity 62
2.9 References 64

Chapter 3 67
Switch Design & Fabrication 67
3.1 Switch Design 67
3.1.1 Design Evolution – PZT SW2.0 68
3.1.2 Actuation and Residual Stress Control 70
3.1.3 Design Evolution – PZT SW3.0 74
3.1.4 Mechanical and High Frequency Simulation of the Primary Designs (PZT SW4.0, PZT SW5.1, & PZT SW5.2) 79
3.2 Fabrication 86
3.2.1 Substrate Selection 86
3.2.2 Elastic Layer Deposition 87
3.2.3 Bottom Electrode Deposition 90
3.2.4 PZT Thin Film Deposition 92
3.2.5 Top Electrode Deposition 94
3.2.6 Piezoelectric Actuator Patterning 95
3.2.7 Creating the RF Components 99
3.2.8 Releasing the Switch Components 104
3.3 References 105

Chapter 4 108
Device Results & Discussion 108
4.1 Material Property Testing 108
4.1.1 Ferroelectric and Dielectric Properties 108
4.1.2 Effective Piezoelectric Coefficient 114
4.2 PZT Thin Film Actuator Characterization 118
4.2.1 Effect of Residual Stress on Static Actuator Deformation 118
4.2.2 Resonance Measurements on Cantilever Actuators 121
4.3 PZT Switch Actuator Characterization 124
4.3.1 Static Deflection 124
4.3.2 Effects of Poling on Static Deformation 125
4.3.3 Piezoelectrically Induced Deformation 127
4.3.4 Resonance Characterization on Switches 132
4.4 RF MEMS Switch Characterization 133
4.4.1 Actuation Voltage 133
4.4.2 Actuation Voltage - Poling & Aging 137
4.4.3 Isolation and Insertion Loss 141
4.4.4 Influence of Elastic Layer on Insertion Loss Characteristics 145
4.4.5 Switching Time 148
4.4.6 Hold down performance 154
4.4.7 Thermal Sensitivity 156
4.4.8 Reliability 164
4.5 Improved PZT Switches (PZT SW5.2) 168
4.5.1 Fabrication and Design Modifications 169
4.5.2 Thermal Sensitivity of New Switches 172
4.5.3 DC Current Handling 174
4.5.4 Influence of Contact Metal Choice on Current Handling 179

4.5.5 RF Power Handling 184
4.6 References 191

Chapter 5 194
Conclusions & Future Work 194
5.1 Conclusions 194
5.2 Recommendations for Future Work 197
5.2.1 Investigating the Degradation of the Ferroelectric Properties During Switch Fabrication 197
5.2.2 Improving Cycle Reliability 200
5.2.3 Switch Miniaturization 204
5.3 References 208

List of Figures

Figure 1.1: Images of RF MEMS switches: a) Rockwell Science Center and b) University of Michigan (from Reference 2 and 7).. 2
Figure 1.2: Schematic illustration of a) ohmic and b) capacitive switch contacts............ 3
Figure 1.3: Illustration of the electrostatic force generated between two metallic plates interspaced with a dielectric material upon the application of a voltage................ 5
Figure 1.4: Illustration of a thermal bimorph actuator.. 6
Figure 1.5: Illustration of the magnetic force attracting two parallel conductors separated by a gap.. 6
Figure 1.6: Illustration of piezoelectric actuation in a unimorph cantilever...................... 8
Figure 1.7: Strain electric field relationship for 3 different types of electrostrictive materials based on lead magnesium niobate-lead titanate (PMN-PT), from Reference 10. 9
Figure 1.8: Schematic diagram of the scattering parameters, S_{ij}, measured with a 2-port network analyzer, where a_1 and a_2 is the incident power at port 1 or 2 and b_1 and b_2 represent either the reflected or transmitted power depending on the port of incident power (from Reference 11)... 10
Figure 1.9: Illustration of the definition of switching time to open (τ_{open}) and close (τ_{close}) the switch. 11
Figure 1.10: Switching operation waveforms: a) hot switch and b) cold switch............. 12
Figure 1.11: Illustration of the current draw through a piezoelectric MEMS switch as a function of applied voltage to the actuators. The actuation voltage is determined as the median voltage between the low and high current states and is indicated by the arrow. 12
Figure 1.12: a) SEM of the Radant MEMS switch and b) switch performance from DC to 40 GHz (Image from Reference 13). Radant MEMS uses "gate" to refer to the actuation bias bad with the "source" and "drain" refer to the input and output transmission line, respectively.. 14
Figure 1.13: a) Image of the Raytheon MEMS switch and b) unactuated and c) actuated switch performance from DC to 40 GHz (images from Reference 18)................ 15
Figure 1.14: a) Image of the MEMtronics capacitive shunt switch and b) a schematic description of the proximity switch with individual dielectric posts for improved dielectric charging resistance (images from Reference 19)................................. 16
Figure 1.15: a) SEM of the Lincoln Laboratory inline ohmic series switch along with performance of b) ohmic switch and c) a capacitive series switch (from References 7and 20)... 17
Figure 1.16: SEM image of a compliant electrostatically actuated RF MEMS switch with an actuation voltage as low as 6 volts (from Reference 22). 18
Figure 1.17: Representation of the cubic (Pm3m) prototype structure of perovskite ABO_3 structure.. 20
Figure 1.18: Illustration of a tetragonal distortion resulting in a positive shift of the A (0.10 Å) and B (+0.12 Å) ions and a slight negative shift of the oxygen ion (-0.03 Å) for $BaTiO_3$ (values taken from Reference 28)... 20

Figure 1.19: Lattice distortions that occur upon cooling below T_c in perovskites: a) In the tetragonal phase, P_s develops along [001] of the original cubic structure, b) in the orthorhombic phase, P_s occurs along [011], and c) in the rhombohedral phase, P_s develops along [111]. The dotted cubes are for the cubic prototype; the solid lines show the distorted unit cells of the ferroelectric phases (images adopted from Reference 26). 21
Figure 1.20: Schematic of the polarization electric field hysteresis loop illustrating the saturation polarization (P_{sat}), remanent polarization (P_r), and coercive field (E_c) (adapted from Reference 26). 22
Figure 1.21: Possible polarization directions relative to the cubic prototype for a) tetragonal perovskite with 6 equivalent <001> directions, b) orthorhombic distortion with 12 equivalent <110> directions, or c) rhombohedral with 8 equivalent <111> directions. 23
Figure 1.22: Phase diagram for the lead zirconate - lead titanate solid solution (from References 27). 28
Figure 1.23: Variation in relative permittivity (K_{33}) and the effective piezoelectric coefficient (d_{33}) as a function of the Zr/Ti ratio and orientation for bulk PZT (from Reference 34). The data given for specific orientations are from phenomenological calculations. 28
Figure 1.24: Illustration of a low frequency thin film PZT unimorph switch developed at Penn State University (from Reference 51). 31
Figure 1.25: SEM image of a bulk micromachined RF MEMS series switch using a thin film PZT actuator to complete the signal path (from References 52 and 53). 31
Figure 1.26: RF performance of a bulk micromachined PZT RF MEMS series switch (from References 52 and 53). 32
Figure 1.27: Schematic illustrating the operating principle of the PZT actuated seesaw switch: a) is the normal (off) state, b) the left actuator is "on", and c) the right actuator is "on" (image from Reference 54). 32
Figure 1.28: SEM images of the evolution of contact damage in Au contacts: a) virgin contact, b) contact after 1,000 cycles, and c) contact after 1,000,000 cycles (from Reference 63). 36

Figure 2.1: Illustration of the measurement setup for the Tencor FLX-3200: a) side view and b) top view. 43
Figure 2.2: (a) Experimental setup and (b) principle of operation of the JA Woollam M2000 ellipsometer. 45
Figure 2.3: Modeled n and k values for the silicon substrate with values based from Reference 3. 46
Figure 2.4: Predicted n and k values for a PECVD SiO_2 thin film (968 Å) using a Cauchy model. 47
Figure 2.5: Refractive index values reported by Rodkiewicz et.al. for a silicon dioxide thin film. 47
Figure 2.6: Predicted n and k values for a PECVD Si_3N_4 thin film (586 Å) using a modified Tauc-Lorentz oscillator model. 48
Figure 2.7: Example of the n and k values reported by Loh et. al. for a silicon nitride thin films as a function of increasing silicon content. 49

Figure 2.8: Predicted n and k values for an infinitely thick platinum layer using a Lorentz oscillator model. 50
Figure 2.9: Predicted n and k values are reported for a PZT thin film (5059 Å) using a modified Pole plus Tauc-Lorentz oscillator model. 51
Figure 2.10: Example of the n and k values reported by Jiang et al. for PZT thin films (approximately 210 nm thick) on platinum coated silicon substrates at several annealing conditions. 52
Figure 2.11: Measurement setup of the Veeco NT1100 optical profilometer. 54
Figure 2.12: Measurement setup of the Polytec LDV with the the hardware specifics (a) and the schematic of the measurement signal paths (b). 55
Figure 2.13: Image of a PZT switch illustrating the location of the LDV scans for assessing the switching behavior of the switch. Scan sites are shown as white circles. 56
Figure 2.14: Image of the probe positions for RF testing of the PZT switch. 57
Figure 2.15: Setup for measuring the contact resistance of the PZT switch. Note, DUT is device under test. 59
Figure 2.16: DC switching time measurement setup. 60
Figure 2.17: Illustration of the current draw through a piezoelectric MEMS switch as a function of the voltage applied to the actuators. The actuation voltage was determined as the median voltage between the low and high current states and is indicated by the arrow. 61
Figure 2.18: RF power handling measurement setup. 62
Figure 2.19: Cycle lifetime measurement setup. 63
Figure 2.20: Description of the actuation (solid line) and RF pulse (dashed line) used for reliability testing of switches under cold-switching conditions. 63

Figure 3.1: SEM images illustrating a PZT actuated capacitive switch design (PZT SW2.0). Gnd is an abbreviation for electrical ground of the CPW transmission line. 69
Figure 3.2: Plot of the experimentally measured effective dielectric properties of a Si_3N_4/SiO_2 (500 / 1000 Å) dielectric stack as a function of frequency. 69
Figure 3.3: Image of PZT SW2.0 design illustrating failure to make contact full contact with the entire CPW transmission line. 70
Figure 3.4: Vertical elongation of small volume of poled PZT with the application of an electric field applied in the poling direction. 73
Figure 3.5: Depiction of the starting wafer composite thin film stack (Si/elastic layer/Ti/TiO_2/Pt/TiO_2/PZT/Pt). 74
Figure 3.6: Image illustrating the major design components of PZT SW3.0. 76
Figure 3.7: Schematic illustration of how the PZT actuator deflection with an applied electric field will result in contact between the RF conductor and RF cantilever. 76
Figure 3.8: Actuated tip deflection as a function of beam length for a PZT cantilever with an actuation voltage of 8 volts. 77
Figure 3.9: Experimental and modeled RF performance of the first functional PZT actuated RF MEMS switch from DC to 40 GHz. Note, the model assumed a contact resistance of 1 Ohm in the closed state. 78

Figure 3.10: SEM images (taken by Matthew Ervin, US Army Research Laboratory) illustrating the (a) exaggerated width curvature of the coupled RF conductor and PZT actuators upon actuation and (b) prevention of device contact as a result of the width curvature. 78
Figure 3.11: a) Image outlining the critical features of PZT SW4.0 that requires 2 ohmic contacts for good RF performance and b) the CAD drawing illustrating the bond pad locations with the ground planes. 80
Figure 3.12: Illustration of the RF conductor width modifications to account for (a) capacitive loading from the DC bias air bridges and (b) the changes to the capacitance within the RF gap from the air cavity underneath the actuators and CPW transmission line. 82
Figure 3.13: Predicted piezoelectric actuator deflection and contact resistance as a function of voltage. 83
Figure 3.14: HFSS simulation of a PZT series switch (PZT SW4.0 & PZT SW5.1) in the open state and closed state. 84
Figure 3.15: PZT switch (PZT SW4.0 & PZT SW5.1) equivalent circuit model with parameters derived from Ansoft's Q3D. 85
Figure 3.16: Equivalent circuit simulation of PZT series switch (PZT SW4.0) in the open state and closed state 86
Figure 3.17: Co-planar waveguide transmission line (T-line) loss as a function of frequency for various substrates. 87
Figure 3.18: X-ray photoelectron spectroscopy (XPS) depth profile highlighting the interfaces in PECVD composite oxide/nitride/oxide thin films. (a) Shows results for a sample grown with a continuous plasma whereas (b) corresponds to a sample prepared with individual deposition and anneals. 88
Figure 3.19: Residual stress variation with temperature in flowing N_2 with (a & b) PECVD SiO_2 and (c & d) Si_3N_4 thin films. The removal of trapped hydrogen ions with temperature transforms the film stress from compressive to tensile. For each film, a second thermal scan illustrates that each film is relatively unaffected by additional thermal processing up to 700ºC. Note, the spikes in the data are attributed to measurement noise generated by cleanroom personnel using equipment adjacent to the stress measurement system during the over 6 hours of temperature testing. 89
Figure 3.20: Example of the measured and modeled ellipsometry results for oxide/nitride/oxide structural layer and the resulting thickness uniformity across a 100 mm wafer. 90
Figure 3.21: Residual stress variation with temperature in air for sputtered (a & b) Ti/TiO_2/Pt and (c & d) Ti/Pt thin films on a SiO_2 (2000 Å) coated silicon substrate. The relaxation of the metal layers with temperature transforms the film stress from compressive to tensile. A second thermal scan illustrates that the stress was stable with additional thermal processing up to 700ºC. Note, the spikes in the data on plot (c) are attributed to measurement noise generated by cleanroom personnel using equipment adjacent to the stress measurement system during the over 6 hours of temperature testing. 91
Figure 3.22: X-ray diffraction results ($\theta - 2\theta$) for a 0.5 μm PZT thin films grown with (a) and without (b) a 10 Å TiO_2 seed layer. 92

Figure 3.23: Ferroelectric, dielectric, and leakage current data recorded as part of the PZT solution test procedure. 93
Figure 3.24: Example of the measured and modeled ellipsometry results (a) for PZT thin films and the thickness uniformity (b) measured across a 100mm substrate. 94
Figure 3.25: Residual stress variation with temperature (a – 350ºC and b – 500ºC) in air for sputtered Pt on top of a PZT thin film. 95
Figure 3.26: Fabrication flow – top electrode patterning. The left image is a 3-D rendering of the device stack with the individual layer thicknesses grossly exaggerated. For all 3-D renderings, the silicon substrate is represented by the large grey block, the elastic layer stack is light blue, platinum electrodes are light grey, PZT is green, gold layers are tones of yellow, and the sacrificial layer is pink. On the right is a top down view. 96
Figure 3.27: Fabrication Flow – PZT and bottom electrode patterning. PZT and the top electrode remain in the active piezoelectric actuator regions, both sets of bond pads, and connecting bias lines. The remaining PZT and bottom electrode material are etched down to the structural elastic layer. 97
Figure 3.28: Fabrication Flow – PZT wet etch and bottom electrode bond pad definition. The PZT was wet etched, exposing the bottom electrode on the bond pads as well as on the stubs adjacent to the actuators so that the air bridge that will ultimately electrically tie both actuators together has access to the bottom electrode........... 98
Figure 3.29: Fabrication Flow – Structural elastic layer patterning. The structural elastic layer is selectively etched to open access to the silicon substrate. The pattern defines the actuators and RF contact pad by defining the perimeter. The exposed silicon will ultimately enable the final process step, a XeF_2 etch, to undercut the silicon beneath the actuators and thus release it from the substrate. 98
Figure 3.30: Fabrication Flow – CPW Transmission line deposition and patterning. The RF conductor and ground planes are patterned on top of the structural dielectric around the actuators and bond pads. 99
Figure 3.31: Fabrication Flow – Contact dimple deposition and patterning. The contact dimples are deposited and patterned onto the RF conductor pad. 100
Figure 3.32: Fabrication Flow – Sacrificial layer deposition and patterning. The sacrificial layer is deposited and defined to cover all but the locations for the vertical posts that will anchor the ground straps, the top and bottom electrode bias line air bridges, and the RF cantilevers. 101
Figure 3.33: Stylus profilometer measurement of the sacrificial layer for the (a) as cured resist and (b) oxygen plasma etch defined counter dimples. 101
Figure 3.34: Results from 2-step photolithographic process to define counter dimples in the sacrificial layer. The sequence of images represent a) 0.2 s, b) 0.4 s, c) 0.6, and d) 0.8 s exposure dose for the second aligned exposure. An exposure of 0.4 s was chosen because it created consistent hemi-spherical counter dimples. 102
Figure 3.35: Stylus profilometer measurements of the sacrificial layer with photo defined counter dimples (0.4 s) in the sacrificial layer (Note, that the optical measurements were made with a thin layer of sputtered Pt deposited onto the cured resist). 103
Figure 3.36: Fabrication Flow – Conformal (unpatterned) gold bridge deposition........ 103

Figure 3.37: Fabrication Flow – Bridge metal patterning. The bridge metal is patterned with argon ion milling, thereby defining the ground straps, the top and bottom electrode bias line air bridges, and the RF cantilevers....................................... 104
Figure 3.38: Fabrication Flow– Sacrificial layer removal. The sacrificial layer is isotropically removed, thus releasing the ground straps, the top and bottom electrode bias line air bridges, and the RF cantilevers....................................... 104
Figure 3.39: Fabrication Flow – XeF_2 silicon etch release of the actuators and RF contact pad. a) The silicon is isotropically etched under the actuator structures, releasing it from the silicon substrate. b) A profile illustrating the region located between the dashed lines on the image to the left. 105

Figure 4.1: Ferroelectric properties observed as a function of process step: a) after the PZT wet etch and b) after the reactive ion etch of the elastic layer. Testing was performed on a PZT (52/48) thin film with a thickness of approximately 0.5 μm using a PZT SW5.1 switch actuator with an actuated length of 65 μm. 109
Figure 4.2: Ferroelectric properties observed as a function of process step: c) after the CPW and dimple liftoff in PRS-3000, d) after the bridge metal liftoff in acetone, e) after a 60min oxygen plasma, and f) after the XeF_2 etch of the silicon. Testing was performed on a PZT (52/48) thin film with a thickness of approximately 0.5 μm using a PZT SW5.1 switch actuator with an actuated length of 65 μm........ 110
Figure 4.3: Modeled results demonstrating the influence a non-switching layer can have on the dielectric displacement – electric field hysteresis loop (from Reference 6). 111
Figure 4.4: P–E hysteresis loop for an unpoled, pulse-poled (450 kV/cm, 2.9 x 106 cycles), and hot poled (160ºC) PZT (15/85) thin films (from Reference 1)....... 111
Figure 4.5: Ultraviolet (UV) induced pinching of the ferroelectric hysteresis loop in a PZT (45/55) thin film (from Reference 7). 112
Figure 4.6: Ferroelectric properties of a PZT (52/48) thin film capacitor from PZT SW4.0 wafer processing with as-fabricated (virgin) and post thermal poling of 125ºC for 10min at 15 volts. 112
Figure 4.7: Pinched ferroelectric hysteresis loop for several device wafers................. 113
Figure 4.8: Static deformation of switch actuators as a function of post process annealing temperature. 113
Figure 4.9: Depiction of a PZT cantilever (actuated and unactuated) illustrating the critical components required for computing the effective piezoelectric coefficient. 115
Figure 4.10: Piezoelectric cantilever beam (125 μm in length) displacement as a function of voltage. 115
Figure 4.11: Effective transverse piezoelectric coefficient ($e_{31,f}$) extracted from FEA models using experimentally determined cantilever tip deflections as a function of voltage: a) bipolar and b) unipolar scans 117
Figure 4.12: Ferroelectric and dielectric properties of the PZT cantilevers tested in Figure 4.11. 118
Figure 4.13: As-fabricated beam curvature for 3 of the cantilevers of the cantilever array measured using an optical profilometer. 120

Figure 4.14: Optical image illustrating the effects of the XeF_2 undercut (~30 μm) on the anchor of the PZT cantilever array. 120
Figure 4.15: Predicted resonance frequency versus length of cantilevers comprised of $SiO_2/Si_3N_4/SiO_2$/Ti/Pt/PZT/Pt with thicknesses indicated on the graph. Circles highlight the design lengths for the cantilever array (i.e. 52 μm, 77 μm, 102 μm, 127 μm, 152 μm, 177 μm). 122
Figure 4.16: Velocity versus frequency plots for individual PZT cantilevers as measured with a laser Doppler vibrometer. The side peaks on either side of the fundamental resonance mode for each cantilever are induced by the mechanical coupling between the adjacent cantilevers by the undercut elastic layer.......................... 123
Figure 4.17: Resonance frequency results for (a) a 102 μm and (b) a 127 m long cantilever comprised of an oxide/nitride/oxide (ONO) elastic layer and a Pt/PZT/Pt actuator for the initial as-fabricated and poled (10 min at 10 V) cantilevers illustrating the existence of some degree of poling in the as-fabricated devices. Each resonance scan was collected with the application of 0.02 V_{p-p} with a 0.01 V_{offset}. 124
Figure 4.18: Actuator tip deflection as a function of poling conditions for PZT switches (PZT SW4.0) having actuators with of varying lengths. 125
Figure 4.19: Predicted tip deflection for a PZT thin film cantilever as a function of length assuming an effective $e_{31,f}$ of -7 N/Vm. 129
Figure 4.20: Predicted tip deflection for a PZT thin film cantilever as a function of length using the as-measured $e_{31,f}$ versus voltage reported in Figure 4.11. 129
Figure 4.21: Predicted stress induced initial tip deflection for a PZT cantilever as a function of beam length with error bars equal to 25%. The error bar size was determined after comparing the average measured deflections to the predicted values and represents an envelope of all of the measured values. 130
Figure 4.22: Initial piezoelectric deformation of a 140 μm long actuator of a PZT series switch (PZT SW4.0). Repeated actuation cycles follow the decreasing field trace indicated on the plot. 131
Figure 4.23: SEM images illustrating how the PZT series switch (PZT SW4.0 and PZT SW5.1 designs) closes with increasing voltage: a) 0 V, b) 3 V, c) 3.5 V, and d) 5 V. 131
Figure 4.24: Repeated actuation deformations for a PZT thin film actuator with an actuated length of 123 μm. 132
Figure 4.25: Forward transmission coefficient (S_{21}) and RF gap between the RF contact pad and the RF out cantilever as a function of applied voltage for a PZT SW4.0 design. The inset shows the deformations of a PZT actuators with an actuated length of 140 μm, as previously discussed (see Figure 4.22). Note, this data was recorded on a low resistivity Si substrate so S_{21} in the "on" state was limited to approximately 4dB. 134
Figure 4.26: Actuation voltage histogram for the as-fabricated (unpoled) PZT switches (PZT SW5.1): a) device A01, b) device A02, c) device A03, d) device A23, and e) device A24. Note, device A24 was analyzed with a reduced number of voltage steps compared with the other scans. 136

Figure 4.27: Measured DC current thru the RF transmission as a function of voltage applied to the PZT actuators for two individual devices under test (DUT). DUT1 appears to break contact at 12 V and then regains contact with increasing voltage presumably due to a high initial contact resistance. 137
Figure 4.28: Actuation voltage histograms of several device designs (PZT SW5.1) after poling for 60 seconds: a) A01, b) A02, c) A03, and d) A23.............................. 138
Figure 4.29: Actuation voltage histograms of several device designs (PZT SW5.1) after a second poling for 60 seconds: a) A01, b) A02, and c) A03............................. 139
Figure 4.30: Actuation voltage histograms for PZT SW5.1 designs following aging of the PZT switches for 15 hours: a) device A01 and b) device A03. 140
Figure 4.31: Normalized actuator tip deflection as a function of aging time for a PZT SW5.1 design, device A03 with an actuated length of 115 µm. The device was poled at 15 volts at room temperature and at 125ºC. Zero time is calculated based on the time the poling voltage is reduced to zero volts..................................... 141
Figure 4.32: Measured RF performance for PZT SW5.1 design A01 (65 µm long actuated beam) in both the open and closed state. These data do not represent the average performance over several devices, instead they illustrate the performance of a single device. 142
Figure 4.33: Measured RF performance for PZT SW5.1 design A02 (90 µm long actuated beam) in both the open and closed state. These data do not represent the average performance over several devices, instead they illustrate the performance of a single device. 142
Figure 4.34: Measured RF performance for PZT SW5.1 design A03 (115 µm long actuated beam) in both the open and closed state. These data do not represent the average performance over several devices, instead they illustrate the performance of a single device. 143
Figure 4.35: Measured RF performance for PZT SW5.1 design A23 (90 µm long actuated beam) in both the open and closed state. These data do not represent the average performance over several devices, instead they illustrate the performance of a single device. 143
Figure 4.36: Measured RF performance for PZT SW5.1 design A24 (115 µm long actuated beam) in both the open and closed state. These data do not represent the average performance over several devices, instead they illustrate the performance of a single device. 144
Figure 4.37: Example of the improvements in S_{21} in the closed state for an actuation voltage of 5 V and 8 V... 145
Figure 4.38: Transmission loss of CPW transmission lines on different dielectrics on a high resistivity silicon substrate... 146
Figure 4.39: X-ray photoelectron spectroscopy (XPS) depth profile of a composite oxide/nitride/oxide (1200 / 486 / 3520 Å) thin film. 147
Figure 4.40: Modification to the fabrication flow – thinning of the elastic layer. Photoresist (purple) is patterned and protects the PZT actuators, RF contact pad, and the release trenches: a) 3-dimensional view and b) plan view. The remainder of the wafer is then etched to remove the silicon nitride and all silicon nitride/silicon oxide interfaces.. 148

Figure 4.41: Insertion loss characteristics of design A05 with a 90 µm long actuated beam (see Section 4.5 for further description of A05) on Wafer 5230 in which the oxide/nitride/oxide layer for all the structures except for the actuators and RF contact pad has been thinned to approximately 800Å with a reactive ion etch.. 148
Figure 4.42: Examples of the switching time measurement for PZT SW5.1 device A02; a) as-fabricated and b) after poling for 2 min at 5V. 149
Figure 4.43: Illustration of the ripple in the contact resistance that results from the bouncing between the RF contact pad and the RF cantilevers. 150
Figure 4.44: Switching time measurement for a PZT SW5.1 switch (A02) in a vacuum of 1 x 10-5 Torr. 150
Figure 4.45: Examples of the switch off time for the PZT SW5.1 device A02; a) with very little evidence of bounce and b) with bounce. 151
Figure 4.46: Time scan for a) the switch actuators of PZT SW5.1 device A02 and b) the RF contact pad and RF cantilevers at the onset of a 0.5V, 1ms pulse applied to the PZT actuators. In part b, the RF-in and RF-out cantilevers do not show any evidence of movement. 151
Figure 4.47: a) Time scan for switch actuators with a 90 µm long actuated length (PZT SW5.1 device A02) at the onset of a 5.0V, 1ms pulse applied to the PZT actuators. Image b) is a zoom image of switch contact occurring during the first 60 microseconds highlighting the transition from an unstable to a stable contact. 152
Figure 4.48: Time scan of PZT SW5.1 device A02 (90 µm long actuated beam) for (a and b) the RF pad and (c and d) the RF in and out cantilevers at the onset of a 5.0V, 1ms pulse applied to the PZT actuators. b) and d) highlight switch contact and bounce occurring during the first 60 microseconds. 152
Figure 4.49: Example of actuation waveform control using a voltage ramp (right side) as opposed to a square wave applied to the piezoelectric as presented by Uchino and Giniewicz. Note, n is a time scale based on half of the resonance period of the actuator. 153
Figure 4.50: Hold down characteristics at 17 GHz of a PZT switch (A02 design) with 5V applied. 155
Figure 4.51: Thermal deformation (at 0 V dc bias) of a PZT actuator with an actuated length of 90 µm from room temperature to 125ºC along with predicted results from ANSYS models covering a temperature range of -55ºC to 125ºC. 157
Figure 4.52: S_{21} values as a function of temperature for PZT SW4.0 switch with an actuated length of 140 µm in the open state (0V) for Wafer 1376 which is comprised of $SiO_2/Si_xN_y/SiO_2/Ti/TiO_2/Pt/PZT/Pt$ (1032/427/3360/20/160/1680/4881/1050 Å). 157
Figure 4.53: S_{21} values as a function of temperature for PZT SW5.1 switches in the open state (0V) for Wafer 5124 comprised of $SiO_2/Si_xN_y/SiO_2/Ti/TiO_2/Pt/PZT/Pt$ (968/586/3473/20/160/1680/5054/1050 Å). The changes in the isolation characteristics may have resulted from changes in the stress deformation induced by thermal poling during measurements of the closed state performance. 158
Figure 4.54: S_{21} values as a function of temperature and voltage for PZT SW4.0 switch having an actuator with an actuated length of 90 µm on Wafer 1376 (low resistivity silicon substrate that limits the closed state performance). 159

Figure 4.55: S_{21} values as a function of temperature and voltage for PZT SW5.1 device A01 (65 µm long actuated beam) on Wafer 5124.. 159
Figure 4.56: S_{21} values as a function of temperature and voltage for PZT SW5.1 device A02 (90 µm long actuated beam) on Wafer 5124.. 160
Figure 4.57: S_{21} values as a function of temperature and voltage for PZT SW5.1 device A03 (115 µm long actuated beam) on Wafer 5124.. 160
Figure 4.58: S_{21} values as a function of temperature and voltage for PZT SW5.1 device A23 (90 µm long actuated beam) on Wafer 5124.. 161
Figure 4.59: S_{21} values as a function of temperature and voltage for PZT SW5.1 device A24 (115 µm long actuated beam) on Wafer 5124.. 161
Figure 4.60: SEM images illustrating a PZT SW5.1 device A02 failing to make contact to both RF cantilevers as a result of a defect in the RF in cantilever: a) 0 V, b) 5 V, c) 10 V, d) 20 V. 162
Figure 4.61: Deformation of the width (a) and length (b) of the RF contact pad as a function of temperature with 0V applied to the actuators. The sharp vertical transitions in length plot are measurement artifacts from the edge of the contact pad.. 163
Figure 4.62: Deformation of the width (a) and length (b) of the RF contact pad as a function of temperature with 15V applied to the actuators. The sharp vertical transitions in length plot are measurement artifacts from the edge of the contact pad.. 163
Figure 4.63: Cycle reliability for a PZT SW4.01 device with an actuated length of 140 µm tested under cold-switching conditions. Note, this device was from Wafer 1376, which was fabricated on low resistivity silicon. A high resistance (i.e. high insertion loss) failure occurred between $8x10^5$ and $2.3x10^6$ cycles.................. 165
Figure 4.64: SEM images of the Pt coated Au contact dimple for the switch cycled in Figure 4.63. 165
Figure 4.65: A sampling of the results from cycle lifetime testing on PZT SW5.1 device A01 having actuators with an actuated length of 65 µm, from Wafer 5124 at 6 GHz. 166
Figure 4.66: SEM image of a switch contact from the testing highlighted in Figure 4.65. 167
Figure 4.67: SEM illustrating a gold particulate from the ion-milling of the evaporated gold affecting the proper closure of the switch contacts.................................. 169
Figure 4.68: Images comparing the sacrificial layer patterning process for a) the gold ion-milling process and b) the gold liftoff process. In the ion-milling process, the resist is patterned to reveal only the anchor regions of all air bridges. For the liftoff process, the resist is patterned such that it is removed for all regions except for the areas where the air bridges will be located... 170
Figure 4.69: SEM image of a non-functioning PZT SW5.2 switch in which the RF-in cantilever has been deformed upward and slightly twisted during the liftoff process. Note that this is an A06 design having an actuator with an actuated length of 115 µm. 171
Figure 4.70: SEM images highlighting the differences between (a) PZT SW5.1 designs A01 – A03 and (b) PZT SW5.2 designs A04 – A06. 172

Figure 4.71: RF performance versus temperature for PZT SW5.2 design A05 having an actuator with an actuated length of 90 μm. Note, this initial wafer was a low resistivity silicon substrate so the insertion loss is limited to 3 – 4 dB. 173
Figure 4.72: RF performance as a function of temperature for PZT SW5.2 device A06 fabricated on a high resistivity substrate (Wafer 5230) and operated at 10V..... 174
Figure 4.73: Contact resistance and insertion loss at 17 GHz for PZT SW5.2 device A06 having an actuator with an actuated length of 115 μm on a low resistivity substrate (Wafer 5165). The actuation voltage applied to the actuators is 9 volts. 175
Figure 4.74: Contact force (μN) as a function of the actuation voltage for a PZT switch having an actuator with an actuated length of 90 μm. ANSYS simulations were completed by Jeffrey Pulskamp (US Army Research Laboratory). 176
Figure 4.75: Contact resistance of contaminant free Pt-Pt and Au-Au contact pairs as a function of contact force. These plots should set the bounds for the PZT switch assuming a contaminant free Au-Pt contact pair. 176
Figure 4.76: ANSYS model highlighting the Joule heating and the thermal conduction paths for the PZT SW5.1 (design A02). The model assumes contact at all 6 contacts and a 1 Ohm resistance per set of 3 contacts (i.e. RF-in or RF-out). For 100mA$_{DC}$, the temperature rise in the RF pad should be approximately 20ºC, whereas the PZT actuators should see a temperature increase of only 4ºC. 177
Figure 4.77: Thermal scans of a PZT SW5.2 (design A06) as a function of applied current: a) 0 mA$_{DC}$, b) 70 mA$_{DC}$, c) 100 mA$_{DC}$, d) 150 mA$_{DC}$, e) 200 mA$_{DC}$, f) 0 mA$_{DC}$. The hot zone is indicated by the white areas and is limited to the RF contact pad region. 178
Figure 4.78: a) Contact resistance and b) temperature change of a PZT SW5.2 (design A06) as a function of DC current along the RF conductor as shown in Figure 4.77. 179
Figure 4.79: SEM image illustrating the presence of a contaminant film on the contact dimples of Wafer 5230.. 181
Figure 4.80: Summary of results for contact resistance on PZT switches with different contact metals: a) Au, b) Au/Pt, c) Au/0.3 μm AuSn/Au/Pt, d) Au/0.1 μm AuSn/Au/Pt. 182
Figure 4.81: SEM image of a 1.0 μm thick evaporated AuSn (80:20) thin film coated with a 0.1 μm thick Au capping layer illustrating (a) softening at 150ºC highlighted by the soft texturing of the surface of the Au thin film and (b) melting of the AuSn after exposure to 300ºC for 2 minutes, highlighted by rippling of the surface gold coating. 183
Figure 4.82: SEM image of a) Au/Pt and b) Au/0.1 μm AuSn/Au/Pt contacts after the DC current tests. The image of the AuSn/Au/Pt contacts is a view looking at the corner of the RF cantilever at the RF contact pad and dimple.......................... 184
Figure 4.83: Examples of the RF power handling for each of the contact dimple metal combinations for PZT SW5.2 devices: a) Au, b) Au/Pt, c) Au/0.3 μm AuSn/Au/Pt, d) Au/0.1 μm AuSn/Au/Pt. 185
Figure 4.84: SEM images of the failures observed for Au contact dimples: a) stiction, RF pad fracture, RF pad disintegration, RF pad fracture and melting of the gold on the RF pad. 186

Figure 4.85: SEM images of the RF contact pad failures observed for Au/Pt contact dimples. ... 187
Figure 4.86: SEM images of the failures observed for Au/0.3 μm AuSn/Au/Pt contact dimples: a) stiction, b) melting of the gold on the RF pad, and c) arcing between the RF pad and RF cantilever ... 187
Figure 4.87: SEM images of the failures observed for Au/0.1 μm AuSn/Au/Pt contact dimples: a) stiction, b) open state failures, and c) grain segregation and melting of the AuSn thin films of the center dimple. ... 188
Figure 4.88: SEM image of an electromigration initiated failure along the center RF conductor. Necking of the elastic layer of the contact pad is indicative of electromigration failures. ... 189
Figure 4.89: DC electromigration failure in a CPW transmission line (image from reference 42). ... 190
Figure 4.90: SEM image of DC electromigration failures in a copper interconnect (image from reference 43) ... 190
Figure 4.91: SEM images of the edge dimple (Au/0.1 μm AuSn/Au/Pt) near the RF-out cantilever for a switch that was successfully operated to 6.3 WRF. The gold in the contact pad shows signs of grain grooving possibly from the heat generated during testing while the contact dimple shows no signs of softening or melting. ... 191

Figure 5.1: Behavior of thin film stress (σ_f) with sputtering conditions: pressure (p), substrate bias, energy bombardment, and the temperature of the substrate (T_s) and melting temperature (T_m) of the thin film (from Reference 5). ... 199
Figure 5.2: Modeled results comparing a PZT thin film cantilever comprised of $SiO_2/Si_3N_4/SiO_2$/Ti/Pt/PZT/Pt with and without a TiO_2 thin film coating on top of the beam of 500, 1000, or 2000 Å. Note, the residual film stress of the TiO_2 was assumed to be 300 MPa based on Reference 4. ... 200
Figure 5.3: Image of the Radant MEMS packaged RF MEMS switch illustrating the height of the packaged relative to that of the RF substrate. ... 202
Figure 5.4: a) Optical image and b) schematic cross-section of an encapsulated RF MEMS switch. ... 202
Figure 5.5: Images highlighting an ARL encapsulated electrostatic switch with a process thought to be compatible with the PZT switch process. ... 203
Figure 5.6: Moore's Law for microprocessors (Reference 17) ... 204
Figure 5.7: Image of a static CMOS inverter with VCC representing the control voltage (Reference 18) ... 205
Figure 5.8: Predicted tip deflection for a scaled PZT actuator with three sub-micron lengths using film thicknesses as labeled. This prediction assumes the same effective $e_{31,f}$ as reported in Section 4.1.2 for the PZT MEMS actuators. ... 207
Figure 5.9: Mechanisms of breakdown across a gap between two conductors. ... 207

List of Tables

Table 1.1: Performance comparison among electrostatic RF MEMS switches, PIN diodes, and FETs (from Reference 2). 3
Table 1.2: Thermodynamic potentials for a polarizable deformable solid with the boundary conditions for each potential. The independent variables are temperature (T), stress (X_{ij}), and electric field (E_m) while the dependent variables are polarization (P_m), strain (x_{ij}), and entropy (S)... 25
Table 1.3: Thermodynamically derived definitions of the four piezoelectric coefficients: d_{mij}, g_{mij}, e_{mij}, h_{mij}... 26
Table 1.4: Comparison of thin film piezoelectric materials with calculated single crystal and bulk ceramic values.. 29

Table 2.1: Modeling parameters used for the Cauchy models for PECVD SiO_2 thin films. The starting values are used at the onset of fitting the model to the experimental data and the fit-values represent an average taken from several measurements... 46
Table 2.2: Modeling parameters used for the user programmable dispersion model for PECVD Si_3N_4 thin films. The starting values are used at the onset of fitting the model to the experimental data and the fit-values represent an average taken from several measurements. 48
Table 2.3: Modeling parameters used for the Lorentz three oscillator model for sputtered Pt thin films (assumed thickness of 1mm). 49
Table 2.4: Modeling parameters used for the modified Pole and Tauc-Lorentz oscillator model for sol-gel PZT (52/48) thin films. The starting values are used at the onset of fitting the model to the experimental data and the fit-values represent an average taken from several measurements. 51

Table 3.1: Average residual stress measured on each of the thin films used in the composite actuator for the PZT switch. 71
Table 3.2: Elastic modulus values used for electromechanical modeling of the PZT switch actuators.. 71
Table 3.3: Thickness parameters (in Å) used in the prediction of residual stress deformation of the composite actuators. The thicknesses for the metal and PZT layers were unchanged for these calculations.. 74
Table 3.4: Dimensional Information for the PZT SW4.0 and PZT SW5.0 80
Table 3.5: List of the nominal component values for the equivalent circuit model shown in Figure 3.15. 85
Table 3.6: Plasma enhanced chemical vapor deposition parameters for silicon dioxide and silicon nitride thin films deposited using a Plasma-Therm 790. 88
Table 3.7: Deposition conditions for all sputtered metals used in the fabrication of the PZT MEMS switch. 91
Table 3.8: Parameters for oxygen plasma processes. 96
Table 3.9: Parameters used for ion-milling PZT, Pt, and Au thin films. 97
Table 3.10: Reactive ion etch parameters for removal of PECVD SiO_2 and Si_3N_4. For ICP etching RF_1 refers to the platen power while RF_2 refers to the ICP coil power. 99

Table 3.11: Process parameters for the evaporation of metals. 100

Table 4.1: Effective high DC bias field transverse piezoelectric coefficient ($e_{31,f}$) for each of the device wafers fabricated. 118
Table 4.2: Comparison of the as-predicted initial deflection and the as-fabricated static deflection measured via optical profilometry for several cantilever lengths (length is the actuated length). 120
Table 4.3: Comparison between the predicted and experimentally measured resonance frequencies for the 3 cantilevers of the test cantilever array for the devices from Wafer 5124 (thicknesses indicated in Figure 4.15). 123
Table 4.4: Comparison of the tip deflections between individual cantilevers and switch actuators. 124
Table 4.5: Change in in-plane strain as a function of poling for switch actuators with an actuated length of 90 μm.. 127
Table 4.6: Resonance frequencies and estimated switching time for each device on Wafer 5124 (PZT SW5.1) with piezoelectric actuators comprised of $SiO_2/Si_xN_y/SiO_2/Ti/TiO_2/Pt/PZT/Pt$ (968/586/3473/20/160/1680/5054/1050 Å). 133
Table 4.7: Summary of the actuation voltage for the PZT SW5.1 designs on wafer 5124 with actuators comprised of $SiO_2/Si_xN_y/SiO_2/Ti/TiO_2/Pt/PZT/Pt$ (968/586/3473/20/160/1680/5054/1050 Å... 135
Table 4.8: Median S_{21} values (from 5 or more samples) in the open and closed states (at 5 V) at 17 GHz for PZT SW5.1 on Wafer 5124 with piezoelectric actuators comprised of $SiO_2/Si_xN_y/SiO_2/Ti/TiO_2/Pt/PZT/Pt$ (968/586/3473/20/160/1680/5054/1050 Å) 144
Table 4.9: Dimensions for PZT SW5.2 designs A04 – A06. Actuator lengths of the new designs remain unchanged from those of PZT SW5.1 designs A01 – A03........ 172
Table 4.10: Median actuation voltages for PZT SW5.2 designs A04 – A06 on Wafer 5165.. 173
Table 4.11: Evaporated contact metals used to examine current handling. 180
Table 4.12: Voltage for softening (V_s) and melting (V_m) for the contact metals used with the PZT switch. *Note that the values for AuSn have been calculated 183

Table 5.1: Results from ICP-MS analysis after soaking 0.5 μm thick PZT (52/48) thin films in various solutions for 60 min. 198

Acknowledgements

This work would not have been possible without the support and assistance of my thesis advisor, Dr. Susan Trolier-McKinstry, my team leader at the US Army Research Laboratory, Dr. Madan Dubey, and my colleagues, Jeffrey S. Pulskamp and Daniel Judy. I would like to thank each of their tutelage and mentoring during my dissertation research. Jeffrey and Daniel are especially commended for all of their hard work, many lengthy discussions on device design, and modeling efforts to enable the successful development of a surface micromachined, piezoelectrically actuated RF MEMS switch.

In addition, I have to thank the technical staff at the US Army Research Laboratory who without their hard work and dedication this work would not have been possible. Richard Piekarz is acknowledged for the sol-gel PZT deposition and many hours of photolithography. John Conrad is acknowledged for the many hours of ion-milling, metal evaporation, and general machining of custom testing equipment. Derwin Washington is acknowledged for his assistance with photolithography, reactive ion etching, and metal evaporation. Prashant Ranade is acknowledged for his many hours of device testing with the optical profilometer, laser Doppler vibrometer, and RF testing. Joel Martin is acknowledged for his fabrication assistance. In addition, Benjamin Heubschman and Edward Viveiros are acknowledged for their assistance with the temperature testing of the RF switches. I would also like to thank Luke Currano for his assistance with mechanical modeling and many hours of fruitful discussions regarding MEMS and device fabrication. I would also like to thank Wayne Churaman and Eugene Zakar for their assistance over the years. Additionally, I would like thank the members of the cleanroom staff at the US Army Research Laboratory with specific mention of Dr. Brett Piekarski.

I would also like to thank my management at the US Army Research Laboratory for their strong encouragement over the years. Specific mention should be given to Dr. Paul Amirtharaj, John Costanza, and Mary Brickerd. I would like to thank Dr. Roger Kaul for his many discussions on RF components, testing of RF devices, and strong encouragement and belief that this technology is vital to the US Army. I would also like to thank each of the members of my defense committee for their tutelage during my

tenure at the Pennsylvania State University, Dr. Clive Randall, Dr. Thomas Shrout, and Dr. Srinivas Tadigadapa.

I could not have completed this work without my friends and family. I need to thank my great friends for their support with specific mention of Marc Palmisiano, Eric Egenolf, and Jamie Snyder. My parents have always pushed me in my endeavors and are acknowledged for their encouragement and love. My brothers, Brandon and Eric, have always been their providing support and well needed relaxation, when necessary. Most importantly my loving wife, Margaret, should be commended for her enduring support, encouragement, and ever-lasting love.

Chapter 1

Introduction & Objectives

The routing of electrical signals is controlled by switches of various types. Fundamental to most radio frequency (RF) circuits, a switch is used not only to control the path of electrical circuits but also the phase and timing of the circuits. The continuous miniaturization of military radar and communication systems requires development of smaller, lower power consumption switches for continuous control of a wide variety of electronic signals.[1] Additionally, switches are required for ever increasing frequencies, making existing solid state technologies less attractive to the system designer because of larger power losses as the frequency increases.[2]

Microelectromechanical systems (MEMS) design and fabrication is an enabling technology that allows the device developer to create a wide variety of mechanical as well as electrical devices monolithically on one substrate. Specifically, MEMS switches provide a very low loss, low power alternative to existing switch technologies. Another key advantage of MEMS switches is their linearity.[3] Unlike electronic switches, PIN diodes and field effect transistors (FET), a well designed MEMS switch is perfectly linear and does not create distortion such as harmonics or intermodulation products, in the electrical signal.[2] Next generation missile seeker radar and communication-on-the-move systems require highly linear, low power, broadband RF switches as a fundamental building block.[1,4,5] This thesis addresses this requirement by targeting the creation of a RF MEMS switch operating at less than 10V with reasonable RF performance from DC to at least 40 GHz.

1.1 MEMS Switches

1.1.1 Historical Perspective

The development of MEMS switches began with the effort of Hughes Research Laboratories on micromachined microwave actuators (MIMACs) and produced a switch capable of operating up to 50 GHz.[6] Following this research, a concentrated effort began in developing switches in both series and shunt configurations for a wide variety of

applications, including lower frequency commercial cell phones and high frequency military radar and communication systems.[1,4,7] A vast majority of this research concentrated on electrostatic actuation as the means of closing the switch contacts. Figure 1.1 illustrates two examples of electrostatic RF MEMS switches. Many of the electrostatic switches that have been developed in recent years exhibit excellent performance characteristics and use voltages ranging from 30 – 100 volts for actuation (see Section 1.1.3 for further discussion).

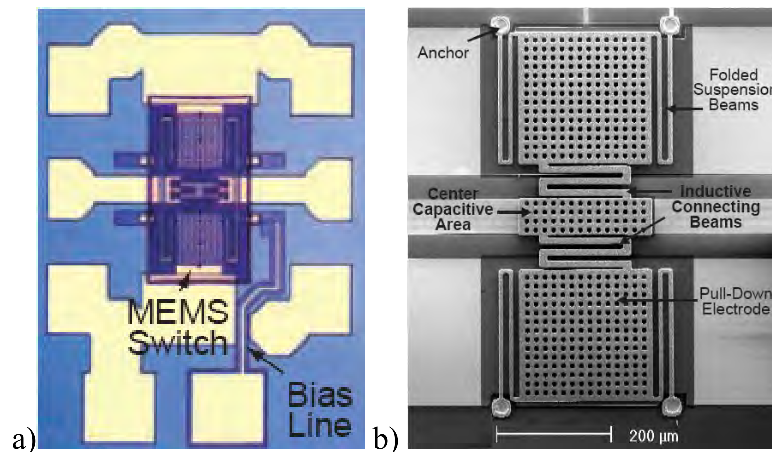

Figure 1.1: Images of RF MEMS switches: a) Rockwell Science Center and b) University of Michigan (from Reference 2 and 7).

For comparison, Table 1.1 highlights critical features for RF MEMS switches, p-i-n junction diodes (PINs), and field effect transistors (FETs). No one technology has a clear advantage over a broad range of frequencies and RF power levels. The aspects for which MEMS switches have clear advantages are high isolation, large third order intercept values (a measure of the linearity of the transmission signal), and extremely low insertion loss at moderate to high frequencies (10 – 100 GHz) for modest RF power levels (< 2 W). One limiting factor for MEMS switches within this specific range of operation is switching time, which still remains orders of magnitude slower than the alternatives. However, there are many commercial and military applications for MEMS switches including phased arrays for communication and radar systems and switch matrices for reconfigurable networks.[1,3,4,5]

Table 1.1: Performance comparison among electrostatic RF MEMS switches, PIN diodes, and FETs (from Reference 2).

Parameter	RF MEMS	PIN	FET
Voltage (V)	20–80	±3–5	3–5
Current (mA)	0	3–20	0
Power consumption[a] (mW)	0.05–0.1	5–100	0.05–0.1
Switching time	1–300 μs	1–100 ns	1–100 ns
C_{up} (series) (fF)	1–6	40–80	70–140
R_s (series) (Ω)	0.5–2	2–4	4–6
Capacitance ratio[b]	40–500[b]	10	n/a
Cutoff frequency (THz)	20–80	1–4	0.5–2
Isolation (1–10 GHz)	Very high	High	Medium
Isolation (10–40 GHz)	Very high	Medium	Low
Isolation (60–100 GHz)	High	Medium	None
Loss (1–100 GHz) (dB)	0.05–0.2	0.3–1.2	0.4–2.5
Power handling (W)	<1	<10	<10
Third-order intercept point (dBm)	+66–80	+27–45	+27–45

[a]Includes voltage upconverter or drive circuitry.
[b]Capacitive switch only. A ratio of 500 is achieved with high-ε_r dielectrics.

1.1.2 Contact in MEMS Switches

RF MEMS switches are defined by two different types of contacts: ohmic and capacitive (see Figure 1.2). Capacitive contact switches utilize a thin dielectric thin film between two metals. At elevated frequencies, the RF energy is capacitively coupled through the dielectric to the switch contact. As a result, capacitive switches are generally limited to higher frequency operation where capacitive coupling is feasible. In contrast, ohmic contacts use two metals to create the switch contact. Ohmic switches provide the opportunity for very broadband operation operating from DC and upward.

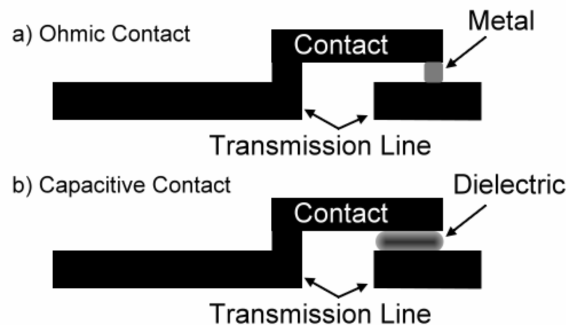

Figure 1.2: Schematic illustration of a) ohmic and b) capacitive switch contacts.

1.1.3 Actuation Mechanisms

Mechanical switches fabricated using MEMS technology utilize several different actuation mechanisms including electrostatic, thermal, magnetic, and piezoelectric. Electrostatic actuation has been the focus of a majority of the MEMS switch programs to date. However, reliability concerns and a drive to reduce actuation voltage have allowed other mechanisms to receive recent focus.

Electrostatic actuation relies on the force generated when a voltage is applied to a set of metallic plates separated by a dielectric (see Figure 1.3). The electrostatic force is governed by Equation 1.1.

$$F_z = \frac{1}{2}\frac{\varepsilon A V^2}{g^2} \qquad \text{Equation 1.1}$$

The force generated along the z-axis is proportional to the dielectric permittivity (ε), the area (A), the square of the voltage (V) applied to the metal plates, and the inverse square of the separation gap (g) between the plates. An important characteristic of electrostatic actuators is the "pull-in" effect where the restoring force associated with the actuator can no longer stand off the attraction force. This instability occurs at approximately 2/3 of the initial gap separation with the "pull-in" voltage (V_p) governed by Equation 1.2 with k representing the spring constant of the actuator.

$$V_p = \left(\frac{8kg^3}{27\varepsilon A}\right)^{0.5} \qquad \text{Equation 1.2}$$

As a result of the "pull-in" effect, the voltage to maintain switch closure can be reduced, which can be beneficial with regard to improved lifetime of the switch.[2] Electrostatic actuators are attractive because of their ease of integration with a wide variety of a

fabrication processes, low power consumption, and high contact forces (10's to 100's of μN).[2]

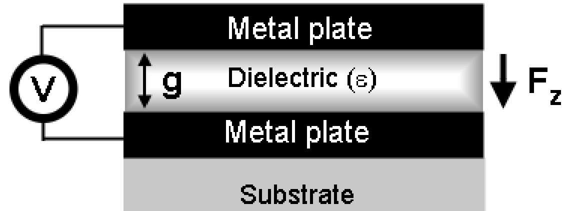

Figure 1.3: Illustration of the electrostatic force generated between two metallic plates interspaced with a dielectric material upon the application of a voltage.

Thermo-mechanical transduction, although primarily used for sensing applications, can be used for actuation.[8] The foundation for thermal actuation is the thermal expansion of materials. All materials have a coefficient of thermal expansion, α_L, defining the dimensional change (ΔL) of a material with a change in temperature, ΔT (see Equation 1.3).

$$\Delta L = \alpha_L L(\Delta T) \quad \text{Equation 1.3}$$

Thermal actuators are generally designed by laminating dissimilar materials and using the difference in thermal expansion coefficients to create movement in a desired direction (see Figure 1.4). An electric heater, typically a resistor material, is included somewhere in the device so that thermal actuation can be controlled electrically. Thermal actuators have a linear relationship between deflection and incident power and can operate in a wide variety of media including liquids. However, the power required for actuation is frequently significantly higher than other actuation mechanisms. Additionally, the speed of the actuators is dictated by thermal time constants and so is slower than many other mechanisms.

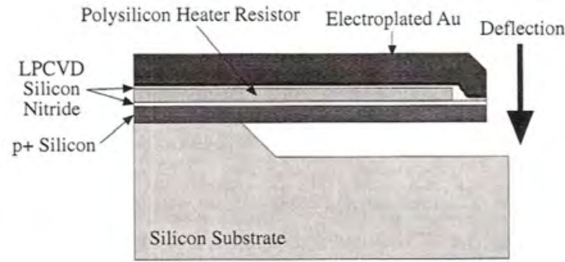

Figure 1.4: Illustration of a thermal bimorph actuator. [8]

Magnetic actuation for MEMS devices can be realized either with an integrated on-wafer magnet or via an external magnet. For integrated on-wafer solutions, a set of parallel conductors carrying current in the same direction will experience an attractive force given by Ampere's law (see Figure 1.5 and Equation 1.4). The force (F_{ba}) generated is proportional to the current (I_a and I_b) within each conductor and the relative magnetic permeability (μ_r) of the medium between the conductors and inversely proportional to the distance between the conductors (g).

$$F_{ba} = \frac{\mu_o \mu_r L I_a I_b}{2\pi g} \qquad \text{Equation 1.4}$$

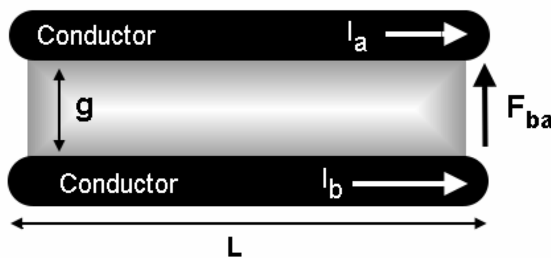

Figure 1.5: Illustration of the magnetic force attracting two parallel conductors separated by a gap. [8]

Similarly, a current-carrying conductor generates a magnetic field capable of interacting with magnetic thin films. The force generated with magnetic actuators can be large and can be used for both attracting and repelling structures. However, the power required for actuation is significantly higher than electrostatic actuation, limiting the applications for which it can be used.

Piezoelectricity is the ability of a material to generate strain linearly proportional to an applied electric field and generate surface charges when exposed to mechanical stresses. The governing equations for piezoelectricity are given in Eqs. 1.5 and 1.6:

$$S_{jk} = d_{ijk} E_i \qquad \text{Equation 1.5}$$

$$D_i = d_{ijk} T_{jk} \qquad \text{Equation 1.6}$$

where the induced strain (S_j) is proportional to the piezoelectric coefficient (d_{ij}) and the electric field (E_i) and the induced electric displacement (D_i) is proportional to the piezoelectric coefficient and the applied stress (T_j). For most thin film actuators, the piezoelectric material is sandwiched between top and bottom electrodes, and is poled the the thickness along the "3" axis. This stack is combined with an elastic layer to maximize the deformation using the transverse piezoelectric coefficient, d_{31} to produce flexure (see Figure 1.6). Thin film piezoelectric actuation offer the potential for lower actuation voltages compared to the other mechanisms, high contact force, high restoring force, and the potential for a small degree of bi-directional deformation. However, the fabrication processes for many of the large piezoelectric coefficient ceramic materials are rather complicated, primarily due to the temperature required for crystallization.

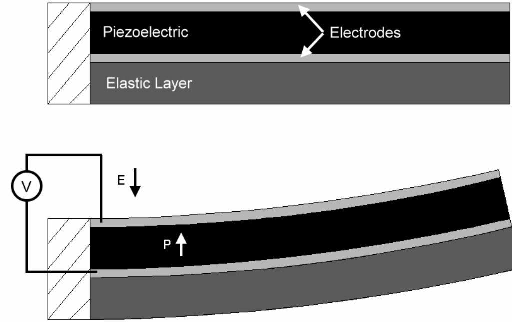

Figure 1.6: Illustration of piezoelectric actuation in a unimorph cantilever.

Another possible mechanism for electric field-induced strain in actuators is electrostriction. Whereas piezoelectricity is a linear relationship with electric field, electrostriction has a quadratic relationship with electric field where M is the electrostriction coefficient, N/m^2V^2 (see Equation 1.7).

$$S_{ij} = M_{ijkl} E_k E_l \qquad \text{Equation 1.7}$$

An additional difference is that piezoelectricity is limited to a certain class of crystals, which will be discussed in Section 1.2, whereas electrostriction can occur in any material regardless of crystal symmetry. In some materials (e.g. some of the relaxor ferroelectrics), the electrostrictive strain is on the same order as that of piezoelectric strain in PZT ceramics (about 0.1 %), however there is very little if any hysteresis, as can be seen in Figure 1.7.[9,10] Finally, many of the materials developed for electrostrictive actuators have a much lower operating temperature range compared with piezoelectrics.[9,10]

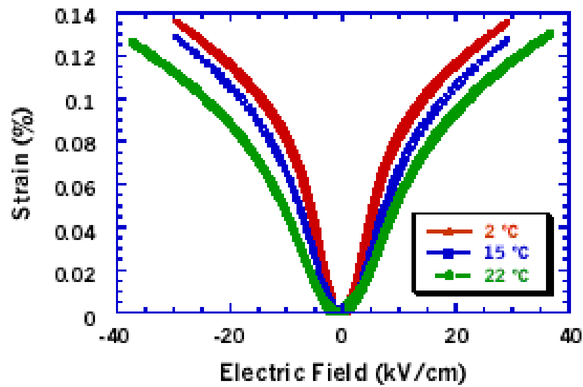

Figure 1.7: Strain electric field relationship for 3 different types of electrostrictive materials based on lead magnesium niobate-lead titanate (PMN-PT), from Reference 10.

1.1.4 Switch Performance Parameters

RF MEMS switches are judged by a handful of useful criteria. These criteria are critical for the system designer and are used to compare competing technologies. The most important parameters are discussed below in relative order of importance to the system designer.

RF measurements are typically made on a two port network analyzer and the two most important parameters are isolation and insertion loss. Isolation is a measure of the power leaking from one port to another via an open switch. By convention, isolation is the ratio of the output power to the source power reported in decibels (see Equation 1.8).[11] Power can be leaked from port to port by capacitive coupling, conductive losses at the surfaces, and mismatch losses.[11] Insertion loss is the power absorbed within the closed switch and is a measure of the incident power minus both reflected and transmitted power. Factors contributing to the insertion loss are contact resistances, conductive losses from skin effects, dielectric absorption, and reflective losses from impedance mismatches.[11] By convention, insertion loss is defined as the ratio of input signal to output signal, given in decibels (see Equation 1.9).[11] As the output power is always less than the input power, insertion loss is reported as a value greater than 0 dB. A network analyzer measures the scattering parameters, S_{ij}, reported in decibels where i represents the output port and j is the input port. The schematic in Figure 1.8 describes each of the four scattering parameters in a 2-port network analyzer. By convention, the forward

transmission coefficient, S_{21}, in the off state of a series switch is equivalent to the isolation. In the on state, the insertion loss is equivalent to the negative of S_{21}.

$$\boldsymbol{Isolation} = 10\,\mathbf{log}\left(\frac{\boldsymbol{P_{output}}}{\boldsymbol{P_{source}}}\right) \qquad \text{Equation 1.8}$$

$$\boldsymbol{Insertion\ \ Loss} = (-10)\,\mathbf{log}\left(\frac{\boldsymbol{P_{output}}}{\boldsymbol{P_{input}}}\right) \qquad \text{Equation 1.9}$$

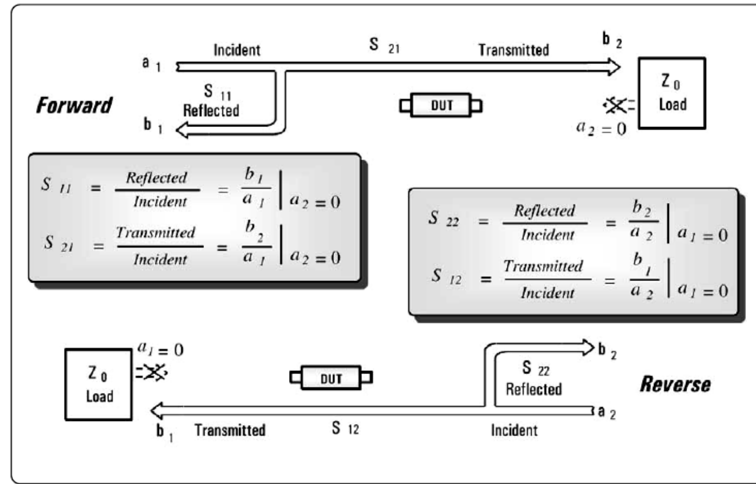

Figure 1.8: Schematic diagram of the scattering parameters, S_{ij}, measured with a 2-port network analyzer, where a_1 and a_2 is the incident power at port 1 or 2 and b_1 and b_2 represent either the reflected or transmitted power depending on the port of incident power (from Reference 11).

Switching time is a measure of the time to open (τ_{open}) and close (τ_{close}) the switch (see Figure 1.9). Depending on the switch architectures, open and closing the switch can refer to turning the circuit on and off or vice versa. The focus of this effort will be on series switches, so from hereon, the switch is “off” in the open state and “on” in the closed state. The closing time is defined as the time to transmit 90% of the incident power when the voltage is changed, whereas the opening time is the time to achieve 10% of the off state power condition.

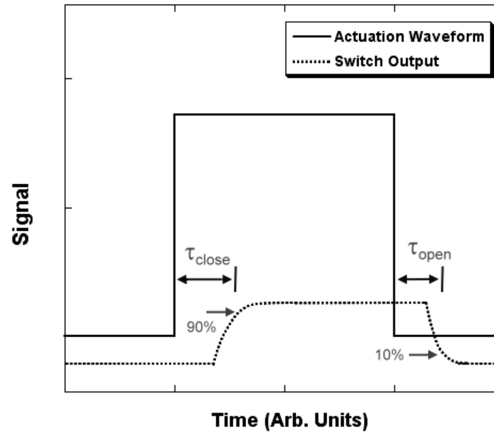

Figure 1.9: Illustration of the definition of switching time to open (τ_{open}) and close (τ_{close}) the switch.

The power handling of a switch is reported with respect to two operation modes: cold switched and hot switched. Hot switching involves operating the switch with the RF power active and is preferred in many applications because of the simplicity in the system design.[12] However, hot-switching of MEMS switches tends to degrade their lifetime as a result of arcing and thermal heating effects similar to those observed due to electrostatic discharge (ESD) events.[2,13] In contrast, cold switching removes the RF power prior to operation of the switch in both opening and closing of the contacts. Cold switching can be easier on the contact materials by removing the possibility of transient currents arcing across the miniscule gaps between the contact materials. Figure 1.10 illustrates the actuation and RF waveforms typically used for the two types of switching operation. Power handling can also be reported as a function of device cycle reliability (discussed later in this section) as high RF power degrades both ohmic and capacitive switch contacts over time.

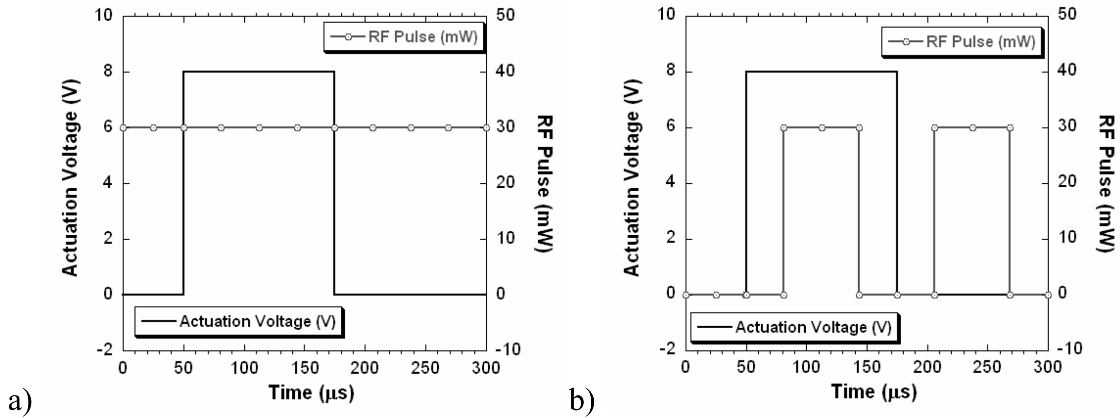

Figure 1.10: Switching operation waveforms: a) hot switch and b) cold switch

Actuation voltage is an important parameter, especially as real estate becomes a premium with further system miniaturization.[2,12] With most microelectronic devices operating at less than 5 volts, large area charge pumps are required to achieve the larger voltages required for most existing MEMS switches.[12] With electrostatic actuation, the actuation or "pull-in" voltage is easily defined as discussed previously. However, other actuation mechanisms may not possess an instability voltage that is easily defined. For this effort, the actuation voltage of the switch will be defined as the median voltage between the high current and low current state of the switch (see Figure 1.11).

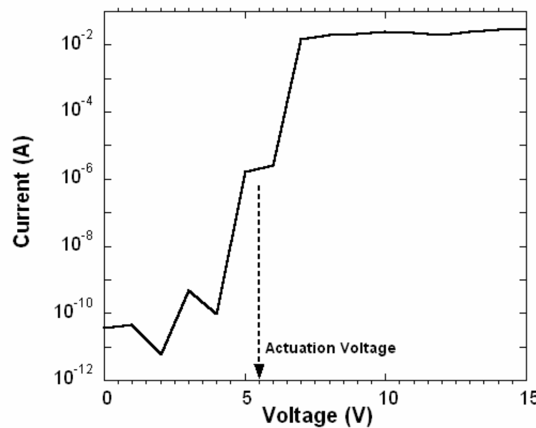

Figure 1.11: Illustration of the current draw through a piezoelectric MEMS switch as a function of applied voltage to the actuators. The actuation voltage is determined as the median voltage between the low and high current states and is indicated by the arrow.

The RF MEMS switch performance parameter receiving the most attention in recent years has been cycle reliability.[14] Depending on the application, switches are required to last from 10^6 to 10^{12} or greater cycles.[14,15,16] As with power handling, cycle reliability will strongly depend on the condition of the RF power upon switch operation, cold versus hot-switched. During cycle testing, both the open and closed switch states are monitored until there is no change observed, indicating failure.[14]

1.1.5 MEMS Switches for RF Applications

Both MEMS series and shunt switches are used in RF and millimeter wave circuits. The series switch uses a broken transmission line and is isolating in the off or open state.[2,12] The actuator is used to complete the transmission line path. Series switches are typically used from DC to 40 GHz and exhibit high isolation (-50 dB at 1 GHz, -20 dB at 40 GHz) and low insertion loss (0.1 – 0.2 dB up to 40 GHz).[2] In contrast, the MEMS shunt switch utilizes a continuous transmission line and passes RF current in the off or open state [2,12] that leads to low transmission line loss limited only by substrate and conductor loss. The actuator is used to short circuit the transmission line to ground in the on state. Shunt switches are ideally suited to higher frequency applications where low insertion loss in the off state (0.05 – 0.1 dB at 6 – 50 GHz) is extremely critical.[12,17] The shunt switch also can possess isolation better than -20 dB from 10 – 50 GHz.[2]

1.1.6 Existing Electrostatic RF MEMS Switches

In this section, examples of existing RF MEMS switches will be discussed. Electrostatic switches have received the most attention in recent years and it is worthwhile to review the leading efforts within this part of the MEMS switch community. The leading electrostatic MEMS switch researchers have each demonstrated reasonable reliability and RF performance and have begun the process of transitioning switches into higher level RF circuit elements. The devices reviewed includes those from the Radant MEMS, Raytheon, and MEMtronics Corporations, as well as one federally funded research institution, Lincoln Laboratory.

Radant MEMS has been at the forefront of MEMS switch reliability. Their first device to demonstrate greater than 100 billion cold switched cycles provided the ground work for MEMS ohmic series switches to break into the commercial and military system markets. The Radant MEMS switch, as illustrated in Figure 1.12, utilizes a thick gold cantilever to complete the circuit between the source and drain. The gate is the DC biasing line that applies the actuation voltage to pull the cantilever into contact with the drain. The gold cantilever is comprised of a 7-9 micron thick electroplated gold layer and uses a copper sacrificial layer for fabrication. The cantilever is actuated with 40 – 120 volts. In addition to the excellent reliability, this switch offers insertion loss better than 0.5 dB from DC to 40 GHz and isolation better than -20 dB (DC to 20 GHz) and better than -12 dB up to 40 GHz.[2,13]

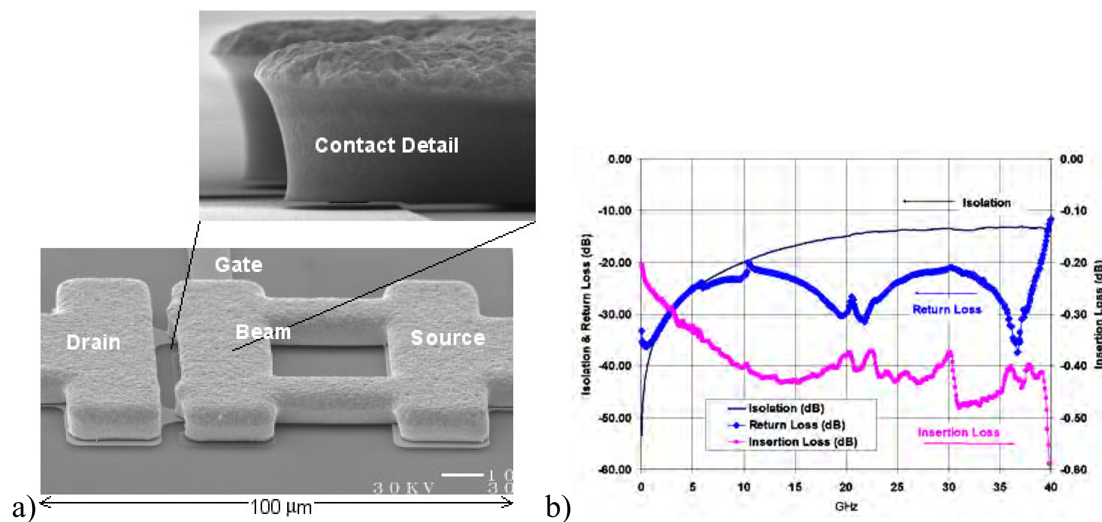

Figure 1.12: a) SEM of the Radant MEMS switch and b) switch performance from DC to 40 GHz (Image from Reference 13). Radant MEMS uses “gate” to refer to the actuation bias bad with the “source” and “drain” refer to the input and output transmission line, respectively.

In contrast to Radant MEMS, Raytheon has developed a capacitive shunt switch using a bridge membrane composed of a 0.5 micron thick aluminum freestanding structure. The bridge membrane is fabricated using sacrificial photoresist and requires 30 to 50 volts for actuation. Figure 1.13 illustrates a Raytheon MEMS switch using a continuous thin dielectric film atop the transmission line. This shunt switch has an

insertion loss better than 0.5 dB from DC to 40 GHz in the unactuated state and an isolation better than -20 dB above 10 – 15 GHz. Below 10 GHz, the isolation is limited by the effective "on" state capacitance of the dielectric film.[2,18]

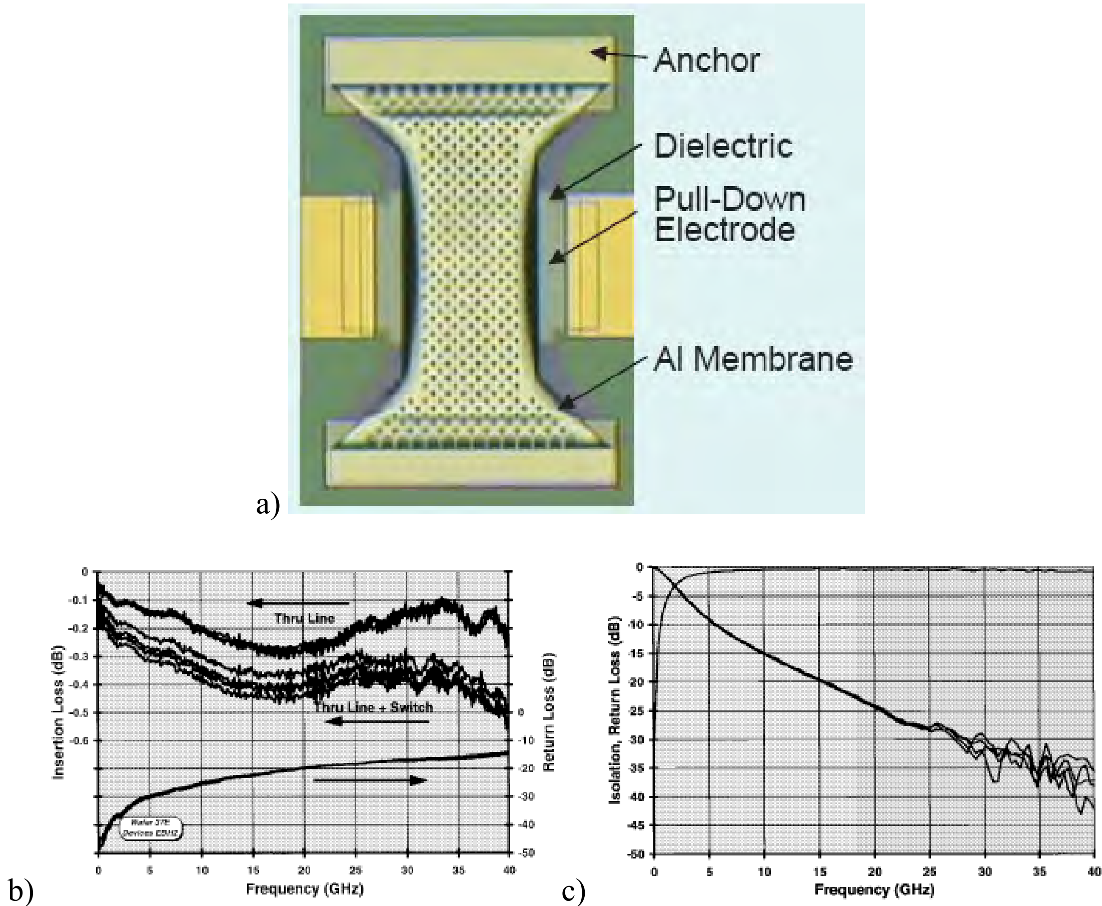

Figure 1.13: a) Image of the Raytheon MEMS switch and b) unactuated and c) actuated switch performance from DC to 40 GHz (images from Reference 18).

Similar to Raytheon, MEMtronics has developed a capacitive shunt switch. One noticeable difference in the two technologies is the recent advances from MEMtronics using a discontinuous dielectric film to minimize the effect of dielectric charging that ultimately controls the lifetime.[19] Instead of the continuous film, the dielectric is patterned into separate posts to reduce the volume of dielectric that can contribute to dielectric charging (see Figure 1.14). The trade-off is in a reduced "on" or actuated state capacitance. However, the switch is still capable of achieving a capacitance ratio (on

state over off state) of 2 to 1, which is the minimum required for phase shifters.[2,4] Because of the similarities to the Raytheon switch, its performance parameters are very similar except for the capacitance ratio.[2]

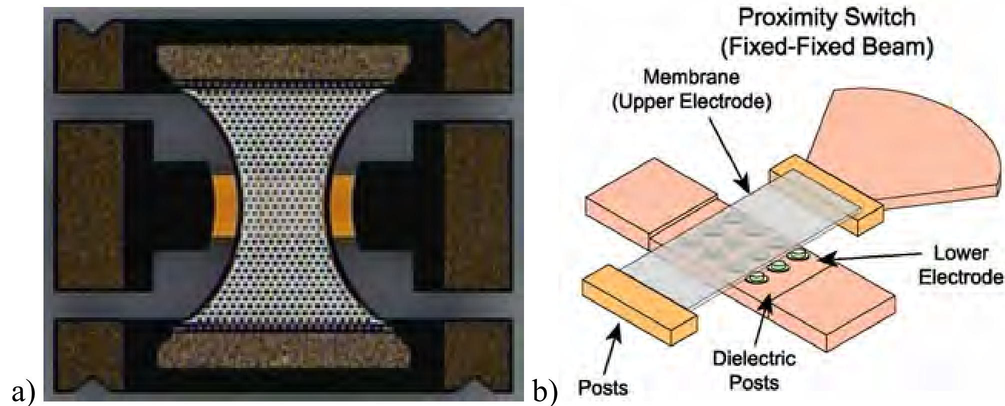

Figure 1.14: a) Image of the MEMtronics capacitive shunt switch and b) a schematic description of the proximity switch with individual dielectric posts for improved dielectric charging resistance (images from Reference 19).

One of the more unique switches developed over the past few years has been the Lincoln Laboratory inline switch. Capable of being configured as either an ohmic or capacitive contact, this switch utilizes the benefits of residual stress engineering to create a structure that has a large vertical gap but yet can be actuated with 30 to 80 volts (see Figure 1.15). As with the Raytheon and MEMtronics switch, this switch uses a photo-definable organic as a sacrificial layer, polyimide in this case. Both the capacitive and ohmic version of this switch have an isolation (S_{21}) of better than -20 dB from DC up thru 20 – 30 GHz. The ohmic version has an insertion loss better than 0.5 dB from DC to 40 GHz, while the capacitive version has an insertion loss better than 0.7 dB from 5 to 40 GHz.[2,20]

These examples illustrate the current state of the art with electrostatically actuated RF MEMS switches. There exist many other examples of functioning electrostatic MEMS switches but none of them have reported as extensively on the achievable reliability, RF performance data, and integrated packaging approaches.

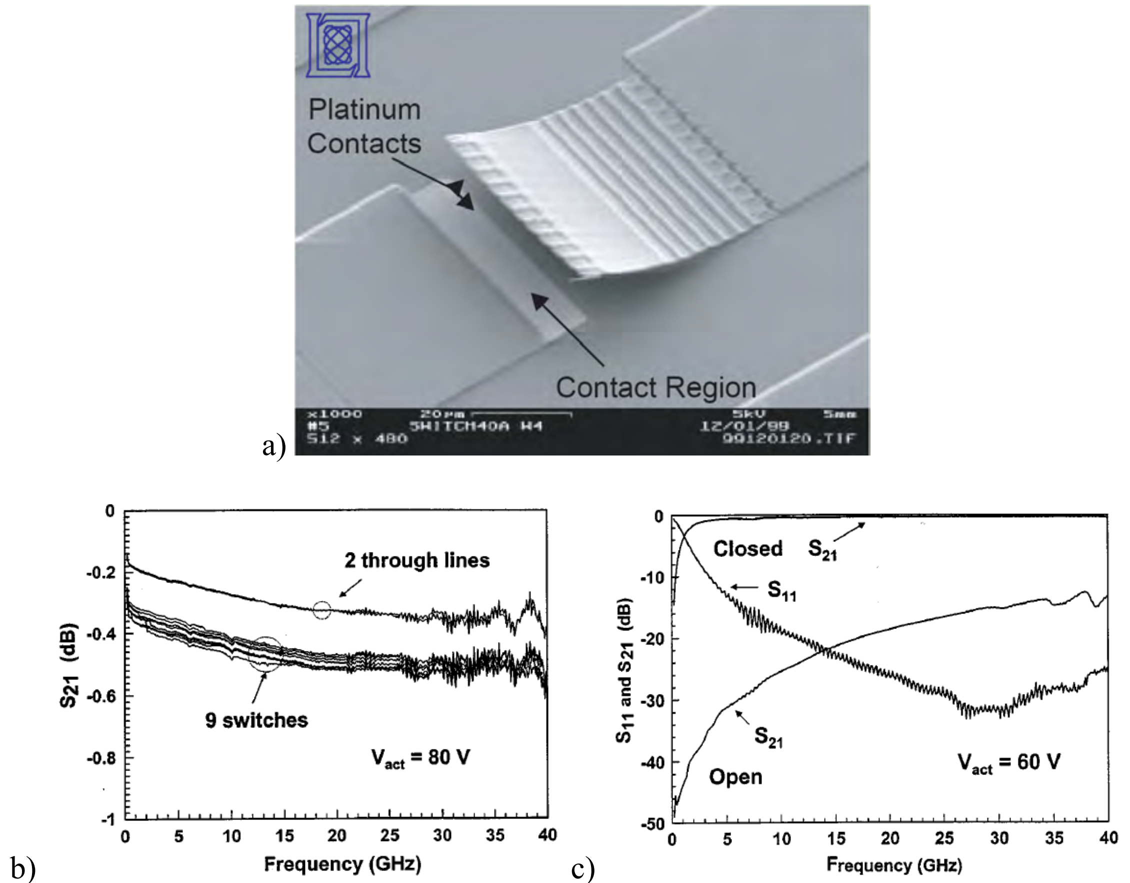

Figure 1.15: a) SEM of the Lincoln Laboratory inline ohmic series switch along with performance of b) ohmic switch and c) a capacitive series switch (from References 7and 20).

1.1.7 Reducing the Actuation Voltage

One of the key limitations of the electrostatic actuation is the inability to combine a low actuation voltage with excellent RF performance and reliability. Attempts to lower the actuation voltage with electrostatic switches generally rely on reducing either the mechanical stiffness of the released structures or the gap between the mechanical bridge/cantilever and the corresponding biasing pad.[22] Reductions in the stiffness can limit the restoring force of the switch and can lead to stiction failures.[21] Decreasing the electrode gap limits the RF performance (in particular, the isolation in the open state for series switches).[2] Peroulis et al. demonstrated electrostatic switches with less than 10 volts using a series of meandering springs to increase the compliance of the structure.[22]

However, the reliability and RF performance suffered as a result of reducing the spring constant of the actuated beam or membrane.

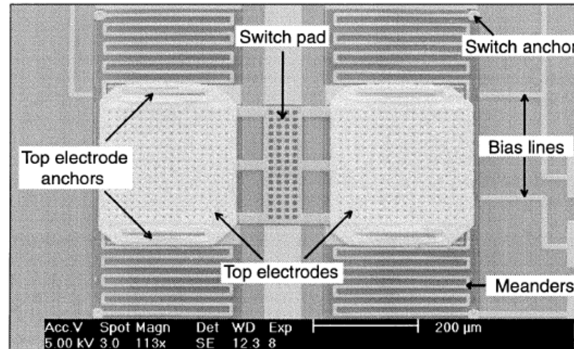

Figure 1.16: SEM image of a compliant electrostatically actuated RF MEMS switch with an actuation voltage as low as 6 volts (from Reference 22).

Alternative actuation mechanisms (including thermal, magnetic, and piezoelectric) have begun to be investigated in an attempt to lower the actuation voltage required while maintaining large restoring forces and excellent RF performance. However, thermal and magnetic actuation approaches require significant power (10 – 100's mW) for operation and are much slower than electrostatic switches. [2] On the other hand, piezoelectric actuation requires extremely low currents ($<10^{-8}$ A) and voltages (<10 V) for operation for an overall power consumption in the hundreds of picowatt range. Combined with the ability to close large vertical gaps and low microsecond switching time, piezoelectric MEMS switches have great potential. At present, their use has been limited because of the fabrication challenges associated with using high performance piezoelectric films.

1.2 Piezoelectricity

This section reviews the fundamentals of piezoelectricity with specific reference to polar materials that are both ferroelectric and piezoelectric. This review is meant to give the reader an understanding of the fundamental principles the enable piezoelectricity in certain materials. Then a detailed discussion on the properties of lead zirconate

titanate (PZT) ceramics and thin films will be undertaken. This section will conclude with examples of existing research efforts aimed at creating piezoelectrically actuated MEMS switches with PZT thin films.

Piezoelectricity allows a material to develop an electric charge when an external stress is applied to it or generate a strain that is directly proporational to the applied electric field, as is discussed in section 1.1.3. This property is limited to a small subset of materials. Examination of the 32 point groups shows that only 20 point groups may be piezoelectric.[23] Of these 20, 10 of the point groups can be classified as polar materials in which an electric dipole moment can be present in the absence of an electric field. If the spontaneous polarization changes with temperature the material is pyroelectric. Within pyroelectric materials, there is a special class of materials in which the spontaneous polarization can be permanently reoriented between crystallographically defined states with an applied electric field. This is the key parameter that distinguished ferroelectric materials from materials which are only polar.

1.2.1 Ferroelectric Materials

The identification of ferroelectric behavior in Rochelle salt in 1928 led to numerous research initiatives on this subject. Over the past 70^+ years, considerable progress has been made in topics such as phenomenology, the basis of ferroelectricity, and the development of useful devices. This section reviews some of the fundamental aspects of ferroelectricity.

As stated above, a ferroelectric material is one in which a spontaneous electric dipole moment can be re-oriented between crystallographically defined stable states by a realizable electric field (i.e. before dielectric breakdown occurs).[24] In the perovskite structure, ABO_3 (see Figure 1.17), where, in general, A is a divalent ion and B is a tetravalent ion, the cubic lattice can undergo distortions at lower temperatures. Some of these distortions result in a shift of the octahedrally coordinated cation from the center of the unit cell. Consequently, a dipole moment is created between the center of negative charge created by the oxygen octahedra and the center of positive charge. For lead

zirconate titanate ($Pb(Zr_xTi_{1-x})O_3$), the shift in position of the A-site, Pb^{+2} ions, as well as the oxygen ion contributes to the dipole properties (see Figure 1.18).[25]

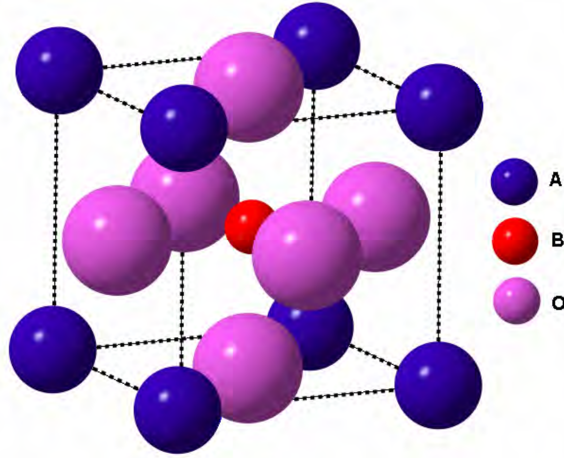

Figure 1.17: Representation of the cubic (Pm3m) prototype structure of perovskite ABO_3 structure.

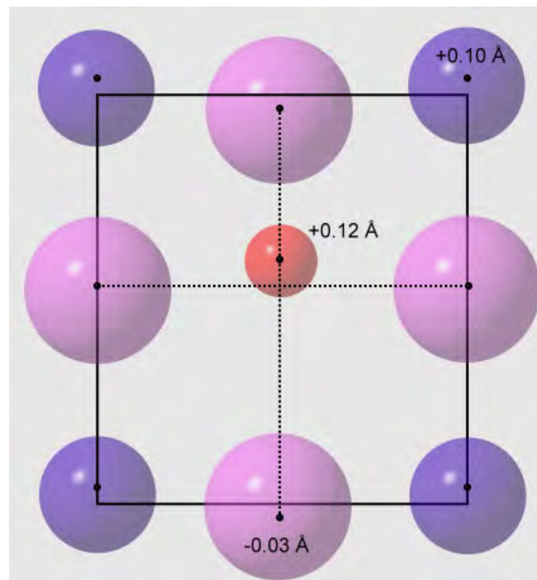

Figure 1.18: Illustration of a tetragonal distortion resulting in a positive shift of the A (0.10 Å) and B (+0.12 Å) ions and a slight negative shift of the oxygen ion (-0.03 Å) for $BaTiO_3$ (values taken from Reference 28).

In perovskites, the development of the dipole occurs at a phase transition from a non-polar paraelectric state to a polar ferroelectric state. In many instances the transition at the Curie temperature (T_c) is associated with a structural change from a centrosymmetric cubic phase to a non-centrosymmetric distorted phase. Additional transitions temperatures can exist between two non-centrosymmetric distorted phases (e.g. tetragonal to orthorhombic or orthorhombic to rhombohedral). Figure 1.19 illustrates the lattice distortions that yield the observed structural changes in barium titanate ($BaTiO_3$). Expansion of the cubic unit cell along the [001] direction results in a tetragonal structure while an expansion along the [011] results in an orthorhombic structure and an expansion along the [111] direction results in a rhombohedral structure.

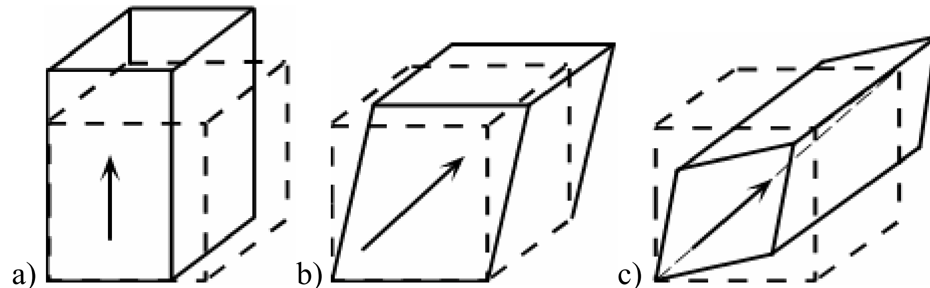

Figure 1.19: Lattice distortions that occur upon cooling below T_c in perovskites: a) In the tetragonal phase, P_s develops along [001] of the original cubic structure, b) in the orthorhombic phase, P_s occurs along [011], and c) in the rhombohedral phase, P_s develops along [111]. The dotted cubes are for the cubic prototype; the solid lines show the distorted unit cells of the ferroelectric phases (images adopted from Reference 26).

The polarization generated at T_c can be permanently re-oriented into different equilibrium states with an applied electric field, leading to the most recognizable aspect of ferroelectricity: the polarization electric field hysteresis loop (see Figure 1.20). This loop results from the change in net polarization of the material as the amplitude and direction of the applied electric field are changed. The polarization electric field hysteresis loop is a fundamental aspect of ferroelectricity and illustrates the reorientability of the dipole moment.

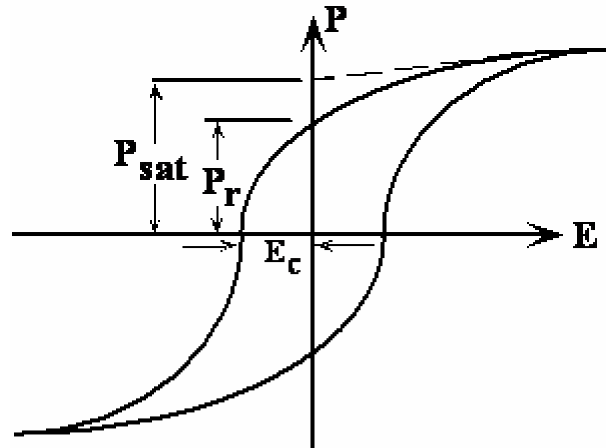

Figure 1.20: Schematic of the polarization electric field hysteresis loop illustrating the saturation polarization (P_{sat}), remanent polarization (P_r), and coercive field (E_c) (adapted from Reference 26).

The saturation polarization, P_{sat}, is defined as the linear extrapolation of the high field polarization to zero field and approximates the maximal amount of dipole alignment achieved at a given electric field. The remanent polarization, P_r, is the retained polarization at zero electric field. For an ideal material, the two polarization values are equal. The coercive field, E_c, is the electric field which results in a net zero polarization and has both a positive and negative value corresponding to each location the loop crosses the field axis.

Upon cooling below T_c, a spontaneous polarization develops in each unit cell of the material. All adjacent cells within a region polarized in the same direction (or at least nearly so) comprise a domain. Domains form both to minimize depolarization energy and stresses present.[26] These domains have polarization orientations that are dictated by the prototype unit cell and the symmetry elements lost at the phase transformation. For PZT, which can possess either a tetragonal, rhombohedral, or monoclinic ferroelectric phase depending on the Zr:Ti ratio, the polarization direction is along the original <001>, <110>, or <111> axes of the cubic prototype, respectively (see Figure 1.21).[26,27] Tetragonally distorted PZT possesses 6 equivalent polarization directions, while rhombohedral distortions have 8 equivalent directions. Domain boundaries (walls) form between adjacent domains of differing polarization directions. These domain walls lie on specific crystallographic planes that minimize the strain across the wall. Tetragonally

distorted perovskites possess 90° and 180° domain walls, while rhombohedral perovskites have 71°, 109°, and 180° domain walls.[28]

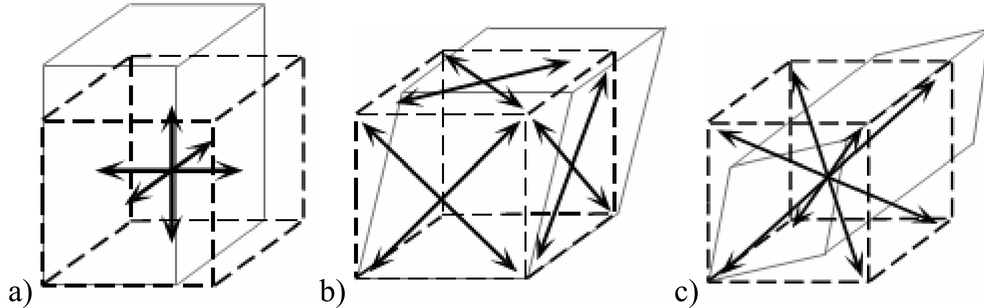

Figure 1.21: Possible polarization directions relative to the cubic prototype for a) tetragonal perovskite with 6 equivalent <001> directions, b) orthorhombic distortion with 12 equivalent <110> directions, or c) rhombohedral with 8 equivalent <111> directions.

Most ferroelectrics possess a very high relative permittivity (ε_r) or dielectric constant (K). Nominally, the dielectric constant is the ratio of the material permittivity (ε) to the permittivity of free space (ε_o),

$$\varepsilon_r = K = \frac{\varepsilon}{\varepsilon_o}. \qquad \text{Equation 1.10}$$

Under ac electrical fields, the dielectric constant can be described as a complex number with in phase and out of phase components with respect to the applied voltage. The out of phase component is primarily due to dielectric absorption, resistive leakage, and domain wall motion. The dielectric loss, represented as D or tan δ, is the ratio of the out of phase and in phase components.[28] The dielectric constant and dielectric loss are very important parameters for determining a material's usefulness as a capacitor (i.e. its ability to store electric charge).

1.2.2 Phenomenology

Many of the physical properties of ferroelectric materials can be described via phenomenology.[29] The brief review here is intended to provide the reader with knowledge of the fundamental principles governing ferroelectricity. The descriptions generated by phenomenology are strictly valid for single domain specimens.

A piezoelectric is a polarizable deformable solid and in thermodynamic equilibrium the system can be characterized by a set of independent variables including electric field (E_m), stress (X_{ij}), and temperature (T).[29] Additionally, the independent variables uniquely determine a set of dependent variables: dielectric displacement (D_m), strain (x_{ij}), and entropy. In the descriptions following, dielectric displacement is replaced by polarization (P_m) through the following relation:

$$P_m = D_m - \varepsilon_o E_m \qquad \text{Equation 1.11}$$

Using the set of independent and dependent variables, a set of thermodynamic potentials (see Table 1.2) develop. These potentials can be used to describe many of the basic material properties by taking the partial derivatives of the thermodynamic potentials.

Reviewing the full Gibbs free energy, the following Maxwellian relations result from the first partial derivative:

$$-S = \left(\frac{\delta G}{\delta T}\right)_{XE}, \quad x_{ij} = \left(\frac{\delta G}{\delta X_{ij}}\right)_{TE}, \quad -P_m = \left(\frac{\delta G}{\delta E_m}\right)_{TX}. \qquad \text{Equation 1.12}$$

Continuing with the second partial derivatives leads to a phenomenological depiction of specific heat (Equation 1.13), elastic compliance (Equation 1.14), and dielectric permittivity (Equation 1.15).

Table 1.2: Thermodynamic potentials for a polarizable deformable solid with the boundary conditions for each potential. The independent variables are temperature (T), stress (X_{ij}), and electric field (E_m) while the dependent variables are polarization (P_m), strain (x_{ij}), and entropy (S).[29]

Thermodynamic Potentials		Boundary Conditions
Helmholtz Free Energy	$\delta A = -S\delta T - X_{ij}\delta x_{ij} + E_m\delta P_m$	T x P
Enthalpy	$\delta H = T\delta S + x_{ij}\delta X_{ij} - P_m\delta E_m$	S X E
Elastic Enthalpy	$\delta H_1 = T\delta S + x_{ij}\delta X_{ij} + E_m\delta P_m$	S X P
Electric Enthalpy	$\delta H_2 = T\delta S - X_{ij}\delta x_{ij} - P_m\delta E_m$	S x E
Full Gibbs Free Energy	$\delta G = -S\delta T + x_{ij}\delta X_{ij} - P_m\delta E_m$	T X E
Elastic Gibbs Free Energy	$\delta G_1 = -S\delta T + x_{ij}\delta X_{ij} + E_m\delta P_m$	T X P
Electric Gibbs Free Energy	$\delta G_2 = -S\delta T - X_{ij}\delta x_{ij} - P_m\delta E_m$	T x E
Internal Energy	$\delta U = T\delta S - X_{ij}\delta x_{ij} + E_m\delta P_m$	S x P

$$\left(\frac{\delta^2 G}{\delta T^2}\right)_{XE} = -\left(\frac{\delta S}{\delta T}\right)_{XE} = -\frac{c_{x_{ij}E_m}}{T} \quad \text{Equation 1.13}$$

$$\left(\frac{\delta^2 G}{\delta X_{kl}{}^2}\right)_{TE} = \left(\frac{\delta x_{ij}}{\delta X_{kl}}\right)_{TE} = s_{ijkl} \quad \text{Equation 1.14}$$

$$\left(\frac{\delta^2 G}{\delta E_m{}^2}\right)_{TX} = -\left(\frac{\delta P_m}{\delta E_m}\right)_{TX} = \varepsilon_o \quad \text{Equation 1. 15}$$

In addition to these direct relationships relating E and P, X and x, and T and S, mixed relationships can be generated by taking the second partial with respect to one of the remaining boundary variables. The relations focused on in this thesis will involve those relating electromechanical properties (i.e. relating E and P to X and x). Again starting with the Gibbs free energy the following electromechanical relationships develop:

$$\left(\frac{\delta^2 G}{\delta E_m \delta X_{ij}}\right)_T = -\left(\frac{\delta x_{ij}}{\delta E_m}\right)_{XT} \qquad \text{Equation 1.16}$$

$$\left(\frac{\delta^2 G}{\delta X_{ij} \delta E_m}\right)_T = \left(\frac{\delta P_m}{\delta X_{ij}}\right)_{ET} \qquad \text{Equation 1.17}$$

$$\left(\frac{\delta^2 G}{\delta E_m \delta X_{ij}}\right)_T = -\left(\frac{\delta x_{ij}}{\delta E_m}\right)_{XT} = \left(\frac{\delta P_m}{\delta X_{ij}}\right)_{ET} = d_{mij} \qquad \text{Equation 1.18}$$

The result is Equation 1.18 equating the second partial derivative of the Gibbs free energy equation to one of the four piezoelectric coefficients, d_{mij}. The remaining piezoelectric coefficients are derived from the remaining thermodynamic potentials in a similar manner and are located in Table 1.3.

Table 1.3: Thermodynamically derived definitions of the four piezoelectric coefficients: d_{mij}, g_{mij}, e_{mij}, h_{mij}.[29]

$$\left(\frac{\delta^2 A}{\delta P_m \delta x_{ij}}\right)_T = -\left(\frac{\delta X_{ij}}{\delta P_m}\right)_{xT} = \left(\frac{\delta E_m}{\delta x_{ij}}\right)_{PT} = h_{mij}$$

$$\left(\frac{\delta^2 H}{\delta E_m \delta X_{ij}}\right)_S = -\left(\frac{\delta x_{ij}}{\delta E_m}\right)_{SX} = \left(\frac{\delta P_m}{\delta X_{ij}}\right)_{SE} = d_{mij}$$

$$\left(\frac{\delta^2 H_1}{\delta P_m \delta X_{ij}}\right)_S = -\left(\frac{\delta x_{ij}}{\delta P_m}\right)_{SX} = \left(\frac{\delta E_m}{\delta X_{ij}}\right)_{SP} = g_{mij}$$

$$\left(\frac{\delta^2 H_2}{\delta E_m \delta x_{ij}}\right)_T = -\left(\frac{\delta X_{ij}}{\delta E_m}\right)_{Sx} = -\left(\frac{\delta P_m}{\delta x_{ij}}\right)_{SE} = e_{mij}$$

$$\left(\frac{\delta^2 G}{\delta X_{ij} \delta E_m}\right)_T = -\left(\frac{\delta P_m}{\delta X_{ij}}\right)_{TE} = -\left(\frac{\delta x_{ij}}{\delta E_m}\right)_{TX} = d_{mij}$$

$$\left(\frac{\delta^2 G_1}{\delta P_m \delta X_{ij}}\right)_T = -\left(\frac{\delta x_{ij}}{\delta P_m}\right)_{TX} = \left(\frac{\delta E_m}{\delta X_{ij}}\right)_{TP} = g_{mij}$$

$$\left(\frac{\delta^2 G_2}{\delta E_m \delta x_{ij}}\right)_T = -\left(\frac{\delta X_{ij}}{\delta E_m}\right)_{Tx} = \left(\frac{\delta P_m}{\delta x_{ij}}\right)_{TE} = e_{mij}$$

$$\left(\frac{\delta^2 U}{\delta P_m \delta x_{ij}}\right)_S = \left(\frac{\delta X_{ij}}{\delta P_m}\right)_{Sx} = \left(\frac{\delta E_m}{\delta x_{ij}}\right)_{SP} = h_{mij}$$

The tensor notation for the aforementioned relationships can be simplified using matrix notation where the subscripts i,j,k,l,m having values 1 – 3 are replaced with the subscripts p and q with values of 1 – 6.[30] As a result, d_{mij} is transformed to d_{ip}. The d_{ip}

and e_{iq} coefficients are the most useful for actuator applications and are related by the stiffness coefficient, c^E_{pq}, by Equation 1.19.

$$e_{iq} = d_{ip} c^E_{pq} \qquad \text{Equation 1.19}$$

For thin films, the out of plane stress, X_3, is always zero while the longitudinal strain, x_3, varies from a combination of the piezoelectric effect and elastic coupling from the Poisson effect. As a result, the thin film piezoelectric coefficient, $e_{31,f}$, can be related to the common piezoelectric coefficients, d_{mij} and e_{mij} (see Equation 1.20).[31,32,33]

$$e_{31,f} = e_{31} - \frac{c^E_{31} e_{33}}{c^E_{33}} = \frac{d_{31}}{\left(s^E_{11} + s^E_{12}\right)} \qquad \text{Equation 1.20}$$

1.2.3 Lead Zirconate Titanate (PZT)

Most solid solutions between $PbZrO_3$ and $PbTiO_3$ possess ferroelectricity and show excellent piezoelectric properties. By varying the Zr^{+4}/Ti^{+4} ratio, both the ferroelectric and piezoelectric properties can be altered significantly. The phase diagram in Figure 1.22 illustrates the structural changes that occur as a result of composition variations. Substitutions of Zr^{+4} for Ti^{+4} in $PbTiO_3$ reduce the tetragonal distortion and cause the structure to become rhombohedral.[26] As seen in the phase diagram, the shift from a tetragonal to a rhombohedral structure occurs at a morphotropic phase boundary (MPB) near the Zr^{+4}/Ti^{+4} ratio of 52/48. A MPB denotes an abrupt structure change with composition at a constant temperature.[28] From phase equilibrium, the MPB is required to be a two-phase mixture of the tetragonal and rhombohedral structures. The presence of both of these structures in this region gives the material an increased number of polarization directions. For MPB compositions, the high polarizability results in extremely large dielectric and piezoelectric properties, as seen in Figure 2.6.[34] The

presence of such large piezoelectric properties near the MPB make PZT an extremely attractive candidate for piezoelectric devices.

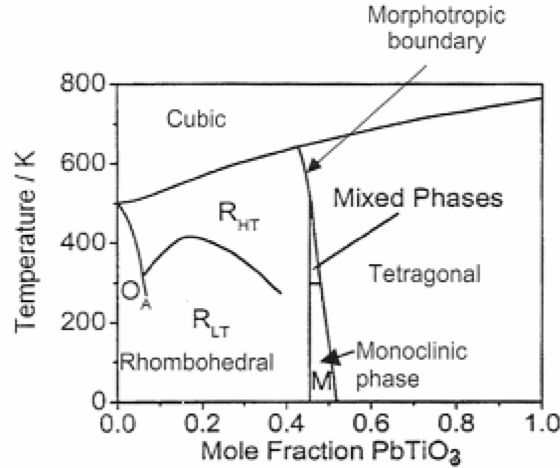

Figure 1.22: Phase diagram for the lead zirconate - lead titanate solid solution (from References 27).

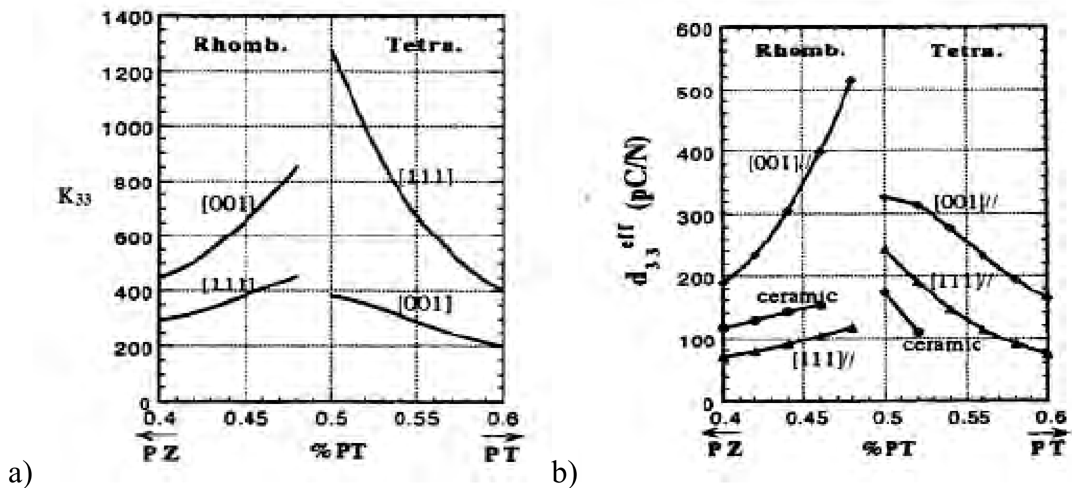

Figure 1.23: Variation in relative permittivity (K_{33}) and the effective piezoelectric coefficient (d_{33}) as a function of the Zr/Ti ratio and orientation for bulk PZT (from Reference 34). The data given for specific orientations are from phenomenological calculations.

The piezoelectric properties of PZT are substantially better than those of more common piezoelectric materials used for MEMS application (see Table 1.4). Both ZnO and AlN are used because of their compatibility with CMOS and relative ease of

fabrication. The high temperature annealing and/or deposition conditions required for high quality PZT thin films limit the possibility for full integration with CMOS and other microelectronic devices. One area that AlN thin films have been examined extensively used is thin film bulk acoustic resonators (FBAR) and they appear ideally suited for this application.[35,36] However, for actuator applications, the significantly lower $e_{31,f}$ of ZnO and AlN gives the advantage to PZT.

Table 1.4: Comparison of thin film piezoelectric materials with calculated single crystal and bulk ceramic values[37]

	ZnO	AlN	PZT
e_{31} (C/m^2)	-0.57	-0.58	-3.0
$e_{31,f}$ calculated	-1.2	-1.05	-16
measured	-0.47	-0.9	-8 .. -10
	-0.43	-1.0	PZT45/55(111)
	-0.80		
	-0.60		PZT40/60(100)
			PZT52/48
d_{33} (pC/N)	12.4	5.0	223
$d_{33,f}$ calculated	7.5	3.9	144
measured	10-12	3.4-3.9	90 (52/48)
			100 (45/55)
ϵ_{33}	10.9	10.7	1200
$\epsilon_{33,f}$ calculated	9.5	10.1	650
$\epsilon_{33,f}$ measured	8-12	10.4	1300 (52/48)

1.2.4 PZT Thin Film Technology

With the drive toward miniature devices, thin film technology has exploded with the development of numerous techniques for depositing thin films. These techniques include chemical vapor deposition, chemical solution deposition, pulsed laser deposition, reactive evaporation, molecular beam epitaxy, and various sputtering procedures. While many of these techniques can be adapted to deposition of multicomponent oxides, chemical solution deposition allows relatively straightforward control of film composition. Additionally, chemical solution deposition enables homogeneous coating over large areas and is easy and cheaper than most methods because it does not require the use of expensive vacuum equipment.[38]

It has been demonstrated by several groups that PZT thin films possess smaller piezoelectric coefficients than bulk ceramics.[39,40,41] One reason for the large deviation from bulk ceramics is clamping of the film to the substrate. The substrate prohibits the

film from expanding or contracting freely in the plane, reducing the amount of observed mechanical strain.[42] Another factor reducing the piezoelectric response may be the limited number or mobility of non-180° domain walls, which can contribute ~50% to the bulk piezoelectric coefficients.[43,44,45]

The most recent work on chemical solution deposited PZT thin films have resulted in effective transverse piezoelectric coefficients, $e_{31,f}$, approaching that of undoped PZT bulk ceramics.[46] Using optimization of the surface nucleation for texture control of the (100) oriented thin films combined with optimized solution chemistry, Muralt et al. have been able to achieve values of -10 to -12 Cm^{-2} approaching that of PZT 4D bulk values.[47] More recent efforts by the same group have demonstrated thin film values as high as -16 Cm^{-2}, although no details about the processing conditions have been released thus far.[48]

1.2.5 PZT Based MEMS Switches

Shortly after the turn of the century, researchers began investigating how to utilize PZT thin film actuators for MEMS switching applications. Hoffmann et al. fabricated a lead zirconate titanate (PZT) thin film actuator for a micromachined switch.[49] Additional work by this same group focused on actuator design for switches, but without any published data pertaining to a functioning switch.[50] The first functioning DC relays were demonstrated by Gross et al. using in-plane poled PZT film actuators.[51] These devices used a cantilever beam with a supporting elastic layer, a PZT thin film as the actuator, and patterned gold structures to act as the electrodes (see Figure 1.24). This device operated as low as 20 V with a switching on time as low as 2 μs.

The first reported working RF MEMS switch using PZT thin films used bulk micromachining to release a unimorph actuator and a suspended transmission line.[52,53] This design utilized a cantilever that is perpendicular to the wave propagation direction along the RF conductor of the co-planar waveguide (CPW). The switch operates as low as 2.5 volts with an insertion loss better than 0.7 dB and isolation better than -21 dB up to 20 GHz (see Figure 1.26).

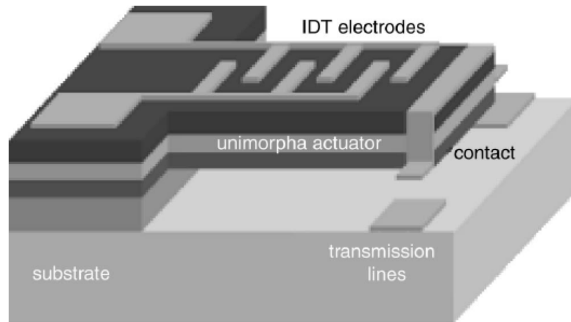

Figure 1.24: Illustration of a low frequency thin film PZT unimorph switch developed at Penn State University (from Reference 51).

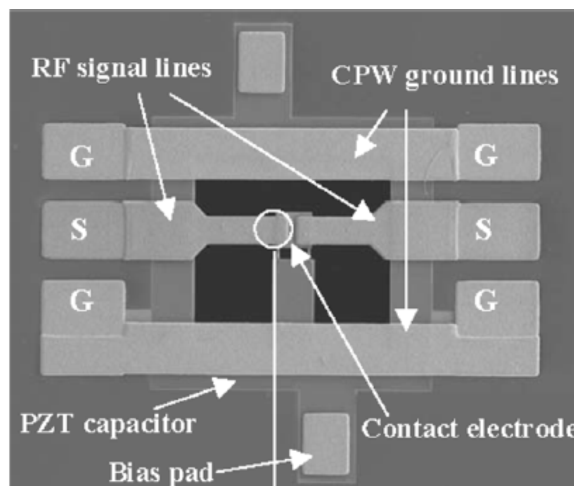

Figure 1.25: SEM image of a bulk micromachined RF MEMS series switch using a thin film PZT actuator to complete the signal path (from References 52 and 53).

Another functioning switch has been recently published that requires the use of two wafers.[54] The first wafer has the PZT actuators which act upon a seesaw actuator. The seesaw actuator then makes contact with the end of a transmission line to complete the RF circuit (see Figure 1.27). Although the fabrication process is quite complicated, this switch offers an integrated package assembly with a functioning switch. Performance data was only reported up to 10 GHz but this device does show reasonable insertion loss (0.5 dB at 5 GHz) and isolation better than -28 dB from DC up to 10 GHz.

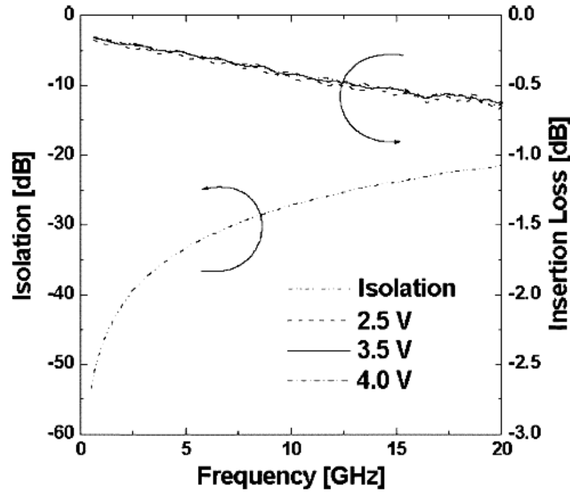

Figure 1.26: RF performance of a bulk micromachined PZT RF MEMS series switch (from References 52 and 53).

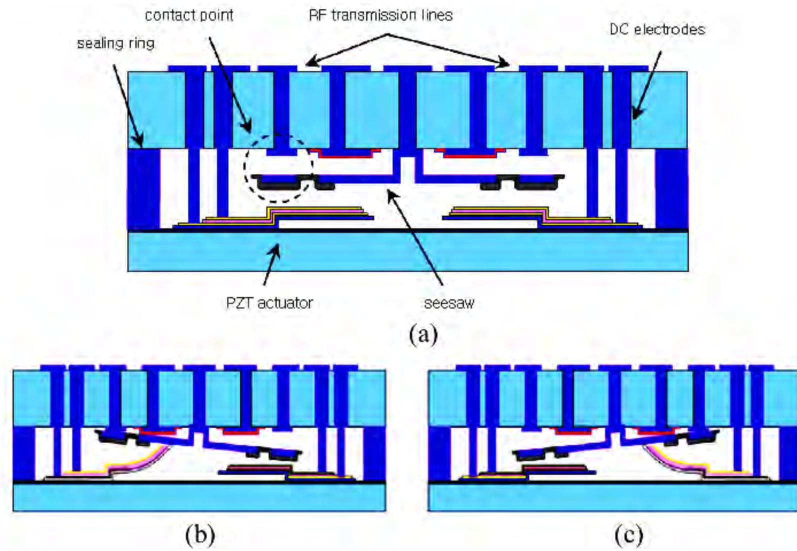

Figure 1.27: Schematic illustrating the operating principle of the PZT actuated seesaw switch: a) is the normal (off) state, b) the left actuator is "on", and c) the right actuator is "on" (image from Reference 54).

One limitation with the existing research has been the successful demonstration of a surface micromachined switch with integrated PZT actuators. Surface micromachining is substantially cheaper and easier to integrate with other fabrication processes than bulk micromachining techniques.[55,56] In addition, a major of the advances in hermetic wafer

level packaging approaches are more amenable to surface micromachined devices.[2] Moreover, the existing work has not yet demonstrated an ability to function at the frequencies required for many phased array radar and communication systems (20 – 40^+ GHz). These points will be addressed in subsequent chapters of this thesis.

1.3 MEMS Ohmic Switch Contacts

A key issue with ohmic switches is the contact materials. The contact materials combined with the contact force determine the contact resistance that can be achieved and in turn the RF performance (insertion loss for a series switch). This section covers a few of the key issues with microrelay contacts and their impact on device reliability.

1.3.1 Contact Area and Resistance

Contact area is the key feature in the design of MEMS contact design.[57] The contact area determines the constriction resistance, the increase in resistance associated with the narrowing of a electric current line at the contact,[58] associated with the switch contact. Higher contact areas result in lower resistances. The actual contact area consists of either one asperity or small number of asperities of similar size.[21,59] Further refinements combining elastic deformation, plastic deformation, and even elastic-plastic deformation models can be used to determine the contact area as a function of contact force (F_c) and the contact materials hardness (Meyer's Hardness - H_M).[60] As an example, the contact radius (r) of a singular circular contact assuming plastic deformation of the contacting surfaces is given by Equation 1.21.[58]

$$\boldsymbol{r = \sqrt{\frac{F_c}{H_M \pi}}} \qquad \text{Equation 1.21}$$

The contact resistance (R_c) is the summation of the constriction resistance (R_{ct}) and the contamination resistance (R_{contam}) as illustrated by Equation 1.20. [61,61]

$$R_c = R_{ct} + R_{contam} \qquad \text{Equation 1.22}$$

This equation highlights the direct effect contact contamination have on the overall contact resistance of a switch. The constriction resistance can be calculated assuming various types of deformation in the contacting surfaces. For a single circular contact undergoing plastic deformation, the constriction resistance assuming diffusive transport ($R_{ct\,DP}$) is described by Equation 1.23 where ρ is the resistivity.[61]

$$R_{ct\,DP} = \frac{\rho}{2}\sqrt{\frac{H_M \pi}{F_c}} \qquad \text{Equation 1.23}$$

Thus, in order to minimize contact resistance, it is desirable to use low hardness, high conductivity metals such as gold combined with a high contact force. As a result, a majority of MEMS switches use gold contacts.[2] The next section will discuss some of the disadvantages with gold contacts.

1.3.2 Contact Materials

The second item of interest for MEMS contacts is the adherence force between the contact metals.[57] After the contacting surfaces come into contact, this adhesion force maintains contact between the two surfaces. At initial contact, asperities are the first to contact. Subsequently, either under higher contact forces or higher temperatures, the asperities deform plastically. As the contacts deform plastically, material can be transferred between the contact surfaces. Material transfer can be crucial when separating the contacts. In order to separate the contacts, the adhesion forces need to be overcome. It has been reported that the adhesion forces can be as high as 40% of the closure forces.[59]

As mentioned in the previous section, contact material hardness is critical for determining the contact area as well as the contact resistance that can be achieved. Gold is a common contact material because of its high conductivity. However, gold also has a high adhesion coefficient.[60,62] An alternative is to use refractory metals, such as platinum and ruthenium.[21,59,61,63] These materials have lower electrical conductivities and are harder than gold, so the contact resistances will be greater than for gold contacts at the same contact force. However, if the contact force is increased into the plastic regime, the lower adhesion coefficients can result in improvements in device performance as a function of cycle operations.

1.3.3 Failure Mechanisms with Ohmic Switches

Failure mechanisms with ohmic switches can be categorized into several categories based on the type of failure as well as the power level applied to the contacts. There are two predominant types of cold-switching failure: high resistance (indicated by an increase in the insertion loss with operation) and stiction (indicated by a failure for switch to open after operation).[2,59] High resistance failures can occur as a result of two mechanisms. The first is organic contaminant build-up. Organic materials begin to build-up at the contact surfaces during repeated operation of the switch as a result of a frictional polymer forming on the metallic surfaces.[64,] This process results in an increase in the contact resistance as a function of time, leading to eventual failure as the contact resistance produces unacceptable insertion loss values. Platinum, ruthenium, and rhodium are common metals used to improve lifetimes in ohmic switches as they prevent stiction and welding between pure gold contacts,[21,59,61,] but each of these materials has a higher rate of frictional polymer formation than pure gold.[60] McGruer et al. demonstrated lower rates of build-up with an increasing percentage of gold in the metallic alloy used for the switch contacts.[59] This failure mechanism can be reduced and possibly eliminated by improved removal of organic sacrificial layers used in the device processing. Wafer level hermetic packaging with inert atmospheres also benefits the measured cycle lifetime for both ohmic and capacitive MEMS switches.[2]

The second cause for high resistance contact failures is pitting and hardening of the contacts and/or dielectric formation on the contacts. These mechanisms are primarily observed at lower power levels (<10 mW).[2] As the contact materials continuously impact each other at the same spot repeatedly, pitting and hardening of the contacts can occur. This process has been identified to occur in 3 phases for gold-gold contact pairs (see Figure 1.28).[63] The first phase occurs in the first 10's of cycles and is characterized by an improvement in contact resistance as the contact adhesion increases slightly. As seen in Figure 1.28B, the contact surfaces deform and flatten as a result of plastic deformation. The second phase is characterized by little change in the contact resistance with additional cycling. However, at the junction between the second and third phases, the adhesion of the contact surfaces starts to rise rapidly. This process results in material transfer and considerable changes to the shape of the contact surfaces and a dramatic increase in the contact resistance (see Figure 1.28C).

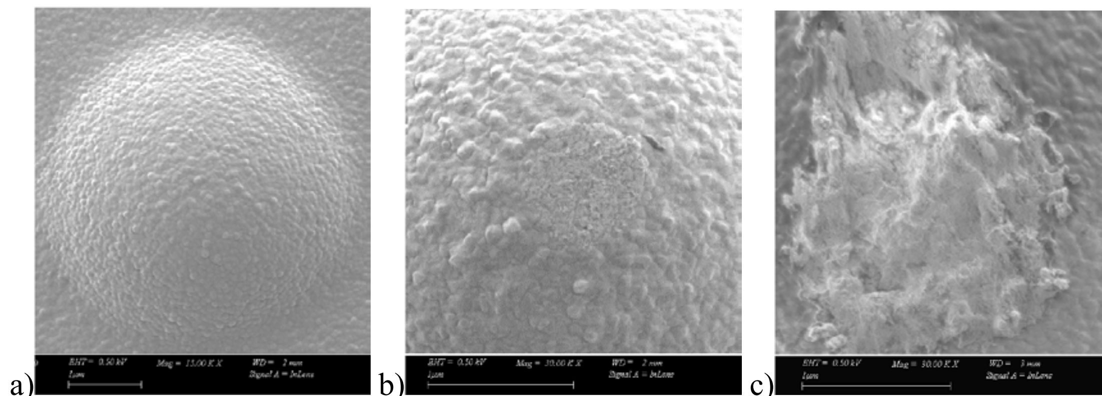

Figure 1.28: SEM images of the evolution of contact damage in Au contacts: a) virgin contact, b) contact after 1,000 cycles, and c) contact after 1,000,000 cycles (from Reference 63).

As the power level is increased (> 10 mW), material transfer, excessively high current density levels at the contact region, and thermal effects dominant the failure modes.[2] Even with modest power levels in the 100's mW, the temperature at the contacts can increase tens of degrees. Depending on the contact materials, the temperature change can increase material transfer as the hardness changes.[60] Further increases of power result in even larger temperature increases. As the temperature increases, the contact

resistance increases, leading to an increase in resistive losses.[60] This in turn causes further increases in temperature until the softening temperature can be achieved. As the contact material softens, the contact area increases, thereby reducing the contact resistance. This process can stabilize the temperature increase.[60] However, the increased contact area and softer contact surface increases the adhesion between the contacting surfaces.[60] Thus, material transfer and subsequent device failures occur at an early number of device operations.

1.4 Thesis Objectives

The aim of this thesis is to develop a robust, surface-micromachined, RF MEMS switch useful for military phased arrays. Reducing the power requirements of the switch requires examination of switches with actuation voltages less than 10 volts. To meet this demand, piezoelectric actuation with thin film PZT actuators will be utilized along with a co-planar waveguide transmission line. The goal is to use the understanding of thin film device fabrication along with electro-mechanical design and high frequency simulation to design and fabricate a surface micro-machined switch that will meet the Army's demand for miniaturized phase arrays for both communication and radar systems. To achieve these goals, the fabricated switch must possess the following attributes:

- Actuation Voltage < 10V
- Isolation > 20 dB (DC → 40 GHz)
- Insertion Loss < 0.5 dB (DC → 40 GHz)
- Switching Time < 100 μs
- Low Temperature Sensitivity of the Drive Voltage (V_{act} < 20 V)
- Power Handling > 5 W_{RF}
- Reliability > 10^6 cycles

Thin film processing and stress engineering will be utilized to design piezoelectric actuators with the correct initial deformation to enable switch operation. Measurement and modeling of these induced deformations will be used to optimize the fabrication process to ensure repeatable device operation. Electro-mechanical models will be used to predict PZT actuator deformations and to design actuators for low voltage switch operation. In addition, the metals within the switch contacts will be examined to enable

better performance with increasing RF power. Eutectic alloys will be examined as a possible way of proving a means of increasing the contact surface area with low RF powers resulting in a decrease in the switch contact resistance.

1.5 References

[1] E. Brown, "RF-MEMS switches for reconfigurable integrated circuits," IEEE Microw. Theory Techn., vol 46, no. 11, pp. 1868 – 1880, 1998.

[2] G. Rebeiz, *RF MEMS Theory, Design, and Technology*, John Wiley & Sons, Hoboken, NJ, 2003.

[3] S. Majumder, J. Lampen, R. Morrison, and J. Maciel, "MEMS switches," IEEE Instrum. Meas. Mag., pp. 12 – 15, March 2003.

[4] G. Rebeiz, G. Tan, and J. Hayden, "RF MEMS phase shifters: device and applications," IEEE Microw. Mag., pp. 72 – 81, June 2002.

[5] J. J. Yao, "RF MEMS from a device perspective," J. Micromech. Microeng., vol. 10 pp. R9–R38, 2000.

[6] L. E. Larson, R. H. Hackett, M. A. Melendes, and R. F. Lohr, "Micromachined microwave actuator (MIMAC) technology – a new tuning approach for microwave integrated circuits," *Millimeter-Wave Monolithic Circuits Symposium Digest*, Boston, MA, June 1991, pp. 27-30.

[7] G. Rebeiz and J. Muldavin, "RF MEMS switch and switch circuits," IEEE Microw. Mag., vol. 2, no. 4, 2001, pp. 59 – 71.

[8] G. T. A. Kovacs, *Micromachined Transducers*, McGraw-Hill, Boston, MA, 1998.

[9] K. Uchino & J. Giniewicz, Micromechatronics, New York, NY, Marcel Dekker, pp. 242-254, 2003.

[10] http://www.trstechnologies.com/Materials/electrostrictive_materials.php

[11] Agilent Application Note, "Agilent Network Analyzer Basics," #2004-09-15, http://www.home.agilent.com/agilent/facet.jspx?cc=US&lc=eng&k=Network+Analyzer+Basics&sm=g&t=80029.k.0

[12] V. Varadan, K. J. Vinoy, and K. Jose, *RF MEMS and Their Applications*, John Wiley & Sons, Hoboken, NJ, 2003.

[13] RadantMEMS Application Note – www.radantmems.com/randments.data/Library/GenAppNote.pdf

[14] DARPA RFMIP and HERMIT programs, www.darpa.mil/mto/programs/

[15] James Mullins, US Army Aviation and Missile Research, Development, and Engineering Center, *private communication*.

[16] Louis Coryell, US Army Communications and Electronic Research, Development, and Engineering Center, *private communication*.

[17] C. Goldsmith, H.T. Lin, B. Powers, W.R. Wu, and B. Norvell, "Micromachined membrane switches for microwave applications," Proc. IEEE Microw. Theory Techn. Symposium, Piscataway, NJ, pp. 1141 – 1144, 1995.

---

[18] C. L. Goldsmith, Z. Yao, S. Eshelman, and D. Denniston, "Performance of low-loss RF MEMS capacitive switch," IEEE Micro. Guided Wave Lett., vol. 8, no. 8, 1998, pp. 269-271.

[19] www.memtronics.com/page.aspx?page_id=5

[20] S. Duffy, C. Bozler, S. Rabe, J. Knecht, L. Travis, P. Wyatt, C. Keast, and M. Gouker, "MEMS microswitches for reconfigurable microwave circuitry," IEEE Microw. Wireless Comp. Lett., vol. 11, no. 3, 2001, pp. 106 – 108.

[21] S. Majumber, N.E. McGruer, P.M. Zavracky, G. Adams, R. Horrison, and J. Krim, "Measurement and modeling of surface micromachined, electrostatically actuated microswitches," Int. Conf. Solid-State Sensors and Actuators (Transducers '97), Chicago, June 1997, pp. 1145 – 1148.

[22] D. Peroulis, S. P. Pacheco, K. Sarabandi, L. Katehi, "Electromechanical considerations in developing low voltage RF MEMS switches," IEEE Trans. Microw. Theory Techn., vol. 51, no. 1, 2003, pp. 259 – 270.

[23] J.F. Nye, *Physical Properties of Crystals*, Oxford University Press, New York, NY, 1990.

[24] IEEE Standard on Piezoelectricity, ANSI/IEEE Std 176, 1987.

[25] W. L. Warren, J. Robertson, D. Dimos, B. A. Tuttle, G. E. Pike, and D. A. Payne, "Pb displacements in $Pb(Zr,Ti)O_3$ perovskites," Phys. Rev. B, vol. 53, pp. 3080 – 3087, 1996.

[26] B. Jaffe, W.R. Cook, and H. Jaffe, *Piezoelectric Ceramics*, R.A.N., Ohio, 1971.

[27] B. Noheda, J. A. Gonzalo, L.E. Cross, R. Guo, S. E. Park, D.E. Cox, G. Shirane, "Tetragonal-to-monoclinic phase transition in a ferroelectric perovskite: The structure of $PbZr_{0.52}Ti_{0.48}O_3$," *Phys Rev. B*, vol. 61, 2000, pp. 8687 – 8690.

[28] A. J. Moulson and J.M Herbert, *Electroceramics*, Chapman and Hill, New York, 1990.

[29] A. F. Devonshire, "Theory of ferroelectrics," Adv. in Physics, vol. 3, 1954, pp. 85 – 130.

[30] N. Setter, "ABC of piezoelectricity and piezoelectric materials," in *Piezoelectric Materials in Devices*, ed. by N. Setter, Ceramics Laboratory EPFL, Lausanne, Switzerland, pp. 1 – 28, 2002.

[31] P. Muralt, "Piezoelectric thin films for MEMS," Integ. Ferro., vol. 17, pp. 297–307, 1997.

[32] P. Muralt, A. Kholkin, M. Kohli, and T. Maeder, "Piezoelectric actuation of PZT thin film diaphragms at static and resonant conditions," Sens. Act. A, vol. 53, pp. 397–403, 1996.

[33] M. Dubois and P. Muralt, "Measurement of the effective transverse piezoelectric coefficient $e_{31,f}$ of AlN and $Pb(Zr_xTi_{1-x}O_3)$ thin films," Sen. Act., vol. 77, pp. 106–112, 1999.

[34] X.-H., U. Belegundu, and K. Uchino, "Crystal orientation dependence of piezoelectric properties of lead zirconate titanate near the morphotropic phase boundary," Appl. Phys. Lett., vol. 72, pp. 2421 – 2423, 1998.

[35] R. Ruby and P. Merchant, "Micromachined thin film bulk acoustic resonators," Proc. IEEE 48th Symp. Freq. Control, pp. 135 – 138, 1994.

[36] US Patent 5,587,620, R. C. Ruby and P. Merchant, "Tunable thin-film acoustic resonators and method for making same."

[37] P. Muralt, "PZT thin films for microsensors and actuators: where do we stand?," IEEE Trans. Ultrason. Ferro. Freq. Control, vol. 47, no. 4, pp. 903 - 914, 2000.

[38] P. Muralt, J. Baborowski, and N. Lederman, "Piezoelectric micro-electro-mechancial systems with $PbZr_xT_{1-x}O_3$ thin films: integration and application issues," in *Piezoelectric Materials in Devices*, ed. by N. Setter, Ceramics Laboratory EPFL, Lausanne, Switzerland, pp. 231 – 260, 2002.

[39] J.F. Shepard, P.J. Moses, S. Trolier-McKinstry, "A technique for the measurement of d_{31} coefficient of piezoelectric thin films," Materials Res. Symp.: Materials for Smart Systems II (Boston, MA, 1997), vol. 459, pp. 225 – 230.

[40] I. Kanno, S. Fujii, T. Kamada, and R. Takayama, "Piezoelectric properties of c-axis oriented $Pb(Zr,Ti)O_3$ thin films," App. Phys. Lett., vol. 70, 1997, pp. 1378 – 1380.

[41] A. Kholkin, "Electromechanical properties and domain-related effects in ferroelectric thin films," *Ferroelectrics,* vol. 221, no. 1/4, 1999, pp. 219 – 228.

[42] K. Lefki and G.J.M. Dorman, "Measurement of piezoelectric coefficients of ferroelectric thin films," J. Appl. Phys., vol. 76, no. 3, 1994, pp. 1764 – 1767.

[43] X. L. Zhang, Z. X. Chen, L. E. Cross, and W. A. Schulze, "Dielectric and piezoelectric properties of modified lead zirconate titanate ceramics from 4.2 to 300K," J. Mat. Sci., vol. 18, 1983, pp. 968 – 972.

[44] Q. M. Zhang, H. Wang, N. Kim, and L. E. Cross, "Direct evaluation of domain-wall and intrinsic contributions to the dielectric and piezoelectric response and their temperature dependence on lead zirconate titanate ceramics," J. Appl. Phys., vol. 75, pp. 454 – 459, 1994.

[45] D. Damjanovic, "Stress and frequency dependence of the direct piezoelectric effect in ferroelectric ceramics," J. Appl. Phys., vol. 82, pp. 1788 – 1797, 1997.

[46] P. Muralt, N. Lederman, J. Baborowski, A. Barzegar, S. Gentil, B. Belgacem, S. Petitgrand, A. Bosseboeuf, and N. Setter, "Piezoelectric micromachined ultrasonic transducers based on PZT thin films," IEEE Trans. Ultrason. Ferro. Freq. Control, vol. 52, no. 12, pp. 2276 – 2288, 2005.

[47] P. Muralt, "Texture control and seeded nucleation of nanosize structures of ferroelectric thin films," J. Appl. Phys., vol. 100, pp. 051605-1 – 051605-11, 2006.

[48] P. Muralt, IEEE Sensors Conference, Daegu, Korea (2006).

[49] M. Hoffmann, H. Kuppers, T. Schneller, U. Bottger, U. Schnakenberg, W. Mokwa, and R. Waser, "Theoretical calculations and performance results of a PZT thin film actuator," IEEE Trans. UFFC, vol. 50, no. 10, pp: 1240-1256, 2003.

[50] C. Kugeler, S. Tappe, U. Bottger, and R. Waser, "A novel design for integrated RF-MEM switches using ferroelectric thin films," Int. Ferro., vol. 76, pp. 59 – 67, 2005.

[51] S. J. Gross, S. Tadigadapa, T. N. Jackson, S. Trolier-McKinstry, Q. Q. Zhang, Appl. Phys. Lett. Vol. 83, pp. 174-6, 2003.

[52] H. C. Lee, J. Y. Park, and J. U. Bu, "Piezoelectrically actuated RF MEMS DC contact switches with low voltage operation," IEEE Microw. Wireless Comp. Lett., vol. 15 (4), pp. 202-204, 2005.

---

[53] H. C. Lee, J. H. Park, J. Y. Park, H. J. Nam, and J. U. Bu, "Design, fabrication, and RF performance of two different types of piezoelectrically actuated ohmic MEMS switches," J. Micromech. Microeng., vol 15, pp. 2098-2104, 2005.

[54] D. Lee, S. Jung, N. Cho, W. Kim, W. Seong, and H. Park, "PZT actuated seesaw SPDT RF MEMS switch," J. Phys: Conf. Series, vol. 34, pp. 304 – 309, 2006.

[55] John Evans, DARPA, *private communication.*

[56] John Evans, DARPA, Disruptive Manufacturing Workshop, 2006.

[57] E. Kruglick and K. Pister, "Lateral MEMS microcontact considerations," J. MEMS, vol. 8, no. 3, pp. 264 – 271, 1999.

[58] R. Holm, Electric Contacts: Theory and Application, Springer-Verlag, New York, 1967.

[59] S. Majumber, N.E. McGruer, and G.G. Adams, "Study of contacts in an electrostatically actuated microswitch," Sens. Act. A, vol. .93, no. 1, pp. 19-26, 2001.

[60] P. Slade, Electrical Contacts: Principles and Applications, Marcel Dekker, 1999.

[61] R. A. Coutu, P. E. Kladitis, R. E. Strawser, R. L. Crane, "Micro-switches and sputtered Au, AuPd, Au-on-AuPt, and AuPtCu alloy electric contacts," IEEE Trans. Comp. Pack. Techn., vol. 29, no. 2, June 2006.

[62] S. P. Sharma, "Adhesion coefficients of plated contact materials," J. Appl. Phys, vol. 47, no. 8, pp. 3573 – 3576, 1976.

[63] N. E. McGruer, G. G. Adams, L. Chen, Z. J. Guo, and Y. Du, "Mechanical, Thermal, and Material Influences on Ohmic-Contact-Type MEMS Switch Operation," Proc. MEMS 2006, pp. 230 - 233, 2006.

[64] N. McGruer, Northeastern Univ., private communication, 2006.

Chapter 2

Experimental Procedures

This chapter describes measurement and characterization procedures used throughout the thesis. Characterization topics include measurement of the residual stress developed in the constituents of the switch stack as a result of the fabrication processes, as well as the ferroelectric and dielectric characterization of the PZT films. Additionally, post fabrication device testing will be covered, including determination of the static deformation of PZT actuators as a function of temperature. Lastly, all of the DC and RF switch testing procedures will be described in detail.

2.1 Residual Stress Measurement

During fabrication of the actuator composite stack, it is crucial to monitor the residual stress within the individual thin films. Ultimately, a negative curvature (cantilever deflection into the substrate) is required for the completed switch actuators. The stress measurement was accomplished using a KLA-Tencor FLX-3200 stress gauge. This instrument provides an optical measurement of the curvature of the silicon substrate at various points in the fabrication process. Changes to the radius of curvature of the wafer due to deposition or etching of thin films on the substrate surface were related to the residual stress in the thin film, σ_f (Pa), through the use of Stoney's equation (Equation 2.1).[1]

$$\sigma_f = \left(\frac{E_s}{1-\nu_s}\right)\frac{t_s^2}{6t_f}\left(\frac{1}{R_1}-\frac{1}{R_0}\right) \qquad \text{Equation 2.1}$$

In Equation 2.1, R_i is the radius of curvature (m) with subscripts 1 and 0 indicating the results with and without the film, respectively. The Young's modulus, E (GPa), and

Poisson's ratio of the substrate are denoted as E_s and ν_s. In addition, both the substrate (t_s) and film thicknesses (t_f) are required for the calculation.

At the start of device fabrication, the initial radius of curvature of each bare substrate was measured by placing the wafer onto quartz pin rests (see Figure 2.1) with the lid enclosure closed. After the wafer is initialized, it is available for further processing. Following deposition and anneal of the elastic layer (see Section 3.2.2), the film thickness was measured by ellipsometry (see Section 2.2) and the residual stress was determined by wafer curvature measurements. The wafer is then re-initialized with the substrate plus elastic layer radius of curvature measured. This value provides the baseline for measuring the residual stress of the titanium/platinum bottom electrode. These same procedures are repeated following each subsequent deposition and anneal procedure to acquire stress values for each individual layer. Additionally, the radius of curvatures for each deposition process can be used to calculate average residual stress values for the entire composite stack.

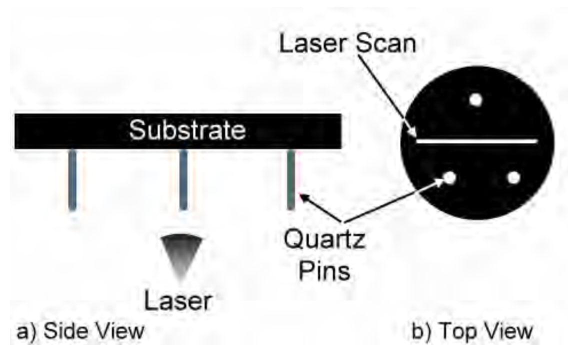

Figure 2.1: Illustration of the measurement setup for the Tencor FLX-3200: a) side view and b) top view.

The Flexus equipment is also equipped with temperature capability. With the PZT anneal setting the upper bound of processing temperatures at 700ºC, it is critical to measure each film as a function of temperature to ensure stable stress values with subsequent annealing procedures. Either flowing nitrogen or air was used as a processing gas during the stress measurements. As the temperature was ramped to the temperature of interest at 5 degrees per minute, stress values were recorded at 5 degree intervals. A

dwell time of 1 or 2 minutes was used at the maximum temperature. Then, the chamber was cooled at a rate of 5 degrees per minute; again, stress values were recorded at 5 degree intervals.

2.2 Film Thickness Measurements

Film thicknesses for each dielectric thin film (SiO_2, Si_3N_4, and PZT) were measured using a JA Woollam M-2000F multi-wavelength, multi-angle ellipsometer (see Figure 2.2a). Measurements were acquired using a linearly polarized incident beam for wavelengths from 240 nm to 1000 nm. The elliptical polarization of the reflected light was then determined (see Figure 2.2b). Data were interpreted using models of the depth profile of the dielectric function. The utility of the models was estimated by examining the mean square error (MSE) output from the JA Woollam software. The mean-squared error (MSE) is the sum of the squares of the differences between each measured and experimental data point, divided by the standard deviation (σ) of the experimental data point (see Equation 2.2). The number of measured psi (Ψ) and delta (Δ) pairs is N, and the total number of real valued fit parameters is M. When the MSE is unity, the calculated data (on the average) lie within one standard deviation of the experimental data.[2]

$$MSE = \sqrt{\frac{1}{2N - M}\sum_{i=1}^{N}\left[\left(\frac{\Psi_i^{mod} - \Psi_i^{exp}}{\sigma_{\Psi,i}^{exp}}\right)^2 + \left(\frac{\Delta_i^{mod} - \Delta_i^{exp}}{\sigma_{\Delta,i}^{exp}}\right)^2\right]} \qquad \text{Equation 2.2}$$

The accuracy of the thickness measurements critically depends on the accuracy of the models used to fit the experimental data. The models used were developed in conjunction with the engineering staff at JA Woollam, Inc. The elastic layer, comprised of plasma enhanced chemical vapor deposited (PECVD) $SiO_2/Si_3N_4/SiO_2$ (see Section 3.2.2), was treated as a composite on an infinitely thick silicon substrate. The silicon substrate is modeled using reference data from Herzinger et al.[3] with modeled refractive

index, n, and extinction coefficient, k, values as plotted in Figure 2.3. The elastic layer is modeled using a combination of a Cauchy model for the silicon dioxide layers and a user programmable dispersion model based on a Tauc-Lorentz oscillator for the silicon nitride film.

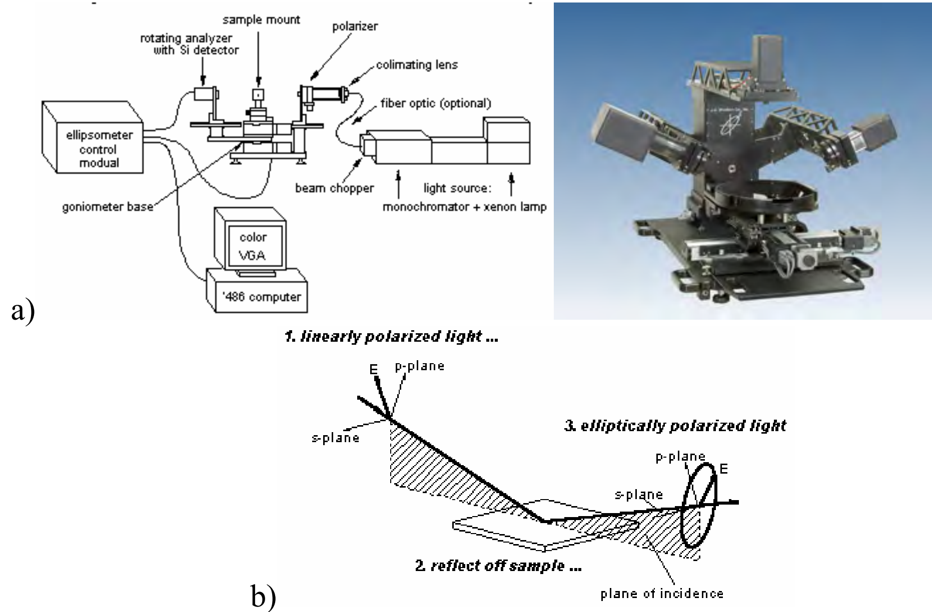

Figure 2.2: (a) Experimental setup and (b) principle of operation of the JA Woollam M2000 ellipsometer.[2]

The Cauchy dispersion relation is an inverse power series containing only even terms in the wavelength and is a commonly used approach for the parameterization of the index of transparent materials, where λ is wavelength and A_n, B_n, and C_n are modeling coefficients describing the index dispersion (see Equation 2.3).[2] In the Cauchy equation, the A_n term describes the long-wavelength asymptotic index value, while the B_n and C_n are the dispersion terms that add upward slope to the index curve as wavelengths become shorter.[4] The starting values for the modeling coefficients are listed in Table 2.1 along with an average of the fit-values acquired after the models have been fit to the experimental data. The predicted n and k values for a PECVD SiO_2 thin film (968 Å) are reported in Figure 2.4. The refractive index is slightly below the stoichiometric value of 1.46 (at 633 nm) but agrees well with previous reports in the literature silicon dioxide

thin films deposited by a variety of deposition techniques (see Figure 2.5 for an example).[5,6,7,8,9]

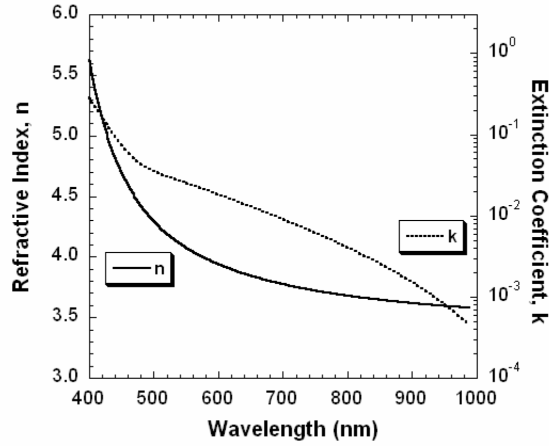

Figure 2.3: Modeled n and k values for the silicon substrate with values based from Reference 3.

$$n(\lambda) = A_n + \frac{B_n}{\lambda^2} + \frac{C_n}{\lambda^4} + \ldots \qquad \text{Equation 2.3}$$

Table 2.1: Modeling parameters used for the Cauchy models for PECVD SiO_2 thin films. The starting values are used at the onset of fitting the model to the experimental data and the fit-values represent an average taken from several measurements.

Cauchy Model Parameters – PECVD SiO_2		
	Starting values	Average Fit-Values
A_n	1.4431	1.4206
B_n (nm^2)	0.00416575	0.004235
C_n (nm^4)	-1.9317×10^{-5}	-1.9241×10^{-5}

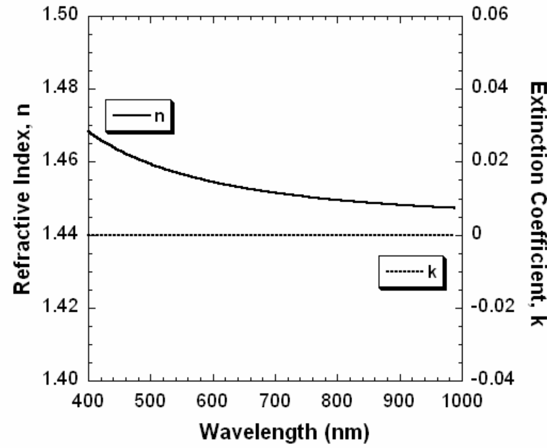

Figure 2.4: Predicted n and k values for a PECVD SiO_2 thin film (968 Å) using a Cauchy model.

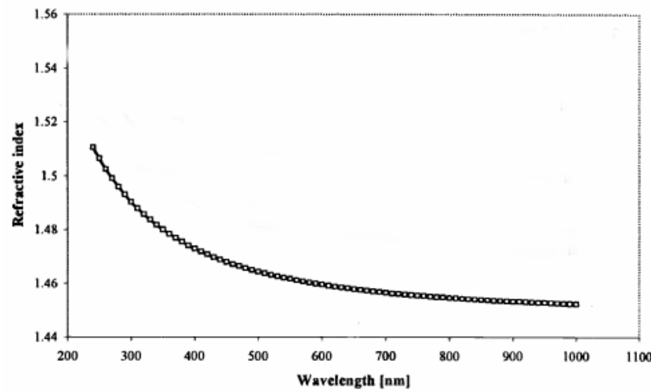

Figure 2.5: Refractive index values reported by Rodkiewicz et.al.[8] for a silicon dioxide thin film.

The silicon nitride layer is modeled using a modified Tauc-Lorentz oscillator term. The Tauc-Lorentz oscillator was developed by Jellison and Modine[10] and it models the dielectric function of many amorphous materials well.[4] The PECVD silicon nitride model incorporates an epsilon infinity term (ε_∞) to account for the background information in the experimental data. In the Tauc-Lorentz oscillator, the complex dielectric function ($\varepsilon_{T\text{-}L}$), see Equation 2.4, can be described as a function of energy (E) with A representing the amplitude of the oscillator, E_o is the center energy, C is the broadening term to describe the dispersion, and E_g is the energy gap.[4]

$$\varepsilon_{Si_3N_4} = \varepsilon_\infty + \varepsilon_{T-L} = \varepsilon_\infty + \left[\frac{AE_oC(E-E_g)^2}{(E^2 - E_o{}^2) + C^2E^2} \bullet \frac{1}{E} \right] \qquad \text{Equation 2.4}$$

The modeling parameters used to model the PECVD silicon nitride thin films are described in Table 2.2. The predicted n and k values for a PECVD Si_3N_4 thin film with a thickness of 586 Å are reported in Figure 2.6. The refractive index at 633nm is greater than the stoichiometric value of 2.0 indicative of a silicon rich silicon nitride.[11] In general, these observed values are consistent with silicon nitride films reported in the literature for silicon rich silicon nitride films (see Figure 2.6 for an example).[5,11,12,13]

Table 2.2: Modeling parameters used for the user programmable dispersion model for PECVD Si_3N_4 thin films. The starting values are used at the onset of fitting the model to the experimental data and the fit-values represent an average taken from several measurements.

User Programmable Dispersion Parameters – PECVD Si_3N_4		
	Starting values	Average Fit-Values
ε_∞ (eV)	1.2316	1.2405
A (eV)	21.487	21.876
E_o (eV)	9.215	9.205
C (eV)	12.002	Fixed
E_g (eV)	2.1396	Fixed

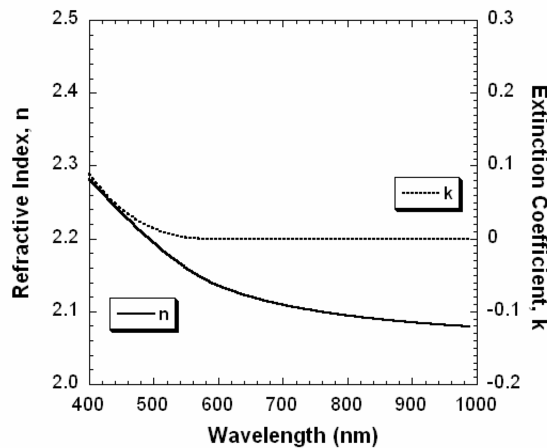

Figure 2.6: Predicted n and k values for a PECVD Si_3N_4 thin film (586 Å) using a modified Tauc-Lorentz oscillator model.

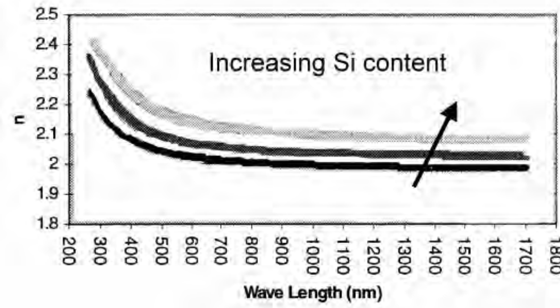

Figure 2.7: Example of the n and k values reported by Loh et. al.[13] for a silicon nitride thin films as a function of increasing silicon content.

For the PZT thin films, an optically thick platinum layer was used as the substrate. The platinum was modeled with a 3 oscillator Lorentz model with the parameters listed in Table 2.3. The Lorentz oscillator is formulated as follows:[4]

$$\varepsilon_{Lorentz} = \frac{A_n Br_n E_n}{E_n^2 - E^2 - iBr_n E} \qquad \text{Equation 2.5}$$

Each oscillator is described by three parameters: A_n is the amplitude of the ith oscillator and is dimensionless, Br_n is the broadening of the ith oscillator having units of (eV), and E_n is the center energy (location) of the ith oscillator, also in units of (eV).[4] The predicted n and k values are reported in Figure 2.8 for an infinitely thick platinum layer.

Table 2.3: Modeling parameters used for the Lorentz three oscillator model for sputtered Pt thin films (assumed thickness of 1mm).

Lorentz Oscillator – Sputtered Pt			
Oscillator	A_n	Br_n (eV)	E_n (eV)
1	123.13	1.1711	0
2	134.24	8.524	4.235
3	85.236	1.3006	8.8409

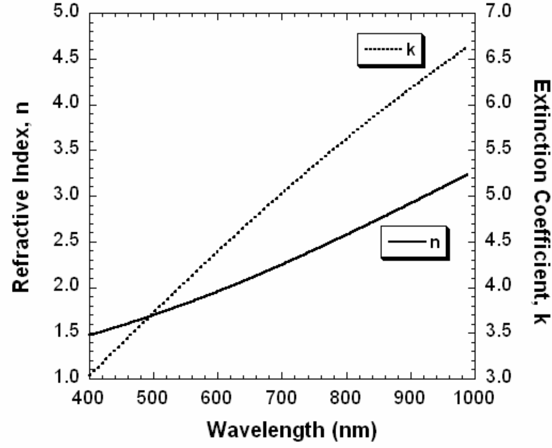

Figure 2.8: Predicted n and k values for an infinitely thick platinum layer using a Lorentz oscillator model.

The PZT thin films were modeled with a modified Pole oscillator plus Tauc-Lorentz oscillator model characterized by Equation 2.6. As with the PECVD silicon nitride thin films, an epsilon infinity term (ε_∞) is added to account for the background information in the experimental data. A Pole oscillator, where A_p is the amplitude and E_p is the center energy, is added to mimic an oscillator outside of the measurement range with broadening that can affect the refractive index and not the absorption coefficient.[14] The list of modeling parameters used to measure the PZT thin films is listed in Table 2.4. To avoid the absorption band edge of PZT, the models were limited to 400 nm to 1000 nm. The predicted n and k values are reported in Figure 2.9 for a PZT thin film (5059 Å). These values correspond well those previously reported for sol-gel PZT thin films (see Figure 2.10).[15,16,17] The differences in the observed extinction coefficient may be attributed to surface microstructure that is not included in the models used in this thesis but was described by Trolier-McKinstry et al.[16] and shown to be important in the full characterization of the optical constants for PZT thin films.

$$\varepsilon_{PZT} = \varepsilon_\infty + \varepsilon_{Pole} + \varepsilon_{T-L} = \varepsilon_\infty + \frac{A_p}{E_p^2 - E^2} + \left[\frac{A E_o C (E - E_g)^2}{(E^2 - E_o^2) + C^2 E^2} \bullet \frac{1}{E} \right] \qquad \text{Equation 2.6}$$

Table 2.4: Modeling parameters used for the modified Pole and Tauc-Lorentz oscillator model for sol-gel PZT (52/48) thin films. The starting values are used at the onset of fitting the model to the experimental data and the fit-values represent an average taken from several measurements.

User Programmable Dispersion Parameters – sol-gel PZT (52/48)		
	Starting values	Average Fit-Values
ε_∞ (eV)	1.6494	1.6387
A_p (eV^2)	0	0.91969
E_p (eV)	7	6.6908
A (eV)	7.0322	Fixed
E_o (eV)	5.3351	Fixed
C (eV)	0.039697	Fixed
E_g (eV)	1.2938	Fixed

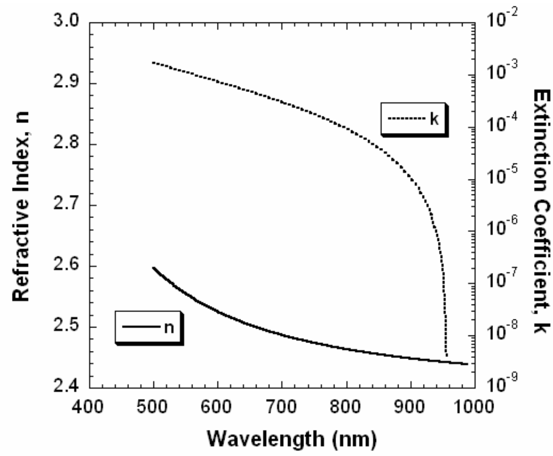

Figure 2.9: Predicted n and k values are reported for a PZT thin film (5059 Å) using a modified Pole plus Tauc-Lorentz oscillator model.

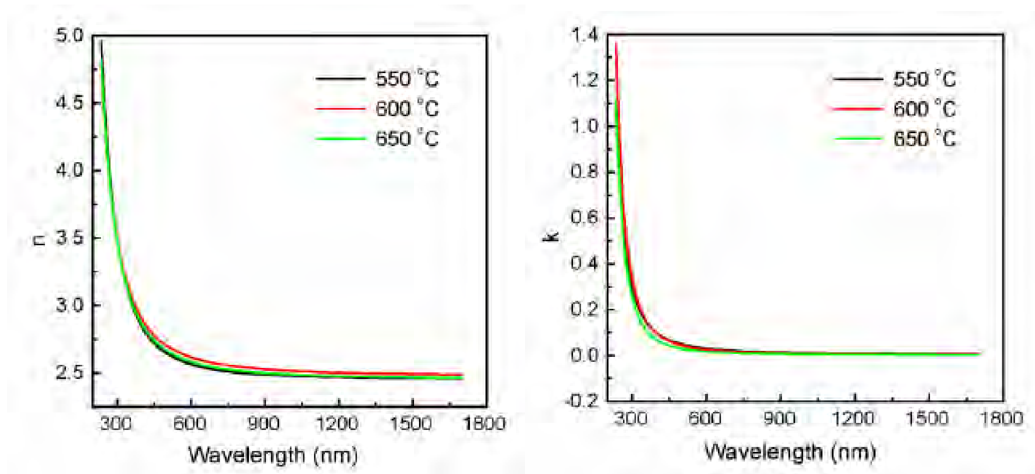

Figure 2.10: Example of the n and k values reported by Jiang et al. for PZT thin films (approximately 210 nm thick) on platinum coated silicon substrates at several annealing conditions.[17]

2.3 X-ray Diffraction

The crystalline characteristics of the PZT thin films were measured with x-ray diffraction. Using a PANalytical X'Pert PRO MRD (Materials Research Diffractometer) X-ray diffraction system, theta 2-theta scans were acquired from 20 to 50 degrees using a scan rate of 0.2 degrees per second. The tube was operated at 45 kV and 40 mA providing Cu *K*α radiation in a line source. All measurements were done by Dr. Eric Readinger (Oak Ridge Associated Universities post-doctoral researcher at the Army Research Laboratory). The PZT samples used for these measurements were test samples deposited on a 2.5 cm x 2.5 cm die with the same thin film stack as that used for the switch fabrication (see Chapter 3.2).

2.4 Ferroelectric & Dielectric Measurements

Electrical characterization of PZT thin film capacitors was used to monitor their ferroelectric and dielectric characteristics. A majority of the measurements were performed using 1.0mm diameter PZT capacitors with a top Pt electrode diameter of 0.8 mm. Polarization – electric field hysteresis loops were gathered to monitor the

ferroelectric characteristics of the PZT thin films used for the actuators. The hysteresis loops were collected using a Radiant Technologies RT-66A measurement unit in conjunction with the RT-66i interface. The dielectric permittivity and dielectric loss were determined from capacitance and loss measurements at 10 kHz with an applied voltage of 50 mV using a HP 4275A or 4284A LCR impedance analyzer.

2.5 Static Deformation Measurements

Following device fabrication, a Veeco WYKO NT1100 optical profilometer (see Figure 2.11) was used to characterize the out-of-plane deformation of the fabricated devices. Using the vertical scanning interferometry (VSI) mode of operation, a scan length of 20 – 30 microns was employed to capture the surface profile. A modulation threshold of 2-3% was chosen to capture as much of the usable signal as possible. The modulation threshold determines the signal-to-noise level for which a given pixel is considered to be "valid." Data points that don't meet the modulation threshold are marked as invalid and are not considered during analyses. Below 2-3%, there is not enough return signal from a point on the surface to register a usable signal. For example, large deformations of a cantilever reflect the optical beam away from the objective lens, thereby reducing the signal strength. These measurements provide information of the residual stress gradient of the released structures. As a result, this technique provides more local information than does wafer curvature. This information was used to compare the as-released deformations to predictions based on the wafer curvature data.

The optical profilometer was also used to measure the static piezoelectric deformations of the switches as well as any aging in the deflection of the piezoelectric actuators, or thermal perturbations in the switch profile. For the piezoelectric deformations, micro manipulators were used to make contact to the actuator contact pads and a DC voltage (ranging from -20 to +20 volts) was applied with a Keithley 2400 source meter. To characterize the thermally induced deformations as well as the effect of temperature on the achievable actuation, a Thermolyne temperature station was placed onto the profilometer stage and a die with PZT switches was placed onto the 5 cm diameter Linkam TMS 91 thermal chuck using a small amount of Dow Corning 340

thermal grease. The temperature was varied between room temperature and 125ºC for studies on poling and aging of the PZT actuators, investigating thermally induced stress deformation, and measuring the piezoelectric induced deformation as a function of temperature. For the poling and aging investigations, the devices were poled at either 25ºC or 125ºC for 15min at 15 volts (approximately 7 times the coercive field). The hot poling samples were heated at 125ºC for 10min and the temperature was ramped to 25ºC for the remaining 5 minutes. The initial optical profilometer scans were acquired 5 minutes after poling and subsequently recorded every minute for the following 5 minutes for the aging studies. To investigate thermally induced stress deformation of the switch actuators and RF contact pad, optical profilometer scans were acquired from 25ºC to 125ºC at 25ºC increments and allowing 2 minutes for the device die to stabilize at each corresponding temperature. Similarly, the piezoelectric induced static actuator deformations were recorded from 25ºC to 125ºC at 25ºC increments recording with 0, 10, 15, and 20 volts applied to the actuators after the device die stabilized for 2 min at each temperature.

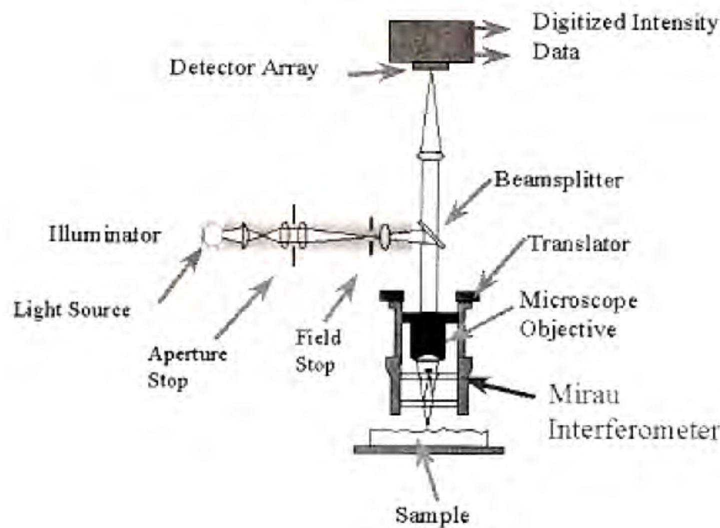

Figure 2.11: Measurement setup of the Veeco NT1100 optical profilometer.[18]

2.6 Resonance Measurements

A Poly-Tec laser Doppler vibrometer (LDV) (see Figure 2.12) was used to characterize the resonance frequency of the switch actuators. The interferometer compares the phase (φ_{mod}) and the frequency (f_{mod}) of the reflected beam from the sample to those of the internal reference φ_o and f_o. The frequency difference is proportional to the instantaneous velocity (v) while the phase difference is proportional to the instantaneous position (x). The resonance frequencies and mode shapes of PZT cantilevers and PZT switch actuators were determined by subjecting the PZT actuators to a small signal pseudorandom AC voltage pulse (10 – 100mV) applied for the duration of the measurement and measuring the mechanical deformation using the input laser. Individual point scans were acquired with the laser at the end of a cantilever or actuator and averaging the results over 32 scans. The resonance mode shapes were analyzed to verify the fundamental resonance vibration mode by acquiring multi-point scan data along the length of the cantilever or actuator and averaging each data point over 16 individual scans.

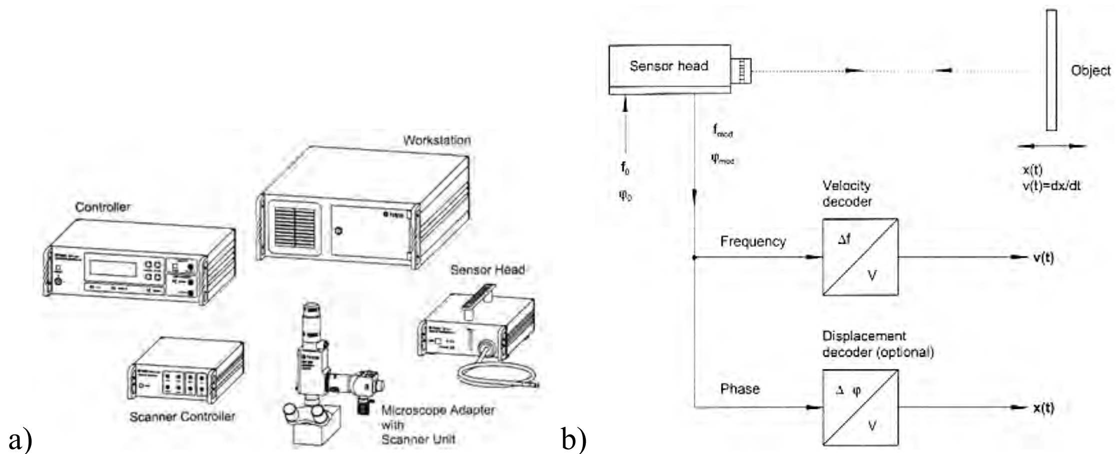

Figure 2.12: Measurement setup of the Polytec LDV with the the hardware specifics (a) and the schematic of the measurement signal paths (b).[19]

In addition, the LDV was configured to capture vibration characteristics of the switches given a single impulse actuation. Using a time scan instead of the fast Fourier

transform scan, a single measurement was triggered upon applying the actuation voltage. Single data point scans were collected at the tip of each actuator, as well as 3 individual data points on the RF pad (left, center, and right), and 3 corresponding data points on the RF-in and RF-out cantilevers (see Figure 2.13). Data were collected for using both 0.5 V and 5.0 V square waves at four different frequencies (0.5, 1.0, 5.0, and 10.0 kHz) applied to the actuators to examine the behavior of the switch operating with and without switch closure.

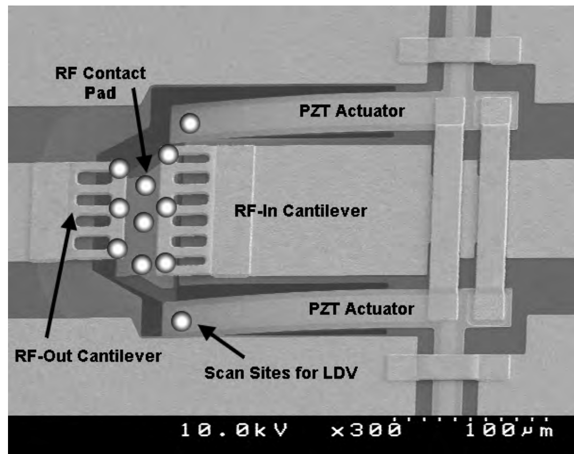

Figure 2.13: Image of a PZT switch illustrating the location of the LDV scans for assessing the switching behavior of the switch. Scan sites are shown as white circles.

2.7 RF Switch Characterization

2.7.1 RF Performance as a Function of Frequency

To characterize the RF performance of the switches, the completed wafers were placed onto a Cascade Microtech probe station configured with two RF probes and two DC probes (see Figure 2.14). Using a HP 8510 Network Analyzer, device performance was measured from 45 MHz to 40 GHz. A 4141B DC source/monitor interfaced with a C^{++} program was utilized to actuate the switches. Scattering parameters (S-parameters) were recorded across the frequency band for both the open and closed states for the PZT series switch. Switch performance is evaluated based on the forward transmission coefficient, S_{21}, in the open state (isolation), S_{21} in the closed state (insertion loss), and

the forward reflection coefficient, S_{11}, in the closed state (return loss). To eliminate the losses associated with the cabling and probes, the network analyzer was calibrated to the probe tips with a short, open, load, through calibration using standards from Cascade Microtech. Measurements up to 65 GHz were made using an Agilent E8361A precision network analyzer at the Air Force Research Laboratory at Hanscom Air Force Base with the aid of Dr. J. Robert Reid (Air Force Research Laboratory).

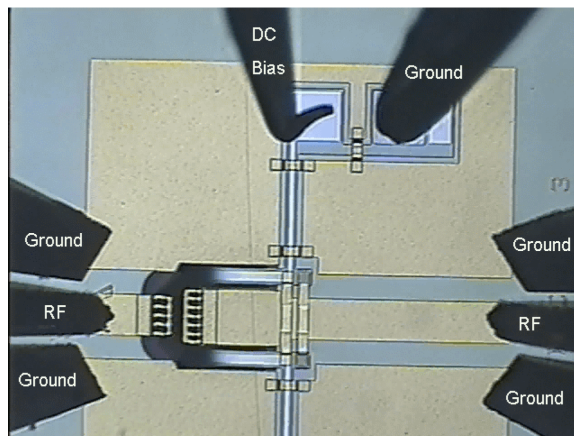

Figure 2.14: Image of the probe positions for RF testing of the PZT switch.

To characterize the influence of the substrate on the switch loss characteristics, varying lengths (100 μm to 8 mm) of co-planar waveguide (CPW) transmission line were patterned onto several different substrates including silicon with a resistivity of 30 Ohm-cm, high resistivity silicon with a resistivity greater than 10 kOhm-cm, z-cut quartz, fused quartz, sapphire, and alumina. Additionally, transmission lines were deposited onto high resistivity silicon substrates coated with silicon dioxide thin films or combinations of silicon dioxide and silicon nitride thin films. The S_{21} values were measured as a function of frequency and plotted either as dB per mm or dB per wavelength for each substrate and thin film combination. The results from these measurements are compared to evaluate the influence of thin film coatings on the transmission line loss characteristics of the substrate and to provide information for choosing the most appropriate low loss substrate for fabrication the PZT switch.

2.7.2 Contact Resistance

One of the most important switch characteristics that directly affects the insertion loss is the contact resistance. To determine the contact resistance of the switch contacts, a Keithley 4141B DC voltage source was used in conjunction with a Keithley 3478A ammeter to monitor the voltage current relationship along the RF conductor in the closed state (see Figure 2.15 for the measurement setup). Once the switch was closed, the current through the switch was measured as a function of DC voltage applied through the bias tees on the RF source. The applied voltage (V) was varied so that the current (I) passing through the switch ranged from 0 mA to 200 mA. The resistance (R) can be computed using Ohm's law (V = IR). The resistive losses associated with the cabling and probes were eliminated by measuring the voltage current relationship on a CPW transmission line assuming the resistance along the CPW transmission line contributes very little to the overall measurement resistance. The resistance of the CPW (R_{cpw}) can then be subtracted from the switch resistance measurements (R_{meas}) to reveal the total resistance of the switch contacts, R_c^{total} (see Equation 2.7).

$$R_c^{total} = R_{meas} - R_{cpw} \qquad \text{Equation 2.7}$$

Furthermore, because the switch is comprised of two contacts in series, the total resistance is the sum of the contact resistance from the RF-in contact (R_c^{RFin}) and the RF-out contact (R_c^{RFin}). It was assumed that the two RF contacts were equal such that the contact resistance is one half of the total resistance (see Equation 2.8).

$$R_c^{total} = R_c^{RFin} + R_c^{RFout} = 2R_c \qquad \text{Equation 2.8}$$

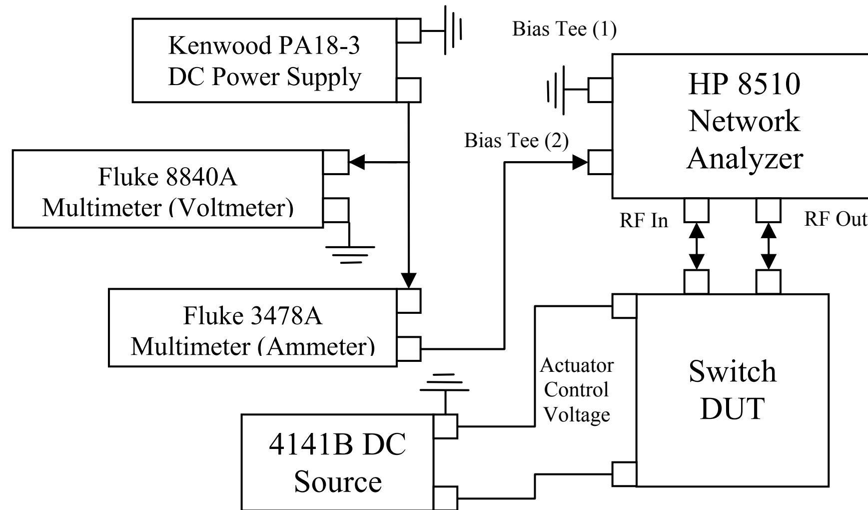

Figure 2.15: Setup for measuring the contact resistance of the PZT switch. Note, DUT is device under test.

2.7.3 Switching Time

The switching time for both the open and closed states was measured using two Agilent 33220A arbitrary waveform generators (as shown in Figure 2.16) with square waves for both the actuation and sensing waveforms. The actuation waveform was triggered by the sensing waveform with a delay of 1.9 μs to ensure that the sensing pulse was at its target value prior to actuating the switch. The 250 Hz applied sensing waveform was 50 mV_{pp} with a 25 mV DC offset. The 500 Hz actuation waveform was 5 V_{pp} with a 2.5 V DC offset. The actuation voltage (CH 2) and the sensing voltage from the RF Out, V_{sense}^{out}, (CH 3) were placed into 50 Ohm loads at the oscilloscope while the input sensing waveform, V_{sense}^{in} went into a 1 MOhm load (CH 1). The contact resistance of the switch can be estimated from the difference between the sensing voltage-input (CH1) and sensing voltage-output (CH3) using Equation 2.9, Equation 2.10, and Equation 2.11. As with the contact resistance measurements in Section 2.7.2, it is important to measure the resistance of the measurement setup using a CPW transmission line to accurately estimate the resistance of the contacts using Equation 2.7.

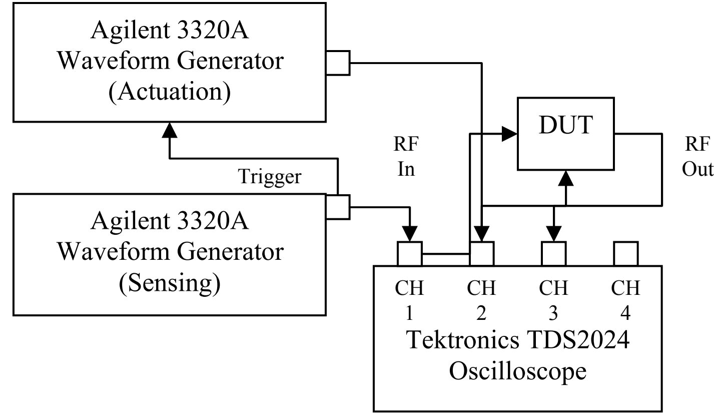

Figure 2.16: DC switching time measurement setup.

$$R_{meas} = R_{input} + R_c^{total} + R_{output} = \left(\frac{V_{sense}^{in} - V_{sense}^{out}}{I_{sense}} \right) \qquad \text{Equation 2.9}$$

$$I_{sense} = \frac{V_{sense}^{out}}{R_{load}} = \frac{V_{sense}^{out}}{50} \qquad \text{Equation 2.10}$$

$$R_{meas} = \left(\frac{V_{sense}^{in} - V_{sense}^{out}}{V_{sense}^{out}} \right) (50) \qquad \text{Equation 2.11}$$

2.7.4 Actuation Voltage

Using an Electroglass autoprober configured with a Hewlett-Packard voltage source meter, the actuation voltage of the switch is determined by calculating the median voltage between the high current and low current state of the switch. Figure 2.17 illustrates the current draw through a PZT switch as the actuation voltage is swept from zero to 15 volts with the actuation voltage indicated by the dotted arrow.

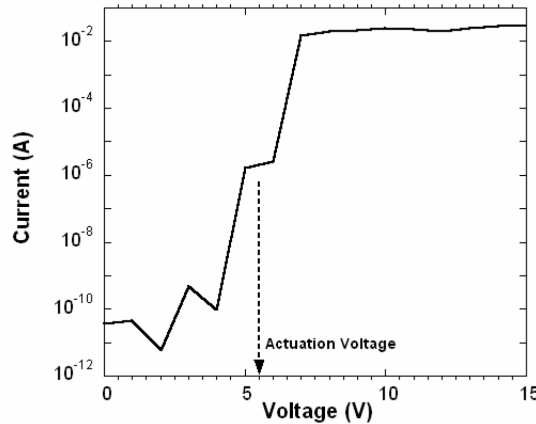

Figure 2.17: Illustration of the current draw through a piezoelectric MEMS switch as a function of the voltage applied to the actuators. The actuation voltage was determined as the median voltage between the low and high current states and is indicated by the arrow.

2.7.5 RF Power Handling

The RF power handling of a MEMS switch is a critical characteristic that is rarely reported in the literature. A host of military applications require the capability of handling up to 2 W and there are many applications for which 5 – 10 W is desirable.[20,21] Using the measurement setup in Figure 2.18, PZT switches were subjected to 7.6 W_{RF} in both operating states. In each case, RF power was delivered to a static switch in order to prevent hot switching. The voltage values from the input source monitor and the detector were monitored before and after exposing the switch to elevated power levels and used to compute the isolation and insertion loss characteristics of the switch. The RF power handling was determined using a scalar measurement of the RF power delivered at the probe tip and the RF power output from the switch. The difference between these two values is equivalent to the isolation in the open state and the insertion loss in the closed state. As a result of calibration drift with time and power level, these values are accurate to +/- 0.25 dB.

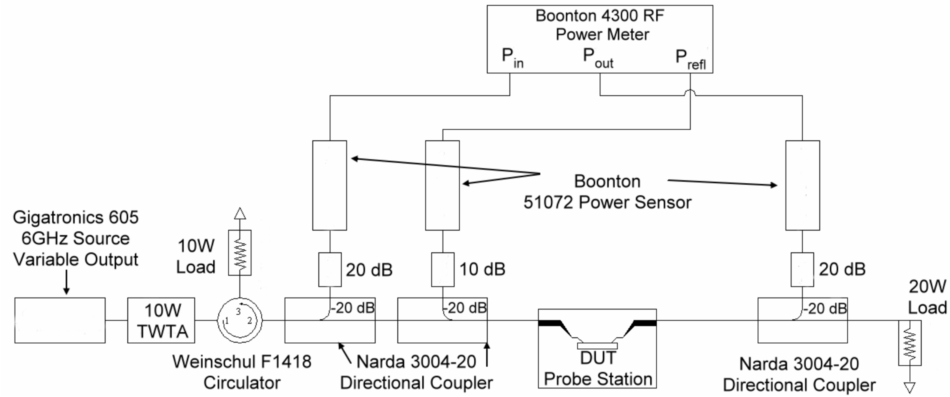

Figure 2.18: RF power handling measurement setup.

2.7.6 Lifetime Characterization

The cycle reliability of the switches is characterized using a Gigatronics model 605 RF signal generator at 8 GHz with a 30 mW RF pulse applied for 62.5 μs at an 8 kHz rate with the measurement setup illustrated in Figure 2.19. The detector output was recorded under cold switching operation (i.e. the RF energy was off during the switch actuation) for both the open and close states of the switch. The actuation waveform was supplied at 4 kHz with a 90º phase offset from the RF pulse (see Figure 2.20). Devices were tested until there was no discernable change between the open and closed states.

2.8 Thermal Sensitivity

The thermal sensitivity of the RF performance of the PZT switch was examined. A Cascade Microtech probe station configured with a heating chuck, a cold plate, and an Agilent E8364A precision network analyzer was used to collect S-parameters at atmospheric pressure with dry nitrogen gas flowing around the wafer surface. The temperature range available for RF testing was approximately -25ºC to 100ºC. During the testing, all probes were raised during the heating or cooling ramp to avoid any damage to the devices from expansion or contraction of the wafer chuck.

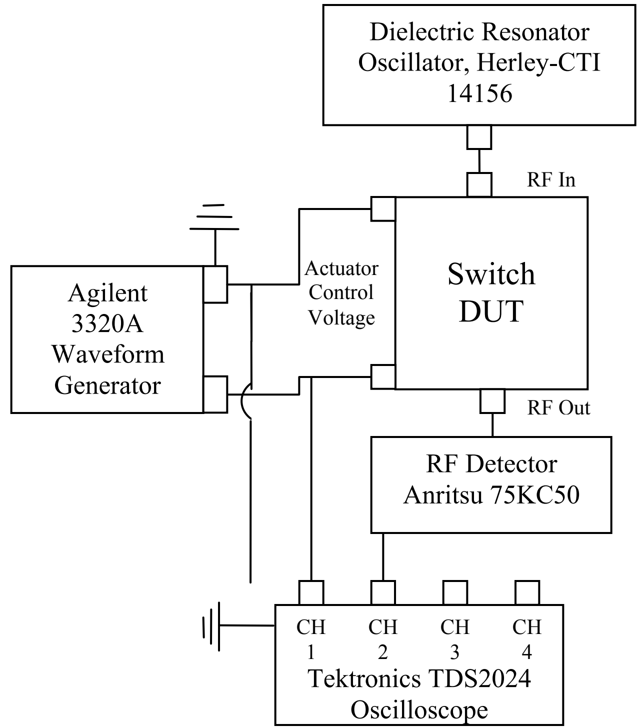

Figure 2.19: Cycle lifetime measurement setup.

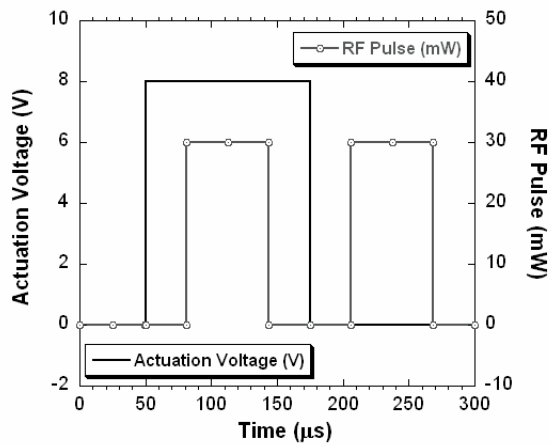

Figure 2.20: Description of the actuation (solid line) and RF pulse (dashed line) used for reliability testing of switches under cold-switching conditions.

2.9 References

[1] G.G. Stoney, The tension of metallic films deposited by electrolysis. *Proc. R. Soc. London A*, 1909, **82**, 172–175.

[2] JA Woollam Hardware and Principle of Operation Manual, 2001.

[3] C.M. Herzinger, G. Johs, W.A. McGahan, and J.A. Woollam, "Ellipsometric determination of optical constants for silicon and thermally grown silicon dioxide via a multi-sample, multi-wavelength, multi-angle investigation," J. Appl. Phys., vol. 83, no. 6, pp. 3323 – 3336, 1998.

[4] JA Woollam WVASE32 Manual Addendum, 2007.

[5] www.mc2.chalmers.se/mc2/nanolab/reports/OPT_Workshop_050913.pdf

[6] M.I. Alayo, I. Pereyra, W.L. Scopel, and M.C.A. Fantini, "On the nitrogen and oxygen incorporation in plasma-enhanced chemical vapor deposition (PECVD) SiO_xN_y films," Thin Solid Films, vol. 402, pp. 154 – 161, 2002.

[7] A. Sassella, A. Borghesi, F. Corni, A. Monelli, G. Ottaviani, and R. Tonini, B. Pivac, M. Bacchetta, and L. Zanotti, "Infrared study of Si-rich silicon oxide films deposited by plasma-enhanced chemical vapor deposition," J. Vac. Sci. Technol. A, vol. 15, pp. 377 – 389, 1997.

[8] W. Rodkiewicz, A. KudIa, A. Misiuk, and S. Lasisz, " Spectroscopic ellipsometry investigation of influence of high pressure-high temperature process on optical properties of $Si0_2$-Si structures," Lightmetry: Metrology, Spectroscopy, and Testing Techniques Using Light, Proceed. SPIE, Vol. 4517, pp. 134 – 139, 2001.

[9] C. M. Herzinger, B. Johs, W. A. McGahan, J. A. Woollam, and W. Paulson, "Ellipsometric determination of optical constants for silicon and thermally grown silicon dioxide via a multi-sample, multi-wavelength, multi-angle investigation," J. Appl. Phys., vol 83, pp. 3323 – 3336, 1998.

[10] G.E. Jellison, Jr. and F.A. Modine, "Parameterization of the optical functions of amorphous materials in the interband region," Appl. Phys. Lett. 69, 371 (1996), Erratum, Appl. Phys. Lett. 69, 2137 (1996).

[11] B. K. Yena, R. L. White, R. J. Waltman, Q. Dai, D. C. Miller, A. J. Kellock, B Marchon, and P. H. Kasai, M. F. Toney, B. R. York, H. Deng, Q. Xiao, and V. Raman, "Microstructure and properties of ultrathin amorphous silicon nitride protective coating," J. Vac. Sci. Technol. A, vol. 21, pp. 1895 – 1904, 2003.

[12] A. M. Pérez, C. Santiago, F. Renero, C. Zuñiga, "Optical properties of amorphous hydrogenated silicon nitride thin films," Opt. Eng., vol. 45, pp. 123802-1 – 123802-4, 2006.

[13] S.Y. Loh, T.K.S. Wong, M.S. Tse, and W.L. Goh, "Process monitoring of LPCVD silicon nitride and polysilicon by variable angle spectroscopic ellipsometry," Micromachining and Microfabrication, Proc. SPIE, vol. 4230, pp. 231 - 240, 2000.

[14] Dr. Martin Liphardt, JA Woollam, *private communication*.

[15] D. Franta, I. Ohlidal, J. Mistrık, T. Yamaguchi, G. J. Hu, and N. Dai, "Optical characterization of sol–gel deposited PZT thin films by spectroscopic ellipsometry and reflectometry in near-UV and visible regions," Appl. Surf. Sc., vol. 244, pp. 338 – 342, 2005.

[16] S. Trolier-McKinstry, H. Hu, S. B. Krupanidhi, P. Chindaudom, K. Vedam, and R. Newnham, "Spectroscopic ellipsometry studies on ion beam sputter deposited $Pb(Zr,Ti)O_3$ films on sapphire and Pt-coated silicon substrates;" Thin Solid Films, vol. 230, pp. 15 – 27, 1993.

[17] Y. P. Jiang, X. G. Tang, Q. X. Liu, Q. Li, and A. L. Ding, "Optical properties of $Pb(Zr_{0.53}Ti_{0.47})O_3$ thin films on Pt-coated silicon substrates measured by spectroscopic ellipsometry in the UV-vis-NIR region," Mat. Sci. Eng. B, vol. 137, pp. 304 – 309, 2007.

[18] WYKO Surface Profilers Technical Reference Manual, ver 2.2.1, (1999).

[19] Polytec Hardware Manual, (2000).

[20] Louis Coryell, US Army Communications and Electronics Research, Development, and Engineering Center, *private communication*.

[21] Dr. Manas Roy, Rockwell Collins, *private communication*.

Chapter 3

Switch Design & Fabrication

This chapter describes the iterations of the PZT switch design process. In particular, this chapter covers aspects of the electromechanical modeling and high frequency simulation that led to the creation of a functional piezoelectric RF MEMS switch. After describing the critical components and actuator requirements, the chapter concludes with a detailed description of the fabrication process for making a piezoelectric switch.

3.1 Switch Design

A RF switch should consist of a transmission line to carry the electromagnetic signal and an actuation mechanism for operating the switch. The transmission line should be comprised of an RF input, RF output, and segmented region for opening or closing the switch. In this work, co-planar waveguides (CPW) were chosen for the transmission line. CPW is an easily fabricated transmission line geometry because it can be created in a single, thin film deposition of a conductive material. For a series switch, the CPW must be segmented to enable an isolating switch state. To operate the switch, an actuated portion of transmission line must complete the segmented transmission line to allow the electrical signal to pass from the input to the output. For a shunt switch, the CPW transmission line is continuous and small portion of conductor is used to short circuit the electrical signal from the RF conductor to the ground plane. As with the series switch, the actuator enables contact between the RF conductor and ground with a small section of conductor. Both types of switches mentioned thus far use ohmic contact for completing the circuit paths. Alternatively, these contacts could utilize a capacitive contact in which a thin dielectric film is positioned between the two conductive regions. At elevated frequencies, the RF energy is capacitively coupled through the dielectric to the switch contact.

The actuator in either switch type should ideally have no effect on the RF performance of the switch, and therefore must have a small footprint and should be

impedance matched with the 50 Ohm transmission line. Furthermore, the actuator should be independently controlled from the transmission line and have an actuation voltage compatible with the system requirements. For this work, piezoelectric actuation has been chosen because of the potential for achieving extremely low actuation voltages. To accomplish this, PZT thin films have been chosen because of their large transverse piezoelectric coefficient.

3.1.1 Design Evolution – PZT SW2.0

The first question in developing a piezoelectrically actuated switch with PZT actuators is choosing what type of switch to create, ohmic or capacitive followed by a series or shunt. Early designs investigated a capacitive shunt switch because of the low insertion loss[1] and the relative ease of integration into a reflection type phase shifter architecture. The initial design question is where to place the actuators so as to minimize their influence on the electrical impedance of the CPW transmission line. One possibility is to place the actuators outside of the CPW so there is minimal interaction. Alternatively, the actuators must be placed with the CPW either parallel or orthogonal to the path of the electrical signal. The first option was chosen for an initial design (PZT SW2.0) of a PZT actuated capacitive switch (see Figure 3.1). For a capacitive shunt switch, the most important parameter for RF performance is the capacitance ratio between the on (C_{on}) and off (C_{off}) states. For an effective phase shifter, a shunt switch must possess an C_{on}/C_{off} ratio in excess of 2:1.[2] The switches for PZT SW2.0 were designed with a dielectric stack of Si_3N_4/SiO_2 (500 / 1000 Å) deposited on top of the CPW at the contact location. The contact pad is designed to achieve a minimum capacitance ratio of at least 2:1 with an on state capacitance of 6.5pF. The on state capacitance was determined by Daniel Judy (US Army Research Laboratory) using an Advanced Design Systems (ADS) simulation for the capacitive shunt switch with the goal of achieving a maximum -20 dB of isolation from DC to 40 GHz. Using an effective dielectric constant of 5.3 for a Si_3N_4/ SiO_2 (500 / 1000 Å) dielectric stack[3] (see Figure 3.2), the shunting pad is designed with dimensions of 310 μm x 208 μm assuming full intimate contact between the shunting contact pad and the dielectric and CPW

transmission line. The contacting areas were designed as follows: each ground capacitor has dimensions of 300 x 30 μm, while the RF capacitor has dimensions of 300 x 10 μm. For these designs the actuators consisted of an elastic layer comprised of SiO_2 (5000 Å) and an active piezoelectric comprised of Ti/Pt/PZT/Pt (200 / 1640 / 5000 / 1640 Å).

a) 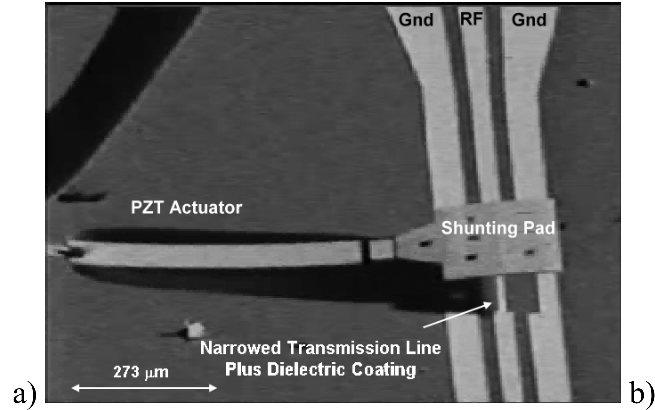 b)

Figure 3.1: SEM images illustrating a PZT actuated capacitive switch design (PZT SW2.0). Gnd is an abbreviation for electrical ground of the CPW transmission line.

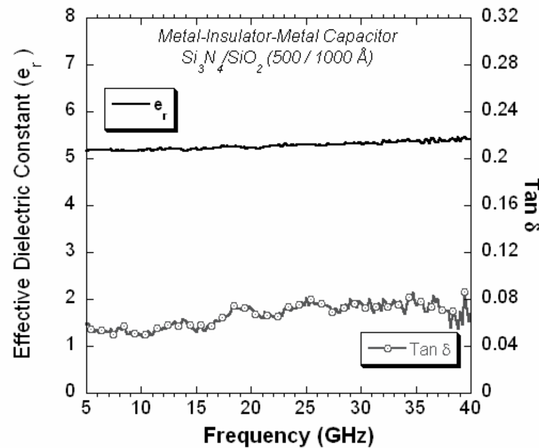

Figure 3.2: Plot of the experimentally measured effective dielectric properties of a Si_3N_4/SiO_2 (500 / 1000 Å) dielectric stack as a function of frequency.

Once this first device was fabricated, it was tested unsuccessfully because of residual stress induced deformations. The residual stress gradient within the actuator stack and shunting pad resulted in deformations in each structure. The actuators posed an

initial positive curvature with the shunting pad initially in the open state upon fabrication. Upon actuation with a voltage opposite the poling field and less than the coercive field, the shunting pad could be closed to make contact with the CPW ground. However, the substantial curvature in the 250 μm long shunting pad prohibited intimate contact between the shunting pad and the dielectric (see Figure 3.3) rendering the switch inoperable.

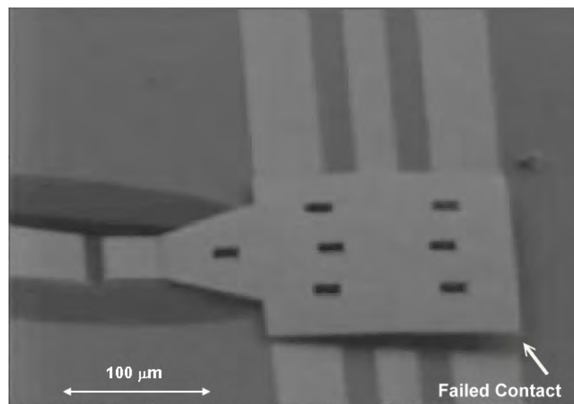

Figure 3.3: Image of PZT SW2.0 design illustrating failure to make contact full contact with the entire CPW transmission line

3.1.2 Actuation and Residual Stress Control

Before addressing the problems identified with PZT SW2.0, it is worth discussing the actuation of the PZT thin films and residual stress control. Thin film PZT generates an in-plane compressive strain at large electric field values applied parallel to the poling direction. The direction of actuation is dictated by two main parameters, the magnitude and sense of the transverse piezoelectric coefficient, $e_{31,f}$, the induced strain (force) and the position of the geometric midplane of the piezoelectric thin film relative to the composite neutral axis (moment arm). If the geometric midplane of the piezoelectric layer lies above the neutral axis, the piezoelectric strain will deflect the actuator up, which is the desired actuation direction for the switch. Therefore, a critical design feature is the negative static deflection of the piezoelectric actuators and RF contact pad visible in Figure 3.11. In order to stress engineer the structures, accurate values of the residual

stress and elastic properties are required. The residual stress values used were obtained from Stoney's equation by measuring the change in wafer curvature following each film deposition with a Tencor FLX-2908 system.[4] The nominal values for each of the thin films used to create the PZT actuators are listed in Table 3.1. The elastic properties for each of the films in the composite stack were obtained from microtensile specimens in collaboration with Dr. William Sharpe of the Johns Hopkins University[5] or from bulk material properties available in the literature [6] (see Table 3.2).

Table 3.1: Average residual stress measured on each of the thin films used in the composite actuator for the PZT switch.

Film	**Nominal Thickness (Å)**	**Stress (MPa)**	**Std Dev (σ)**
SiO_2	1000	33.1	10
Si_3N_4	500	800	200
SiO_2	3500	33.1	10
$Ti/TiO_2/Pt/TiO_2$	160/90/1640/10	323	83.3
PZT	5000	175	7.26
Pt	1050	76.3	16.5

Table 3.2: Elastic modulus values used for electromechanical modeling of the PZT switch actuators.

Film	**Young's Modulus (GPa)**	**Reference**
SiO_2	60.2	5
Si_3N_4	310	6
Ti/Pt	Assumed to be equivalent to Pt	5
PZT	70.1	5
Pt	141.4	5

To determine the neutral axis of the actuator composite, a transformed section method[7] was employed to first redefine each of the thin film layers' cross sectional areas using the Young's modulus of the silicon dioxide within the structural elastic layer as the reference layer (See Equation 3.2).

$$b_n = b * \frac{E_n}{E}, \qquad \text{Equation 3.1}$$

where b is the original width of a particular section, b_n is the transformed width, E is the original Young's modulus and E_n is the transformed modulus. For this effort, the transformed modulus was taken as that of SiO_2 layer but could just as easily be taken as any of the films within the stack. Next, the transformed layer cross sectional areas were calculated, where t_n is thickness (see Equation 3.3). The location of the neutral axis ($\bar{y}$) can be calculated with Equation 3.4 with $\tilde{y}_n$ representing the distance from the centroid of layer n to the arbitrary reference axis (chosen as the bottom of the structural elastic layer).

$$A_n = b_n t_n, \qquad \text{Equation 3.2}$$

$$\bar{y} = \frac{\sum_n \tilde{y}_n A_n}{\sum_n A_n}, \qquad \text{Equation 3.3}$$

Assuming the neutral axis is located below the geometric midplane of the PZT, it is possible to determine if a positive piezoelectric bending moment can be induced. For a poled PZT thin film, application of an electric field in the poling direction causes a vertical elongation (see Figure 3.4) and a lateral contraction of the film. The lateral contraction of the PZT film above the neutral axis results in the actuator moving upward. Thus, it is possible to induce a positive bending moment in the actuator given the location of the neutral axis within the composite actuator. In contrast, the application of a small electric field opposite to the poling direction will result in vertical contraction and lateral expansion for fields less than the coercive field. In this case, a negative bending moment will be generated and the actuator will move downward. Above the coercive field, a vertical elongation occurs once again as the material begins to pole in the opposite direction. As such, the actuator begins to bend upward again. For thin films where the coercive field can be achieved with relatively small voltages (2-3V), this necessitates that

the primary mode of operation be unipolar at elevated field levels to avoid re-writing the film domain state. Thus, the remainder of the discussion will concentrate only on the first case in which the applied field is in the poling direction, i.e. positive piezoelectric bending moment. With a positive bending moment generated, the piezoelectric actuators will deform upward with the application of an electric field.

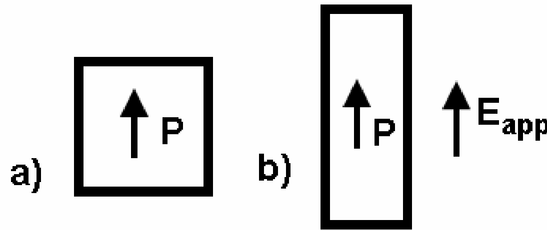

Figure 3.4: Vertical elongation of small volume of poled PZT with the application of an electric field applied in the poling direction.

To create the negative curvature in the actuator, the residual stress gradient within the composite was controlled through the deposition of a dielectric multilayer film consisting of silicon dioxide and silicon nitride. The average residual stress values measured during the formation of the composite actuators are shown in Table 3.1. The large tensile stress of the silicon nitride is coupled with the small tensile stress of the silicon dioxide to counter the stresses within the metal - actuator - metal stack. The film thicknesses must be of the correct magnitude so that the correct deformation is achieved after release from the substrate. To determine what thickness combinations would yield an initial negative curvature to the actuators, the modeled develop by Pulskamp et al. was modified to include a composite of silicon nitride and silicon dioxide instead of pure silicon dioxide for the structural elastic layer.[8] Using an actuator length of 100 μm and the same metal and PZT thicknesses for reference, different combinations of silicon dioxide and silicon nitride thicknesses were input into the model to predict the direction of static beam curvature, see Table 3.3. There are a multitude of combinations that yield the correct beam curvature and the initial composite chosen and subsequently confirmed with experimental testing was $SiO_2/Si_3N_4/SiO_2$ (1000/500/3500 Å). The complete composite thin film stack is depicted in Figure 3.5. It is important to note that the neutral axis associated with this composite stack lies very close to the interface between the

dielectric composite and the base metal. The location ensures positive deflection with actuation and, combined with the residual stress gradient of the composite, ensures the static negative curvature.

Table 3.3: Thickness parameters (in Å) used in the prediction of residual stress deformation of the composite actuators. The thicknesses for the metal and PZT layers were unchanged for these calculations.

Iteration	SiO_2 (Å)	Si_3N_4 (Å)	SiO_2 (Å)	$Ti/TiO_2/Pt/TiO_2$ (Å)	PZT (Å)	Pt (Å)	Deflection of 100μm Actuator (μm)
1	5000	0	0	1908	5000	1050	4.8
2	2250	500	2250	1908	5000	1050	1.0
3	1000	500	3500	1908	5000	1050	-0.6
4	1000	1000	3000	1908	5000	1050	-3.6
5	750	750	3500	1908	5000	1050	-2.5

Figure 3.5: Depiction of the starting wafer composite thin film stack (Si/elastic layer/$Ti/TiO_2/Pt/TiO_2/PZT/Pt$).

3.1.3 Design Evolution – PZT SW3.0

The problems with PZT SW2.0 required a re-examination of the switch design. Instead of creating a capacitive shunt switch, the focus shifted toward creating an ohmic series switch. Upon further examination of the residual stress induced deformations; it was decided to utilize the aforementioned stress engineering to create actuators with an initial negative beam curvature along with a positive actuated tip deflection.

The next concern to be dealt with was the compliance of the actuator. To minimize the length of the actuator, design approaches were examined that placed the

actuators within the RF gap between the RF conductor and ground. As before, Daniel Judy modeled the placement of the PZT actuators within the RF gap except that high frequency signal simulation (HFSS) was used instead of ADS. Although the motivation for placement of the actuators within the RF gaps was initially inspired by electromechanical design, the high frequency numerical modeling suggested an additional advantage of the placement. The actuators are released by etching the underlying silicon substrate with xenon difluoride (see Section 3.2.8). The etch isotropically removes silicon from underneath the actuators as well as adjacent regions. As a result, a portion of the silicon substrate in the vicinity of the switch contacts is removed. This creates an air pocket within the RF gap as well as under and near the RF conductor. The air within these regions considerably changes the local characteristic impedance of the transmission line. Achieving a characteristic 50Ω impedance for the transmission line without the PZT actuators requires an approximate 4 μm gap in the air-dominated sections of the transmission line. At first glance, a gap of 4 μm prohibits the inclusion of PZT actuators within the RF gap because of contact lithography fabrication tolerances with the existing fabrication equipment available at the Army Research Laboratory and processing design rules for photomask offset and overlap. However, the presence of the top and bottom Pt electrodes on the actuators allows the actuators to be "absorbed" into the CPW transmission line. At microwave frequencies, the transmission line sees the piezoelectric actuator as an RF short and essentially extends the width of the RF conductor and increases the RF gap required to maintain a 50Ω impedance. As a result, the total gap required can be split between the two available gaps: the gap between the RF conductor and actuators and the gap from the actuators to the ground plane. This relieves the fabrication constraints on the RF gap and allows PZT actuators to remain in the gap (one on each side of the RF conductor).

Not only are the PZT actuators placed within the RF gap but they are also mechanically linked to the RF conductor using a common elastic layer. In this manner, two actuators flank the center conductor (see Figure 3.6) with the actuators electrical linked together using a pair of air bridges for the bias network. The series switch electrical path is completed using a cantilever (RF cantilever) comprised of gold that overhangs the end of the released portion of the RF center conductor. With the

application of an electric field across the PZT actuators, the entire structure bends upward causing the RF conductor to contact the RF cantilever (see Figure 3.7). The RF cantilever is created using a sacrificial resist with a thickness of approximately 1.8 μm. The thickness of the resist combined with any initial stress deformation dictates the contact gap in the final structure, usually 4 μm of tip deflection (see Section 4.2.1).

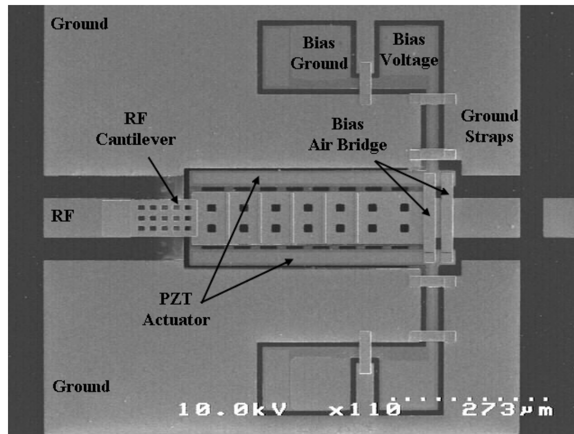

Figure 3.6: Image illustrating the major design components of PZT SW3.0.

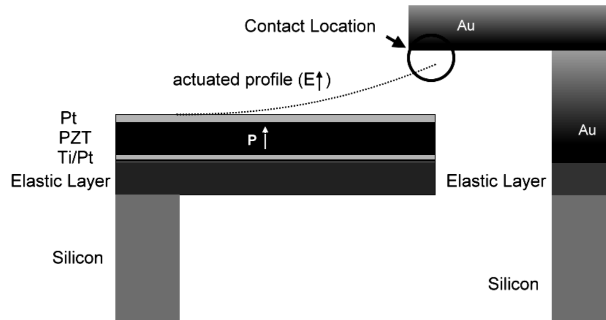

Figure 3.7: Schematic illustration of how the PZT actuator deflection with an applied electric field will result in contact between the RF conductor and RF cantilever.

The required actuator length is derived from the operational requirements for the switch. For an actuation voltage less than 10 volts, the initial tip deflection of the actuators and RF contact gap are important parameters. Additional constraints include switching time with initial goals of 100 μs targeted for missile seeker applications.

Assuming an effective piezoelectric coefficient ($e_{31,f}$) of -14.7 N/V-m (see Section 4.1.2 for further information on the effective piezoelectric coefficient), the actuated tip deflection (at 8 V) as a function of actuator length is plotted in Figure 3.8 for a PZT cantilever comprised of $SiO_2/Si_3N_4/SiO_2$/Ti/Pt/PZT/Pt. The value for $e_{31,f}$ was chosen based on the experimentally determined values for an effective $e_{31,f}$ at 8 volts (see Section 4.1.2). This data can be combined with the anticipated residual stress-induced tip deflection, approximately 4 μm (see Section 4.2.1), and resist thickness (1.8 – 2.0 μm) to choose actuator lengths with the best probability for success. These designs include actuator lengths ranging from 150 – 300 μm.

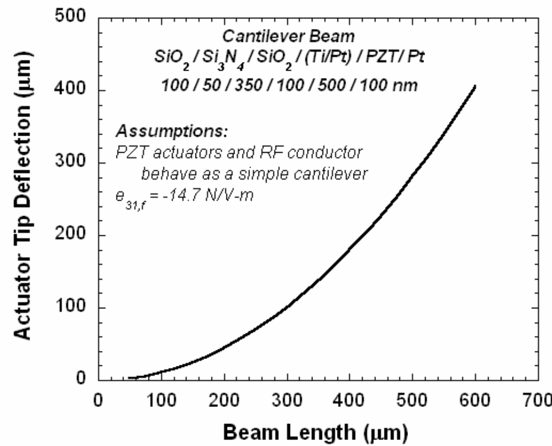

Figure 3.8: Actuated tip deflection as a function of beam length for a PZT cantilever with an actuation voltage of 8 volts.

Using these design principles, the first working RF MEMS series switch actuated by PZT thin films was created (see Figure 3.9).[9] In the open (off) state, the switch had better than -20 dB of isolation below 20 GHz and better than -15 dB up through 40 GHz. In the closed (on) state, the insertion loss was better than 1 dB from DC to 35 GHz. However, the device yield was very low (approximately 30 %) as a result of the mechanical coupling between the actuators and RF conductor. The coupling had a dramatic effect on the actuators' displacement sensitivity by loading the compliance of the PZT cantilevers with the large stiffness of the unactuated gold center conductor. The result is a structure with severe width curvature (see Figure 3.10a). As a result, the simple cantilever assumption is invalid. Furthermore, when an electric field was applied,

the actuator and conductor deflected upward out of the surface plane as designed except that the width curvature is exaggerated (see Figure 3.10a). The width curvature led to non-repeatable device performance along with limited and sometimes zero contact between the RF conductor and RF cantilever as the RF cantilever contacted the elastic layer instead of the RF conductor (see Figure 3.10b).

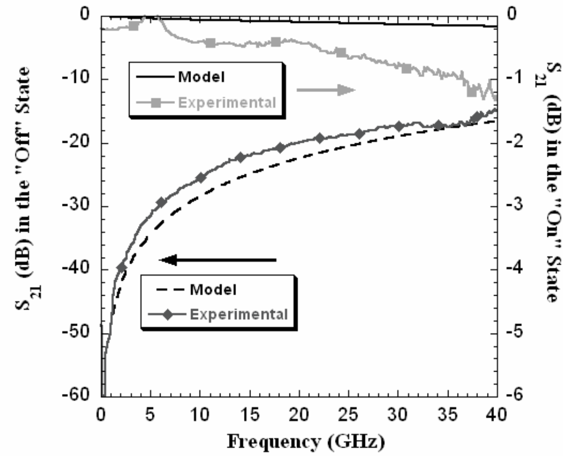

Figure 3.9: Experimental and modeled RF performance of the first functional PZT actuated RF MEMS switch from DC to 40 GHz. Note, the model assumed a contact resistance of 1 Ohm in the closed state.

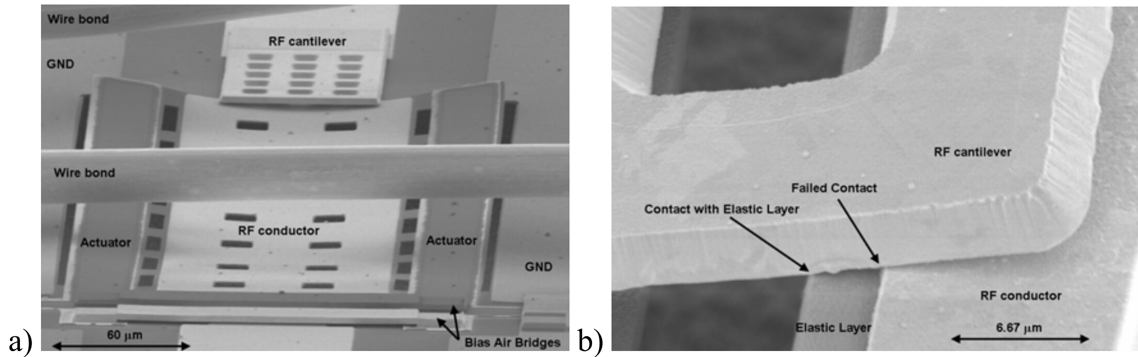

Figure 3.10: SEM images (taken by Matthew Ervin, US Army Research Laboratory) illustrating the (a) exaggerated width curvature of the coupled RF conductor and PZT actuators upon actuation and (b) prevention of device contact as a result of the width curvature.

3.1.4 Mechanical and High Frequency Simulation of the Primary Designs (PZT SW4.0, PZT SW5.1, & PZT SW5.2)

Improvements to the PZT SW3.0 design were undertaken through a close iterative process between the requirements of the mechanical, high frequency electro-magnetic, and fabrication design processes. Modified designs sought to improve upon the successes exhibited with the PZT SW3.0 design. In particular, the actuator displacement sensitivity imposed by the aforementioned coupled RF conductor, the insertion loss, and the reproducibility of the RF performance were targeted for improvement. The results of a collaboration between Jeffrey Pulskamp, Daniel Judy, and myself yielded several successful adaptations of the original PZT SW3.0 design with improved performance, reliability, and repeatability. Designs PZT SW4.0 and PZT SW5.1 are nearly identical with slight variations on actuator length and will be discussed below. In contrast, PZT SW5.2 will be discussed in Section 4.5.

To eliminate the width curvature induced by the mechanically attached center conductor, designs were investigated that kept a majority of the center conductor fixed to the substrate. Rather than releasing a large section of RF conductor and mechanically coupling it to the entire length of the PZT cantilevers, a much smaller section of RF conductor is mechanically attached at the ends of the PZT cantilevers (see Figure 3.11).[10] In essence, the actuators become separate individual cantilevers. As a result of this modification, an additional RF cantilever must be attached to the input side of the RF transmission line. The additional RF cantilever transforms the switch into a two contact point switch as the RF contact pad must contact both RF cantilevers to complete the electrical circuit. This approach eliminates the influence of the mechanically coupled RF conductor on the actuators, potentially at the expense of a higher contact resistance from a two contact switch. These design modifications and the subsequent switch performance will be the focus of much of this thesis. The critical features along with design dimensions for PZT SW4.0 and PZT SW5.1 are listed in Table 3.4.

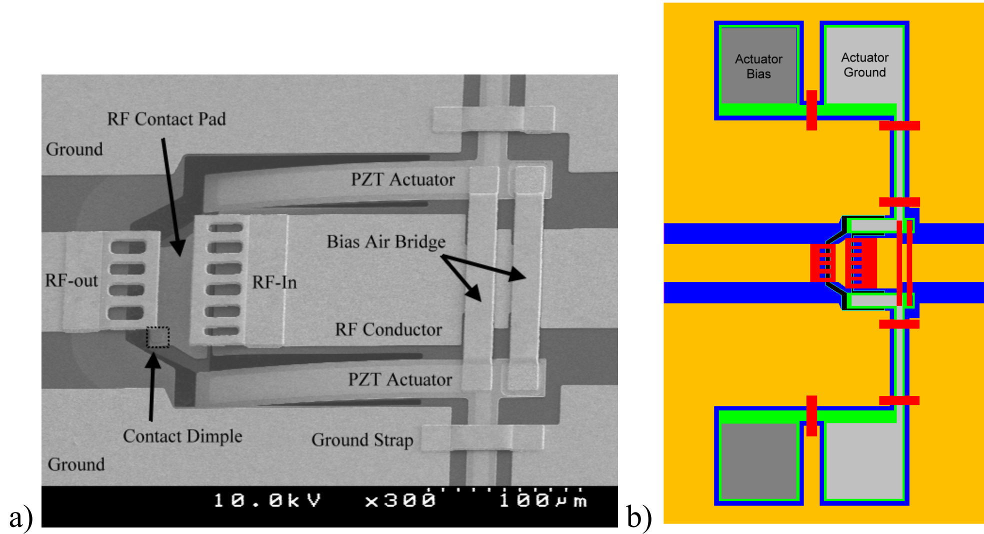

Figure 3.11: a) Image outlining the critical features of PZT SW4.0 that requires 2 ohmic contacts for good RF performance and b) the CAD drawing illustrating the bond pad locations with the ground planes.[10]

Table 3.4: Dimensional Information for the PZT SW4.0 and PZT SW5.0

Feature	**Width (μm)**	**Length (μm)**
RF conductor (outside of actuators)	75	>150 (depends on probe test and packaging requirements
RF conductor (under air bridges)	50	10
RF Gap (between actuators)	40	
RF Gap (outside of actuators)	50	
Ground Plane	440	660
PZT Actuator (actuated length)	40	SW4.0 (90, 115, 140) SW5.0 (65, 90, 115)
RF Cantilever (in)	100	37.5
RF Cantilever (out)	75	37.5
RF Contact Pad (in)	120	
RF Contact Pad (out)	77	
Bias Air Bridges	170	10
Ground Straps	18	80

During switch operation, an applied voltage to the PZT actuators results in an upward deformation of the actuators. In conjunction, the RF contact pad moves upward

enabling switch closure. The contact pad completes the RF circuit by making contact to the two cantilevers suspended above the RF contact pad. Two bias lines, one for each actuator, are electrically tied with air bridges over the RF conductor and reside within the ground plane. The actuator bias lines allow the actuation voltage to be applied independent from the RF conductor. The bias air bridges load the RF line with capacitance which changes the impedance of the CPW transmission line. The capacitive loading can be compensated for by using Equation 3.4 which equates the characteristic impedance per unit length (Z) to the characteristic inductance per unit length (L) and capacitance per unit length (C). The capacitive loading is reduced and compensated with an increase in inductance of the transmission line by narrowing the RF conductor underneath the bias air bridges to maintain 50 Ohm impedance (see Figure 3.12). In addition, the RF transmission line is widened in the regions where the PZT actuators are located to maintain the proper impedance because of a reduction in the effective dielectric constant of the substrate. As previously mentioned, the etch process to release the PZT cantilevers also removes silicon from underneath portions of the RF transmission line. This air cavity beneath portions of the CPW reduces the effective dielectric constant within this region, resulting in an increase in characteristic impedance of the transmission line (see Equation 3.4). The decreased capacitance can be increased by reducing the gap between the RF and ground conductors, thereby increasing the characteristic capacitance per unit length (see Equation 3.5, where A is area, g_{RF} is the RF gap, ε_o is the permittivity of free space, and ε_r is the relative permittivity of the material of the RF gap, unity for air).

$$Z = \sqrt{\frac{L}{C}} \qquad \text{Equation 3.4}$$

$$C = \frac{\varepsilon_o \varepsilon_r A}{g_{RF}} \qquad \text{Equation 3.5}$$

Other notable features include the bond pads for the actuators which are located within the ground plane regions. Ground strap air bridges are used to maintain electrical continuity of the ground planes along the length of the bias lines. In order to improve the contact resistance of the switch, metallic bumps or dimples are added to the RF contact pad and the underside of the RF cantilevers is modified to include a dimple as well. The contact dimples allow for different metals to be used for contact to minimize the potential for stiction or microwelding of the contacts, thereby improving device lifetime.[4,11,12,13,14]

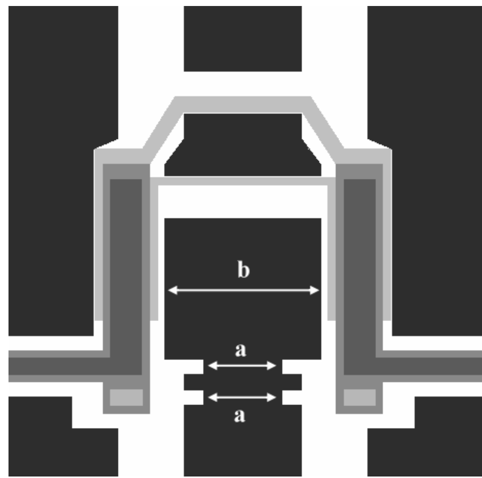

Figure 3.12: Illustration of the RF conductor width modifications to account for (a) capacitive loading from the DC bias air bridges and (b) the changes to the capacitance within the RF gap from the air cavity underneath the actuators and CPW transmission line.

Electromechanical analytical and ANSYS™ finite element analysis (FEA) models were developed by Jeffrey Pulskamp (US Army Research Laboratory) to analyze the performance of the actuators in terms of actuator displacement, resonance characteristics, switching speed, temperature sensitivity, and contact behavior. The FEA models suggested that a piezoelectrically actuated cantilever with a short contact pad at the end of the cantilever is capable of operating below 10 volts with a reasonable contact force, leading to a contact resistance in the range of 2 – 5 Ohms (see Figure 3.13). The contact resistance was computed (Equation 3.1) assuming a diffusive transport and plastic deformation model as discussed in Chapter 1.3.1,

$$R_{ct\,DP} = \frac{\rho}{2}\sqrt{\frac{H_M \pi}{F_c}}$$ Equation 3.6

where $R_{ct\ DP}$ is the contact resistance, F_c is the contact force, ρ is the resistivity of the contacting metals ($1.06e^{-7}$ Ohm-m for Pt), and H_M is the Meyer hardness of the contact material (3.5 GPa for Pt).[15,16] As illustrated, the actuators deform upward relative to the wafer surface until they close the switch contacts at approximately 5.5 volts, at which point the contact force starts to increase. At 10 volts, the computed contact force should be 5.5 μN corresponding to a contact resistance of 2.48 Ohms, assuming a Pt to Pt contact pair.

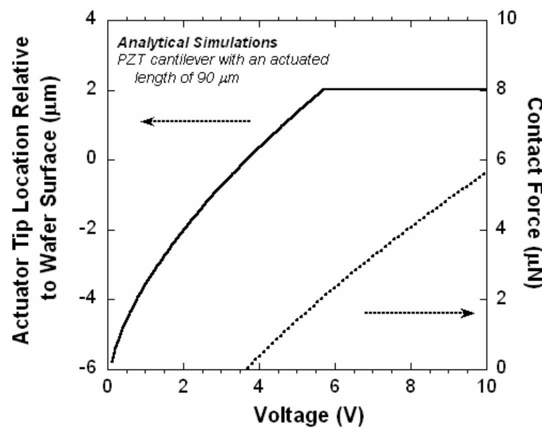

Figure 3.13: Predicted piezoelectric actuator deflection and contact resistance as a function of voltage.

In order to design the switch for elevated frequencies, Ansoft's High Frequency Structure Simulator (HFSS) was used by Daniel Judy (US Army Research Laboratory) to simulate the switch design and to optimize the switch and transmission line geometries to ensure minimal disturbance to the RF transmission line impedance and loss characteristics. The results of the HFSS model are illustrated in Figure 3.14. As shown, S_{21} in the open state, or the isolation, is better than the 20 dB goal from essentially DC to above 40 GHz. Furthermore, S_{21} in the closed state, the insertion loss, is better than 1 dB from DC up thru 40 GHz. The insertion loss is higher than the goal value of 0.5 dB as a

result of substrate losses (added to the model to account for experimentally observed substrate losses) that that will be discussed in Chapter 4.4.4.

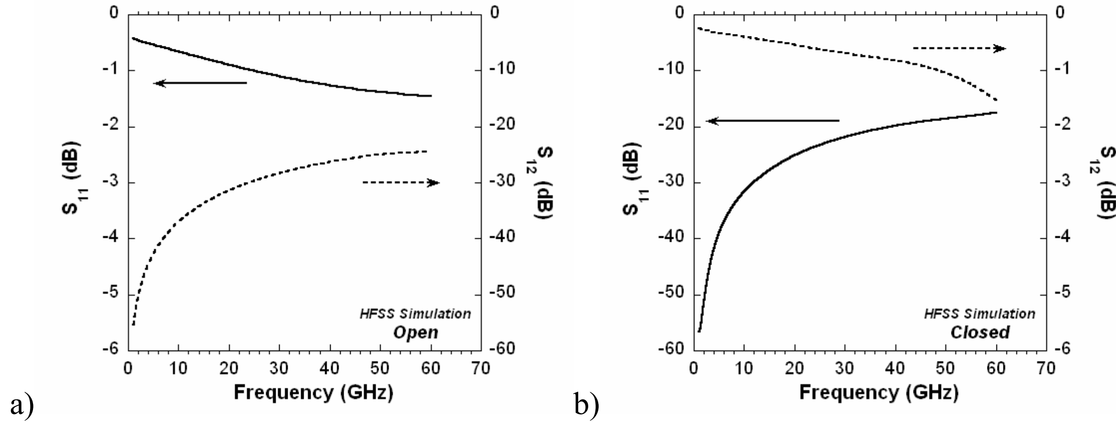

Figure 3.14: HFSS simulation of a PZT series switch (PZT SW4.0 & PZT SW5.1) in the open state and closed state.

In addition to the HFSS simulations, an equivalent circuit model was developed for a PZT switch using Advanced Design System (ADS) software (see Figure 3.15). Ansoft's Q3D extractor was used to extract the capacitances and inductances for this model. The solid model that was used for the HFSS model was imported to Q3D and all of the CPW geometry was removed, leaving the geometry for the actuators, input and output cantilevers, and the switch contact pad. Table 3.5 shows the resulting component parameters for the on and off states of the switch. The inductances of the circuit are described with L_i representing the input cantilever inductance, L_o is the output cantilever inductance, and L_c is the contact pad inductance. Similarly, C_{ic} is the capacitance from the input cantilever to the contact pad, C_{oc} is the capacitance from the output cantilever to the contact pad, and C_{io} is the capacitance from the input cantilever to the output cantilever. Finally, R_{cic} and R_{coc} are the contact resistances from the input cantilever to the contact pad and from the output cantilever to the contact pad respectively. These components encapsulate the essence of the switch. The input CPW (CPW_i) and output CPW (CPW_o) were added to better match the measured results. In addition, the R_{subi} and R_{subo} resistors were added to model the effects of the excessive substrate loss (see Chapter 4.4.4 for discussion). The results of the equivalent circuit model were very

similar to the HFSS models (see Figure 3.16) with the exception of closed state S_{11} performance. The reason for the discrepancy is that the closed state ADS model includes a contact resistance for each switch contact whereas the HFSS model does not. As a result, the HFSS model overestimates the DC isolation.

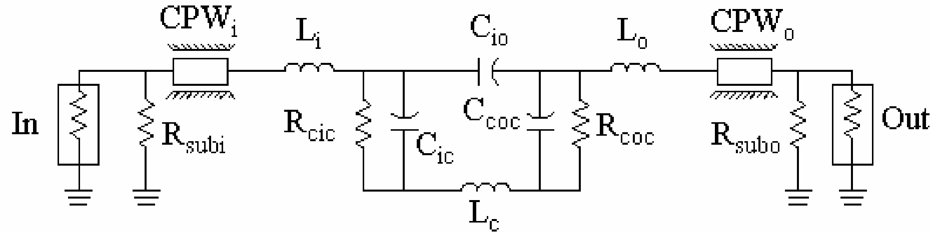

Figure 3.15: PZT switch (PZT SW4.0 & PZT SW5.1) equivalent circuit model with parameters derived from Ansoft's Q3D.

Table 3.5: List of the nominal component values for the equivalent circuit model shown in Figure 3.15.

Item	On	Off
R_{subi}	2000 Ω	2000 Ω
L_i	39 pH	39 pH
R_{cic}	3.5 Ω	∞
C_{ic}	4.9 fF	25 fF
L_c	7 pH	7 pH
C_{io}	2.6 fF	2.6 fF
C_{oc}	1.9 fF	14 fF
R_{coc}	3.5 Ω	∞
L_o	9.9 pH	9.9 pH
R_{subo}	2000 Ω	2000 Ω

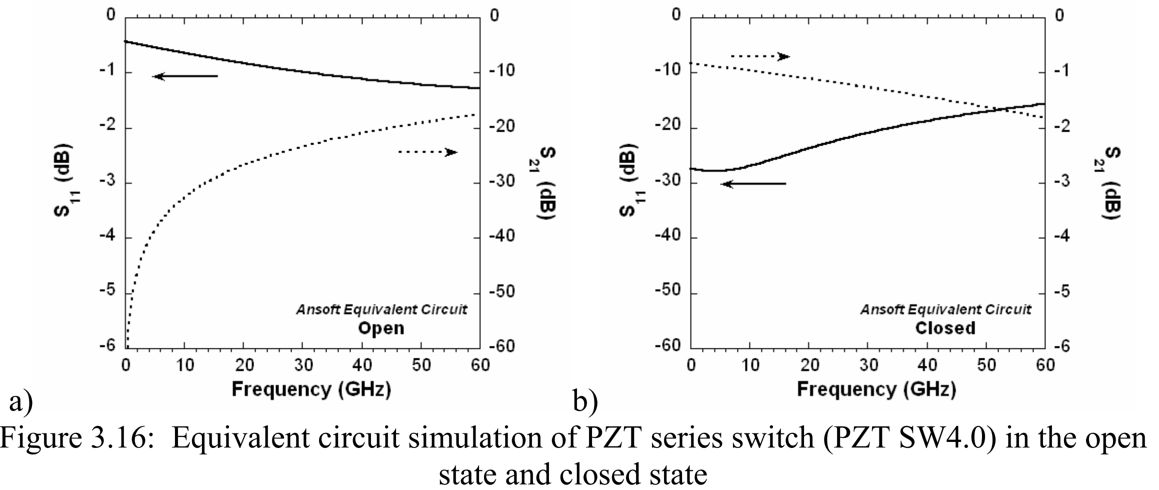

Figure 3.16: Equivalent circuit simulation of PZT series switch (PZT SW4.0) in the open state and closed state

3.2 Fabrication

3.2.1 Substrate Selection

Switch fabrication [9,10] was done in the US Army Research Laboratory's Specialty Electronic Materials and Sensors Cleanroom Facility and began with choosing the appropriate substrate for the high frequency transmission lines. The preferred substrate is silicon because of the wealth of knowledge on fabrication processes as well as previous history with processing PZT thin films on platinized silicon substrates. However, as illustrated in Figure 3.17, a standard resistivity (1-30 Ohm-cm) silicon substrate has extremely poor transmission line loss at microwave frequencies. Traditional microwave substrates, alumina and sapphire[2], have transmission line losses less than 0.04 dB/wavelength (see Figure 3.17). Even though high resistivity silicon is not commonly thought of as a microwave substrate, it performs quite well, with a transmission line loss of ~0.05 dB/wavelength at 40 GHz (see Figure 3.17). The transmission line loss is reported as dB/wavelength and not dB/mm because the primary aim of the PZT switch is in distributed RF circuits. As a consequence, the interest is in designing the smallest low loss circuits such as phase shifters and tunable antenna receivers. As the microwave wavelength depends on the dielectric constant of the substrate, other substrates such as quartz and fused silica usable for transmitting energy point-to-point, where dB/mm is important, require much larger circuits to maintain a

particular wavelength. The result is that the line loss per wavelength increases. For this effort, high resistivity (> 10 kOhm-cm) Czochralski-grown (100) silicon substrates were chosen for the PZT switch.

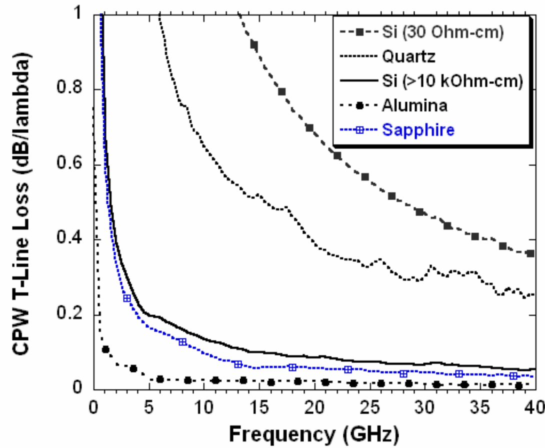

Figure 3.17: Co-planar waveguide transmission line (T-line) loss as a function of frequency for various substrates.

3.2.2 Elastic Layer Deposition

The structural layer was deposited via plasma-enhanced chemical vapor deposited (PECVD) with the deposition parameters for each of the materials listed in Table 3.6. To reduce the influence of interfacial stresses on the composite, the multilayer stack was deposited with a continuous plasma source with the gas flows changing at the appropriate time intervals. The effect of the continuous plasma deposition was also observed in the average residual stress of the composite stack. The average stress for the continuous plasma was 51 MPa (± 28 MPa) whereas the stress for a composite stack deposited with individual layers was 155 MPa (± 45 MPa). X-ray photoelectron spectroscopy (XPS), performed by Dr. Unchul Lee of the US Army Research Laboratory, was used in an attempt to ascertain the difference between using a continuous versus discrete deposition of the composite. However, as shown in Figure 3.18, both deposition conditions exhibited nearly identical XPS sputter depth profiles, with narrow transitions between each layer of the composite.

Table 3.6: Plasma enhanced chemical vapor deposition parameters for silicon dioxide and silicon nitride thin films deposited using a Plasma-Therm 790.

Material	SiH_4 in 5% He (sccm)	He (sccm)	$N_2$0 (sccm)	N_2 (sccm)	NH_3 (sccm)	Pressure (mT)	Temp (ºC)	Power (W)
SiO_2	70	93	390	0	0	900	250	25
Si_3N_4	90	488	0	160	3.00	900	250	45

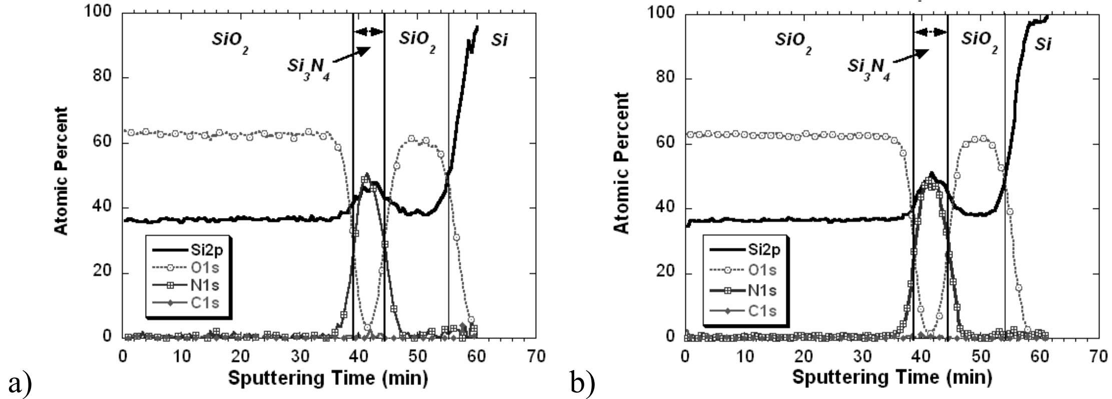

Figure 3.18: X-ray photoelectron spectroscopy (XPS) depth profile highlighting the interfaces in PECVD composite oxide/nitride/oxide thin films. (a) Shows results for a sample grown with a continuous plasma whereas (b) corresponds to a sample prepared with individual deposition and anneals.

Following PECVD deposition, the structural layer was annealed at 700ºC in flowing N_2 (~5 sccm) for 60 seconds to eliminate loosely attached hydrogen ions from the dielectric thin films.[17,18,19] The hydrogen release resulted in a restructuring of the atomic bonds within the film, altering the residual stress within the PECVD films. This transformed them from compressive to tensile, which was recorded using the method described in Chapter 2.1 (see Figure 3.19). The stress versus temperature scans were run a second time to confirm that the stress change after the initial anneal was stable and would not be affected by subsequent processing at 700ºC. After the anneal, the film thicknesses were measured with a JA Woollam M-2000F multi-wavelength, multi-angle ellipsometer. The film thicknesses were determined from a model in which the optical properties were treated with Tauc-Lorentz and Cauchy-based models. The accuracy of the model results was judged by examining the mean square error (MSE), a measure of

the deviation of the model from the measurements (see Chapter 2.2 for further discussion). The model was believed to be appropriate when the MSE was less than 50 for PZT films and less than 25 for the oxide nitride composites (see Figure 3.20 for a representative example of the ellipsometry model).

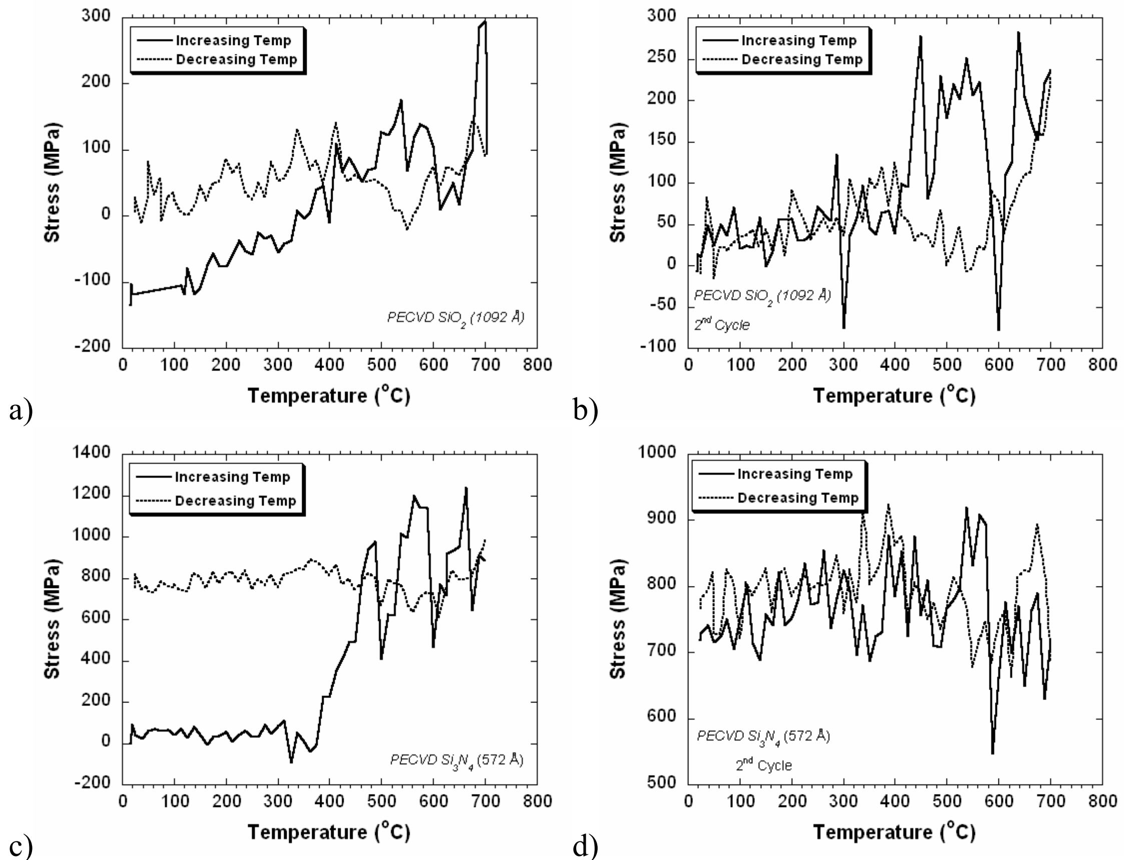

Figure 3.19: Residual stress variation with temperature in flowing N_2 with (a & b) PECVD SiO_2 and (c & d) Si_3N_4 thin films. The removal of trapped hydrogen ions with temperature transforms the film stress from compressive to tensile. For each film, a second thermal scan illustrates that each film is relatively unaffected by additional thermal processing up to 700ºC. Note, the spikes in the data are attributed to measurement noise generated by cleanroom personnel using equipment adjacent to the stress measurement system during the over 6 hours of temperature testing.

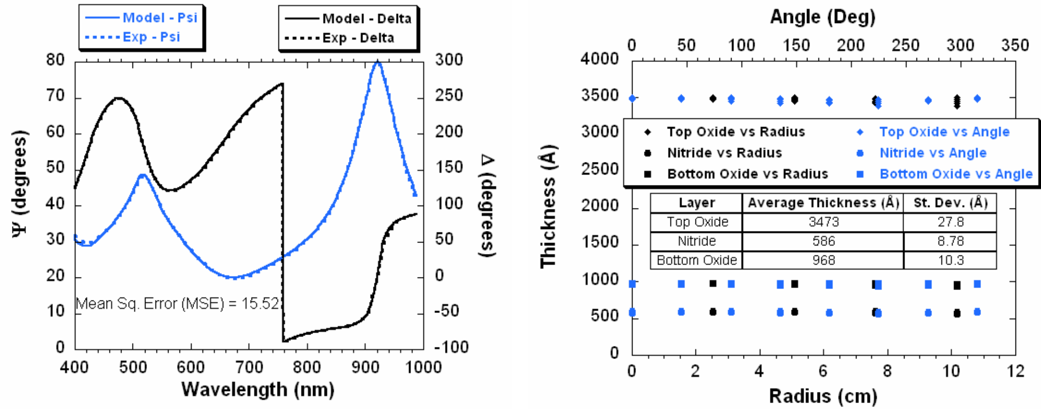

Figure 3.20: Example of the measured and modeled ellipsometry results for oxide/nitride/oxide structural layer and the resulting thickness uniformity across a 100 mm wafer.

3.2.3 Bottom Electrode Deposition

Next, the base electrode for the piezoelectric actuators was deposited via DC magnetron sputtering using a Unaxis Clusterline 200 multi-chamber clustertool. This layer consisted of a combination of titanium, titanium dioxide, and platinum thin films. The deposition conditions are outlined in Table 3.7. A base layer of titanium (~160 Å) was first deposited to serve as an adhesive layer for the remaining layers. Immediately following, a 90 Å titanium dioxide thin film was deposited to serve as diffusion barrier to prevent titanium from penetrating into the platinum.[20] Finally, a 1640 Å thick platinum thin film was deposited. An alternative metal stack used for the switch fabrication was Ti (200 Å) followed by Pt (820 Å). After the deposition, the entire thin film stack was annealed at 700ºC in flowing compressed dry air (~5 sccm). The anneal resulted in a stress relaxation of the metal thin films, with an increase in the tensile stress of the metal layer (see Figure 3.21). Following the anneal, a 10 Å titanium dioxide thin film was deposited in an attempt to seed the growth of a textured (111) oriented $PbZr_{0.52}Ti_{0.48}O_3$ (PZT) thin film.[21,22]. The seeding was part of the existing ARL fabrication process flow. However, as illustrated in Figure 3.22 efforts to create a highly textured (111) thin film were unsuccessful. The PZT films remained a mixture of (100) and (111) orientations along with a small percentage of (110).

Table 3.7: Deposition conditions for all sputtered metals used in the fabrication of the PZT MEMS switch.

Material	Ar (sccm)	O_2 (sccm)	Pressure (mTorr)	Temp (ºC)	Power (W)
Ti	30	0	5	500	1000
TiO_2	20	20	5	500	1000
Pt	50	0	5	500	500
TiO_2 (seed)	20	20	5	500	1000
Pt (top layer)	50	0	5	300	500

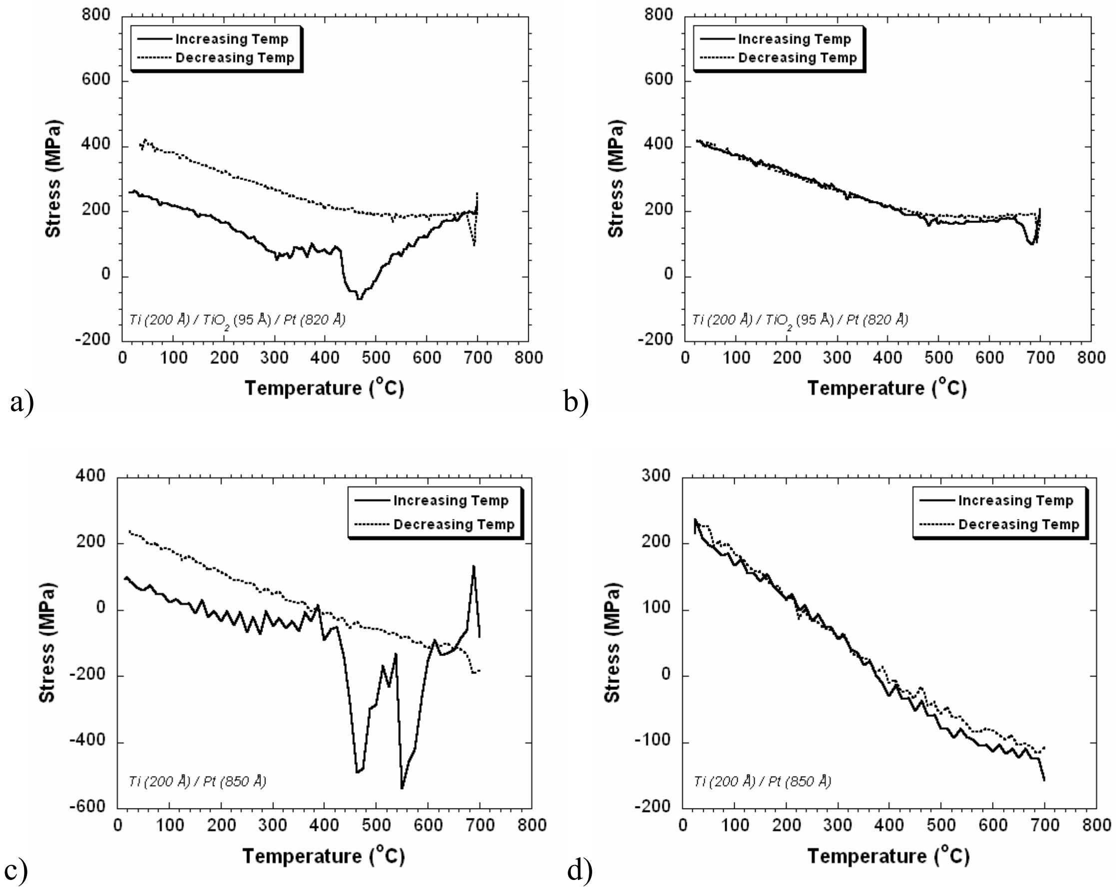

Figure 3.21: Residual stress variation with temperature in air for sputtered (a & b) $Ti/TiO_2/Pt$ and (c & d) Ti/Pt thin films on a SiO_2 (2000 Å) coated silicon substrate. The relaxation of the metal layers with temperature transforms the film stress from compressive to tensile. A second thermal scan illustrates that the stress was stable with additional thermal processing up to 700ºC. Note, the spikes in the data on plot (c) are attributed to measurement noise generated by cleanroom personnel using equipment adjacent to the stress measurement system during the over 6 hours of temperature testing.

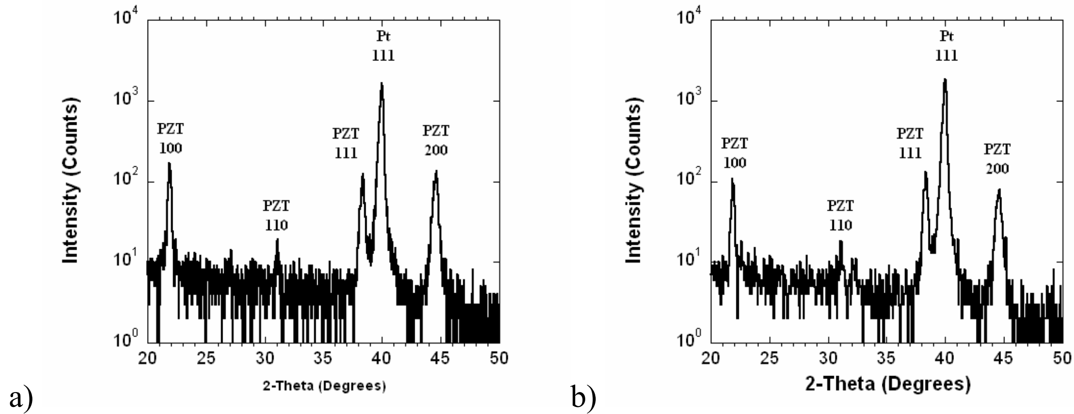

Figure 3.22: X-ray diffraction results (θ – 2θ) for a 0.5 μm PZT thin films grown with (a) and without (b) a 10 Å TiO_2 seed layer.

3.2.4 PZT Thin Film Deposition

The PZT thin films were prepared via a metal organic solution chemistry process modified from the one outlined by Budd, Dey, and Payne.[23] The sol-gel solution was prepared using lead acetate trihydrate, zirconium n-propoxide, and titanium iso-propoxide as a precursor and 2-Methoxyethanol (2-MOE) as the solvent. The process begins by combining 36.46 g of the lead precursor (batched with 12 mol% excess lead) with 150 mL of 2-MOE. The mixture was heated to 120ºC using a rotary evaporator at 120 rpm and a silicone oil bath. After mixing for 20 minutes, the water was removed using vacuum distillation with a base pressure of -30 in Hg. While the lead precursor was mixing, 20.0 mL of the zirconium and 12.43 mL of the titanium precursors were combined with 120 mL of 2-MOE in an Ehrlenmeyer flask. After the lead precursor cooled back to room temperature, the zirconium, titanium, and 2-MOE mixture was added to the dehydrated lead and 2-MOE solution. The entire solution was then refluxed for 3 hours at 120ºC. After the solution was cooled to room temperature, 8.6 mL of formamide (4 vol %) was added to the solution as a drying control agent. The final solution molarity was 0.4 M. The solution was then sealed in a pyrex bottle and stirred on a magnetic stir plate overnight. For quality control, each new solution was used to deposit a 5000 Å thick PZT layer onto a 2.5 cm^2 silicon substrate coated with 2000 Å SiO_2 and Ti/Pt (200 Å / 1640 Å). Next, 1050 Å thick platinum electrodes (500x500 μm) were sputter deposited onto the wafer surface and patterned with a liftoff technique (see

Chapter 3.2.7 for more details). Finally, the test wafer piece was patterned with a Clariant AZ 5200 photoresist, allowing the corner of the test piece to be placed into an acid bath to remove the PZT, thereby exposing the bottom platinum electrode. The wet etch procedure will be discussed in a following section. The completed test specimens were subjected to both ferroelectric and dielectric measurements. Solutions were considered to be of acceptable quality if the remanent polarization was >15 μC/cm^2 and the dielectric constant was approximately 1000 (see Figure 3.23). In addition, leakage current measurements were taken with values targeted at maintaining values less than 10^{-6} A/cm^2 at 380 kV/cm.

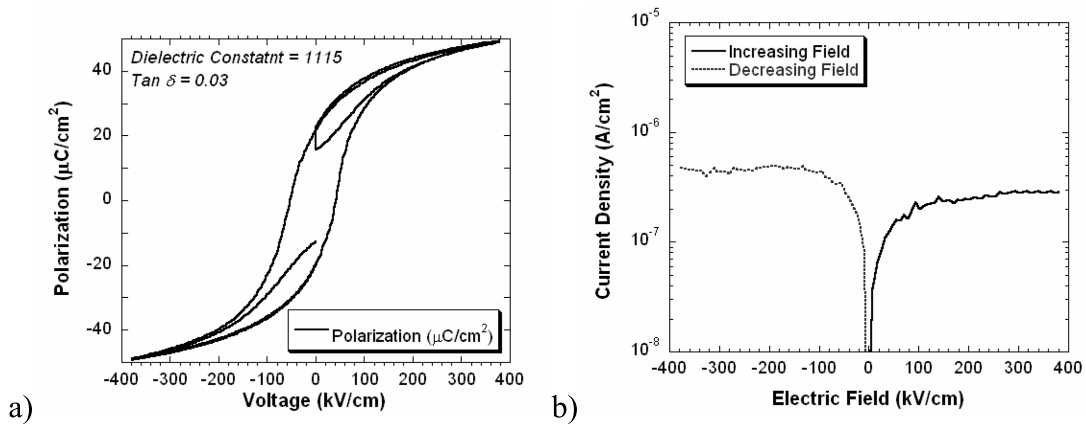

Figure 3.23: Ferroelectric, dielectric, and leakage current data recorded as part of the PZT solution test procedure.

Following a successful test deposition to ensure proper quality control of the PZT solution, the sol-gel could be deposited onto device substrates. The solution was dispensed onto the prepared substrate and then spun at 2000 rpm for 30 seconds. After spinning, the wafer was transferred to a hot plate at 350ºC, where pyrolysis removes most of the organics after a 2 min bake. This deposition, spin, and pyrolysis step were repeated for a total of 4 cycles. After the 4th cycle, the amorphous film was crystallized in a rapid thermal anneal furnace at 700ºC in flowing compressed dry air (~5 sccm) for 30 seconds, resulting in PZT thickness of approximately 2500 Å. The entire process was repeated once more to achieve a film thickness close to 5000 Å. The final film thickness was measured with a multi-wavelength, multi-angle ellipsometer. The film thicknesses

were modeled with Cauchy based optical model targeting with a MSE less than 50 (see Figure 3.24 for a representative example of the ellipsometry model).

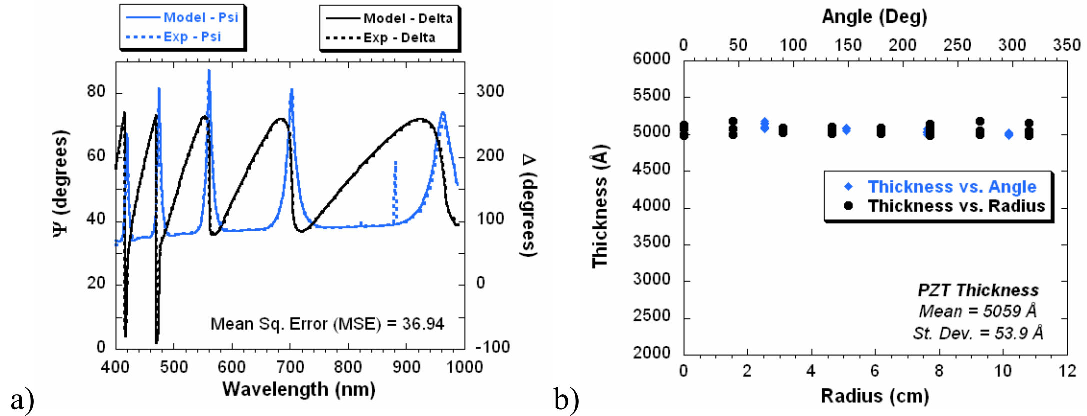

Figure 3.24: Example of the measured and modeled ellipsometry results (a) for PZT thin films and the thickness uniformity (b) measured across a 100mm substrate.

3.2.5 Top Electrode Deposition

Following the PZT deposition and characterization, a 1050 Å platinum thin film was sputter deposited onto the PZT surface. The platinum layer served as the top electrode of the PZT actuator. In order to improve adhesion of the platinum and heal the surface induced sputtered damage, the wafers undergo a rapid thermal anneal at 350°C for 2 minutes in air. As seen in Figure 3.25, the tensile stress within the platinum layer increases with increasing temperature. However, there is no permanent change in the residual stress of the platinum as it returns to room temperature. If the anneal temperature is increased to 500°C, the room temperature stress increases to approximately 305 MPa as the platinum stress relaxes at higher temperature.

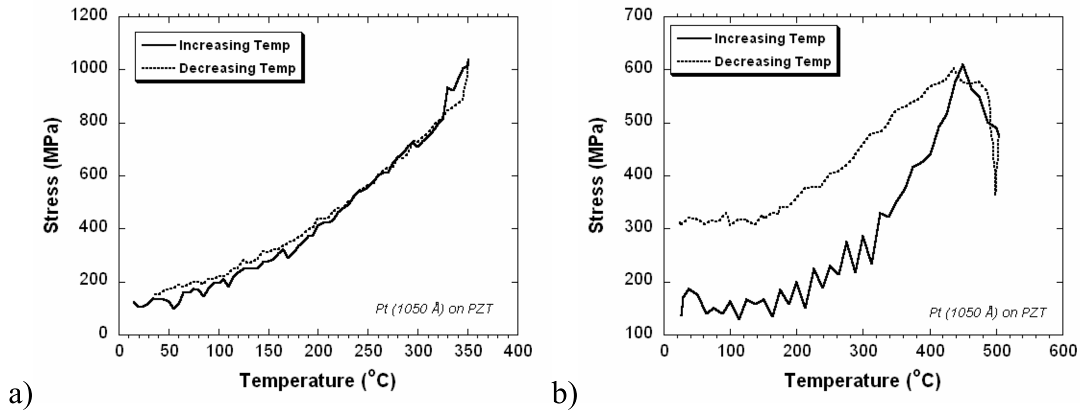

Figure 3.25: Residual stress variation with temperature (a – 350ºC and b – 500ºC) in air for sputtered Pt on top of a PZT thin film.

3.2.6 Piezoelectric Actuator Patterning

The process to define the critical components of the switch began with the creation of the actuators by defining the top metal with argon ion-milling (see Figure 3.26). This process started by patterning a ~2.0 µm thick layer of Clariant AZ 5200 series resist cured at 110ºC. This same photoresist was used throughout the fabrication process. The photoresist was patterned using a Karl Suss MA/BA-6 mask aligner and subsequently developed using a Karl Suss ACS 200 resist cluster tool. Following inspection of the photoresist pattern, the wafer underwent a descum procedure to remove any remnant resist. The descum process was completed following each photoresist patterning procedure. The details of the descum procedure are outlined in Table 3.8. Next, the resist underwent an ultra-violet (UV) curing process at 200ºC for 30 seconds to reduce the potential of platinum being redeposited during the ion-milling process. High temperature curing of photoresist can improve the resistance of the photoresist to damage during reactive ion etching and ion implantation processes.[24,25] The UV curing process removes the solvents in the resist and leaves a completely homogenous cross-linked resist.[26,27] This process minimizes the potential of etched non-volatile species from being embedded in the resist. The exposed metal layers were removed using a Commonwealth Scientific argon ion mill. The milling was accomplished using the parameters listed in Table 3.9. The angle of incidence was manually controlled to 85° for the bulk of the milling procedure. To minimize re-deposition on the sidewalls of the

resist, the final 30 seconds were milled at an angle of 50°. After the ion-mill, the resist was ashed using the parameters detailed in Table 3.8.

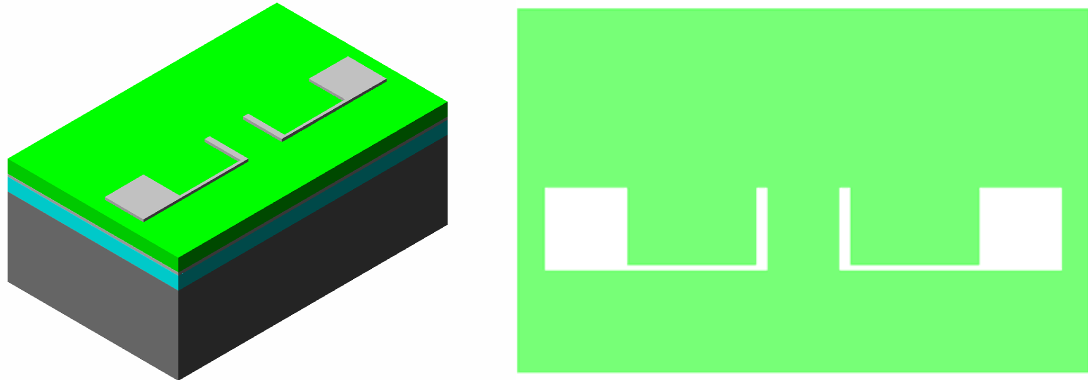

Figure 3.26: Fabrication flow – top electrode patterning. The left image is a 3-D rendering of the device stack with the individual layer thicknesses grossly exaggerated. For all 3-D renderings, the silicon substrate is represented by the large grey block, the elastic layer stack is light blue, platinum electrodes are light grey, PZT is green, gold layers are tones of yellow, and the sacrificial layer is pink. On the right is a top down view.

Table 3.8: Parameters for oxygen plasma processes.

Description	**Equipment**	**O_2 (sccm)**	**Pressure (mTorr)**	**Temp (°C)**	**Power (W)**
Descum	Metroline (ML4)	200	525	~70	200
Resist removal (ash)	Metroline (ML4)	500	1000	~160	400
Sacrificial layer removal	Anatech	680	~1380	~145	800

In the next step, the PZT and underlying metal layers were patterned using the same resist process and ion-milling procedure described above (see Figure 3.27). To aid in the removal of re-deposited platinum on the sidewalls of the PZT thin film, the time allotted to ion-milling at an angle of 50° was increased to 45 seconds. Additionally, the wafer clamping ring was removed to improve the etching uniformity. The resist was removed using the ashing process outlined previously.

Table 3.9: Parameters used for ion-milling PZT, Pt, and Au thin films.

Item	Voltage (V)	Current (mA)
Cathode	11.5	14
Discharge	40	2.5
Beam	500	300
Accelerator	100	34
Neutralizer		500
Bias	36	
Ar (sccm)	10	
Operating Pressure (Torr)	7×10^{-4}	
Chuck rotation (rpm)	5	

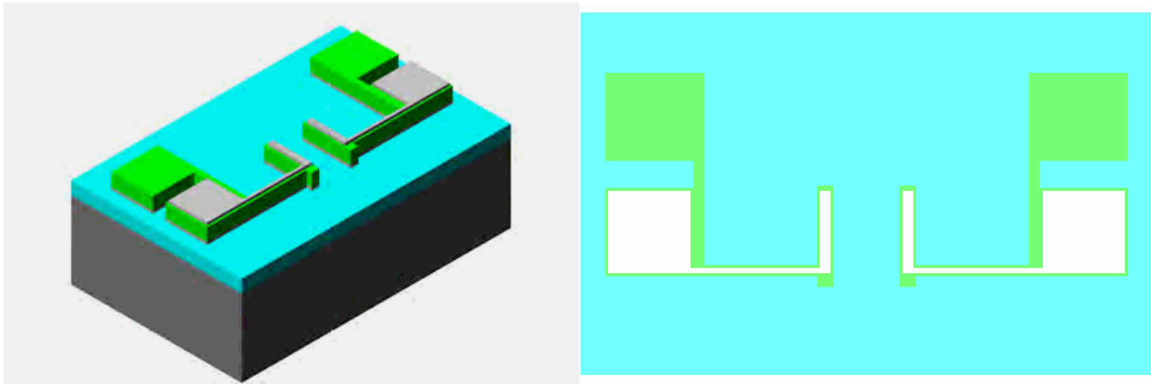

Figure 3.27: Fabrication Flow – PZT and bottom electrode patterning. PZT and the top electrode remain in the active piezoelectric actuator regions, both sets of bond pads, and connecting bias lines. The remaining PZT and bottom electrode material are etched down to the structural elastic layer.

To gain access to the bottom electrode, a H_2O:HCl:HF (2:1:0.04) wet etch was used to locally remove the PZT (see Figure 3.28). The wafer was patterned with resist and the immersed into an etchant bath. The etch rate for this mixture was approximately 300 Å/s with a lateral undercut of approximately 600 Å/sec. After etching, the resist was removed with the ashing procedure described previously. At this juncture, the ferroelectric and dielectric properties of the PZT thin film were measured for several 800 μm diameter test capacitors.

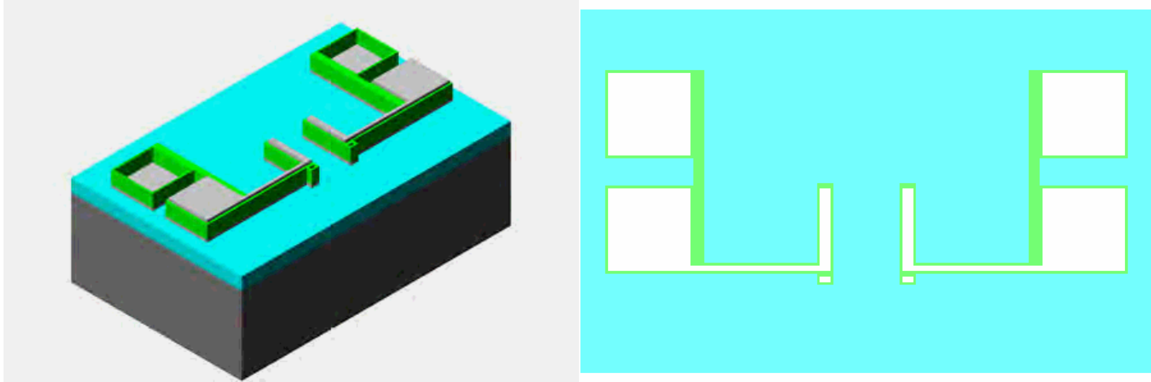

Figure 3.28: Fabrication Flow – PZT wet etch and bottom electrode bond pad definition. The PZT was wet etched, exposing the bottom electrode on the bond pads as well as on the stubs adjacent to the actuators so that the air bridge that will ultimately electrically tie both actuators together has access to the bottom electrode.

The final step required to define the PZT actuators was removal of the structural layer from the perimeter of each actuator and the RF contact pad (see Figure 3.29). The structural layer was selectively removed with a reactive ion etch using one of the two processes described in Table 3.10. Etched regions were monitored with a Nanospec 3000PHX reflectometer to ensure the entire structural layer was removed, thereby exposing the silicon substrate. Afterwards, the resist was removed with the ashing procedure described previously.

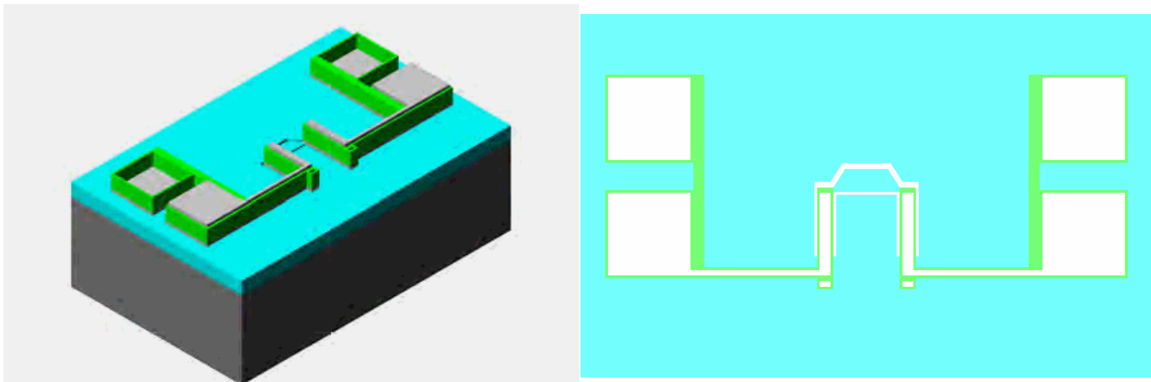

Figure 3.29: Fabrication Flow – Structural elastic layer patterning. The structural elastic layer is selectively etched to open access to the silicon substrate. The pattern defines the actuators and RF contact pad by defining the perimeter. The exposed silicon will ultimately enable the final process step, a XeF_2 etch, to undercut the silicon beneath the actuators and thus release it from the substrate.

Table 3.10: Reactive ion etch parameters for removal of PECVD SiO_2 and Si_3N_4. For ICP etching RF1 refers to the platen power while RF2 refers to the ICP coil power.

Machine	**CHF_3 (sccm)**	**CF_4 (sccm)**	**He (sccm)**	**Pressure (mTorr)**	**RF1 (W)**	**RF2 (W)**	**SiO_2 Etch Rate (Å/min)**	**Si_3N_4 Etch Rate (Å/min)**
LAM 490	30	90	170	2800	N/A	800	750	~1000
Unaxis Versalock ICP etch	5	15	N/A	5	50	500	~1600	~2200

3.2.7 Creating the RF Components

The process to form the RF transmission lines began with patterning a resist layer (see Figure 3.30). After the descum process, the wafers were placed into a CHA evaporator for deposition of 200 Å titanium / 7300 Å gold. The deposition parameters are listed in Table 3.11. After deposition, CPW transmission lines were patterned with liftoff by placing the wafers into a heated bath at 85ºC of Baker PRS-3000 positive resist stripper. The wafers were soaked until all regions with unwanted metallization were detached from the wafer surface. Afterwards, the wafers were rinsed with de-ionized water. To ensure the metal features have clean edges (i.e. to remove wings), the wafers undergo 10 seconds of ultrasonic cleaning in de-ionized water.

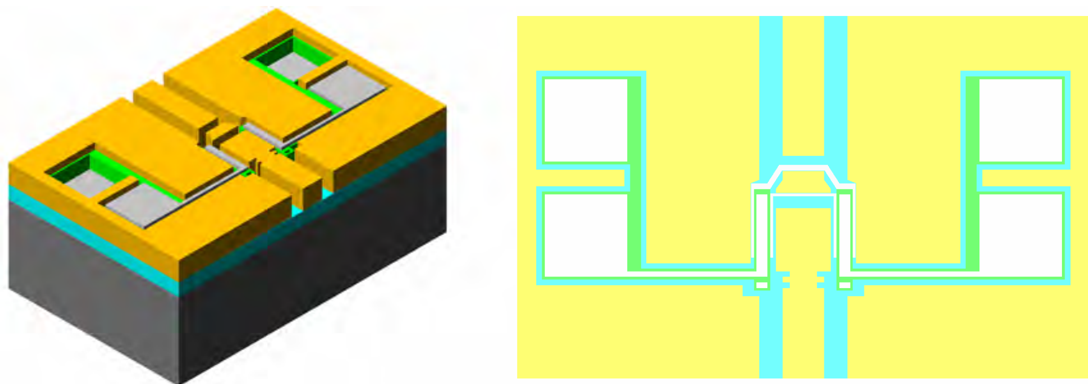

Figure 3.30: Fabrication Flow – CPW Transmission line deposition and patterning. The RF conductor and ground planes are patterned on top of the structural dielectric around the actuators and bond pads.

Table 3.11: Process parameters for the evaporation of metals.

Material	**Filament Current (mA)**	**Deposition Rate (Å/sec)**
Ti	10	2
Pt	10	3
Au	10	4
Au/Sn (80/20)	10	4

To improve the contact resistance of the final switch, contact dimples were deposited onto the RF contact pad (see Figure 3.31). The dimples were designed to be 10 μm in diameter and were comprised of evaporated Au/Pt (4000 / 1000 Å) and were patterned via the previously described liftoff technique. The platinum coating was used to improve the lifetime of the switch by eliminating the potential for Au-Au microwelding of the contacts.[11,12,13,14,16]

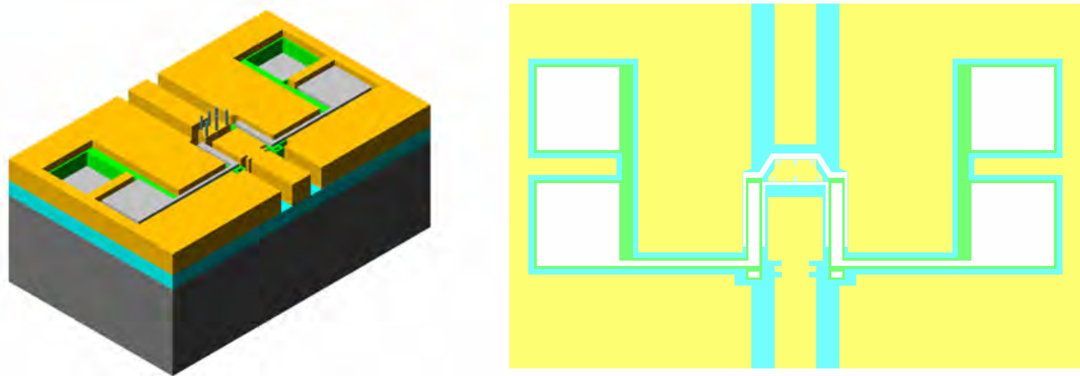

Figure 3.31: Fabrication Flow – Contact dimple deposition and patterning. The contact dimples are deposited and patterned onto the RF conductor pad.

The next step was to deposit the sacrificial layer for the air bridges and RF cantilevers. The sacrificial layer was a photodefinable organic (Clariant AZ 5200 resist) that was first patterned using normal photolithography. After developing the resist, it was cured at 200°C for 120 seconds in flowing N_2 (see Figure 3.32). The next step was to pattern counter-dimples aligned above the existing dimples on the RF contact pad into

the top of the resist layer. This process was accomplished by patterning the cured resist with another layer of photoresist and using an oxygen plasma to partially etch the cured resist (~3000Å) Afterwards, the uncured resist was removed with acetone. These counter dimples served to improve the contact resistance of the switch by ensuring intimate contact between the dimples and the RF cantilevers. Without the counter dimples, the non-planar characteristic of the sacrificial resist created a pocket for the contact dimple to fit within during switch contact, increasing the contact resistance of the switch (see Figure 3.33a).

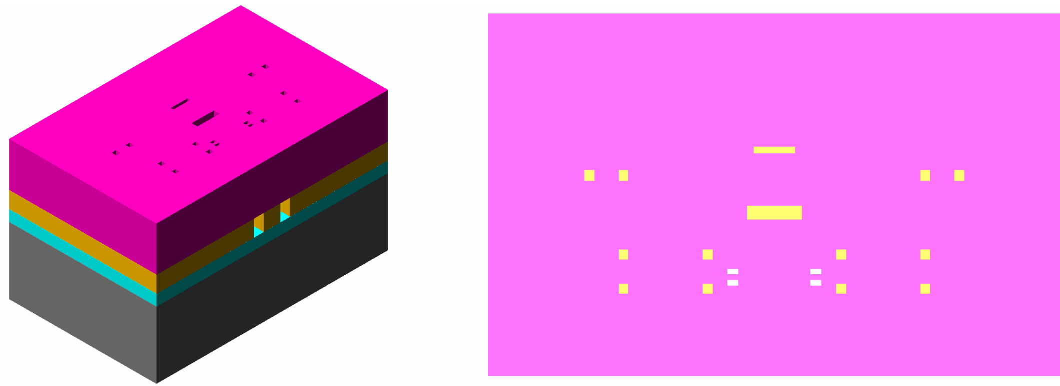

Figure 3.32: Fabrication Flow – Sacrificial layer deposition and patterning. The sacrificial layer is deposited and defined to cover all but the locations for the vertical posts that will anchor the ground straps, the top and bottom electrode bias line air bridges, and the RF cantilevers.

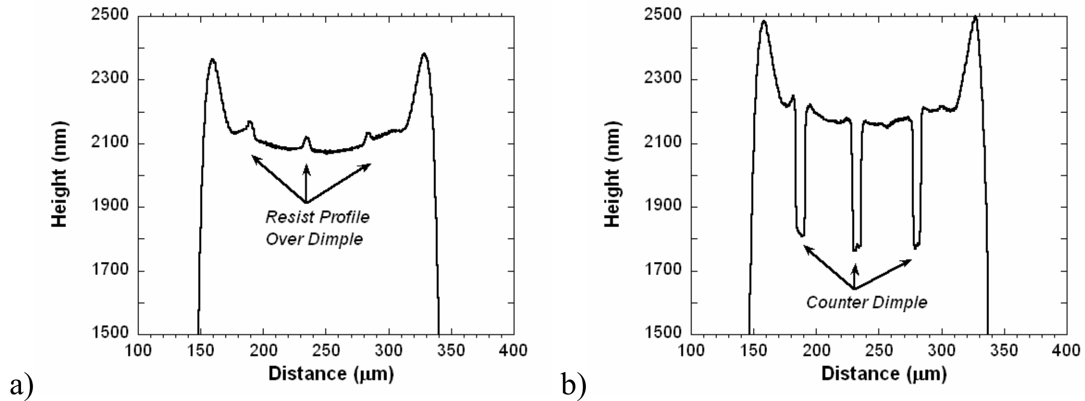

Figure 3.33: Stylus profilometer measurement of the sacrificial layer for the (a) as cured resist and (b) oxygen plasma etch defined counter dimples.

To improve the shape and contour of the counter dimples, a photo-definable process was developed. In this process, a two-step photolithography process was used to expose the counter dimple region with a small dose of UV light and expose the unwanted regions of resist with the normal dose. The process consisted of first exposing the unwanted regions with the proper dose of UV energy (3.2 s). Next, a dark field photomask was used to protect the wafer except for the location of the counter dimples. A second exposure of 0.4s was chosen because of the depth, shape, and consistency of the counter dimple profile after curing of the resist (see Figure 3.34). As illustrated in Figure 3.35, this process creates a more hemi-spherical counter dimple than the oxygen plasma etch process illustrated in Figure 3.33.

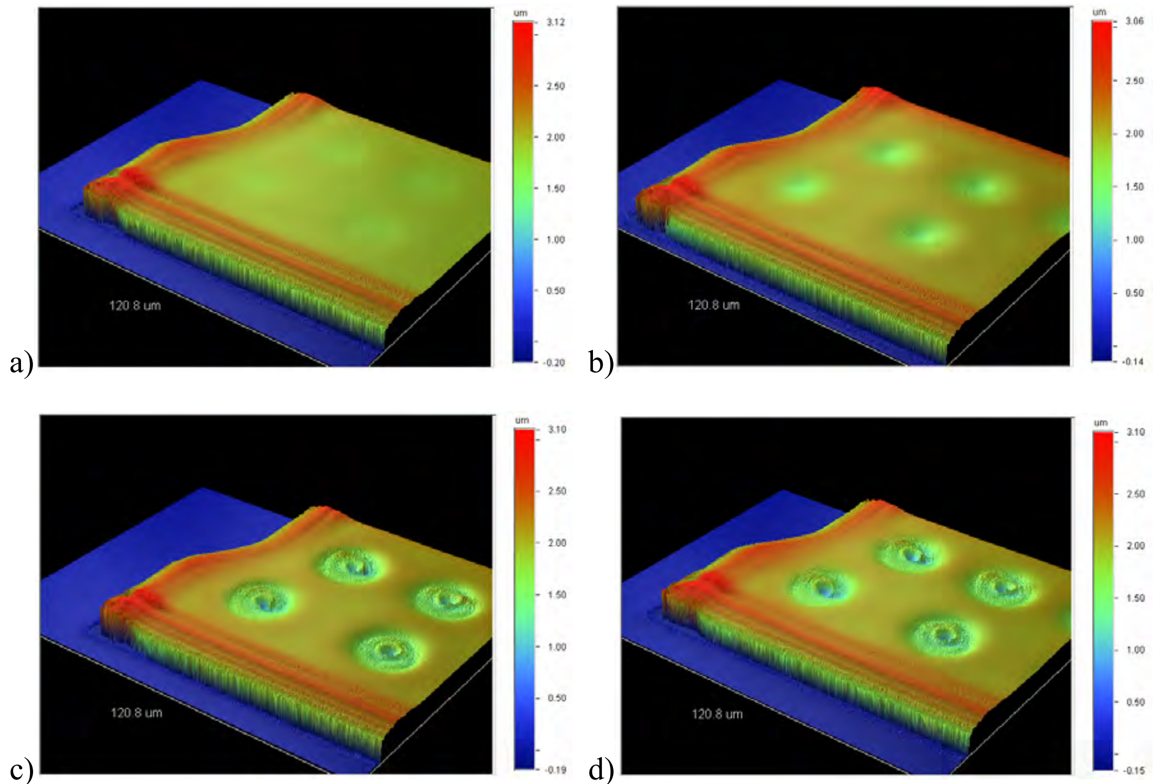

Figure 3.34: Results from 2-step photolithographic process to define counter dimples in the sacrificial layer. The sequence of images represent a) 0.2 s, b) 0.4 s, c) 0.6, and d) 0.8 s exposure dose for the second aligned exposure. An exposure of 0.4 s was chosen because it created consistent hemi-spherical counter dimples.

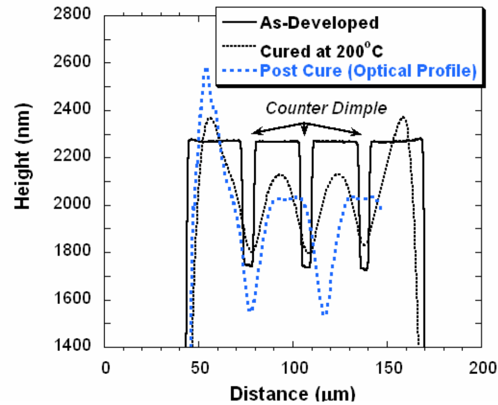

Figure 3.35: Stylus profilometer measurements of the sacrificial layer with photo defined counter dimples (0.4 s) in the sacrificial layer (Note, that the optical measurements were made with a thin layer of sputtered Pt deposited onto the cured resist).

The air bridges were comprised of evaporated gold with a thickness of 2 microns. The gold layer was blanket deposited by evaporation onto the wafer surface (see Figure 3.36). To pattern the air bridges, photoresist was patterned onto the gold surface and the exposed gold was removed using the argon ion-milling procedure previously discussed for removal of Pt and PZT thin films (see Figure 3.37). At the end of the ion-milling process, the angle of incidence was changed from 85° to 50° to aid in removal of the resist and reduce excessive re-deposited gold particles on the wafer surface.

Figure 3.36: Fabrication Flow – Conformal (unpatterned) gold bridge deposition.

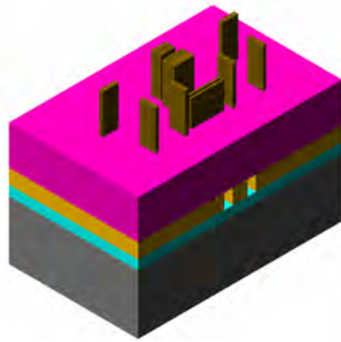

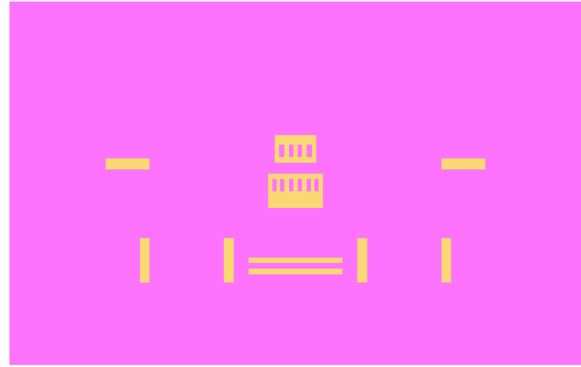

Figure 3.37: Fabrication Flow – Bridge metal patterning. The bridge metal is patterned with argon ion milling, thereby defining the ground straps, the top and bottom electrode bias line air bridges, and the RF cantilevers.

3.2.8 Releasing the Switch Components

To release the gold air bridges, the sacrificial layer was isotropically removed using an oxygen plasma with the process parameters listed in Table 3.8 (see Figure 3.38). Prior to placing the wafer into the process chamber, the chamber was warmed up by running the process parameters for 5 minutes. With the chamber warmed to approximately 75-100ºC, the wafer was then placed into the process chamber and run for 50-60 minutes.

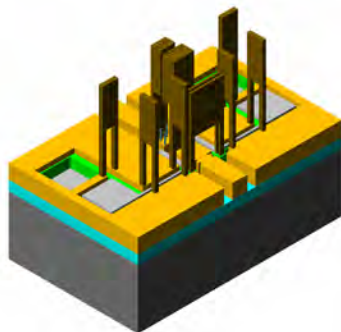

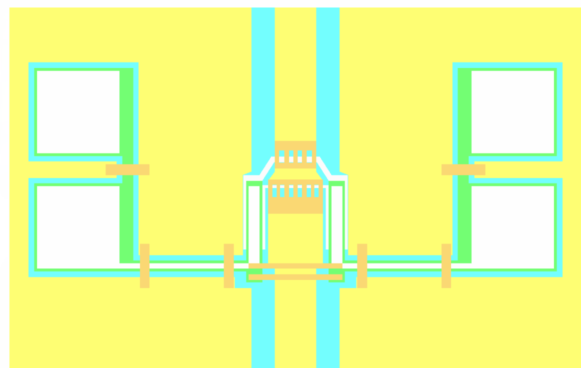

Figure 3.38: Fabrication Flow– Sacrificial layer removal. The sacrificial layer is isotropically removed, thus releasing the ground straps, the top and bottom electrode bias line air bridges, and the RF cantilevers.

After optical inspection of the wafers to ensure that all of the sacrificial layer was removed, the wafer was prepared for the final process step. The final step in the fabrication of a PZT MEMS switch was to isotropically etch the silicon substrate from underneath the PZT actuators (see Figure 3.39). Prior to the release etch, the wafer was exposed to a 20 second RIE plasma (see Table 3.10) to remove a surface oxide that developed on the exposed silicon surfaces. In the release etch, the silicon was removed using a non-plasma, dry process with a combination of XeF_2 (2 Torr) and N_2 (20 Torr) gases with an etch cycle of 20 seconds using a Xactix Xetch etch tool. Each etch was completed with approximately 55 – 60 etch cycles. Following the release, the wafer was ready to undergo DC and RF testing for performance verification.

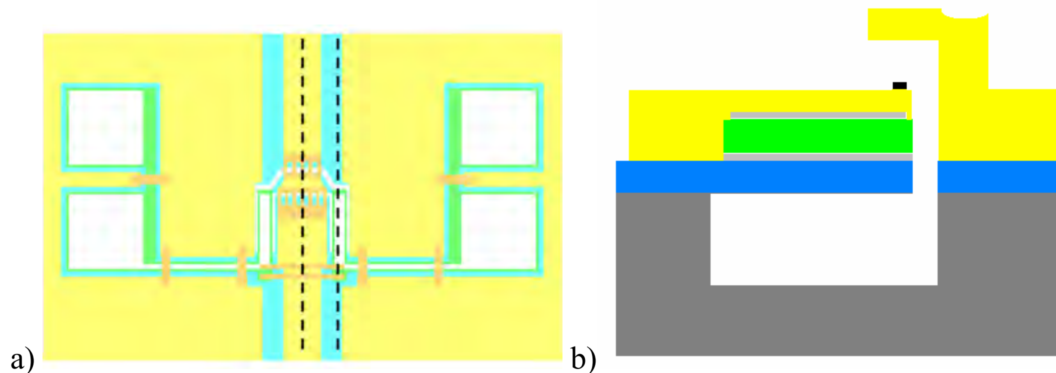

Figure 3.39: Fabrication Flow – XeF_2 silicon etch release of the actuators and RF contact pad. a) The silicon is isotropically etched under the actuator structures, releasing it from the silicon substrate. b) A profile illustrating the region located between the dashed lines on the image to the left.

3.3 References

[1] G. Rebeiz, G. Tan, and J. Hayden, “RF MEMS phase shifters: device and applications,” IEEE Microw. Mag., pp. 72 – 81, June 2002.

[2] G. Rebeiz, *RF MEMS Theory, Design, and Technology*, John Wiley & Sons, Hoboken, NJ, 2003.

[3] D. Judy, R.G. Polcawich, and J. Pulskamp, US Army Research Laboratoray, *unpublished results*.

[4] G.G. Stoney, The tension of metallic films deposited by electrolysis. *Proc. R. Soc. London A*, 1909, **82**, 172–175.

[5]William Sharpe, Johns Hopkins University, Baltimore, MD, private communication, 2004.

[6] O. Tabata, K. Kawahata, S. Sugiyama, and I. Igarashi "Mechanical proeprty measurements of thin films using load-defelction of composite rectangular membranes," Sens. Actuators, vol. 20, pp. 135 – 141, 1989.

[7]J. Gere & S. Timoshenko, Mechanics of Materials, Boston, MA, PWS Publishing, 1997, pp. 400-403.

[8]J. S. Pulskamp, A. Wickenden, R. Polcawich, B. Piekarski, M. Dubey, & G. Smith, "Mitigation of residual stress deformation in multilayer microelectromechanical systems cantilever devices," J. Vac. Sci. Techol. B, 21, pp. 2482-2486, 2003.

[9] J.S. Pulskamp, R.G. Polcawich, and D. Judy, "Piezoelectric inline RF MEMS switches and method of manufacture," US Patent filed Feb 6, 2006.

[10] J.S. Pulskamp, R.G. Polcawich, and D. Judy, "RF MEMS series switch using piezoelectric actuation and method of fabrication," US Patent filed Sep 2006.

[11]S. Majumber, N.E. McGruer, and G.G. Adams, "Study of contacts in an electrostatically actuated microswitch," Sens. Act. A, vol. .93, no. 1, pp. 19-26, 2001.

[12]J. Schimkat, "Contact measurements providing basic design data for microrelay actuators," Sens. Act. A., vol. 73, pp. 138-143, 1999.

[13]R.A. Coutu, P.E. Kladitis, R.E. Strawser, R.L. Crane, "Micro-switches and sputtered Au, AuPd, Au-on-AuPt, and AuPtCu alloy electric contacts," IEEE Trans. Comp. Pack. Techn., vol. 29, no. 2, June 2006.

[14]N.E. McGruer, G.G. Adams, L. Chen, Z.J. Guo, and Y. Du, "Mechanical, Thermal, and Material Influences on Ohmic-Contact-Type MEMS Switch Operation," Proc. MEMS 2006, pp. 230-3, 2006.

[15]R. Holm, *Electric Contacts: Theory and Applications.* Berlin, Germany: Springer, 1969.

[16]R.A. Coutu, P.E. Kladitis, K.D. Leedy, and R.L. Crane, "Selecting metal alloy electric contact materials for MEMS switches," J. Micromech. Microeng., vol. 14, pp. 1157-1164, 2004.

[17]M. S. Haque, H. A. Naseem, W. D. Brown, "Residual stress behavior of thin plasma-enhanced chemical vapor deposited silicon dioxide films as a function of storage time," J. Appl. Phys., 81, pp. 3129-3133, 1997.

[18]E. Zakar, R. Polcawich, M. Dubey, J. Pulskamp, B. Piekarski, J. Conrad, and R. Piekarz, "Stress analysis of SiO_2/Ta/Pt/PZT/Pt stack for MEMS application," Proc. 12th IEEE Intern. Symp. Appl. Ferro., pp. 757-59, 2000.

[19]E. Zakar, M. Dubey, R. Polcawich, B. Piekarski, R. Piekarz, J. Conrad, and R. Widuta, "Study of PZT film stress in in multilayer structures for MEMS devices," MRS Fall Symposium Proceedings, 605, pp. 287-292 (2000).

[20] T. Maeder, L. Sagalowicz, and P. Muralt, "Stabilized platinum electrodes for PZT thin film deposition using Ti, Zr, and Ta adhesion layers," Jap. J. Appl. Phys., Vol. 37, pp. 2007-2012, 1998.

[21]P. Muralt, T. Maeder, L. Sagalowicz, S. Hiboux, S. Scalese, D. Naumovic, R.G. Agostino, N. Xanthopoulos, H.J. Mathieu, L. Pattey, E.L. Bullock, "Texture

control of $PbTiO_3$ and PZT thin films with TiO_2 seeding," J. Appl. Phys., vol. 83, no. 7, pp. 3835-3841, 1998.
[22]P. Muralt, J. Baborowski, and N. Ledermann, "Piezoelectric micro-electro-mechanical systems with $PbZr_xTi_{1-x}O_3$ thin films: integration and application issues," in Piezoelectric Materials in Devices ed. by N. Setter, EPFL, Lausanne, Switzerland, 2002, pp. 231 – 260
[23]K. Budd, S. Dey, and D. Payne, " Sol-gel processing of $PbTiO_3$, $PbZrO_3$, PZT, and PLZT thin films," Brit. Ceram. Proc, 36, 107-121, 1985.
[24] R. Mohondro, J. Eisele, D. Whiteside, T. Romig and M. Bishop, "Photostabilization: the process of improvement", Future Fab Internat., vol. 3, pp. 235-247, 1997.
[25] D. Marshall, B. Freer, M. Ameen, D. Whiteside, G. Dahrooge, and Don Getchell, "Stabilization and stripping of high current implanted photoresists," Proc. IEEE Internat. Conf. Ion Implant. Techn., pp. 582 – 585, 1999.
[26] R. Allen, M. Foster and Y.T. Yen, "Deep U.V. hardening of positive photoresist patterns," J. Electrochemical Soc., vol. 129, pp. 1379 - 1381, 1982.
[27] G. Jordhamo and W. Moreau, "Deep UV hardening of deep UV resist", Proc. SPIE Internat. Soc. Opt. Eng., vol. 2724, pp. 588 - 600, 1996.

Chapter 4

Device Results & Discussion

This chapter describes the experimental test results for thin film PZT actuators and switches. Topics discussed include PZT material properties, actuator characteristics, switch performance parameters, and switch contact performance. Individual cantilever arrays were tested to verify residual-stress-induced static deformations, piezoelectric deformations as a function of voltage, and the influence of poling and aging. Following actuator characterization, RF switches are analyzed for a host of parameters including insertion loss and isolation as function of frequency, switching time, and several aspects of device reliability. Investigations into switch reliability include hold down tests, thermal sensitivity, and cycle reliability.

4.1 Material Property Testing

4.1.1 Ferroelectric and Dielectric Properties

During device fabrication, the first point at which the PZT material characteristics could be measured was after both the top platinum and PZT were defined via ion-milling and the bottom contact was exposed with a wet etch (refer to Section 3.2.6). To assess processing-induced damage and to help quantify the expected device performance, the PZT electrical properties were recorded for sample capacitors with a diameter of 800 μm and for switch actuators of varying geometries. Additional measurements were recorded as available during the fabrication process and when the devices completed fabrication. It was found that very little change in the dielectric properties occurs as a function of these fabrication steps with the dielectric constant ranging between 1050 and 1155 and with a dielectric loss of 0.03 – 0.05. In contrast, the ferroelectric properties are adversely affected by the fabrication process (see Figure 4.1 and Figure 4.2). The initial hysteresis loop after the PZT wet etch has very reasonable properties with a remanent polarization of 20 – 22 $\mu C/cm^2$. Following the reactive ion etch of the elastic layer, the hysteresis loop has a small shift of the polarization electric field (P–E) loop along the voltage axis without any significant changes to the saturated polarization or dielectric properties. This

voltage shift is consistent with a preferential polarization pointed upward out of the surface of the wafer. Further processing with Baker PRS-3000 for metal liftoff reveals an even larger shift of the PE loop (DC bias) along with a pinching of the bottom tail of the loop. Additionally, the dielectric constant decreases to 816. In the next process step, the wafers undergo a several hour soak in acetone resulting in a tilting of the PE loop with a decrease of the remanent polarization to 15 μC/cm^2 and reduction in the dielectric constant to 786. In the next process, the wafer is exposed to a 60 min oxygen plasma resulting in a pinching of the hysteresis loop along with an increase in the dielectric constant 862. The final step is a XeF_2 etch in which there is no significant change in the PE loop or dielectric properties. Throughout the process there is no significant change in saturated polarization. Additional testing revealed the ferroelectric hysteresis loop can become completely pinched near the origin (see Figure 4.7), while the low field dielectric properties remain essentially unchanged. This will significantly degrade the remanent piezoelectric coefficient.

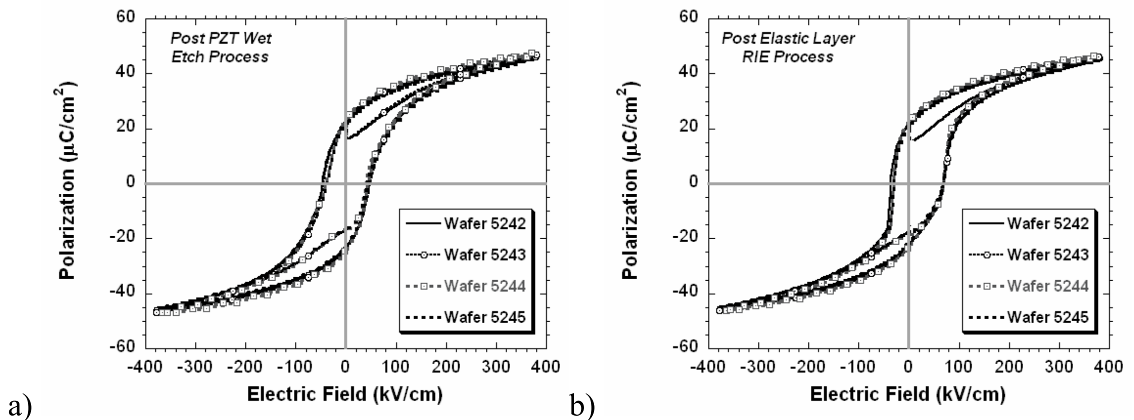

Figure 4.1: Ferroelectric properties observed as a function of process step: a) after the PZT wet etch and b) after the reactive ion etch of the elastic layer. Testing was performed on a PZT (52/48) thin film with a thickness of approximately 0.5 μm using a PZT SW5.1 switch actuator with an actuated length of 65 μm.

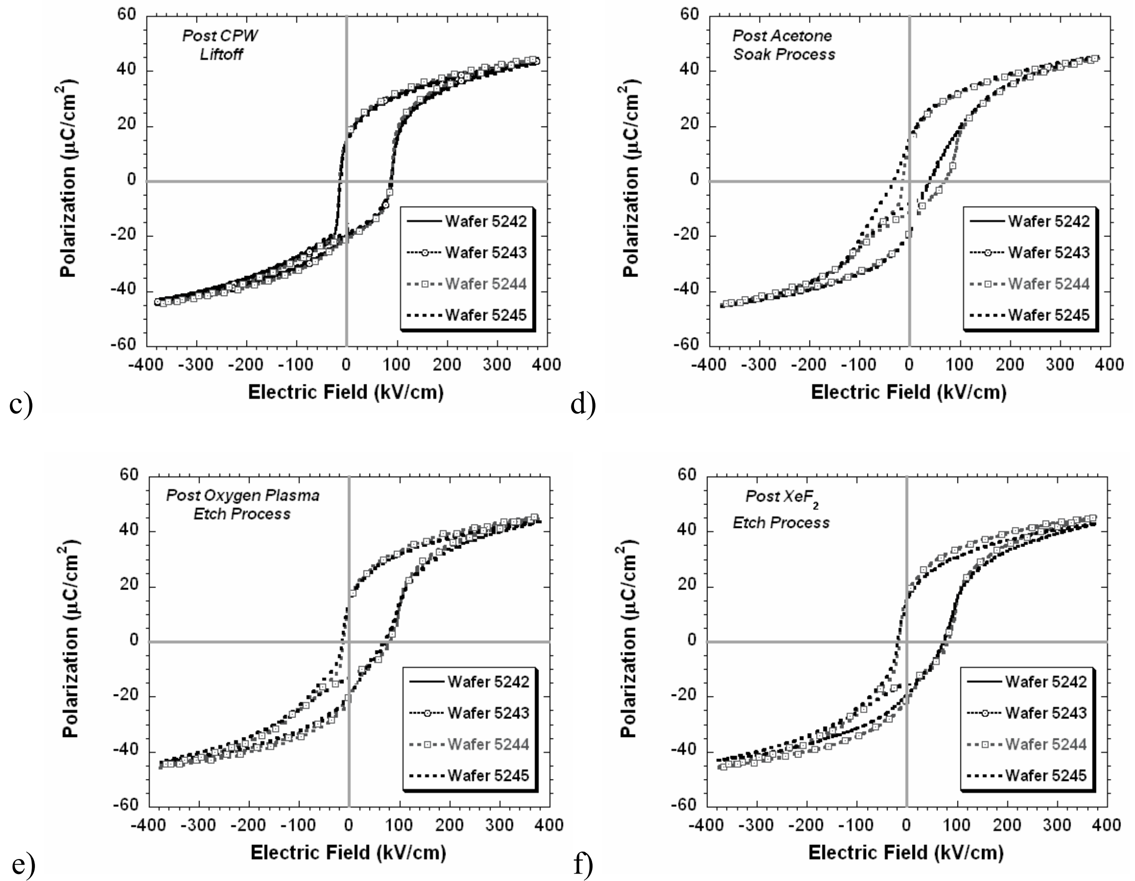

Figure 4.2: Ferroelectric properties observed as a function of process step: c) after the CPW and dimple liftoff in PRS-3000, d) after the bridge metal liftoff in acetone, e) after a 60min oxygen plasma, and f) after the XeF_2 etch of the silicon. Testing was performed on a PZT (52/48) thin film with a thickness of approximately 0.5 μm using a PZT SW5.1 switch actuator with an actuated length of 65 μm.

The observed changes in the ferroelectric and dielectric properties may be the result of point defects created at the surface of the exposed surface of the PZT thin film. The DC bias shift is likely to be caused by an internal electric field associated with defects.[1] Possible defects include charged defects and defect-dipole complexes including complexes with oxygen and lead vacancies and impurity compounds such as iron.[1,2,3,4,5] As processing generated defects accumulate, the result is a P–E loop with a pinched tail along with DC bias shift along the electric field axis (see Figure 4.3 and Figure 4.4).[6] An additional possibility is the creation of space charges which can fix the domain structure in a thin film.[7] During the fabrication process, oxygen and lead vacancies may be

generated by several mechanisms including leaching of lead from the wet solvent baths and removal of oxygen and lead by fluorinated plasmas.[8] If space charges are evident, thermal poling or UV assisted poling (see Figure 4.5) can be used to restore the hysteresis loop.[1,7] As seen in Figure 4.6, the virgin pinched hysteresis loop (from PZT SW4.0) can be reconditioned to a normal P-E loop with a DC bias shift, presumably due to defect dipole realignment.

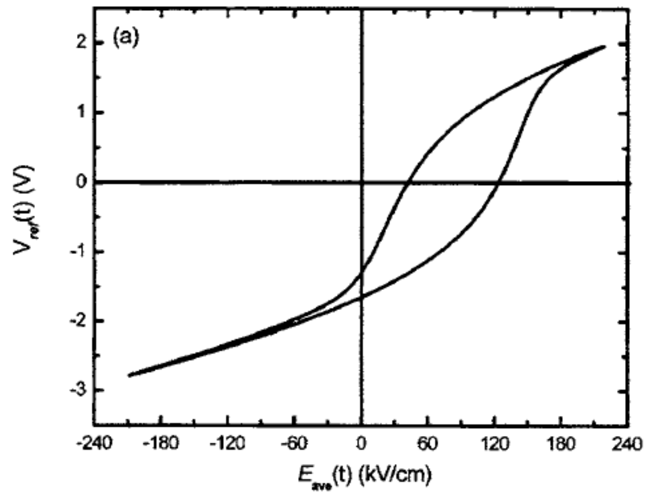

Figure 4.3: Modeled results demonstrating the influence a non-switching layer can have on the dielectric displacement – electric field hysteresis loop (from Reference 6).

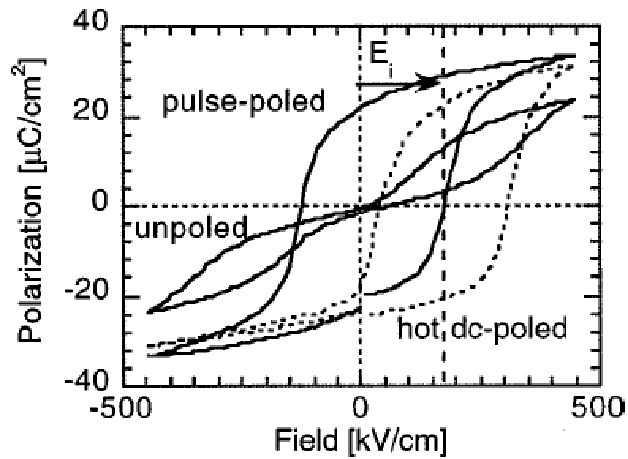

Figure 4.4: P–E hysteresis loop for an unpoled, pulse-poled (450 kV/cm, 2.9 x 10^6 cycles), and hot poled (160ºC) PZT (15/85) thin films (from Reference 1).

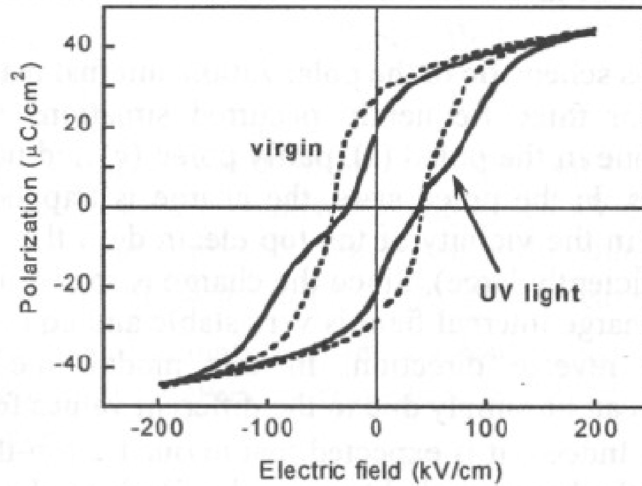

Figure 4.5: Ultraviolet (UV) induced pinching of the ferroelectric hysteresis loop in a PZT (45/55) thin film (from Reference 7).

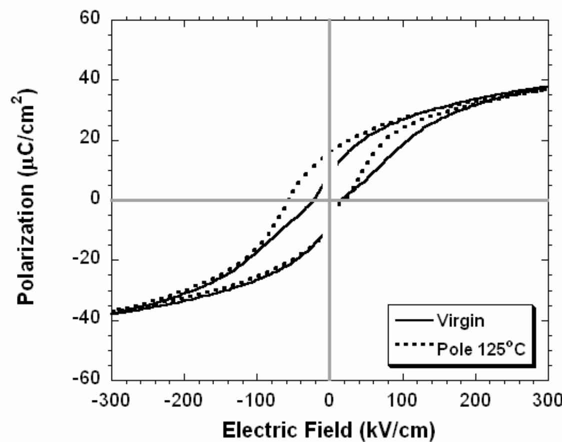

Figure 4.6: Ferroelectric properties of a PZT (52/48) thin film capacitor from PZT SW4.0 wafer processing with as-fabricated (virgin) and post thermal poling of 125ºC for 10min at 15 volts.

In principle, hysteresis loops altered by domain pinning can be recovered with thermal annealing.[9,10,11] However, the residual stress of the top platinum layer was shown in Section 2.2.5 to increase significantly for annealing temperatures greater than 350ºC. The effect of post fabrication annealing temperature on the residual stress gradient within the PZT actuators is shown in Figure 4.8. For this example, the as-fabricated devices were annealed after the actuators were completely fabricated. As illustrated, the

static deformation of the actuators changes with annealing temperature. For the standard 350ºC anneal, the actuator static tip deflection is reduced to less than -2 μm on average for the different designs and the switches can operate normally. However for an annealing temperature of 500ºC, the tip deflections become positive and render the switches inoperable. Thus, in order to retain the desired cantilever curvature, the annealing temperature for the top platinum layer was fixed to 350ºC.

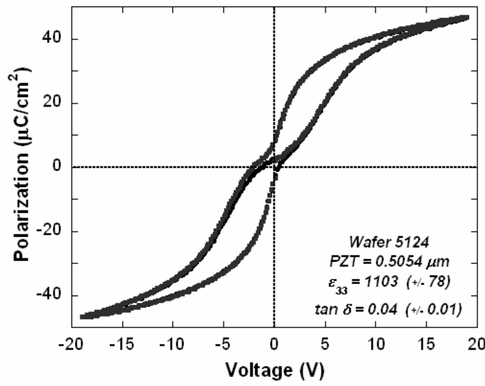

Figure 4.7: Pinched ferroelectric hysteresis loop for several device wafers.

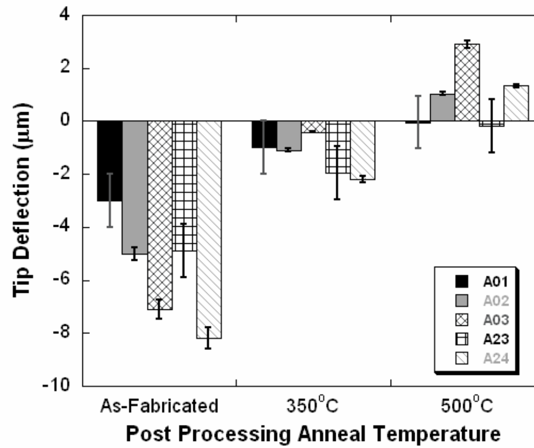

Figure 4.8: Static deformation of switch actuators as a function of post process annealing temperature.

Although the ferroelectric properties were not ideal following the fabrication process, the switches still performed as desired as will be discussed in the following sections. Improving the ferroelectric properties such that they are stable with the fabrication process is strongly desired, since a low remanent polarization in films with pinched loops degrades the piezoelectric response of the PZT. One possibility is to use a barrier coating to protect the PZT from chemical attack. A thin titanium oxide thin film may provide the necessary protection to the actuators.[12] However, the added residual stress from a thin layer atop the actuators may have a significant affect on the stress-induced tip deflection of the actuators. This potential solution and others will be left for future work.

4.1.2 Effective Piezoelectric Coefficient

To measure the effective $e_{31,f}$ piezoelectric coefficients of the PZT, static deformation measurements on the cantilever arrays were recorded as a function of applied dc voltage. The actuator stack for these measurements is the same as the switch: consisting of an elastic layer, platinum metallization, and the PZT thin film (see Figure 4.9). For each voltage, the cantilever tip displacement is recorded and subsequently plotted as a function of voltage for cantilevers 125 μm in length (see Figure 4.10). The asymmetry in the displacements results is likely to be the result of the preferred polarization within the PZT thin film. For these devices, the preferred polarization direction is upward out of the surface plane. The tip deflection versus voltage data were analyzed using the finite element models generated by Jeffrey Pulskamp to extract the effective transverse piezoelectric coefficient ($e_{31,f}$) as a function of voltage (see Figure 4.11). The model computes $e_{31,f}$ from Equation 4.1, with (E_{PZT} / (1-ν_{PZT})) representing the biaxial modulus of PZT (100 GPa), EI_{comp} is the composite stiffness of the beam, Y_{tip} is the tip displacement, V is voltage, w is the actuator width, h is the piezoelectric actuation arm length (i.e. the distance from the PZT centroid to the neutral axis), and L is the beam length.

$$d_{31,f}\frac{E_{PZT}}{(1-\upsilon_{PZT})}=e_{31,f}=\frac{2EI_{comp}Y_{tip}}{VwhL^2} \qquad \text{Equation 4.1}$$

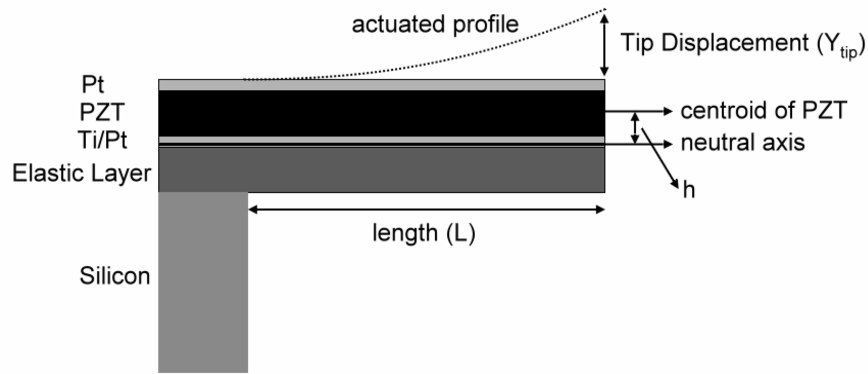

Figure 4.9: Depiction of a PZT cantilever (actuated and unactuated) illustrating the critical components required for computing the effective piezoelectric coefficient.

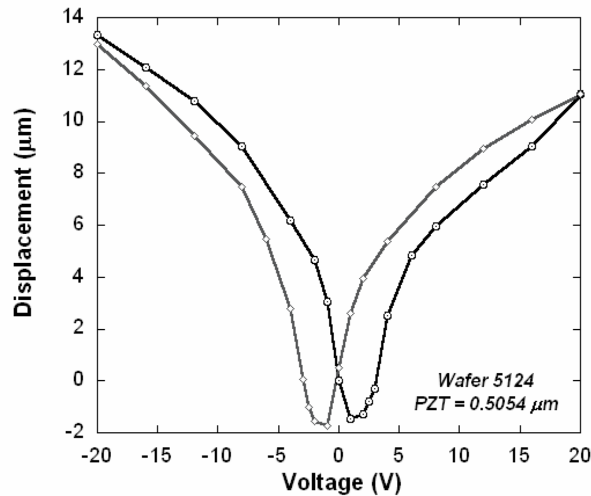

Figure 4.10: Piezoelectric cantilever beam (125 μm in length) displacement as a function of voltage.

The results from the computations are illustrated in Figure 4.11 for both bipolar and unipolar actuation cycles. Several important characteristics result from this analysis. First, the low voltage values for $e_{31,f}$ are unreasonable for well-poled PZT thin films. The best values obtained to date on PZT thin films have been reported at -16 C/m^2.[13] To

explain these anomalously large values, the ferroelectric and dielectric properties were examined (see Figure 4.12). The ferroelectric hysteresis loop is pinched, resulting in a small remanent polarization (~5 $\mu C/cm^2$). This behavior directly affects the apparent piezoelectric coefficient. As a result of the pinched hysteresis loop, the polarization undergoes a significant increase towards its saturation value as the voltage increases from zero. The large increase in polarization yields a substantial change in beam curvature which causes the anomalously large $e_{31,f}$ values from zero to 5 volts.

It would be interesting to determine the origin of the large apparent piezoelectric coefficients. Towards this end, it would be important to know whether the strain is intrinsic or extrinsic, piezoelectric or electrostrictive in origin. A possible method of ascertaining some of the answers would be to measure both the actuator tip deflections and the polarization as a function of applied electric field. The resulting strain-electric field and polarization-electric field relationships could be plotted to create a strain-polarization (S-P) relationship for the thin film PZT actuator. The S-P relationship can be used to determine the influence electrostriction has on the overall strain response of the actuator. This testing is not trivial as the polarization measurements must be made at near dc conditions.

Another important characteristic of the extracted $e_{31,f}$ plots is the saturation values observed near 10 volts. Table 4.1 summarizes the saturation values of the effective piezoelectric coefficients for several of the switch wafers. Except for wafers 5165 and 5230, the $e_{31,f}$ values have been in the – 7 to – 9 C/m^2 range. The drop in $e_{31,f}$ for these two wafers resulted in an increase in the actuation voltage but did not affect the switch RF performance. Given the XRD results reported in Section 3.2.3, the films should be expected to have an $e_{31,f}$ in the -5 to -7 C/m^2 range based on the results reported by Trolier-McKinstry and Muralt.[14] The larger values observed at saturation may result from several factors including increased the presence of non-180º domain wall mobility, electrostriction, and/or 180º domain wall mobility. Moreover, the $e_{31,f}$ values reported here are extracted from deflection measurements at electric fields well above the coercive field. This is another reason that they may differ from the values reported in previous work, which were obtained at low to zero electric field conditions based on the wafer flexure technique or bending cantilever measurements.[15,16] The higher electric fields

increase the extracted piezoelectric coefficient in two ways. One, the polarization changes with increasing voltage result in an increase in the piezoelectric coefficient. Second, the higher voltages increase in the contribution of electrostriction response to the overall strain response with electric field. Additionally, there is recent evidence that the 180º domain wall mobility contributes to piezoelectric non-linearity in a dynamic poling process.[17] Another potential contribution is an increase in the mobility of non-180º domain walls from a reduction in substrate clamping. Substrate clamping is well known to limit the piezoelectric properties in PZT thin films by limiting the number and/or mobility of non-180º domain walls.[18,19] However, atomic force microscopy measurements on PZT thin film capacitors demonstrated a nearly 2x increase in the d_{33} piezoelectric coefficient on capacitors that were machined into micron and nano sized mesas.[20] Similar results may be expected with thin film cantilevers in which the silicon substrate is removed beneath the cantilevers.

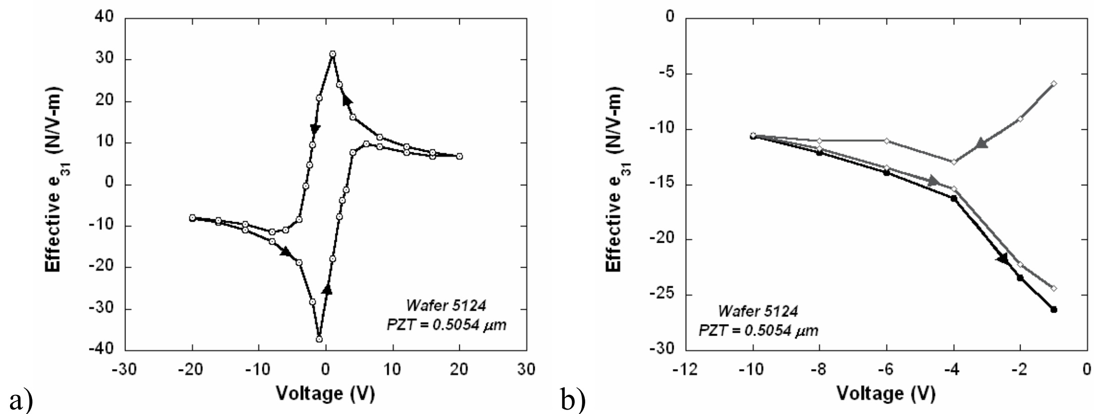

Figure 4.11: Effective transverse piezoelectric coefficient ($e_{31,\,f}$) extracted from FEA models using experimentally determined cantilever tip deflections as a function of voltage: a) bipolar and b) unipolar scans

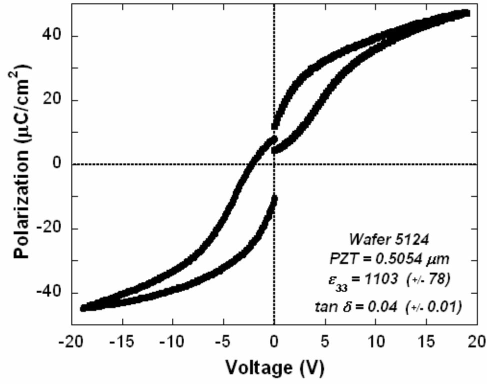

Figure 4.12: Ferroelectric and dielectric properties of the PZT cantilevers tested in Figure 4.11.

Table 4.1: Effective high DC bias field transverse piezoelectric coefficient ($e_{31,\,f}$) for each of the device wafers fabricated.

Wafer ID	PZT Thickness (Å)	$e_{31,\,f}$ (sat) (N/V-m)
1376	4881 Å	–7.2 (± 0.5)
5124	5054 Å	–8.4 (± 1.7)
5126	5084 Å	–9.6 (± 1.6)
5165	4732 Å	–3.5 (± 1.0)
5230	5030 Å	–4.1 (± 1.2)

4.2 PZT Thin Film Actuator Characterization

4.2.1 Effect of Residual Stress on Static Actuator Deformation

As described in Section 3.1.2, the residual stress gradient within the actuator stack is expected to produce initial curvature of the cantilevers. Verification of the predicted cantilever deflections was completed by measuring the as-fabricated tip displacement of the actuators with an optical profilometer (see Figure 4.13). Measurements were recorded for both single cantilevers of varying lengths and for the coupled cantilevers used in switches on unpoled as-fabricated devices. Table 4.2 compares the measured static deflection and predicted results for cantilevers of three different lengths on three different wafers. In general, the deflection *direction* is accurately predicted but the *magnitude* it is consistently underestimated by the model. The large error may be the

result of non-ideal boundary conditions at the anchor of the cantilevers. The cantilever arrays and switch actuators are modeled as ideal structures with a perfect anchor. However, the XeF_2 etch isotropically undercuts the anchor of the cantilever and the region adjacent to each of the cantilevers, creating a free-standing membrane consisting of the elastic layer mechanically coupling the cantilevers to one another. An example of the device undercut, 30 μm, is illustrated in Figure 4.14 for an array of PZT cantilevers. In general, the undercutting pushes the substrate anchor back approximately 30 microns. For design purposes, it is assumed that the elastic layer is stiff enough to prevent deformation from occurring in the undercut region. For the tip deflection measurements, very little deformation is observed in the undercut region.

To eliminate the possibility of run-to-run variations in material properties from affecting the stress deformation predictions, each wafer was tracked by inspecting the ferroelectric, dielectric, and residual stress properties throughout the fabrication process as discussed in Section 4.1. The dielectric constant deviates minimally, with a range of 1050 – 1150 observed. The ferroelectric properties have a similarly small deviation, with a pinched hysteresis loop exhibiting a remanent polarization ranging from 15 – 17 $\mu C/cm^2$. Similarly, the residual stress of each thin film was monitored to minimize any significant changes that would adversely affect device performance. As discussed in Section 3.1.3, the residual stress of each layer has a minimal run-to-run variation with the exception of the silicon nitride. The silicon nitride stress is very dependent on the chamber condition and has a larger variability than the PECVD silicon dioxide. In general, any run-to-run variations are accounted for in the model by inputting the as-measured stress values into the model for each wafer (see the variation in predicted deformations for each wafer in Table 4.2). However, the exact stress values for each PECVD layers cannot be known because the elastic layer is grown in a single three-layer deposition process. The average stress of this composite (78 MPa) is measured with a run-to-run variation less than 25 MPa. These composite stress values fail to highlight any significant change in the stress from run to run.

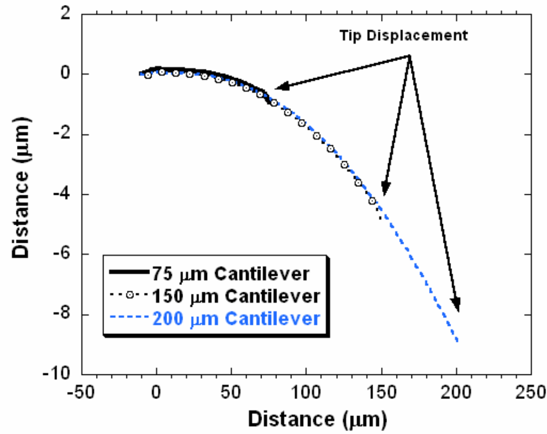

Figure 4.13: As-fabricated beam curvature for 3 of the cantilevers of the cantilever array measured using an optical profilometer.

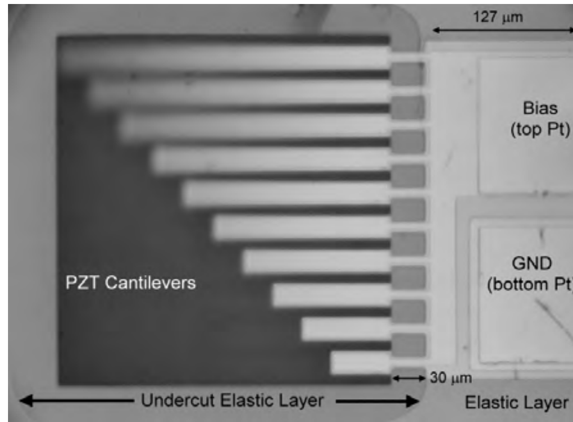

Figure 4.14: Optical image illustrating the effects of the XeF_2 undercut (~30 μm) on the anchor of the PZT cantilever array.

Table 4.2: Comparison of the as-predicted initial deflection and the as-fabricated static deflection measured via optical profilometry for several cantilever lengths (length is the actuated length).

Wafer ID	$SiO_2/Si_xN_y/SiO_2$ Thickness (Å)		52 μm Cantilever	77 μm Cantilever	102 μm Cantilever
5124	968/586/3473	Predicted (μm)	-0.69	-1.51	-2.65
		Measured (μm)	-1.024	-2.193	-3.200
5126	1684/453/2945	Predicted (μm)	-0.28	-0.61	-1.08
		Measured (μm)	-0.9	-2.5	-4.3
5165	1018/445/3515	Predicted (μm)	-0.46	-1.00	-1.76
		Measured (μm)	-0.85	-1.8	-2.5

Additional factors affecting the error in the predictions are differences in the PZT remanent strain and residual stress gradients within one or more of the thin film layers. There was no convenient method of including stress gradients within ANSYS and thus they were ignored in the current model. The PZT remanent strain was assumed to be zero in the initial predictions. That is, the residual stress state measured for the PZT films was on unpoled samples, and it was presumed that the domain population in the unpoled cantilevers was comparable. However, experimental results described in Section 4.2.2 illustrate that the devices are at least partially poled as-fabricated, possibly as the result of exposure to the various plasma processing steps. The finite remanent polarization results in a remanent strain contributing to the difference between the predicted and experimental cantilever tip deflection measurements. The influence of the remanent strain on the cantilever will be further discussed in Section 4.3.2.

4.2.2 Resonance Measurements on Cantilever Actuators

The fundamental resonance frequency of the cantilevers will also ultimately determine the limiting switching time of the device. As will be discussed in Section 4.3.4, the resonance frequency can be used to gage the lower limit of the switching time. The resonant frequency of a cantilever beam is computed by Equation 4.2, where f_i is the frequency (Hz) of the ith vibration mode, L is the beam length, E is the Young's modulus, m is the mass per unit length, and λ is a dimensionless parameter that is a function of the boundary conditions and is equal to 1.8751 for the fundamental mode of a cantilever.[21]

$$f_i = \frac{\lambda_i^2}{2\pi L^2}\sqrt{\frac{EI}{m}} \qquad \text{Equation 4.2}$$

For a composite beam comprised of SiO_2, Si_3N_4, Ti/Pt, PZT, and Pt, the EI terms can be computed using the transformed section method described in Chapter 3.1.3.[22] A plot of resonance frequency versus beam length is illustrated in Figure 4.15 with circles highlighting the target lengths of each beam of the cantilever array test structures. Two

such plots were generated with one highlighting the frequency response for beams equal to the design length and the other including the XeF_2 undercut discussed in reference to Figure 4.14. An artifact of the undercut is the mechanical coupling between the individual cantilevers. This coupling may limit the influence the undercut length will have on the resonance frequency because it mechanically constrains the cantilevers. As such, the calculated values in Figure 4.15 should represent the upper and lower bounds on the expected resonance frequencies. To compare the validity of the predictions, the resonance frequency for three of the cantilevers in the cantilever array were measured by laser Doppler vibrometry (LDV) in which the mechanical resonance is induced by the piezoelectric response with a 0.1 V_{ac} pseudorandom pulse applied to the PZT thin film. The measured values are compared with predictive models (see Table 4.3) with the modeled values consistently overestimating the resonance frequency; even including the 30 μm overetch. One possible explanation for the mismatch between the modeled and measured results could be the uncertainty in the thin film elastic properties, specifically if any of the values reported in Section 3.1.2 are larger than that in the devices tested. In addition, the LDV results illustrated that there is mechanical coupling between the individual cantilevers (see Figure 4.16). This coupling can also impact the resonance characteristics by influencing the boundary conditions of the cantilevers.

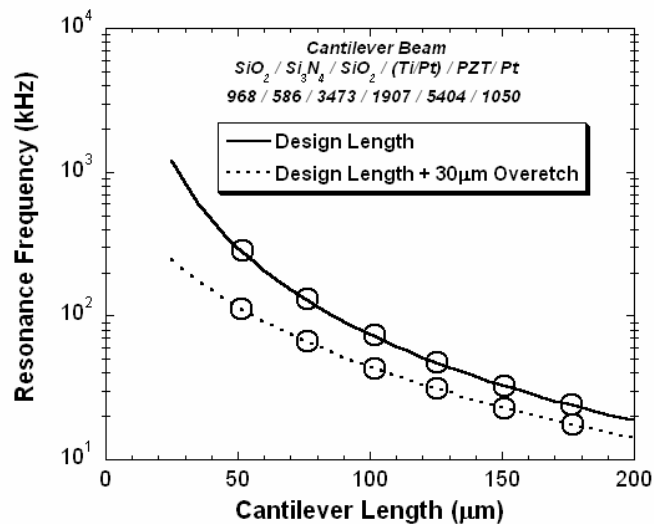

Figure 4.15: Predicted resonance frequency versus length of cantilevers comprised of $SiO_2/Si_3N_4/SiO_2$/Ti/Pt/PZT/Pt with thicknesses indicated on the graph. Circles highlight the design lengths for the cantilever array (i.e. 52 μm, 77 μm, 102 μm, 127 μm, 152 μm, 177 μm).

Additional information on the state of the remanent polarization in as-fabricated devices can be extracted from the resonance frequency evaluation. Figure 4.17 compares the response between an as-fabricated and a poled cantilever. It was found that the resonance frequency could be detected prior to poling the ferroelectric films. This suggests that there was a non-zero remanent polarization in the PZT thin film. The substantially smaller response of the as-fabricated sample is a possible indication of a smaller initial piezoelectric response in the virgin device.

Table 4.3: Comparison between the predicted and experimentally measured resonance frequencies for the 3 cantilevers of the test cantilever array for the devices from Wafer 5124 (thicknesses indicated in Figure 4.15).

	Frequency (kHz)		
	77 µm Cantilever	102 µm Cantilever	127 µm Cantilever
Predicted - Design Length	126	71.5	46.1
Predicted - Design Length + 30 µm Overetch	65	42.7	30.2
Experimental	63.45	41.78	29.08

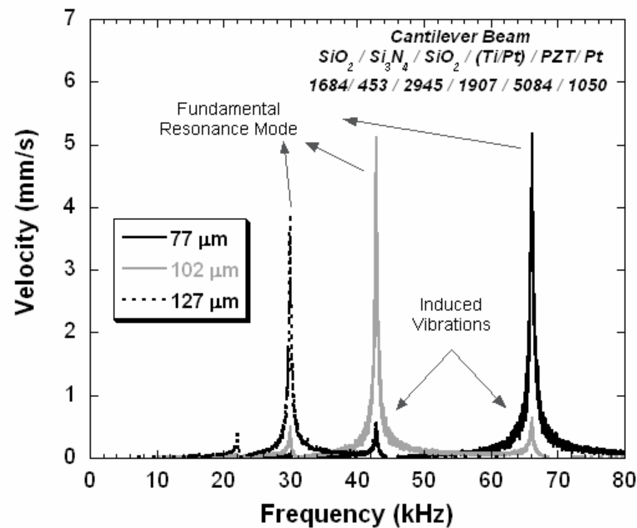

Figure 4.16: Velocity versus frequency plots for individual PZT cantilevers as measured with a laser Doppler vibrometer. The side peaks on either side of the fundamental resonance mode for each cantilever are induced by the mechanical coupling between the adjacent cantilevers by the undercut elastic layer.

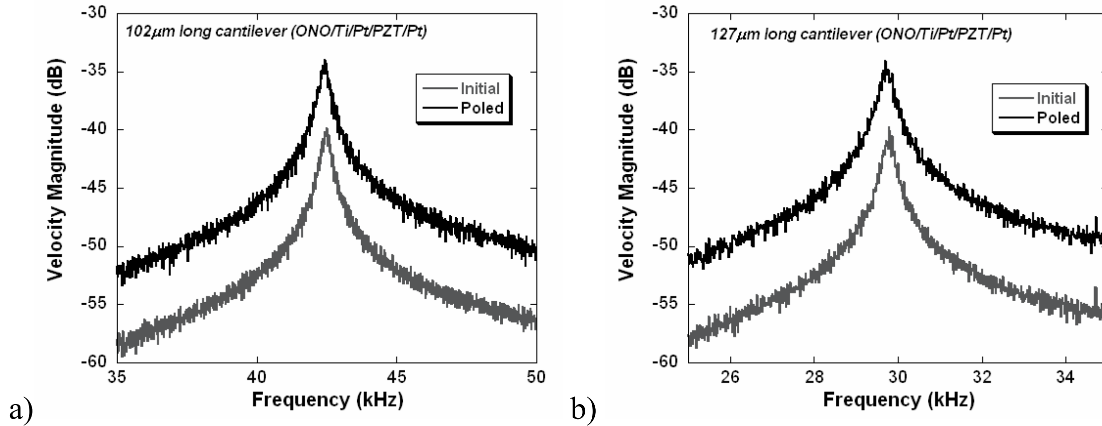

Figure 4.17: Resonance frequency results for (a) a 102 μm and (b) a 127 m long cantilever comprised of an oxide/nitride/oxide (ONO) elastic layer and a Pt/PZT/Pt actuator for the initial as-fabricated and poled (10 min at 10 V) cantilevers illustrating the existence of some degree of poling in the as-fabricated devices. Each resonance scan was collected with the application of 0.02 V_{p-p} with a 0.01 V_{offset}.

4.3 PZT Switch Actuator Characterization

4.3.1 Static Deflection

The switch actuator static deformation was also determined via optical profilometry. Initial scans were acquired for the switches on each wafer to ensure a negative static deflection in the PZT switch actuators. These data were also compared against that of the individual cantilevers. Any differences in the deformation were assumed to be a result of the different boundary conditions between the cantilever arrays and the switch actuators. A comparison of the differences is listed in Table 4.4.

Table 4.4: Comparison of the tip deflections between individual cantilevers and switch actuators.

				Initial Tip Deflection	
Wafer Number	Design	Device Label	Actuated Length (μm)	Switch Actuator (μm)	102 μm Cantilever (μm)
1376	SW4.0	2	90	-5.8	-4.9
5124	SW5.1	A02	90	-3.4	-1.5
5165	SW5.1	A02	90	-4.7	-3.4

4.3.2 Effects of Poling on Static Deformation

Following the initial optical profilometry scans on the switch actuators, the effect of poling on the static deformation was investigated. On poling, the actuators develop a small degree of residual deflection upward relative to the unpoled state, presumably due to changes in the PZT film domain state. Thus, it is essential to ensure sufficient initial negative deflection so that the switches do not permanently close. The changes in actuator position with poling are shown in Figure 4.18 for switch actuators having a lengths of 65, 90, and 140 μm. For a switch with an actuated length of 115 μm, poling with 15V at room temperature for 15 minutes resulted in a 1.2 micron change in the initial position of the actuators. In comparison, poling at 125ºC resulted in 3.9 micron change. In both cases, a negative actuator deflection profile remains after poling, therefore maintaining the possibility of a functioning RF switch. This remains true for all the switch actuators tested regardless of length.

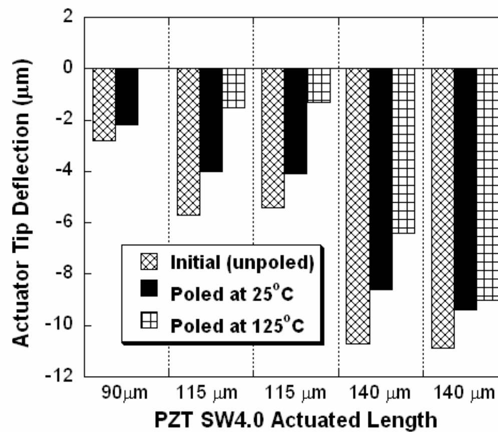

Figure 4.18: Actuator tip deflection as a function of poling conditions for PZT switches (PZT SW4.0) having actuators with of varying lengths.

Assuming pure bending with a linear strain field within the composite actuator, the change in static deformation state can be equated to a change in in-plane strain within the PZT layer. The tip deflection (y_{tip}) of a cantilever of length (L) can be equated to the

beam curvature (ρ_k) using Equation 4.3 assuming small angular deflections (i.e. sin θ = θ).[22]

$$\rho_k = \frac{L^2}{2y_{tip}}$$ Equation 4.3[22]

Furthermore, the strain (ε(z)) at a given location in the beam can be computed with Equation 4.4 from the beam curvature and the distance from the neutral axis of the beam to the position of interest within the beam (z).

$$\varepsilon(z) = \frac{z}{\rho_k}$$ Equation 4.4[22]

Using the tip deflections for a PZT switch actuator from both the initial and poled conditions, the change in strain (Δε) can be computed for any position in the beam cross section using Equation 4.5.

$$\Delta\varepsilon = \varepsilon(z_{poled}) - \varepsilon(z_{initial})$$ Equation 4.5

Assuming the change in beam deflection is related to a change in the in-plane strain of the PZT thin film, the change in strain has been computed for each of the PZT-Pt interfaces for each of the poling conditions (see Table 4.5). The change in strain of the PZT at the top interface is computed at either 0.02 or 0.038 percent, depending on the poling procedure. These values are reasonable given the maximum strain observed in a PZT ceramic is on the order of one percent for high DC electric fields.[23]

Table 4.5: Change in in-plane strain as a function of poling for switch actuators with an actuated length of 90 μm.

Condition	Tip Deflection (μm)	Δε Bottom Pt – PZT Interface	Δε Top Pt – PZT Interface
Initial	-5.43	—	—
Poling at 25ºC	-4.04	1.5×10^{-5}	2.0×10^{-4}
Poling at 125ºC	-1.40	2.9×10^{-5}	3.8×10^{-4}

4.3.3 Piezoelectrically Induced Deformation

The PZT actuators bend upward with the application of an electric field parallel to the poling direction by the moment created by the piezoelectric strain. The tip deflection of the beam (y_{tip}) can be estimated using Equation 4.6 for a cantilever beam subjected to a moment (M) applied at the end of the beam.[22]

$$y_{tip} = \frac{ML^2}{2EI} \quad \text{Equation 4.6}$$

The moment can be computed from Equation 4.7 using the force (F) generated by the piezoelectric and the distance from the centroid of the piezoelectric to the neutral axis of the beam (d_n).[22]

$$M = Fd_n \quad \text{Equation 4.7}$$

To first order, the force can be estimated using Equation 4.8 with the piezoelectric free strain (S), the effective transverse piezoelectric coefficient for thin films ($d_{31,f}$), applied voltage (V), and the area (A_{piezo}) and thickness (t_{piezo}) of the piezoelectric material.[22]

$$F = S \times E \times A_{piezo} = \frac{d_{31,f} \times V \times E \times A_{piezo}}{t_{piezo}} \quad \text{Equation 4.8}$$

Assuming a value for $d_{31,f}$ of -70 pm/V ($e_{31,f}$ of -7 N/Vm using a biaxial modulus of 100 GPa), a PZT thin film cantilever with an actuated length of 90 μm is expected to produce a tip deflection of 3.3 μm. The linear relationship between the tip deflection and actuation voltage is shown in Figure 4.19 for cantilevers with actuator lengths of 90, 115, and 140 μm. However, from the effective piezoelectric coefficient measurements in Section 4.1.2, the $e_{31,f}$ (and corresponding $d_{31,f}$) are not a linear function with voltage. Incorporating an extracted $e_{31,f}$ versus voltage relationship into Equation 4.8, the predicted tip deflections become a non-linear function with voltage as shown in Figure 4.20. Using these values, an actuator with a length of 90 μm is expected to achieve a tip deflection of 8.7 μm at 10V. The actuated tip deflection can be compared to the predicted initial stress induced deformations to identify whether or not the actuators will close the switch below the 10 V threshold. Using the predicted stress induced tip deflections in Figure 4.21 combined with the assumption that the actuators must deflect 2 μm above the wafer surface in order for the contacts to close, one can determine that a switch with an actuated length of 90 μm should close the contacts at a voltage of 2 to 3 volts. However, as discussed in Sections 4.2.1 and 4.3.1, the predicted stress induced deformations tend to underestimate the tip deflections. Therefore, the actuation voltage is expected to be higher than this value. An additional note, although longer actuators undergo greater tip deflections than shorter actuators for a given voltage, they also have a larger initial stress-induced deflection. As a result, the actuation voltage difference between switch with varying actuated lengths is not expected to be very large.

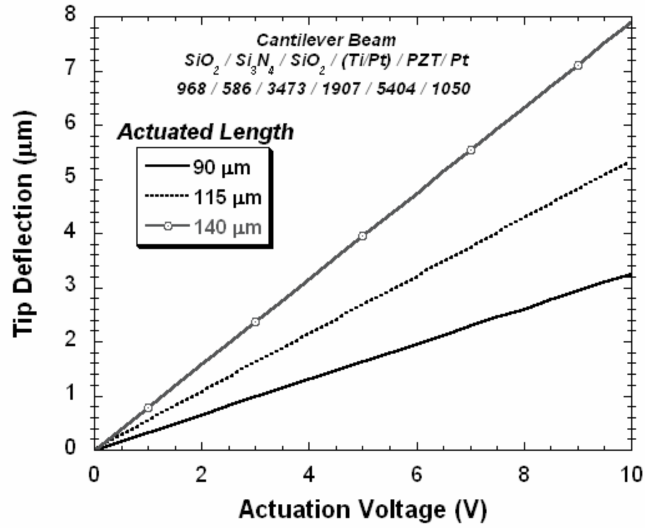

Figure 4.19: Predicted tip deflection for a PZT thin film cantilever as a function of length assuming an effective $e_{31,f}$ of -7 N/Vm.

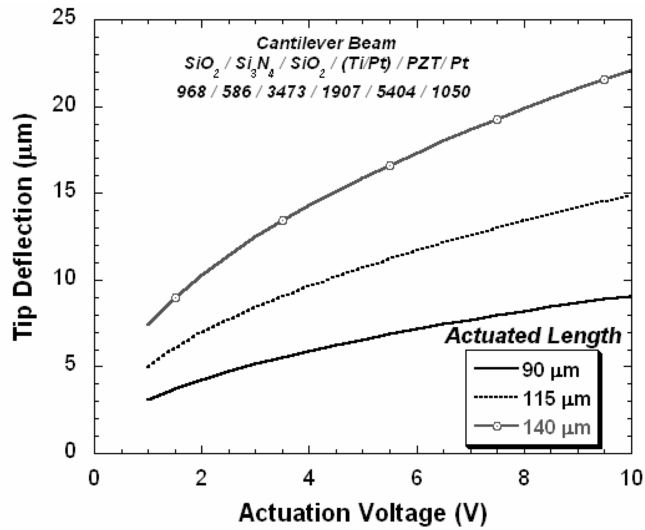

Figure 4.20: Predicted tip deflection for a PZT thin film cantilever as a function of length using the as-measured $e_{31,f}$ versus voltage reported in Figure 4.11.

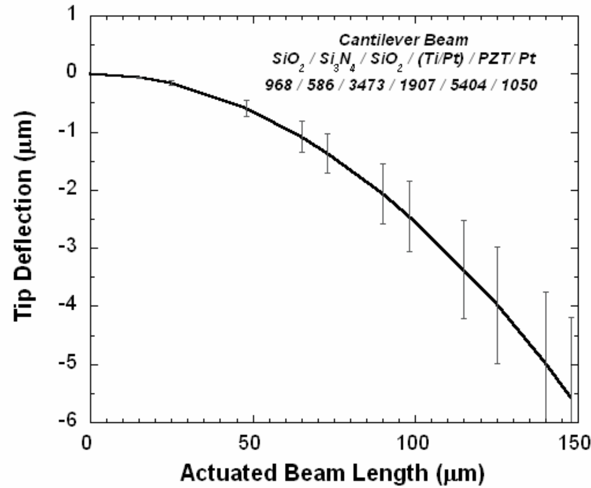

Figure 4.21: Predicted stress induced initial tip deflection for a PZT cantilever as a function of beam length with error bars equal to 25%. The error bar size was determined after comparing the average measured deflections to the predicted values and represents an envelope of all of the measured values.

Optical profilometry was used to experimentally characterize the piezoelectrically induced deformation of the switch actuators. As the voltage increases, the switch actuators deform upward due to the lateral contraction of the PZT (see Figure 4.22 for the behavior of a switch with 150 µm long actuators). At approximately 5 volts the actuators and RF contact pad are nearly planar with the CPW transmission line. Contact with the RF cantilevers occurs near 7 volts; further increases in voltage resulting in very little continued deformation in the actuators. As the voltage is reduced, the actuators and RF gap appear to remain in contact until 5 volts. Continued decreases in voltage result in additional negative deformations of the actuators and opening of the switch contacts. At zero volts, the actuators possess a negative curvature with the switch in the open state, albeit at a slightly reduced deflection when compared to the unpoled initial state. The difference between the initial and ending states result from poling of the PZT thin film (see Chapter 4.3.2). Subsequent actuation cycles show a deflection versus voltage curve similar to the downward trend indicated in Figure 4.22. A further illustration of how the switch contacts close with increasing voltage is shown in Figure 4.23. As the vertical gap diminishes, the RF contact pad first makes contact with the RF-out cantilever (~3.5 V).

The circuit is completed when increased piezoelectric deformation results in the RF contact pad contacting the RF-in cantilever (~5 V).

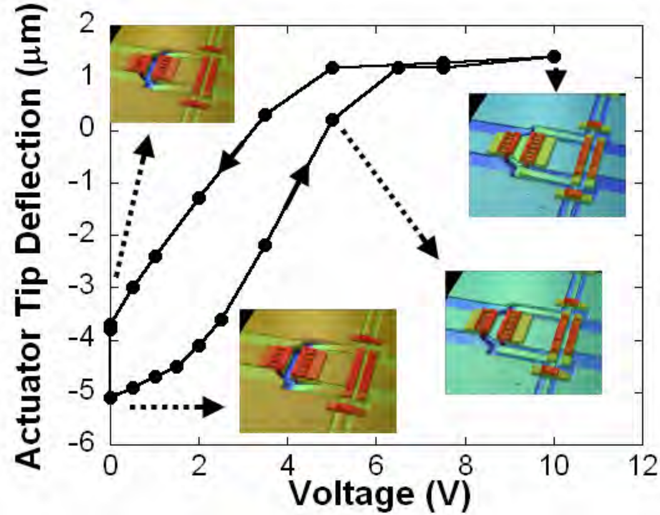

Figure 4.22: Initial piezoelectric deformation of a 140 μm long actuator of a PZT series switch (PZT SW4.0). Repeated actuation cycles follow the decreasing field trace indicated on the plot.

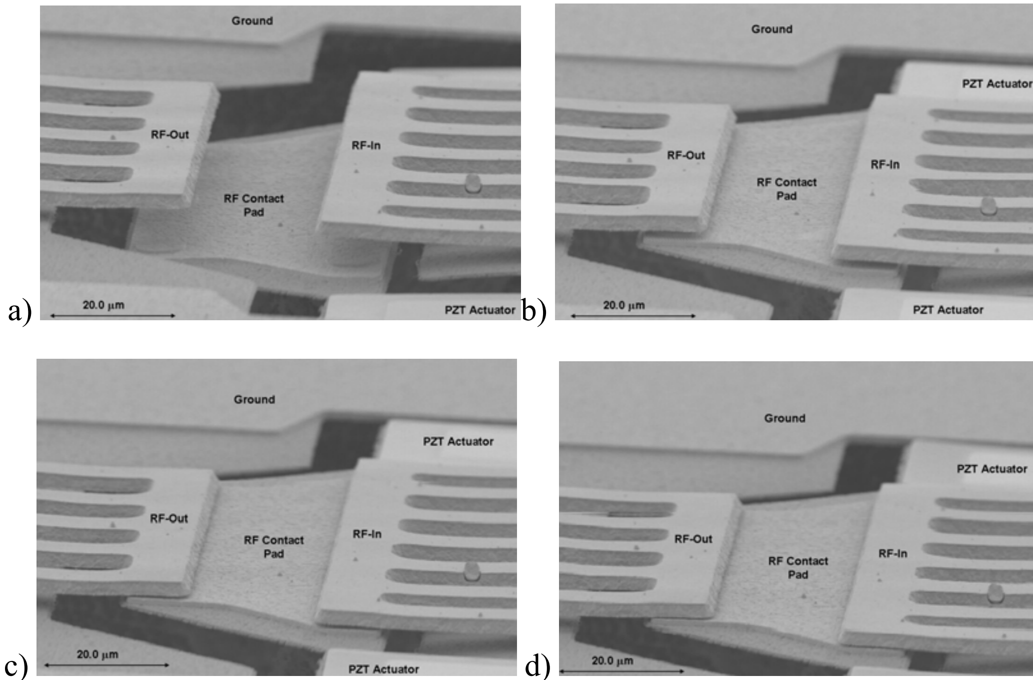

Figure 4.23: SEM images illustrating how the PZT series switch (PZT SW4.0 and PZT SW5.1 designs) closes with increasing voltage: a) 0 V, b) 3 V, c) 3.5 V, and d) 5 V.

It should be noted that the hysteresis in the actuator deformation observed in Figure 4.22 is only observed for the first actuation cycle. The data presented in Figure 4.24 illustrate the repeatable actuation deformations of a PZT actuator with an actuated length of 123 μm for repeated cycling.

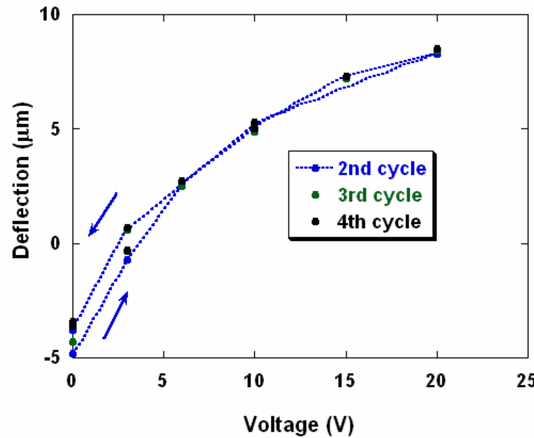

Figure 4.24: Repeated actuation deformations for a PZT thin film actuator with an actuated length of 123 μm.

4.3.4 Resonance Characterization on Switches

The resonance frequency of the switch actuator structure (comprised of the two PZT actuators and the RF contact pad) sets the lower limit of the switching time. The resonance frequencies and standard deviations were measured for each design with the results listed in Table 4.6. The fundamental resonance frequencies are in the range of 15 to 22 kHz. Thus, the lower limit for the time to open the series switch, $\tau_{open,}$ will be approximately 2 - 3 μs using Equation 4.9. These results indicate the possibility of achieving the 100 μs switching time goal for the PZT switch. However, additional factors such as the initial gap, the velocity at impact, and the actuation waveform will ultimately determine the switching time. These will be discussed in Section 4.4.5.[24]

$$\tau_{open} \propto \frac{1}{3}\left(\frac{1}{f_r}\right) \qquad \text{Equation 4.9}$$

Table 4.6: Resonance frequencies and estimated switching time for each device on Wafer 5124 (PZT SW5.1) with piezoelectric actuators comprised of $SiO_2/Si_xN_y/SiO_2/Ti/TiO_2/Pt/PZT/Pt$ (968/586/3473/20/160/1680/5054/1050 Å).

Design	Actuated Length (µm)	Resonance Frequency (kHz)	Std Dev		Estimated Switching Time (µs)
A01	65	21.75	0.3		15.3
A02	90	19.40	0.4		17.2
A03	115	15.63	0.3		21.3
A23	90	20.13	0.2		16.6
A24	115	16.32	0.4		20.4

4.4 RF MEMS Switch Characterization

This next section will cover the RF performance characteristics of the PZT switch. The objectives for the performance of the PZT switch are listed below.

- Actuation Voltage < 10V
- Isolation > 20 dB (DC → 40 GHz)
- Insertion Loss < 0.5 dB (DC → 40 GHz)
- Switching Time < 100 µs
- Temperature Sensitivity (V_{act} < 20 V)
- Power Handling > 5 W_{RF}
- Reliability > 10^6 cycles

4.4.1 Actuation Voltage

The actuation voltage of the switch was defined as the median voltage between the low and high current states of the switch (see Section 2.7.4). Electrical tests verify that the switch closes and completes the RF electrical circuit at or near 6 volts, agreeing with the optical data (see Figure 4.25). The figure shows the RF gap as determined by optical profilometry and the forward transmission coefficient (S_{21}) plotted as a function of voltage. In the off state, even though the actuators are deflected -5 microns, the RF gap is nearly -15 microns. The beam curvature of the actuators is transferred to the RF contact pad by the mechanical connection between the two structures. To first order, the RF contact pad can be thought to be a non-active extension of the PZT actuators

following the same curvature. The RF gap decreases with applied voltage with a trend similar to that of the actuator tip deflection shown in the inset of Figure 4.25. On the other hand, S_{21} exhibits very little change for small applied voltages; it increases from -34 to -30 dB from zero to 4 volts. Further increases in voltage result in a sharp decrease in S_{21} as the RF gap closes and the switch completes the RF circuit at or near 6 volts. S_{21} in the "on" state is limited to -4 dB for this particular device because the switch was fabricated on a low resistivity silicon substrate. Of particular interest is the minimal change in S_{21} below 4 volts. Although the RF gap is changing significantly (nearly 11 microns), the isolation (S_{21} in the "off" state) remains relatively unchanged. This characteristic allows for stable temperature performance in the off state, given that the PZT actuators are multilayer composites and will have different initial curvatures as a function of temperature (see Section 4.4.6).

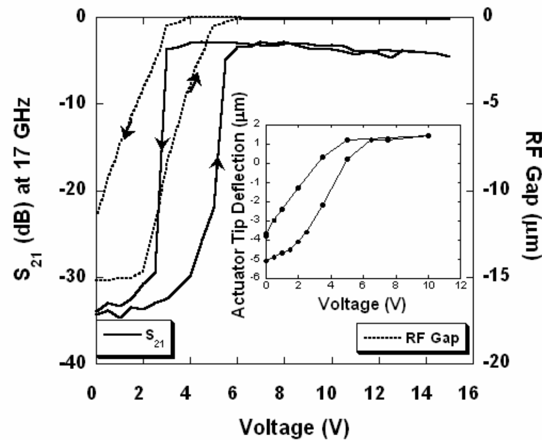

Figure 4.25: Forward transmission coefficient (S_{21}) and RF gap between the RF contact pad and the RF out cantilever as a function of applied voltage for a PZT SW4.0 design. The inset shows the deformations of a PZT actuators with an actuated length of 140 µm, as previously discussed (see Figure 4.22). Note, this data was recorded on a low resistivity Si substrate so S_{21} in the "on" state was limited to approximately 4dB.

An examination of devices from Wafer 5124 with an Electroglass autoprober reveals better than 85% yield for any particular device geometry. Histograms of the DC actuation voltages required for switch closure are shown in Figure 4.26 for all device types. As-fabricated devices generally exhibit a skewed distribution with a median actuation voltage of 5 to 6 volts and a standard deviation of 2 to 3 volts. The median

actuation voltage for each of the designs is summarized in Table 4.7. As shown, there is little change in median actuation voltage between designs with different length actuators. Similarly, the A23 and A24 designs which incorporate a pair of etch holes in the RF contact pad to facilitate a faster release etch correspond well with the A02 and A03 designs. The large standard deviations may be attributed to the measurement method of determining the actuation voltage. The actuation voltage is computed as the voltage corresponding to the average current between the median low current and median high current state (see Chapter 2.7.4). The slope of the current versus actuation voltage plot will strongly contribute to the determination of the actuation voltage (see Figure 4.27). A slow rising current versus voltage relationships will result in a computed actuation voltages significantly larger than the initial switch closure voltage as the median high current value will be skewed.

Table 4.7: Summary of the actuation voltage for the PZT SW5.1 designs on wafer 5124 with actuators comprised of $SiO_2/Si_xN_y/SiO_2/Ti/TiO_2/Pt/PZT/Pt$ (968/586/3473/20/160/1680/5054/1050 Å

Design	Key Feature	Median Actuation Voltage (V) ±1σ
A01	65 μm actuated length	5.00 ± 1.7
A02	90 μm actuated length	5.20 ± 2.0
A03	115 μm actuated length	5.90 ± 3.0
A23	Same as A02 with release holes in RF contact pad	6.40 ± 2.9
A24	Same as A03 with release holes in RF contact pad	4.00 ± 1.5

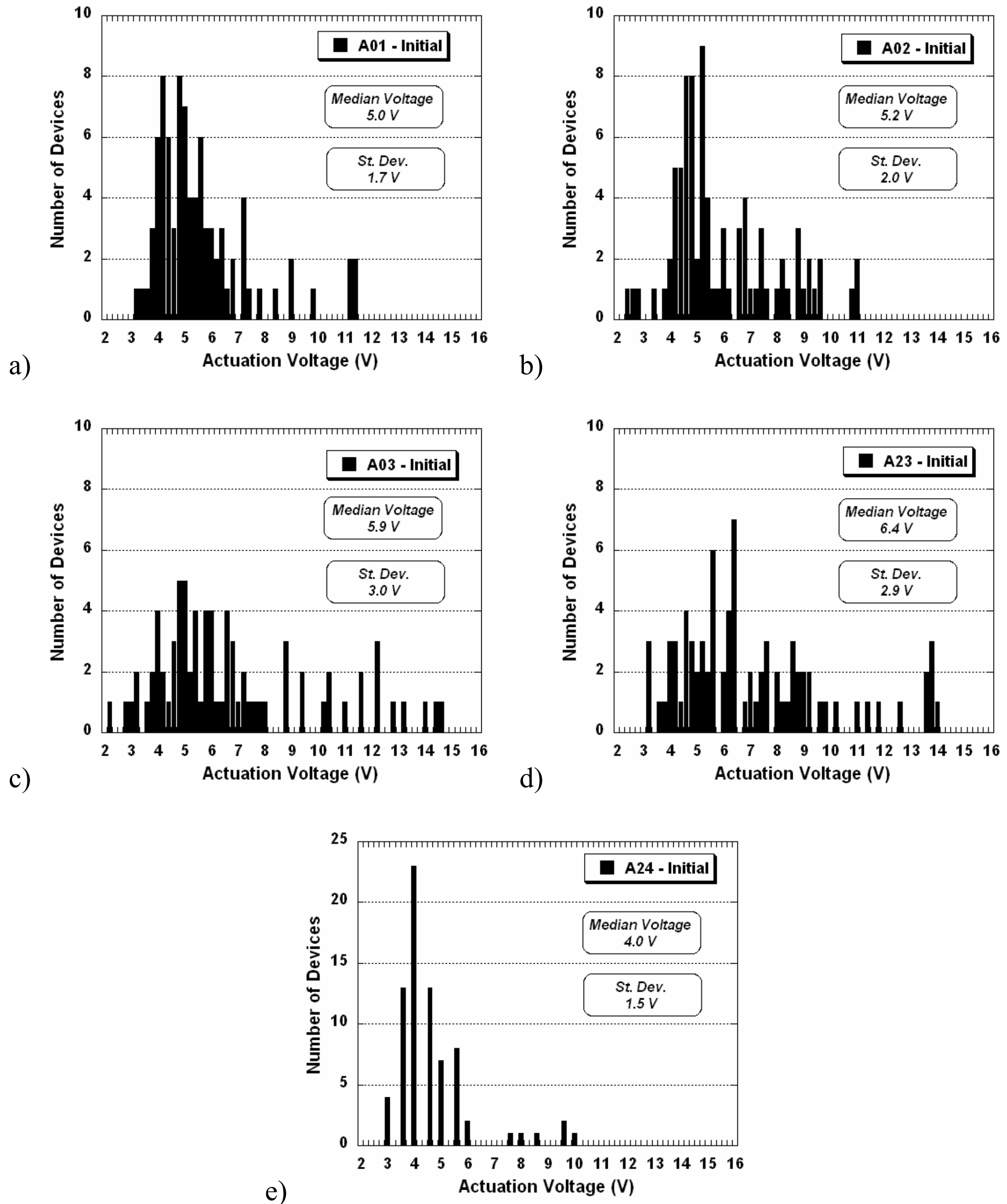

Figure 4.26: Actuation voltage histogram for the as-fabricated (unpoled) PZT switches (PZT SW5.1): a) device A01, b) device A02, c) device A03, d) device A23, and e) device A24. Note, device A24 was analyzed with a reduced number of voltage steps compared with the other scans.

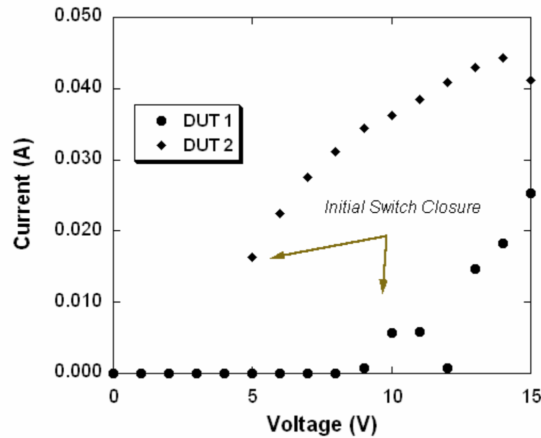

Figure 4.27: Measured DC current thru the RF transmission as a function of voltage applied to the PZT actuators for two individual devices under test (DUT). DUT1 appears to break contact at 12 V and then regains contact with increasing voltage presumably due to a high initial contact resistance.

4.4.2 Actuation Voltage - Poling & Aging

As previously discussed, poling of the PZT thin film is critical to fully realizing the piezoelectric potential. The poling process not only improves the piezoelectric coefficient, but as discussed previously, can alter the static deformation of the piezoelectric actuators. These two effects combine to reduce the actuation voltage. To determine the effects of poling on the actuation voltage, the actuation voltage of different switch designs are evaluated with an Electroglass autoprober as a function of poling and aging. Poling is generally done with an elevated voltage, 2 – 3 times the coercive field, applied for 10 – 15 minutes. However, the current configuration of the autoprober could only accommodate a short poling time of 60 seconds with 15 volts (approximately 7 times the coercive field). After an initial scan to pole the actuators and measure the actuation voltage (see Figure 4.26), the wafer was rescanned. The median actuation voltage reduced to 3.9 volts with a standard deviation of 1.1 volts (see Figure 4.28a). In addition, the distribution of actuation voltages became tighter. The poling procedure was repeated with very little change in the median voltage and further tightening of the distribution (see Figure 4.28b). After the second poling, several devices closed at less than 3 V, with the lowest voltage device switching at 2 V. If the actuators are poled for

longer times at elevated temperatures, further enhancements in the piezoelectric coefficient and therefore reductions in median actuation voltage are expected. However, the autoprober was not configured with a thermal chuck, so these experiments will be left for future efforts.

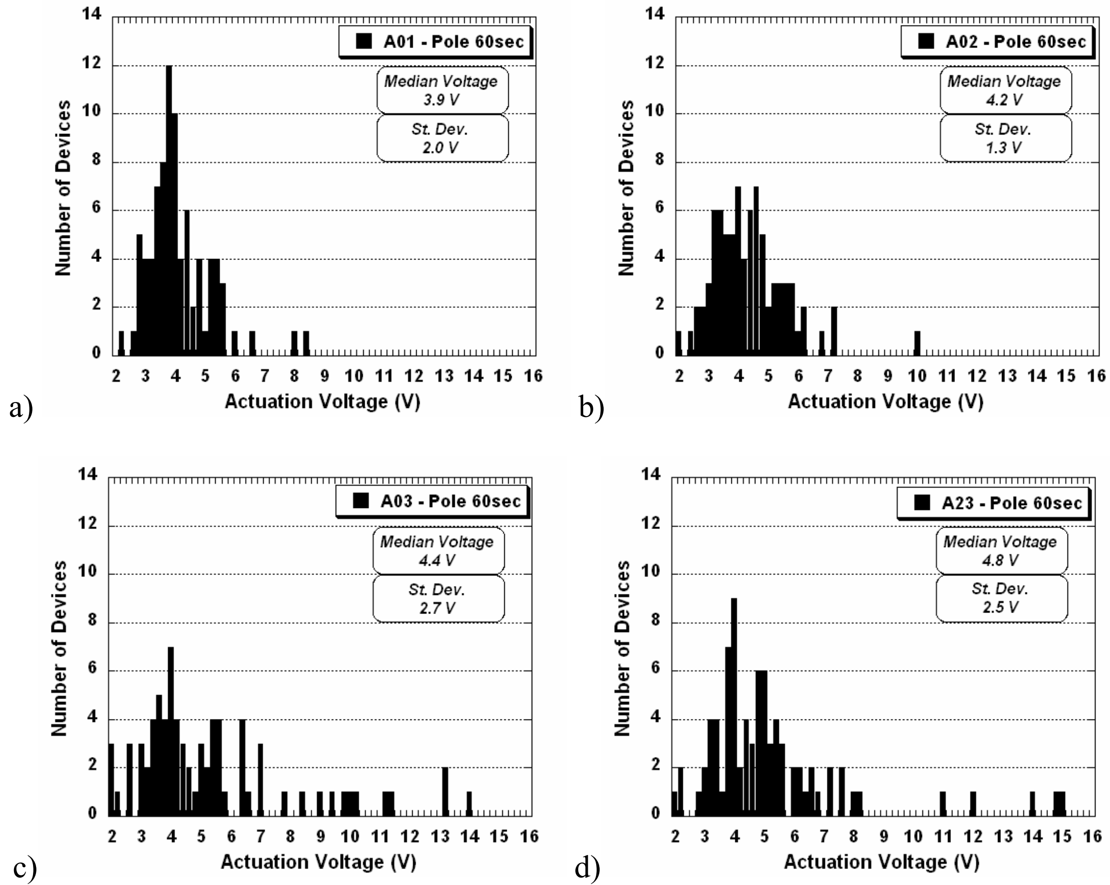

Figure 4.28: Actuation voltage histograms of several device designs (PZT SW5.1) after poling for 60 seconds: a) A01, b) A02, c) A03, and d) A23.

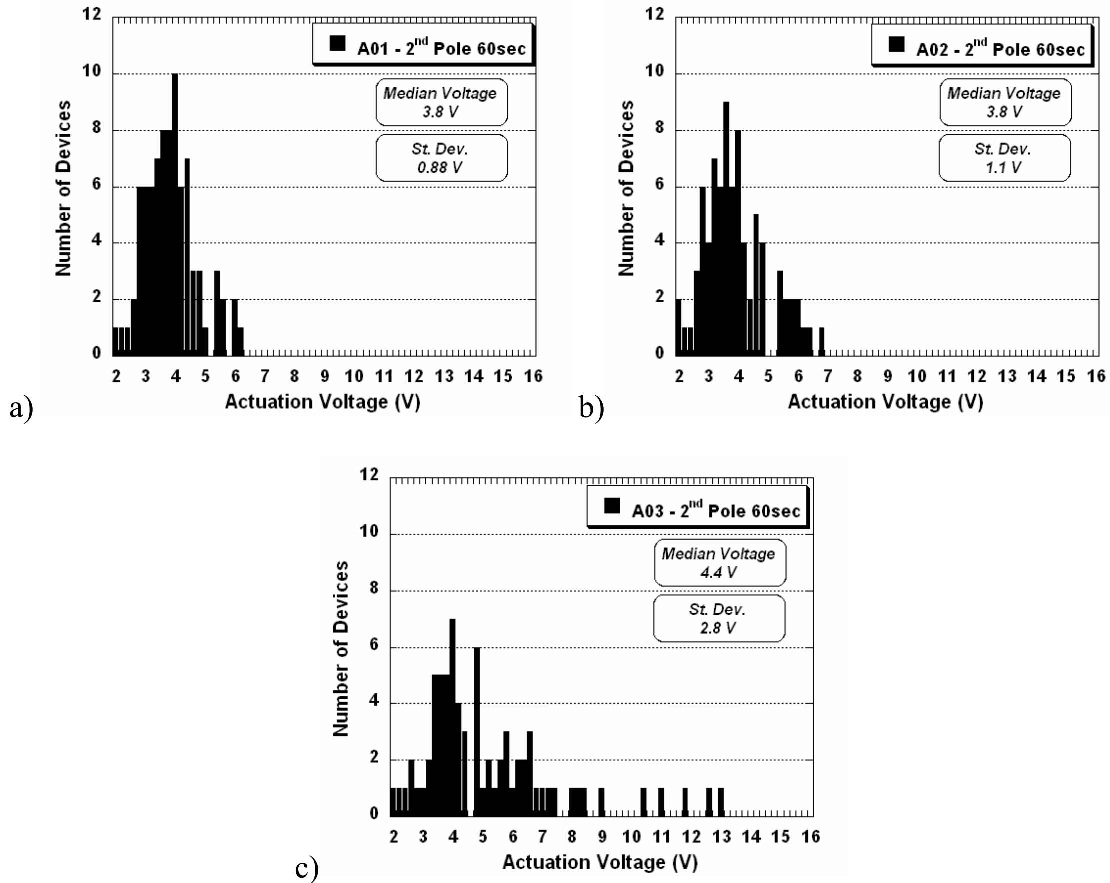

Figure 4.29: Actuation voltage histograms of several device designs (PZT SW5.1) after a second poling for 60 seconds: a) A01, b) A02, and c) A03.

Aging of the ferroelectric poses a long term storage issue, as the piezoelectric coefficient reduces over time. Many PZT thin films have piezoelectric aging rates ranging from 3 – 9% per time decade.[30] As the piezoelectric coefficient decays over time, the actuation voltage should gradually increase. To estimate the magnitude of this problem, following the second poling procedure described above, the switches were aged overnight and rescanned after 15 hours. The resulting histogram broadened slightly, with the median actuation voltage rising to 4.2 V with a standard deviation of 1.1 V (see Figure 4.30). The aging characteristics of the switch actuators were also measured with the optical profiler over time. After poling the switch actuators, the static tip deflection of the actuators is monitored as a function of time with zero volts applied to the actuators. The deformations shown in Figure 4.31 illustrate that after 3 hours there is approximately

a 15% (1-1.5 micron) change in the zero field tip deflection for actuators poled at 125ºC for 15 minutes and approximately a 25% (1.6-2.5 micron) change for actuators poled at 25ºC for 15 minutes. It should be mentioned that a portion of this change may be attributed to a finite DC voltage in the measurement resulting from an improper ground loop in the measurement setup that decays after approximately 300 seconds. These changes in the actuator tip deflection compared with the RF gap (10 – 15 microns) are consistent with the small increase in actuation voltage observed in Figure 4.30. It should be mentioned that the increase in actuation voltage will only affect the first cycle of switch operation as any further application of voltage will result in the re-poling of the PZT actuators as mentioned above.

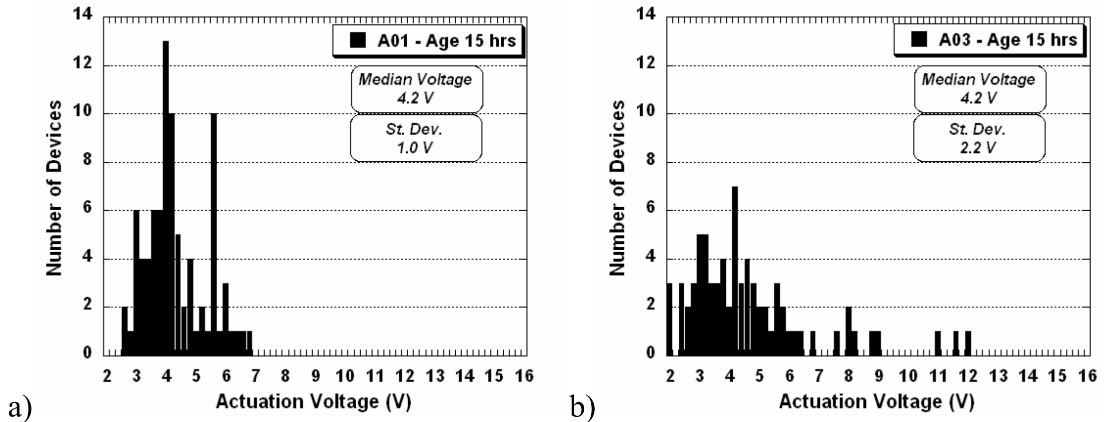

Figure 4.30: Actuation voltage histograms for PZT SW5.1 designs following aging of the PZT switches for 15 hours: a) device A01 and b) device A03.

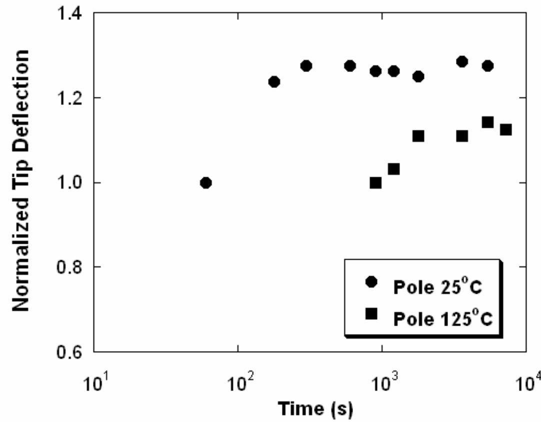

Figure 4.31: Normalized actuator tip deflection as a function of aging time for a PZT SW5.1 design, device A03 with an actuated length of 115 μm. The device was poled at 15 volts at room temperature and at 125ºC. Zero time is calculated based on the time the poling voltage is reduced to zero volts.

4.4.3 Isolation and Insertion Loss

A sample of the RF performance of the PZT switch from 100 MHz to 65 GHz is plotted for each device design (see Figure 4.32 thru Figure 4.36). As mentioned previously in Table 4.7, the primary difference between each of the device designs is the length of the PZT actuator (65, 90, or 115 μm). Each design has excellent isolation (S_{21} in the open state) across the frequencies tested, with values as low as -60 dB below a few gigahertz steadily increasing but remaining below -20 dB above 40 GHz. In the actuated (closed) state, the insertion loss (absolute value of S_{21}) was good, with values less than 1 dB up to 40 GHz and rising up to 2 dB at 65 GHz. A summary of the isolation and insertion loss characteristics for each of the series switch designs on Wafer 5124 is listed in Table 4.8. Note that the sample size for the RF summary measurements is much smaller (5 devices) compared to the autoprobed DC results (90^+ devices) discussed previously. As expected, there is very little variation in the isolation values among the switch designs: further indication that the in-plane gap between the two RF cantilevers is the main factor responsible for the isolation. In the closed state, each of the designs performs well, with insertion loss values below 1 dB at 17 GHz. For the sample size tested, the median insertion loss of Designs A02 and A23 (both with actuators having

actuated lengths of 115 μm with A23 having etch holes in the RF contact pad) exhibited a slight improvement over the other designs when actuated at 5 volts.

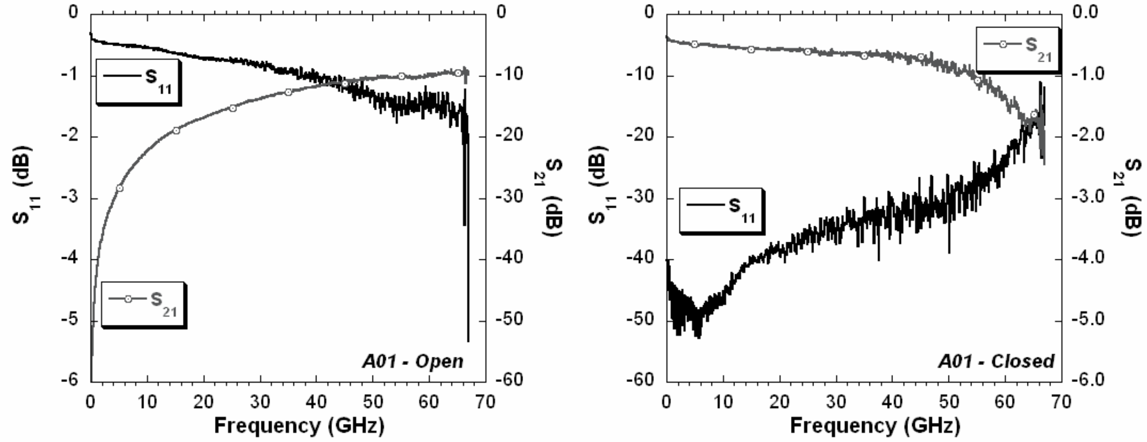

Figure 4.32: Measured RF performance for PZT SW5.1 design A01 (65 μm long actuated beam) in both the open and closed state. These data do not represent the average performance over several devices, instead they illustrate the performance of a single device.

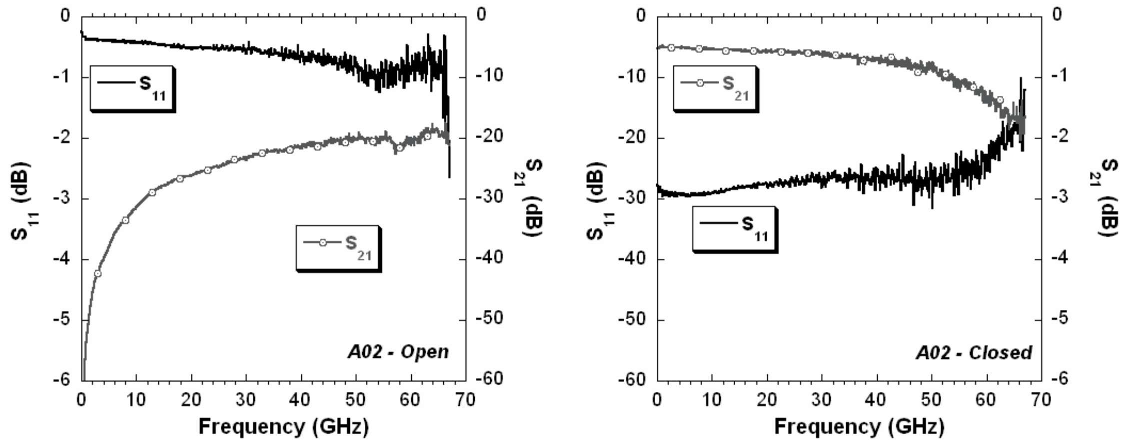

Figure 4.33: Measured RF performance for PZT SW5.1 design A02 (90 μm long actuated beam) in both the open and closed state. These data do not represent the average performance over several devices, instead they illustrate the performance of a single device.

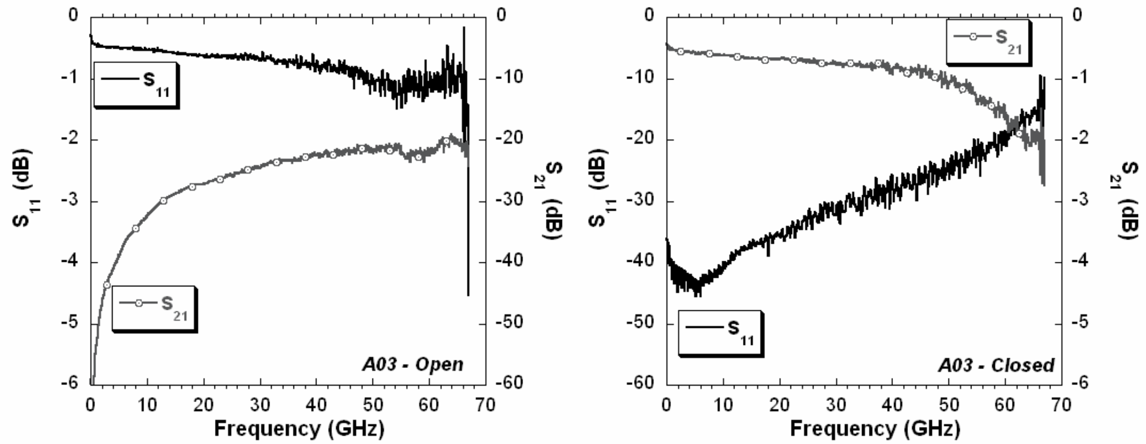

Figure 4.34: Measured RF performance for PZT SW5.1 design A03 (115 µm long actuated beam) in both the open and closed state. These data do not represent the average performance over several devices, instead they illustrate the performance of a single device.

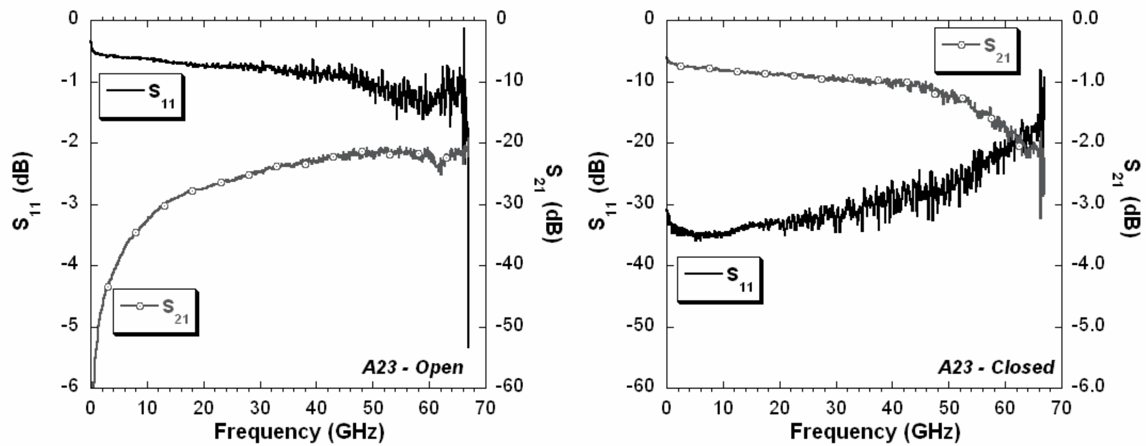

Figure 4.35: Measured RF performance for PZT SW5.1 design A23 (90 µm long actuated beam) in both the open and closed state. These data do not represent the average performance over several devices, instead they illustrate the performance of a single device.

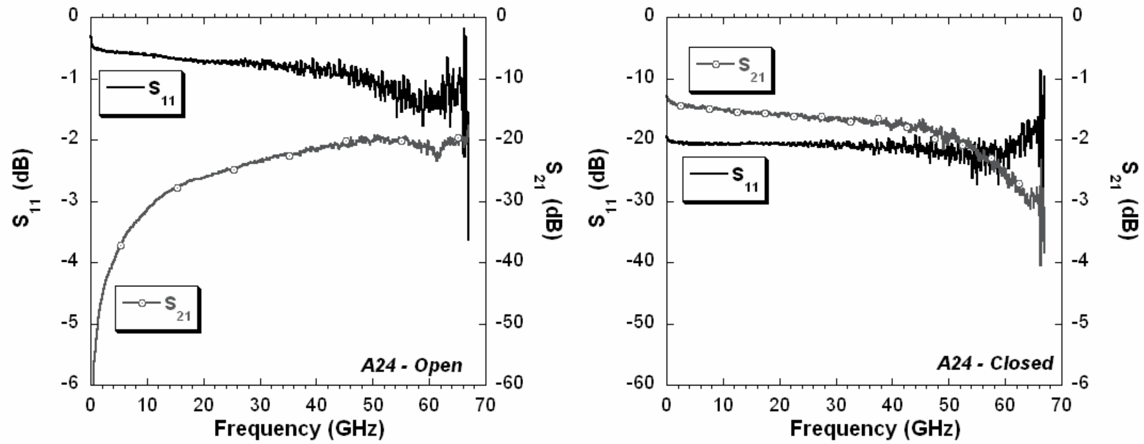

Figure 4.36: Measured RF performance for PZT SW5.1 design A24 (115 μm long actuated beam) in both the open and closed state. These data do not represent the average performance over several devices, instead they illustrate the performance of a single device.

Table 4.8: Median S_{21} values (from 5 or more samples) in the open and closed states (at 5 V) at 17 GHz for PZT SW5.1 on Wafer 5124 with piezoelectric actuators comprised of $SiO_2/Si_xN_y/SiO_2/Ti/TiO_2/Pt/PZT/Pt$ (968/586/3473/20/160/1680/5054/1050 Å)

Design	Key Design Feature	S_{21} (open) at 17 GHz	S_{21} (closed) at 17 GHz
A01	65 μm actuated length	-24.34 (±3.36) dB	-0.88 (±0.10) dB
A02	90 μm actuated length	-28.56 (±0.65) dB	-0.58 (±0.08) dB
A03	115 μm actuated length	-29.78 (±1.35) dB	-0.89 (±0.12) dB
A23	Same as A02 with release holes in RF contact pad	-32.84 (±0.76) dB	-0.62 (±0.14) dB
A24	Same as A03 with release holes in RF contact pad	-33.63 (±0.40) dB	-0.80 (±0.10) dB

The existing insertion loss performance leaves room for improvement. To compete with existing electrostatic switches, the insertion loss must be improved to 0.1 to 0.3 dB from 20 to 40 GHz.[24] As will be discussed in Section 4.4.4, excessive substrate losses resulted in a substantially higher transmission line loss than was anticipated. Additionally, the insertion loss characteristics improve with increasing actuation voltage as illustrated in Figure 4.37. The reduction in S_{21} may result from an increase in the contact force with increased deformation of the actuators. Another mechanism for improvement could be a decrease in the contact resistance from a reduced influence of

contaminant films between the contact surfaces. This is especially true for the example in Figure 4.37 exhibiting an insertion loss of nearly 3 dB when actuated at 5 volts. This topic of contact surface contamination and its effect on switch performance will be discussed in further detail in Section 4.5.3.

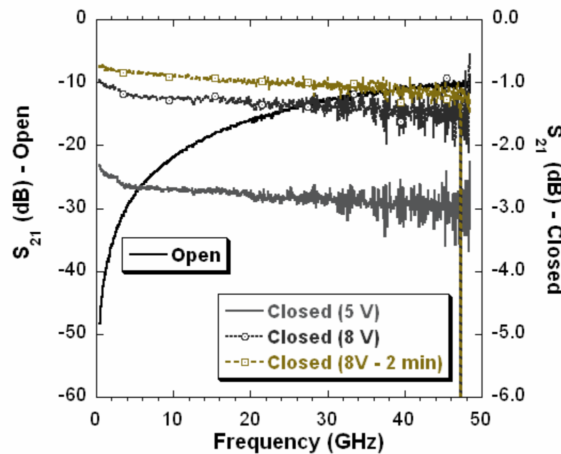

Figure 4.37: Example of the improvements in S_{21} in the closed state for an actuation voltage of 5 V and 8 V.

4.4.4 Influence of Elastic Layer on Insertion Loss Characteristics

The existing fabrication process places the CPW transmission lines on the oxide/nitride/oxide elastic layer. The result is a higher than anticipated transmission line loss resulting from the elastic layer used to control the initial curvature of the PZT actuators. Examination of CPW transmission lines with varying dielectric thin films between the CPW and a high resistivity silicon substrate reveals transmission losses as large as 1.25 dB/mm at 40 GHz (see Figure 4.38). The transmission line loss with the elastic layer is nearly an order of magnitude higher than one using a silicon dioxide thin film (0.18 dB/mm). The elastic layer cannot be eliminated from the substrate because of its role in controlling the residual stress of the PZT actuators. However, the elastic layer can be thinned under the CPW transmission line. If the elastic layer is thinned to 1000 Å, approximately half the transmission loss can be eliminated. Further thinning of the

elastic layer to 300 Å resulted in a transmission loss of 0.2 dB/mm at 40 GHz, comparable to that obtained with a 2000 Å silicon dioxide thin film.

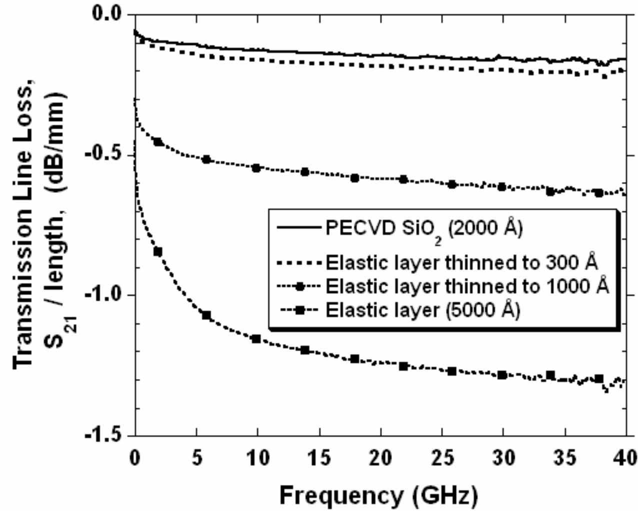

Figure 4.38: Transmission loss of CPW transmission lines on different dielectrics on a high resistivity silicon substrate.

The evidence in Figure 4.38 highlights that the silicon nitride layer and the two nitride/oxide interfaces are responsible for the higher insertion loss characteristics. It is possible that the loss is a result of charge trapping in the silicon nitride/silicon dioxide stack. Previous work on stacked dielectrics for gate dielectrics in field effect transistors highlights the charge trapping observed in silicon nitride as well as at the oxide/nitride interface.[25,26,27]

To improve the substrate loss, the exact amount of thinning strongly depends on the width of the interface arising from the plasma enhanced chemical vapor deposition conditions and any diffusion from subsequent annealing. As illustrated in the depth profile results in Figure 4.39, the silicon nitride is confined to a relatively small region with sharp transitions. Therefore, thinning of the dielectric can proceed using the measured thickness of the oxide/nitride/oxide composite.

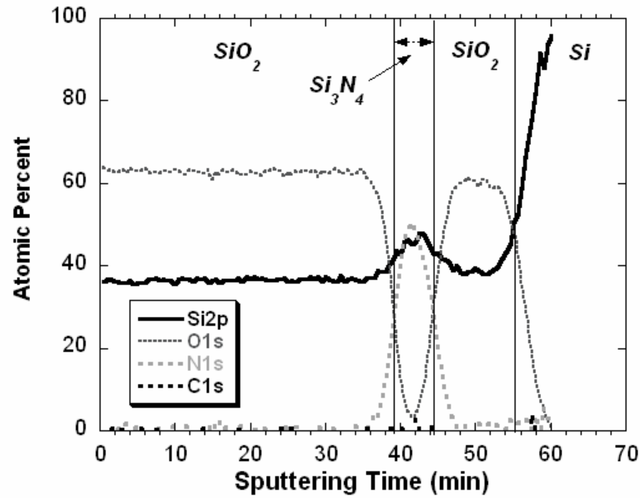

Figure 4.39: X-ray photoelectron spectroscopy (XPS) depth profile of a composite oxide/nitride/oxide (1200 / 486 / 3520 Å) thin film.

The fabrication process was subsequently modified to improve the insertion loss characteristics of the switch. Referring to Section 3.2.7, a reactive ion etch (RIE) step was added to thin the elastic layer prior to deposition of the CPW metallization. In this process, the critical features of the switch including the actuators, RF contact pad, and release trenches were protected with photoresist (see Figure 4.40). This pattern leaves the remaining elastic layer exposed to the RIE. Using the same RIE process outlined in Section 3.2.6, the elastic layer was thinned to expose the bottom silicon dioxide layer. It is assumed that the oxide/nitride interface is less than 200Å thick. The remaining elastic layer was measured with the ellipsometer to ensure that the target thickness was achieved. Following the etching, the resist was removed with an oxygen plasma. An example of the improved insertion loss characteristics of a PZT switch is shown in Figure 4.41. In this example, S_{21} remains below -0.5 dB from DC to 40 GHz.

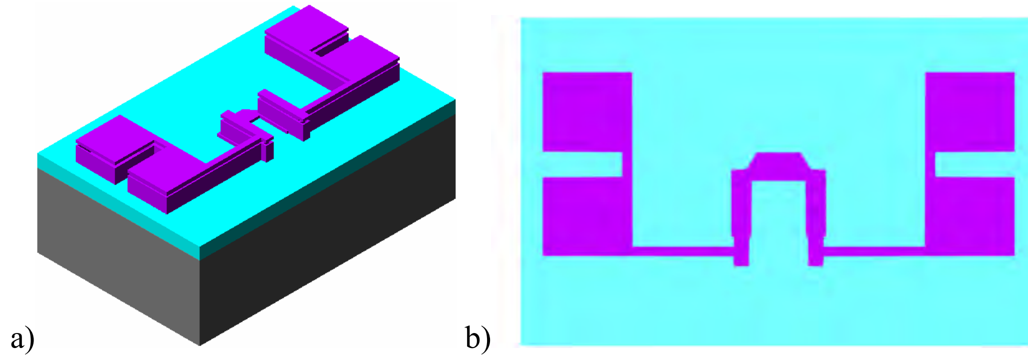

Figure 4.40: Modification to the fabrication flow – thinning of the elastic layer. Photoresist (purple) is patterned and protects the PZT actuators, RF contact pad, and the release trenches: a) 3-dimensional view and b) plan view. The remainder of the wafer is then etched to remove the silicon nitride and all silicon nitride/silicon oxide interfaces.

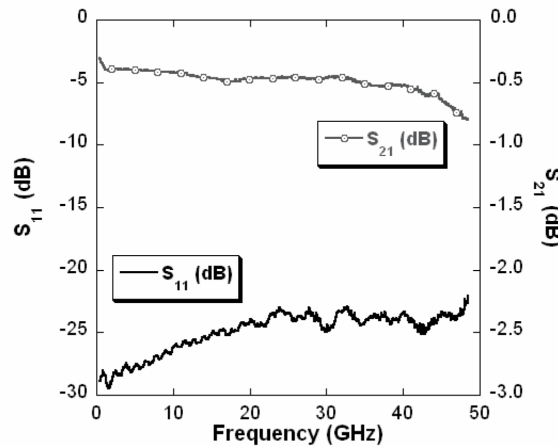

Figure 4.41: Insertion loss characteristics of design A05 with a 90 μm long actuated beam (see Section 4.5 for further description of A05) on Wafer 5230 in which the oxide/nitride/oxide layer for all the structures except for the actuators and RF contact pad has been thinned to approximately 800Å with a reactive ion etch.

4.4.5 Switching Time

Based on the discussion in Section 4.3.4, the switching time was expected to be on the order of 2 – 4 microseconds, depending on the initial gap between the RF pad and RF cantilevers. However, the switching times measured using a square actuation waveform are on the order of 60 μs for as-fabricated devices and approximately 40 μs for poled samples (see Figure 4.42). For these measurements, the sense voltage-in represents

the input sensing voltage applied to the RF-in side of the switch while the sense voltage-out refers to the output from the RF-out side. The initial contact generally occurred within 4 – 8 μs for all designs, but final closure is delayed by bouncing between the contacts. The faster switching speed observed for poled samples is a result of the reduced vertical gap after poling the actuators. A smaller gap decreases the velocity at impact, thereby reducing the settling time. Further evidence of switch bouncing limiting the switching time is provided by the small oscillations in the sensing voltage apparent for extended periods of time after contact (see Figure 4.43). Furthermore, experiments under vacuum increase the time to switch closure past 100 μs (see Figure 4.44). In contrast to the switch on time, the switch off time is not limited by bouncing, although some degree of bouncing was observed for a small number of devices (see Figure 4.45). The switch off time average is approximately 0.5 μs for all device designs.

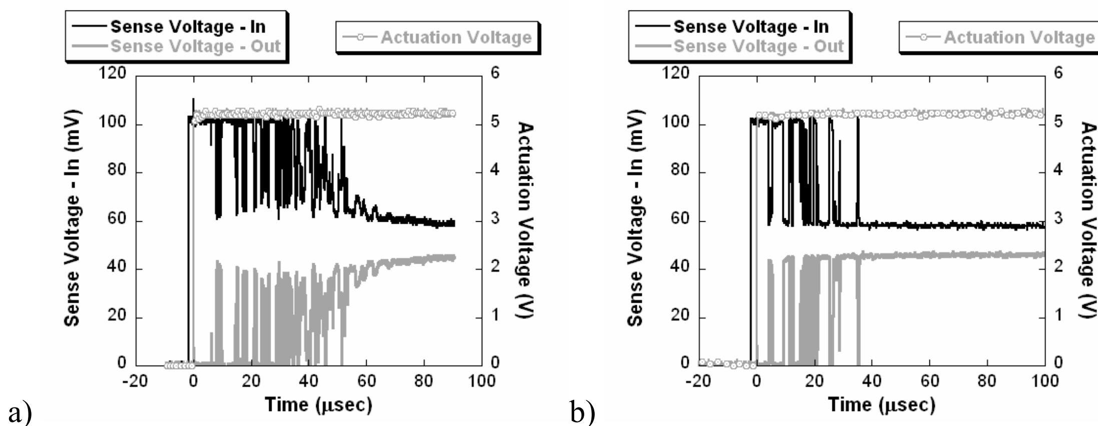

Figure 4.42: Examples of the switching time measurement for PZT SW5.1 device A02; a) as-fabricated and b) after poling for 2 min at 5V.

To verify that the switch is bouncing, the laser Doppler vibrometer (LDV) was used to measure the velocity of the major components of the switch as a function of time for a single actuation pulse. These measurements were made at atmospheric pressure. A series of data was taken with the switch open (0.5 V applied) followed by measurements at 5V to analyze contact phenomena. At 0.5 V, the actuators ring for nearly 400 μs of the 1 ms pulse (see Figure 4.46a). Similarly, the RF contact pad rings for over 200 μs (see

Figure 4.46b). As expected, the RF cantilevers show no sign of movement at 0.5V as the contacts fail to make contact at this voltage.

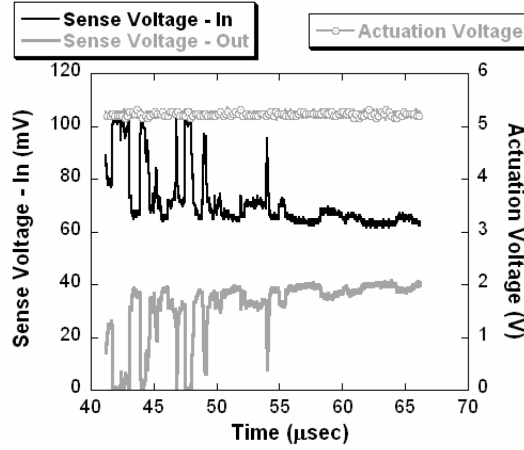

Figure 4.43: Illustration of the ripple in the contact resistance that results from the bouncing between the RF contact pad and the RF cantilevers.

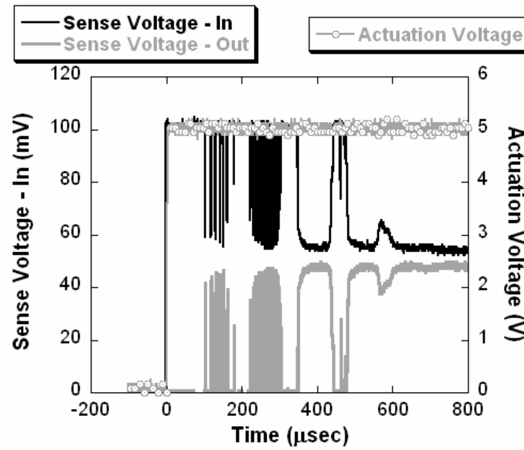

Figure 4.44: Switching time measurement for a PZT SW5.1 switch (A02) in a vacuum of 1×10^{-5} Torr.

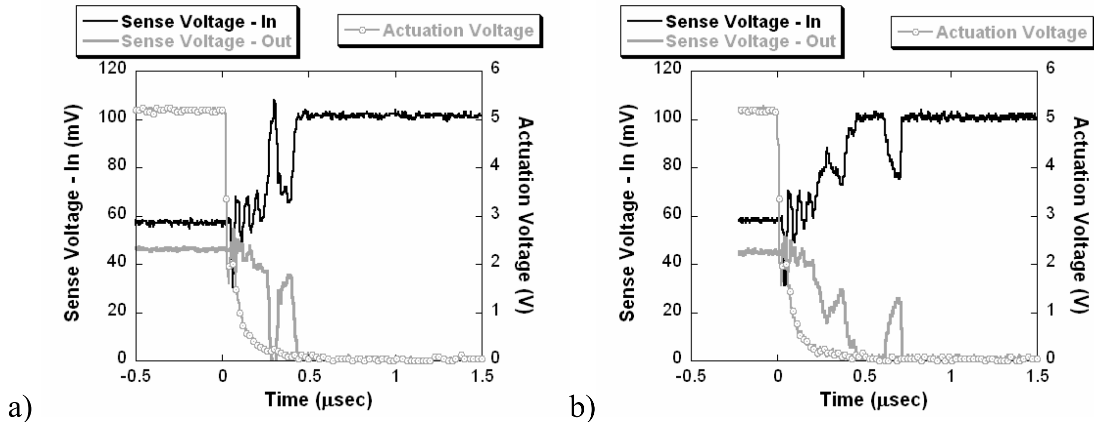

Figure 4.45: Examples of the switch off time for the PZT SW5.1 device A02; a) with very little evidence of bounce and b) with bounce.

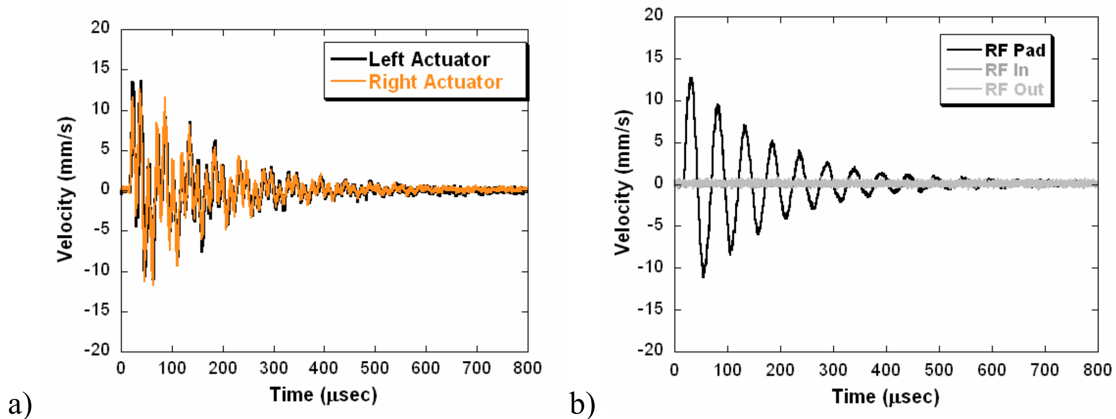

Figure 4.46: Time scan for a) the switch actuators of PZT SW5.1 device A02 and b) the RF contact pad and RF cantilevers at the onset of a 0.5V, 1ms pulse applied to the PZT actuators. In part b, the RF-in and RF-out cantilevers do not show any evidence of movement.

On applying 5V, the vibration response of the first 60 μs may be characterized as chaotic as the switch contacts impact on several occasions within this time period. Following the first 60 μs, the actuators exhibit a normal ring down response that persists for greater than 400 μs (see Figure 4.47). Figure 4.48 shows that the RF pad and both RF cantilevers exhibit nearly matching vibration responses after the contacts begin to settle (after approximately 100 μs - see Figure 4.48 a and c). The velocity fluctuations in the first 60 μs are indicative of impact events.

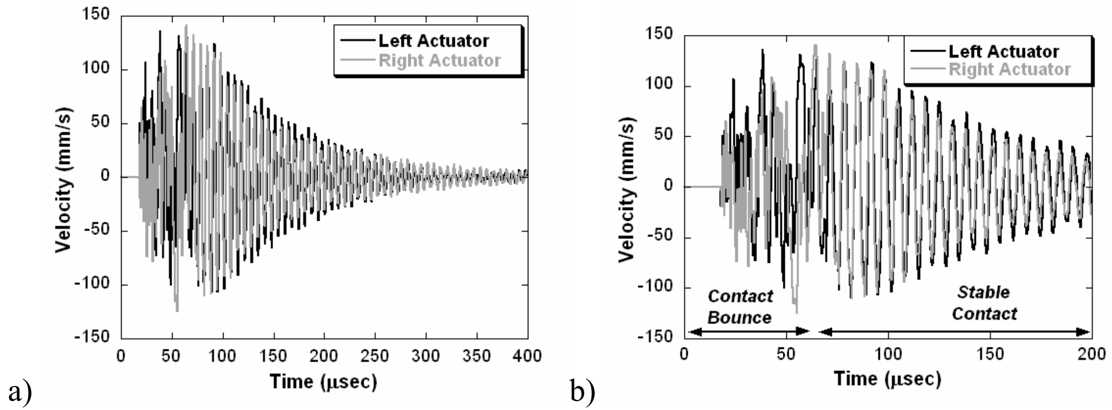

Figure 4.47: a) Time scan for switch actuators with a 90 μm long actuated length (PZT SW5.1 device A02) at the onset of a 5.0V, 1ms pulse applied to the PZT actuators. Image b) is a zoom image of switch contact occurring during the first 60 microseconds highlighting the transition from an unstable to a stable contact.

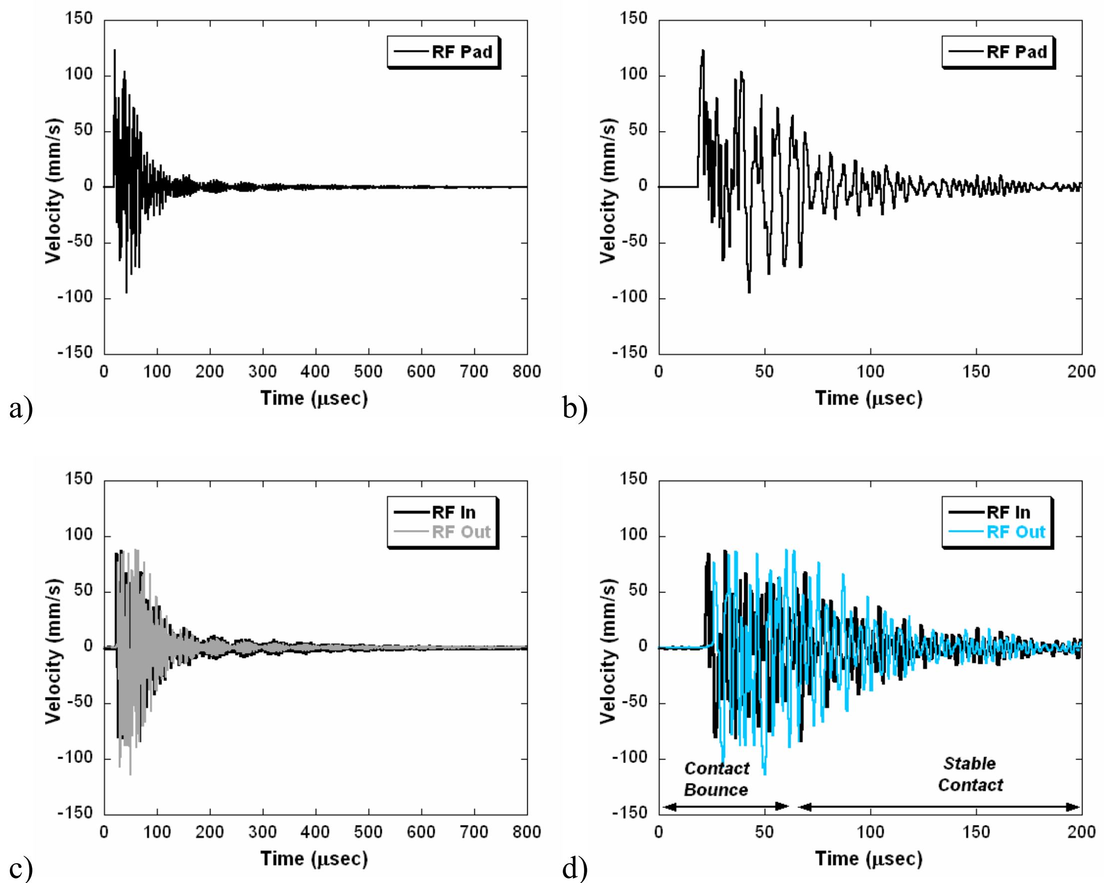

Figure 4.48: Time scan of PZT SW5.1 device A02 (90 μm long actuated beam) for (a and b) the RF pad and (c and d) the RF in and out cantilevers at the onset of a 5.0V, 1ms pulse applied to the PZT actuators. b) and d) highlight switch contact and bounce occurring during the first 60 microseconds.

Methods to improve the switching speed to less than 20 μs are currently under investigation and will be left for future work. One option is to use damping to suppress the vibration of the actuators and RF cantilevers. In principle, one way of lowering the mechanical quality factor and thus damping the vibration response of a PZT actuator is to donor dope the PZT to create a "soft" PZT. Soft PZT has a larger piezoelectric hysteresis than hard PZT resulting in increased loss and a reduced mechanical coupling.[28] This could lower the mechanical quality factor (Q) of a thin film PZT actuator. However, in many cases, the mechanical Q of the structure is not controlled by the PZT itself. Thus, it is not clear whether this method would work.

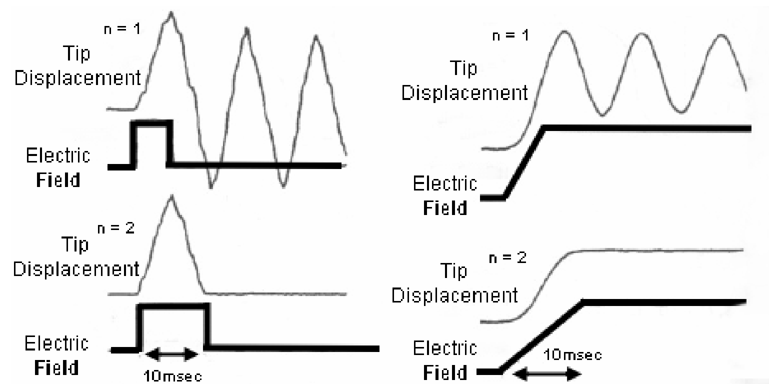

Figure 4.49: Example of actuation waveform control using a voltage ramp (right side) as opposed to a square wave applied to the piezoelectric as presented by Uchino and Giniewicz.[29] Note, n is a time scale based on half of the resonance period of the actuator.

Another possible method focuses on waveform actuation control that has been described by Uchino and Giniewicz.[29] As illustrated in Figure 4.49, changing the rise time of actuation waveform from a simple square wave to a ramped waveform with a rise time equal to one full resonance period can be used to reduce the vibration ringing in a piezoelectric actuator. With a ramped waveform, the ringing response is highly sensitive to the rise time with deviations as small as 10% of the resonance period unable to fully control the actuator ringing. An additional concern is that this technique may work for a single stand alone actuator but the response may change from the interaction of two free vibrating entities. As the RF contact pad makes contact with each of the RF cantilevers, the interaction sends each cantilever into vibration. A possible solution to minimize this

vibration may be to reduce the initial gap between the RF contact pad and RF cantilevers by use a multi-pulse actuation waveform, thereby limiting the velocity at impact.

4.4.6 Hold down performance

The RF performance of the switch as a function of hold time is also crucial for communication systems where continuous signal transmission must be maintained for extended periods of time. To analyze hold down performance, the transmission scattering parameter, S_{21}, was monitored as a function of time with the switch in the actuated state. At the conclusion of the test, the switch was checked to insure that it returned to the open state.

There are two potential concerns about how the PZT actuator will behave under continuous dc bias; the first entails a change in the poling state of the film, and the second is time dependent dielectric breakdown. Earlier studies on time dependent dielectric breakdown of sol-gel PZT thin films prepared with a very similar process to that described in Section 3.2.4 provide estimates that the average time to device failure ($\tau_{50,1}$) for a switch operating at an operating field (E_1) of 100 kV/cm at room temperature should be on the order of 2.7 x 10^8 hours. This was calculated from Equation 4.10 using an activation energy of failure (E_a) of 0.78 eV, a voltage acceleration factor (N) of 7.8, $\tau_{50,2}$ of 136 hours at 120 C and 250 kV/cm (E_2), and k is Boltzmann's constant.[30] Thus, time dependent dielectric breakdown is not expected to provide the real limit to the switch lifetime. Note, one very significant difference between the PZT samples from the previous research and the switches is the PZT capacitors from the earlier work did not see any harsh processing steps (i.e. oxygen plasmas, wet chemistry baths, or reactive ion etches with fluorine). As discussed previously, these steps can significantly affect the surface chemistry and defect distribution throughout the film which can then affect the dielectric breakdown characteristics.

$$\tau_{50,1} = \tau_{50,2}\left(\frac{E_2}{E_1}\right)^{-N} \exp\left[\frac{E_a}{k}\left(\frac{1}{T_1} - \frac{1}{T_2}\right)\right] \qquad \text{Equation 4.10}$$

As mentioned previously, continuous application of the actuation voltage increases the piezoelectric coefficient of the PZT through poling. The increased piezoelectric coefficient increases the contact force, resulting in improvements to the insertion and return loss characteristics of the switch during the hold down tests (see Figure 4.50). For the device illustrated, the insertion loss improved from 1 dB to 0.5 dB over a period of nearly 46 hours. Note that these values are the raw insertion loss values including the aforementioned substrate losses from the elastic layer. In addition, the actuation voltage decreased from 5 volts to 1 – 2 volts at the completion of the test. A few of the devices tested required a short negative voltage (< -1.0 V) pulse to open, suggesting either a change in the static deformation of the actuators or stiction in the contacts. Following the negative voltage pulse, the switch operated normally, opening at zero volts, suggesting that stiction between the RF contact pad and the RF cantilevers may have been responsible for the observed behavior. If stiction is the problem, incorporating a wafer level hermetic package would both minimize water-induced stiction and reduce the impact of contamination on the surface of the contacts. Additionally, the restoring force of the switch can be increased by engineering the stress of the elastic layer to increase the negative curvature of the switch actuators.

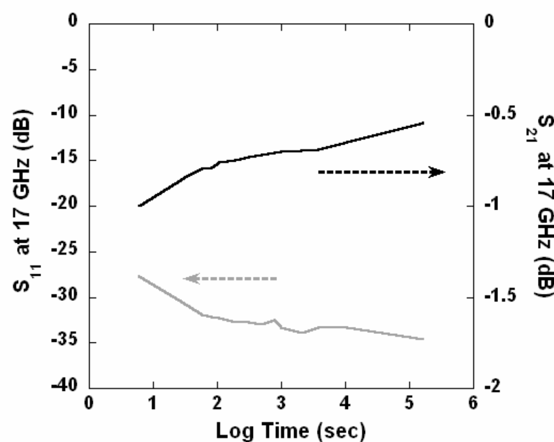

Figure 4.50: Hold down characteristics at 17 GHz of a PZT switch (A02 design) with 5V applied.

4.4.7 Thermal Sensitivity

The piezoelectric switches described here rely on stress engineering of a multi-layer composite actuator to control the initial deflection. Differences in the coefficient of thermal expansion between the individual layers cause the actuators to deflect with temperature. The thermal deformation of a switch actuator with an actuated length of 90 μm at zero volts was monitored with the optical profilometer and compared to the ANSYS™ thermal modeling results (performed by Jeffrey Pulskamp at the Army Research Laboratory) displayed in Figure 4.51. From 25ºC to 125ºC, the actuators deflect nearly 2 microns away from the RF cantilevers (increasing the gap), in good agreement with the ANSYS™ predictions. The results from Figure 4.25 indicate that these relatively small thermal deformations should not affect the isolation. However, the additional displacements may increase the actuation voltage required for switch closure. Models of a switch at -55ºC show that the downward tip deflection of an actuator with an actuated length of 90 μm is decreased by 1.5 microns relative to the room temperature position. This results in the actuator tip being 0.5 microns above zero displacement (i.e. the wafer surface). Switch closure does not occur until the actuator tip is approximately 1.4 microns above zero displacement due to the suspension of the RF in and RF out contacts. Thus, the switch should operate normally, albeit with a smaller actuation voltage at the lower end of the military temperature specification.

The RF characteristics, from DC to 50 GHz, were measured from 25ºC to 125ºC. As anticipated from the optical profilometry and ANSYS™ predictions, the isolation remains unchanged over this temperature range (see Figure 4.53). Additional measurements taken on different device wafers demonstrated that the isolation remains relatively unchanged to -25ºC. One device wafer (Wafer 5124) had a small number of devices exhibit significant changes in the isolation with varying temperatures. For this wafer, it was determined that the initial stress deformation was insufficient to maintain the initial negative curvature during the temperature and actuation cycles. In addition, thermal poling induced changes to the initial stress deformation (see Section 4.3.2) may result in the vertical gap no longer large enough to result in significant isolation.

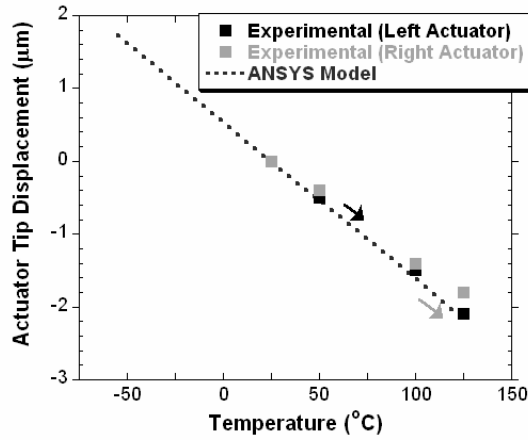

Figure 4.51: Thermal deformation (at 0 V dc bias) of a PZT actuator with an actuated length of 90 µm from room temperature to 125ºC along with predicted results from ANSYS models covering a temperature range of -55ºC to 125ºC.

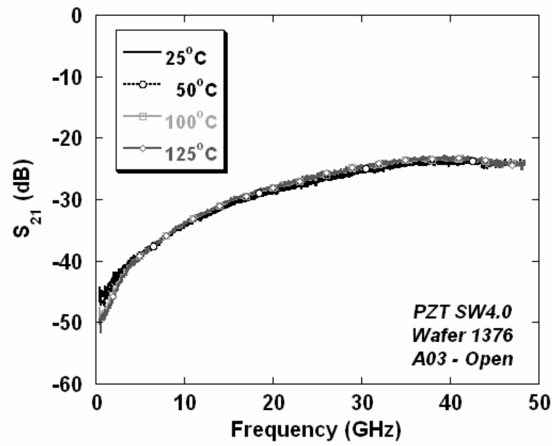

Figure 4.52: S_{21} values as a function of temperature for PZT SW4.0 switch with an actuated length of 140 µm in the open state (0V) for Wafer 1376 which is comprised of $SiO_2/Si_xN_y/SiO_2/Ti/TiO_2/Pt/PZT/Pt$ (1032/427/3360/20/160/1680/4881/1050 Å).

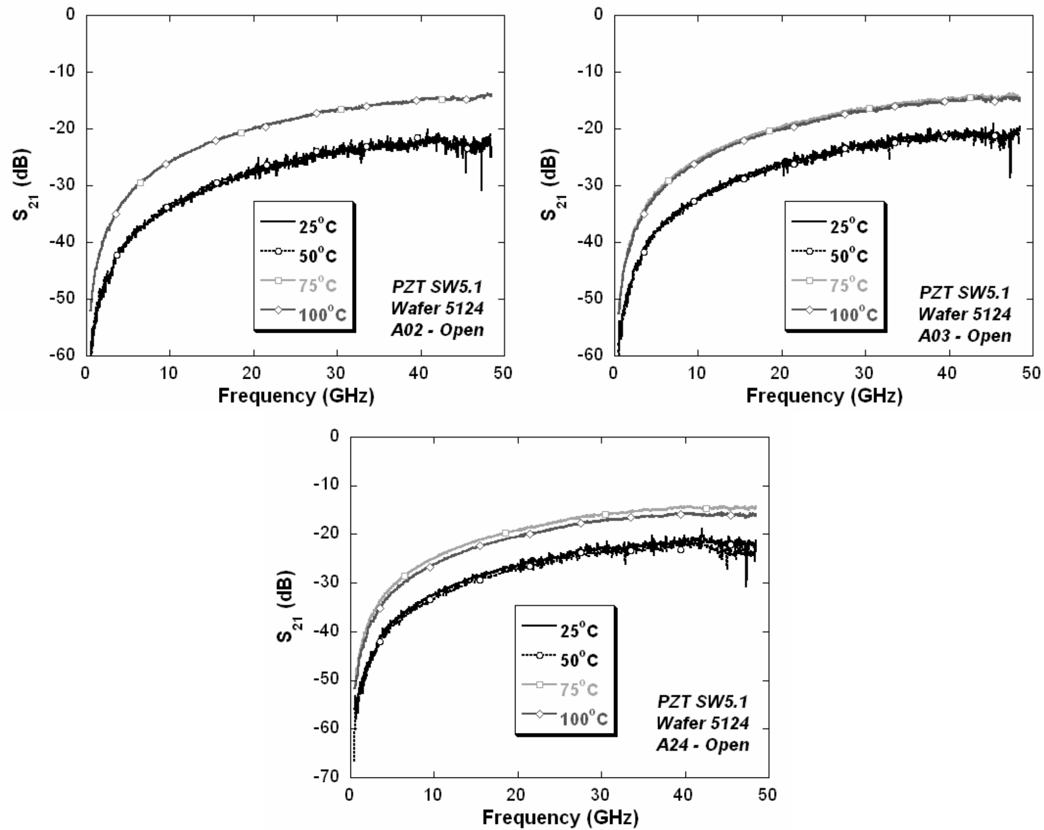

Figure 4.53: S_{21} values as a function of temperature for PZT SW5.1 switches in the open state (0V) for Wafer 5124 comprised of $SiO_2/Si_xN_y/SiO_2/Ti/TiO_2/Pt/PZT/Pt$ (968/586/3473/20/160/1680/5054/1050 Å). The changes in the isolation characteristics may have resulted from changes in the stress deformation induced by thermal poling during measurements of the closed state performance.

The increased negative deflection of the actuators with temperature results in an increase the actuation voltage for the PZT series switch designs (see Figure 4.54). The first thermal scans on a switch from Wafer 1376 (low resistivity silicon substrate) having an actuator with an actuated length of 90 μm showed an increase in the actuation voltage from 5 volts to 15 to 20 volts as the temperature reached 100ºC. An additional set of experiments was completed on Wafer 5124 to further investigate the thermal sensitivity of the PZT switches on a high resisitivity silicon substrate. As illustrated in the series of plots in Figure 4.54 to Figure 4.59, each of the switch designs tested failed to maintain switch contact at less than 10 volts at 100ºC. Most of the designs tested only partially closed between 75ºC to 100ºC at 10 volts. The partial closure is indicative of failure of

the RF contact pad to contact both RF cantilevers. If only one of the cantilevers is in contact, the isolation can be reduced roughly in half, as witnessed in the thermal response characteristics. This behavior was also observed during actuation of the switches in a scanning electron microscope. Specifically, partial contract can occur when the RF-in cantilever is deformed so that it is lower than the RF-out cantilever (see Figure 4.60). In this case, regardless of the actuation voltage, the switch cannot complete the RF circuit. Similarly, thermal deformations in the RF contact pad can result in a failure to contact both cantilevers.

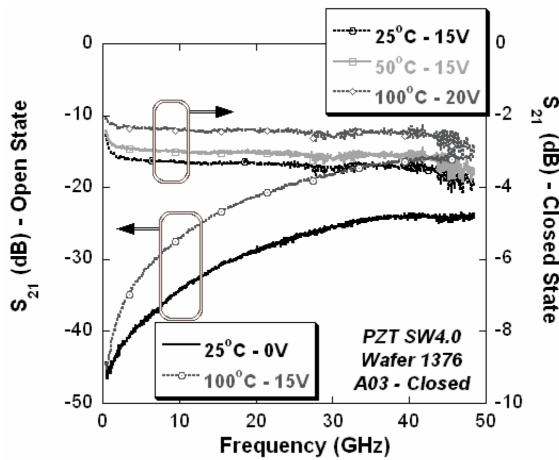

Figure 4.54: S_{21} values as a function of temperature and voltage for PZT SW4.0 switch having an actuator with an actuated length of 90 µm on Wafer 1376 (low resistivity silicon substrate that limits the closed state performance).

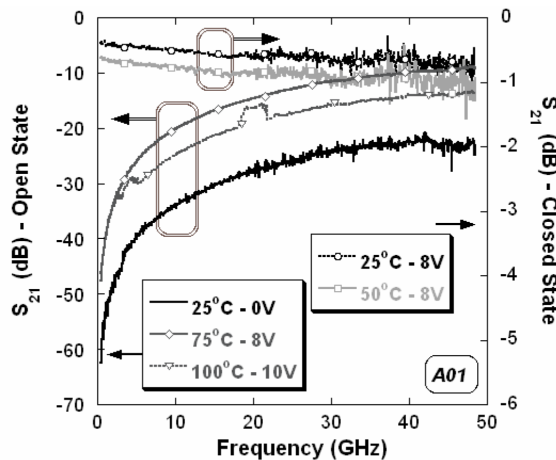

Figure 4.55: S_{21} values as a function of temperature and voltage for PZT SW5.1 device A01 (65 µm long actuated beam) on Wafer 5124.

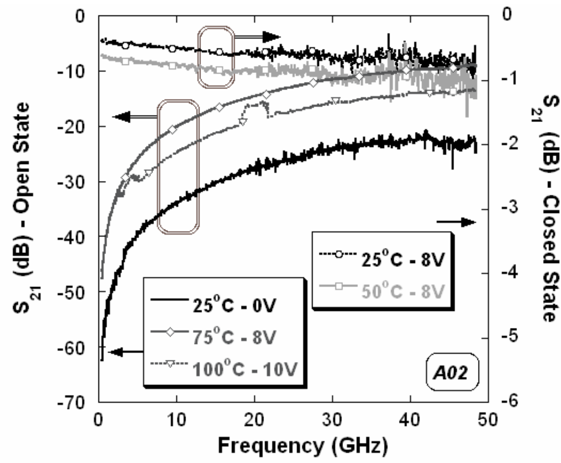

Figure 4.56: S_{21} values as a function of temperature and voltage for PZT SW5.1 device A02 (90 µm long actuated beam) on Wafer 5124.

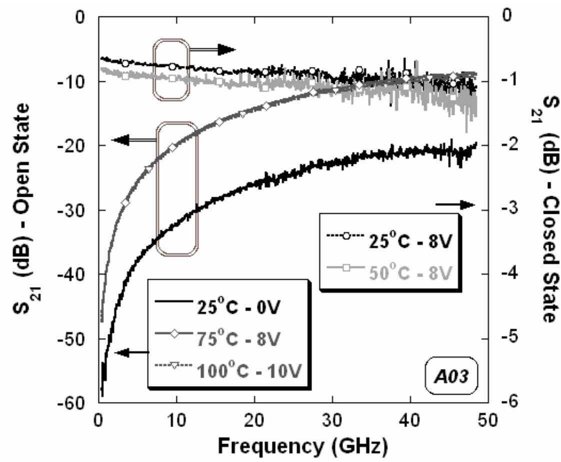

Figure 4.57: S_{21} values as a function of temperature and voltage for PZT SW5.1 device A03 (115 µm long actuated beam) on Wafer 5124.

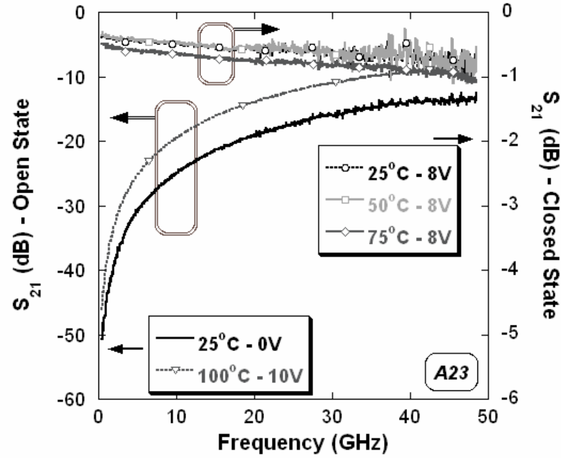

Figure 4.58: S_{21} values as a function of temperature and voltage for PZT SW5.1 device A23 (90 μm long actuated beam) on Wafer 5124.

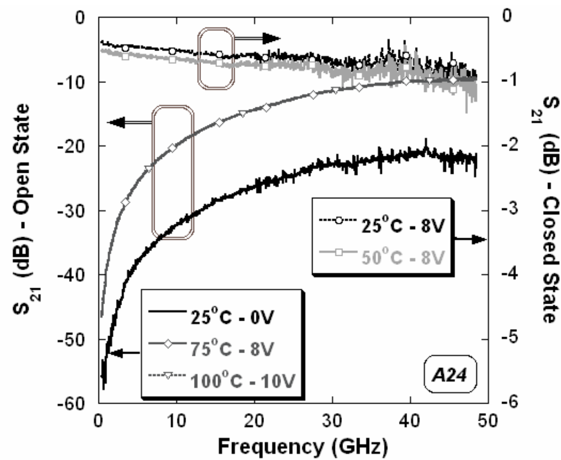

Figure 4.59: S_{21} values as a function of temperature and voltage for PZT SW5.1 device A24 (115 μm long actuated beam) on Wafer 5124.

The thermal deformations in the RF contact pad were also studied in order to understand their contribution to the overall temperature-dependence of the switch performance. For the RF contact pad, thermal deformations can occur in both the length and width. In the off state, the RF contact pad undergoes approximately 0.75 μm of vertical deformation along its length (see Figure 4.61). Perhaps more importantly, there is a significantly larger deformation at the very end of the RF contact pad occurring at 100ºC to 125ºC. In addition, the width curvature of the RF contact pad changes from

concave up to a more flattened structure at 125ºC (see Figure 4.61b). These changes in the length and width curvature are suspected to be the main cause for the opening of the actuated switch at 100ºC with 15 volts applied. The thermal deformation of the RF contact pad with voltage applied to the PZT actuators is shown in Figure 4.62. The edges of the RF contact pad do not move from their average vertical position along its width, but the center does flatten with increasing temperature. With this movement, the two contact dimples at the edges of the RF contact pad would be expected to retain contact. In contrast to the deformations in the width, the tip of the RF contact pad (see Figure 4.62b) undergoes a dramatic change along its length beginning at 100ºC as it did in the off state condition. As the tip deforms, the contact at the RF-out cantilever is lost until the temperature is reduced.

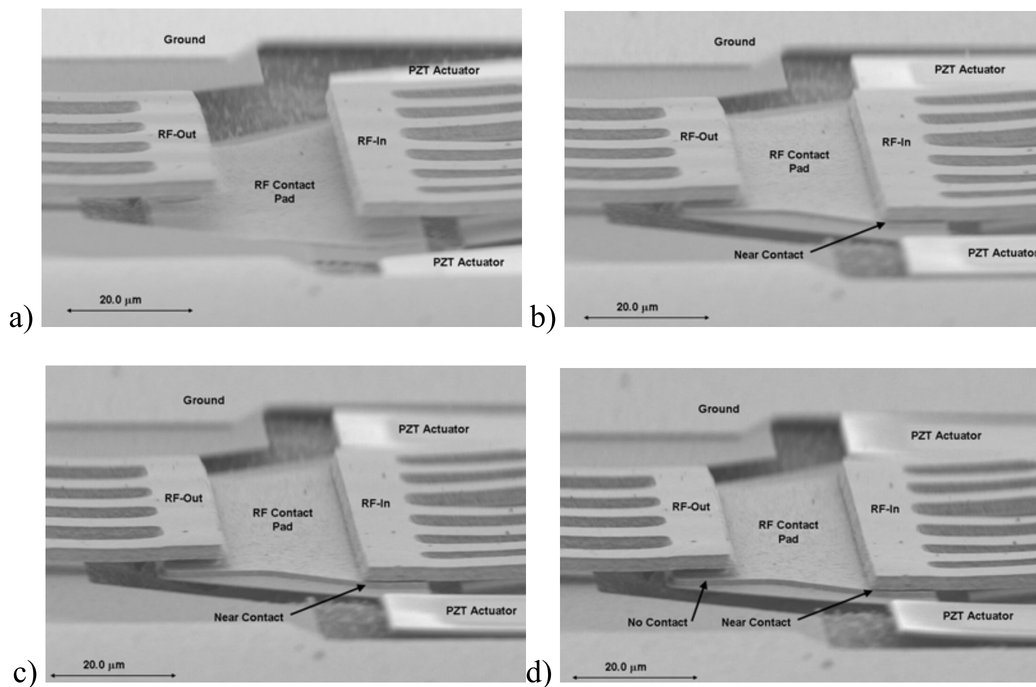

Figure 4.60: SEM images illustrating a PZT SW5.1 device A02 failing to make contact to both RF cantilevers as a result of a defect in the RF in cantilever: a) 0 V, b) 5 V, c) 10 V, d) 20 V.

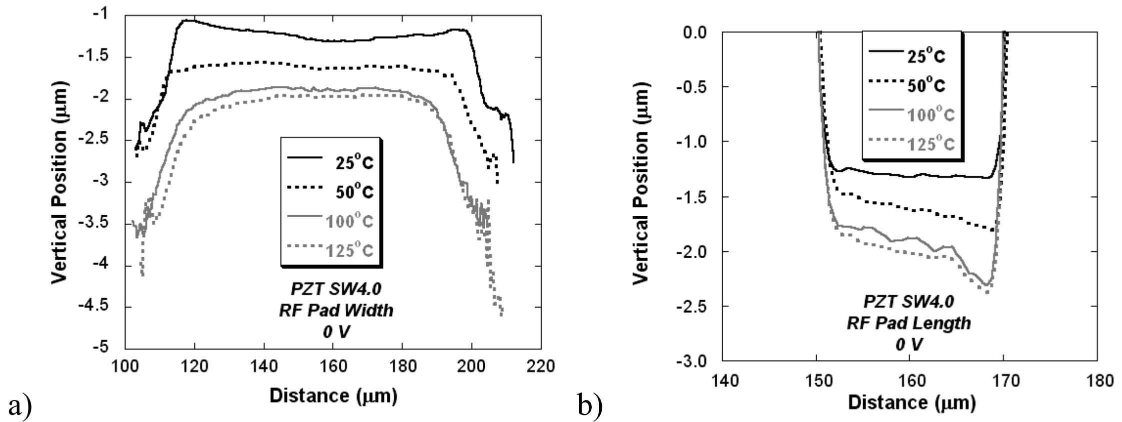

Figure 4.61: Deformation of the width (a) and length (b) of the RF contact pad as a function of temperature with 0V applied to the actuators. The sharp vertical transitions in length plot are measurement artifacts from the edge of the contact pad.

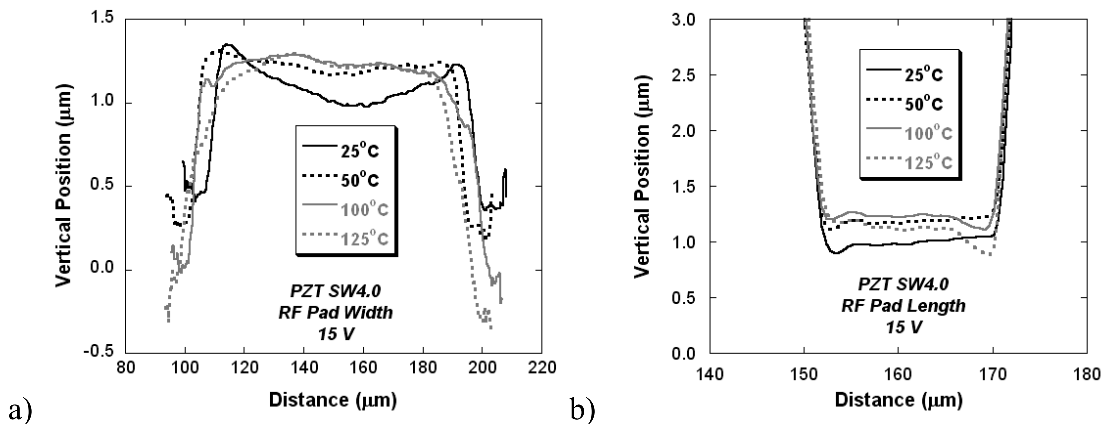

Figure 4.62: Deformation of the width (a) and length (b) of the RF contact pad as a function of temperature with 15V applied to the actuators. The sharp vertical transitions in length plot are measurement artifacts from the edge of the contact pad.

The behavior of the RF contact pad can be controlled to some degree by the residual stress characteristics of the elastic layer and the CPW metallization so as to minimize the temperature dependence. However, any changes will also affect the actuator deformation, making this approach quite difficult and cumbersome. An alternative is a design modification to the RF contact pad and RF cantilevers. This approach will be discussed in Section 4.5.

4.4.8 Reliability

Long cycle lifetimes are essential to implementing RF MEMS switches into commercial and military products. There are two principle concerns regarding the long-terms reliability of the PZT RF MEMS switches: the PZT thin film actuators and the switch contacts. Previous work on mechanical[31] excitations of thin film PZT yielded excellent lifetimes of up to billions of cycles with little degradation in mechanical strength and stiffness (at a strain level of 0.05%). Polcawich et al., demonstrated that thin film PZT capacitors tested with electrical (unipolar)[30] excitation survive at least to 10^9 cycles. During this unipolar stressing to fields up to 5 times the coercive field, there was a gradual increase in the piezoelectric coefficient. Thus, it seems probable that the PZT actuators will not limit the reliability. Consequently, contact failures of the switches were considered. Contact failures common to ohmic contact electrostatic switches include increases in contact resistance from contamination build-up and shorting failures from microwelding of the contacts.[32,33,34,35,36]

To ascertain cycle reliability, the PZT switches were tested under cold switching conditions in order to minimize the possibility of arcing with hot switching. During the testing, the isolation and insertion loss were monitored as a function of operation cycles. The initial tests were conducted on Wafer 1376 (low resistivity silicon substrate) on a Cascade probe station. To limit the possibility of hot switching, the RF probes were lifted out of contact with the CPW transmission line as the actuators were cycled at 5 V at a rate of 1 kHz. Periodically the cycling of the actuators was stopped, the RF probes were lowered, and the isolation and insertion loss characteristics of the switch were measured. For this test, the PZT switches exhibit a high contact resistance (open) degradation/failure between 8×10^5 and 2.3×10^6 cycles (see Figure 4.63). After cycling, the switch actuators were examined with an optical profilometer. It was found that the actuator deformations were similar to those prior to the cycle testing. Following confirmation that the switch actuators perform as designed, the switch contacts were examined with a scanning electron microscope. As illustrated in Figure 4.64, the switch contacts show no sign of degradation or material transfer between the contacts. Furthermore, the contacts appear to be clean of any remnant resist. Previous work on macro relay contacts and MEMS switch contacts discuss that platinum contacts are prone

to the build-up of a frictional polymer with repeated cycling.[36,37,38] Frictional polymers are organic materials that are built up on rubbing contact surfaces possibly from the polymerization of hydrocarbons.[37] Palladium, platinum, ruthenium, and chrome are all strong catalysts for the creation of frictional polymers.[37,38] However, higher magnification SEM images fail to verify the existence of any contaminant films.

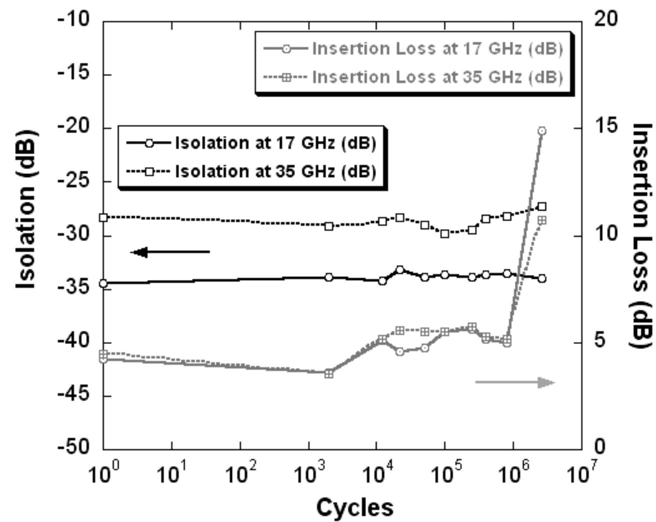

Figure 4.63: Cycle reliability for a PZT SW4.01 device with an actuated length of 140 μm tested under cold-switching conditions. Note, this device was from Wafer 1376, which was fabricated on low resistivity silicon. A high resistance (i.e. high insertion loss) failure occurred between $8x10^5$ and $2.3x10^6$ cycles.

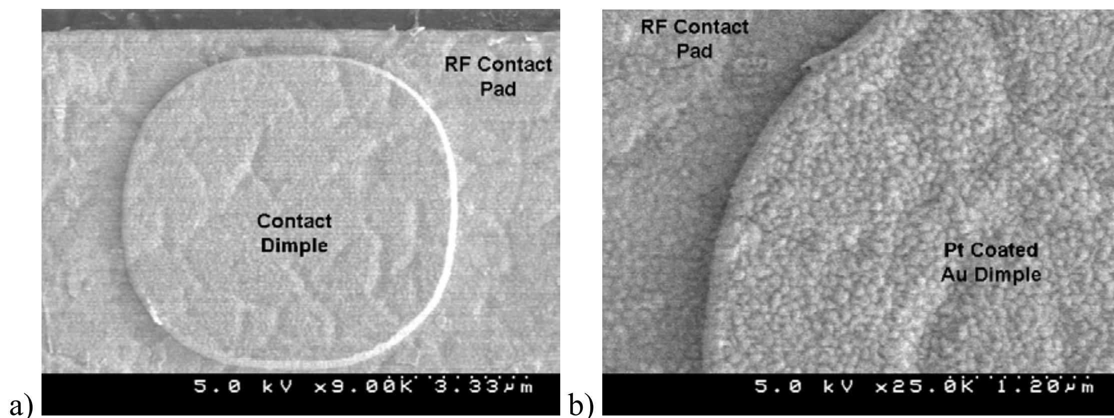

Figure 4.64: SEM images of the Pt coated Au contact dimple for the switch cycled in Figure 4.63.

Additional cycle tests were performed on switches fabricated on high resistivity silicon substrates, wafer 5124, with the data automatically collected for both open and closed states at 8 GHz. A series of images in Figure 4.65 illustrate the results from a few of the switches. All eight devices failed in an open, high resistance contact, mode. For a few of the devices, the switches returned to normal operation for a brief period with continued cycling. In addition, the switch returned to normal operation for a period of cycles if the RF incident power was increased, further indication that an insulating contaminant film may be affecting the closed state performance of the switch. In all cases, the actuators were examined with optical profilometry after failure; normal deformation with applied voltage was observed. As with the other test results, these results suggest build-up of a contaminant film as the culprit for device failure. The SEM was used to investigate the appearance of the switch contacts. As illustrated in Figure 4.66, the switch contacts are intact with no evidence of damage or wear. Higher resolution SEM images failed to verify the existence of an organic contaminant between the contacts.

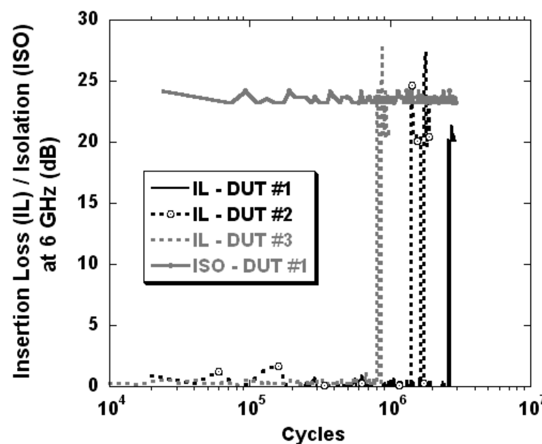

Figure 4.65: A sampling of the results from cycle lifetime testing on PZT SW5.1 device A01 having actuators with an actuated length of 65 μm, from Wafer 5124 at 6 GHz.

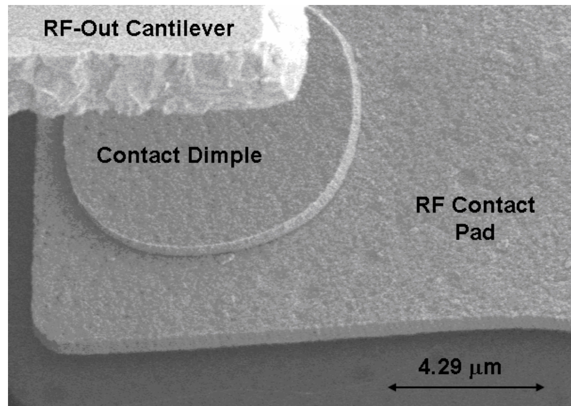

Figure 4.66: SEM image of a switch contact from the testing highlighted in Figure 4.65.

Ameliorating the cycle reliability of the PZT switches will necessitate creating and maintaining clean contacts and a potential change in the contact metals to metals less prone to the catalyze the polymerization of hydrocarbons. One potential problem area in the existing fabrication process is the resist curing and removal process. The technical staff at AZ Electronic Materials (AZ-EM) indicated the potential for the creation of an oxide skin on the resist during the 200ºC resist curing process.[39] Removing this potential contamination layer can be quite difficult, possibly requiring the use of hydrofluoric acid. Another avenue of concern is the chamber processing temperature achieved during the oxygen plasma. According to the staff at AZ-EM, carbonization of the resist can occur prior to resist removal if the surface temperature becomes too high.[39] An alternative resist strip using 400 W instead of 800 W of RF power may be investigated to lower the temperature the resist is exposed to during the release process.

In each of the RF test conditions outlined previously, the devices were tested using a Cascade probe station either in open air or with a dry nitrogen environment (relative humidity as low as 10%). Wafer level packaging of the switches would provide superior hermiticity than either of the approaches utilized here Recent work under the Defense Advanced Research Agency (DARPA) RF MEMS Improvement Program (RFMIP) and Harsh Environment Robust MicroMechanical Transducer (HERMIT) Program has highlighted the improvements to cycle reliability that can be achieved using wafer level packaging.[40,41]

Another important factor influencing ohmic contact switch reliability is the impact force, impact velocity, and repetitive impacts with switch bounce. Each of these factors reduces the lifetime of MEMS switches.[33,36] Impact force and velocity are critical in the determination of the contact mechanics for the switch.[38] These factors define the coefficient of restitution, the ratio of impact velocity with the separation velocity, which can be used to determine the total bounce time. Each impact has four main stages: (1) elastic deformation of the contact surface, followed by (2) partial plastic deformation where the local pressure exceeds the yield point, followed by (3) full plasticity where the impact kinetic energy is absorbed, and (4) release of the elastic energy resulting in separation and rebound.[38] Furthermore, arcing can occur along with each impact event[38] if the switches are operated under hot switching conditions with the appropriate current levels. For cold-switch operation, each impact can further increase the amount of frictional polymer developed at the contact surface. In Section 4.4.5, both electrical and laser Doppler vibration measurements identified a significant number of impact events occurring with switch closure. The number of impacts can easily exceed several hundred impacts before the switches completely settle. To mitigate this situation, as described in Section 4.4.5, an actuation waveform control solution may be used to reduce the impact force and velocity thereby reducing the coefficient of restitution and number of switch bounces.

4.5 Improved PZT Switches (PZT SW5.2)

The PZT switch designs described above were modified to address the temperature sensitivity and to mitigate issues with the RF contact pad contacting both RF cantilevers. In addition, the fabrication process was slightly modified to reduce contamination from ion-milling of the gold metallization used to create all free standing bridges and cantilevers. Furthermore, these process changes enable the inclusion of a wafer level package (which is left for future work).

4.5.1 Fabrication and Design Modifications

There exist two major sources of contamination of the switch contacts in the previous fabrication process. The most critical of these is residual resist remaining on the contact surfaces either from the carbonization of the resist during the oxygen plasma etch or the creation of an oxide skin on the resist from the curing process. Possible solutions include reducing the RF power during the oxygen plasma etch so as to reduce the surface temperature of the resist and prevent carbonization. In addition, hydrofluoric acid containing solutions and/or fluorine containing reactive ion etches may be used to remove an oxide skin on the resist prior to the gold deposition. However, this process poses challenges to process compatibility because of the exposed PZT and silicon dioxide surfaces. Any changes to the resist processing or to the choice of the resist and the release process are suggested for future work.

The other contamination source is the ion-milling of the 2 microns of evaporated gold. Re-deposition of gold particles can lead to micromasking in which small particulates impede the etching of undesired features. This process results in gold particulates which can interfere with the switch operation (see Figure 4.67). The tolerances required for release holes and several of the air bridges eliminate wet etching as a patterning approach for the gold. As an alternative, a liftoff process was developed in conjunction with the sacrificial layer process. Liftoff procedures are generally cleaner than etch processes as they eliminate the possibility of re-deposition of etched material.

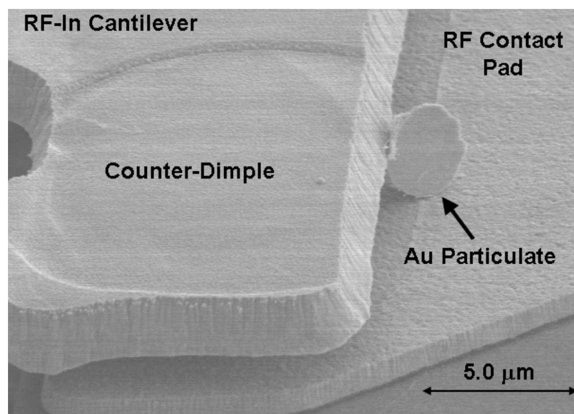

Figure 4.67: SEM illustrating a gold particulate from the ion-milling of the evaporated gold affecting the proper closure of the switch contacts.

The liftoff process required a change in the mask for the sacrificial layer. Previously, the openings in the sacrificial layer defined the anchor locations for the released gold structures. In the new process, the sacrificial layer remains only in the areas where it defines the free-standing structures (see Figure 4.68). To facilitate a clean liftoff of the 2 microns of gold, the AZ 5200 resist used for liftoff was thickened to 3.2 – 3.4 microns. The resist and metal layers were lifted using an acetone soak at room temperature for 2 – 3 hours. The wafers underwent a 10 sec ultrasonification in acetone and were then rinsed in methanol, isopropyl alchohol, and de-ionized water sequentially.

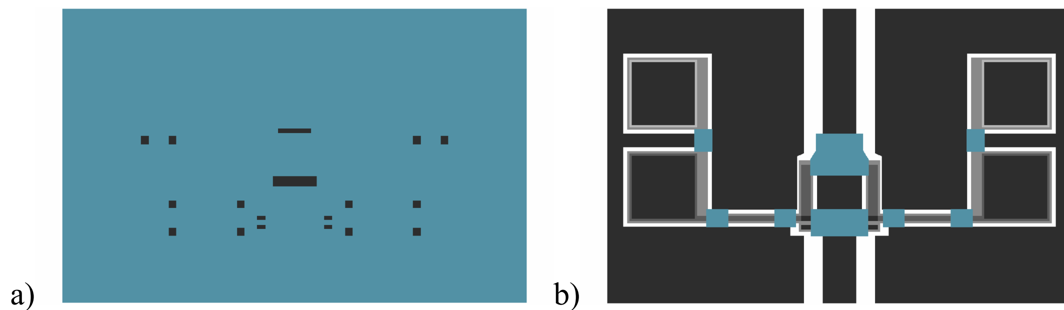

Figure 4.68: Images comparing the sacrificial layer patterning process for a) the gold ion-milling process and b) the gold liftoff process. In the ion-milling process, the resist is patterned to reveal only the anchor regions of all air bridges. For the liftoff process, the resist is patterned such that it is removed for all regions except for the areas where the air bridges will be located.

Although liftoff removes the large particulates left from the ion-mill, there were still imperfections in the resulting devices. The two problems most prevalent in the new process were removal of gold contaminants generated from the creation of the etch holes in the air bridges and deformations in the RF cantilevers created during the wafer cleaning process. The gold contaminants can be minimized by using an acetone bath for ultrasonic cleaning rather than de-ionized water. In the acetone bath, the gold pieces remain suspended in solution rather than attaching to surfaces of the switch by Van der Waal forces. Another concern is deformation in the RF cantilevers (see Figure 4.69) for the modified switch designs that address the temperature sensitivity, which will be

discussed in the following paragraphs. The cantilevers are only weakly attached to the sacrificial layer because of the poor adhesion of gold to the surface of the resist. The counter dimples (see Section 3.2.7) patterned into the sacrificial layer aid in the adhesion of the RF cantilevers by increasing the contact surface area, but cantilever deformations can still occur. The two main causes of cantilever deformation are aggressive ultrasonic agitation and aggressive water rinses and wafer drying with high pressure nitrogen. A mild power setting for the ultrasonic bath combined with low pressure, low flow solvent and water rinses minimized the agitation deforming the RF cantilevers. Furthermore, drying of the wafer surface with dry nitrogen must be done with a low flow, with the direction of air flow perpendicular to the wafer surface.

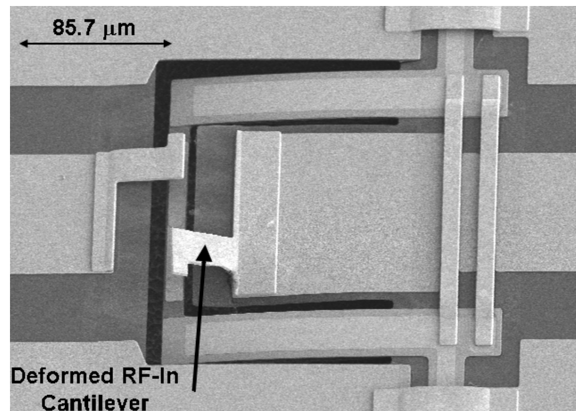

Figure 4.69: SEM image of a non-functioning PZT SW5.2 switch in which the RF-in cantilever has been deformed upward and slightly twisted during the liftoff process. Note that this is an A06 design having an actuator with an actuated length of 115 μm.

To address the temperature sensitivity, the RF contact pad was modified to minimize temperature-induced deformations. Recall from Section 4.4.7 that deformations at the end of the RF contact pad prevented switch closure. The edge deformation was eliminated by modifying the RF contact pad from a trapezoid shape to a simple rectangular beam connecting the two PZT actuators (see Figure 4.70). In addition, the RF cantilevers were changed from two wide cantilevers facing each other into two cantilevers offset from one another. In this manner, the cantilevers and RF contact pad enable contact with both the RF-In and RF-Out cantilevers along the same plane at the

same time. In the previous design, the contacts are along the same plane but the RF-out cantilever had to contact prior to the RF-in cantilever, otherwise the switch was inoperable. The key attributes of the new designs are outline in Table 4.9.

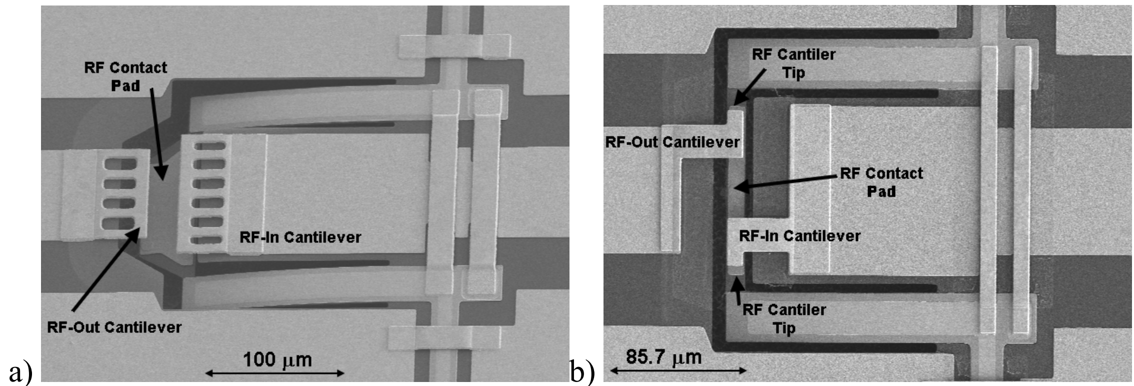

Figure 4.70: SEM images highlighting the differences between (a) PZT SW5.1 designs A01 – A03 and (b) PZT SW5.2 designs A04 – A06.

Table 4.9: Dimensions for PZT SW5.2 designs A04 – A06. Actuator lengths of the new designs remain unchanged from those of PZT SW5.1 designs A01 – A03.

Feature	Width (μm)	Length (μm)
RF-In & RF-Out Cantilever	20	37.5
RF Cantilever Tip	10	8.5
RF Contact Pad	10	100
PZT Actuator (actuated length)	20	65, 90, or 115

4.5.2 Thermal Sensitivity of New Switches

The RF performance as a function of temperature for the new designs, PZT SW5.2 A04 – A06, was examined on a Cascade probe station. The first fabrication run implementing the design modifications was completed on a low resistivity silicon substrate. The median actuation voltages for the new designs (PZT SW5.2) are less than 10 volts (see Table 4.10), but were slightly higher than those reported for the PZT SW5.1

designs A01 – A03 in Table 4.7. The higher voltages are the result of the greater built-in deformation in wafer 5165.

Table 4.10: Median actuation voltages for PZT SW5.2 designs A04 – A06 on Wafer 5165.

Design	Key Feature	Median Actuation Voltage (V) ±1σ
A04	65 μm actuated length	8.0 ± 1.3
A05	90 μm actuated length	7.0 ± 0.84
A06	115 μm actuated length	8.0 ± 1.8

The temperature performance of design A05 is illustrated in Figure 4.71. As expected, the isolation remains relatively constant across the temperature range investigated (-25ºC – 100ºC). The changes to the RF contact pad and RF cantilevers are aimed at improving the temperature sensitivity in the closed state. For the new design, the switch retains contact with 9V applied to the actuators for all temperatures explored. There are some minor temperature-dependent changes in the forward transmission coefficient. However, the higher losses resulting from the use of a low resistivity silicon substrate limit the ability to assess whether or not these differences are indicative of higher contact resistances at different temperatures.

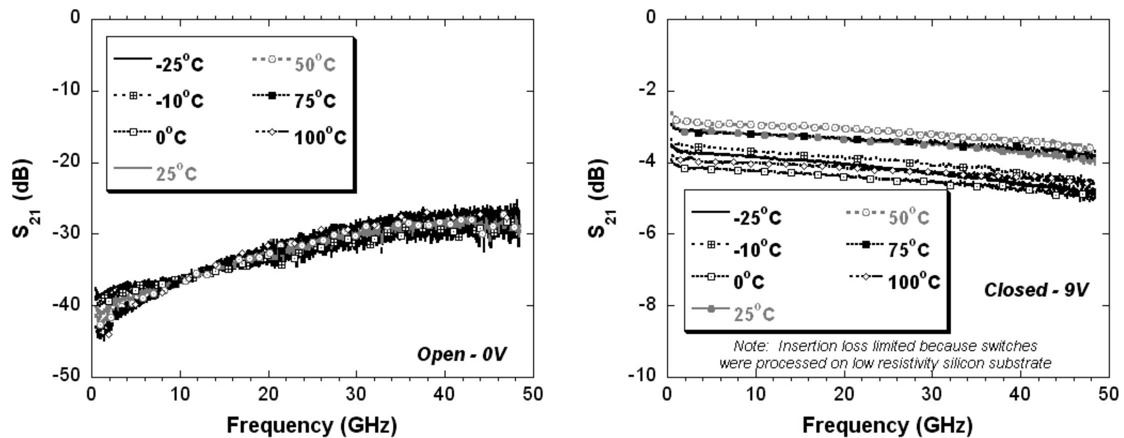

Figure 4.71: RF performance versus temperature for PZT SW5.2 design A05 having an actuator with an actuated length of 90 μm. Note, this initial wafer was a low resistivity silicon substrate so the insertion loss is limited to 3 – 4 dB.

To further assess the thermal sensitivity of PZT SW5.2, additional switches were fabricated on a high resistivity silicon substrate. As illustrated in Figure 4.72, PZT SW5.2 designs has very minimal changes in either isolation or insertion loss as a function of temperature for an actuation voltage of 10 V. The insertion loss change with temperature is less than 0.1 dB for the range of -25ºC to 100ºC. The design changes to RF contact pad and RF cantilevers were designed to eliminate the thermal sensitivity of the switch design by reducing the thermally induced deformations of the RF contact pad. As designed, these changes enabled switch operation over a much wider temperature range without a change in the actuation voltage.

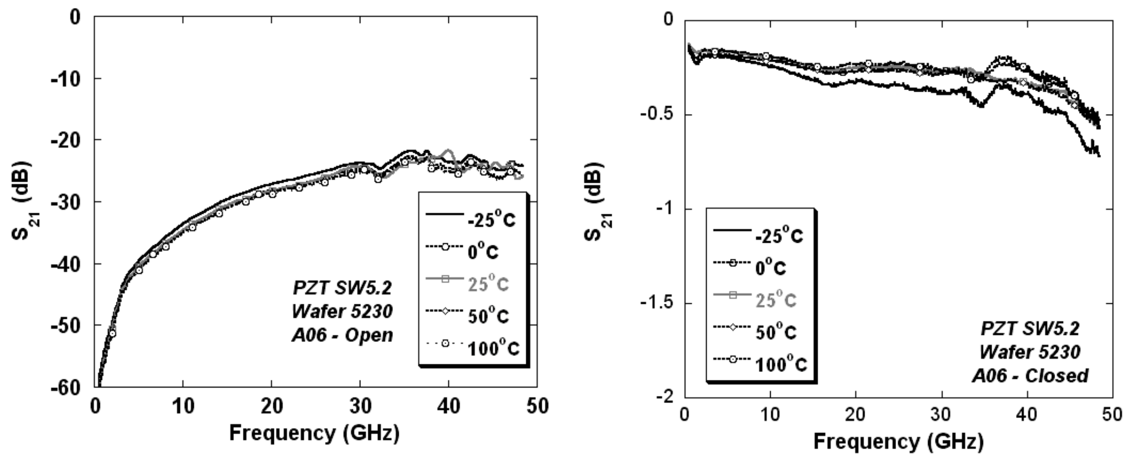

Figure 4.72: RF performance as a function of temperature for PZT SW5.2 device A06 fabricated on a high resistivity substrate (Wafer 5230) and operated at 10V.

4.5.3 DC Current Handling

The first analysis of the power handling capabilities of the switch were completed by passing DC current along the center conductor. During the tests, the initial contact resistance ranged from 7 – 18 Ohm for currents less than 20 mA_{DC} (see Figure 4.73). These values are comparatively high given an expected contact force in excess of 60 μN (see Figure 4.74). Using the contact resistance equation discussed in Section 1.3.1, the contact resistance of contaminant-free contact pairs can be plotted as a function of

contact force (see Figure 4.75). This contact resistance equation is only valid for contact pairs of the same material (i.e. Pt-Pt or Au-Au). Therefore it can only be used to predict the upper and lower bounds on clean contacts. Given the data presented in Figure 4.75, a contact resistance in the range of 0.12 to 0.72 Ohms is anticipated if the contacts are clean and there is a contact force of at least 60 μN. As discussed in Section 4.4.8, the presence of organic contaminants can result in an increased resistance. Unfortunately, no clear evidence of organic contaminants was revealed during examination with a scanning electron microscope. However, it was noted that the contact resistance decreases as higher currents are passed through the contacts, as does the insertion loss. This is often indicative of an insulating layer of contaminants.[38] As the current increases, the insulating films breakdown, allowing a clean metal-to-metal contact.[38] An important point not illustrated on the plot is that the insertion loss remains low (at 2.3 dB) upon removal of the applied current, indicating a permanent change in the contact resistance of the switch, further evidence that the insulating contaminant film has undergone electrical breakdown. As will be illustrated and discussed in the following paragraphs, the contacts themselves do not exhibit any sign of physical change. Therefore, it is believed that the main reason for the high initial contact resistance is the presence of a resistive barrier between the contacts that can be removed or punched through with applied current.

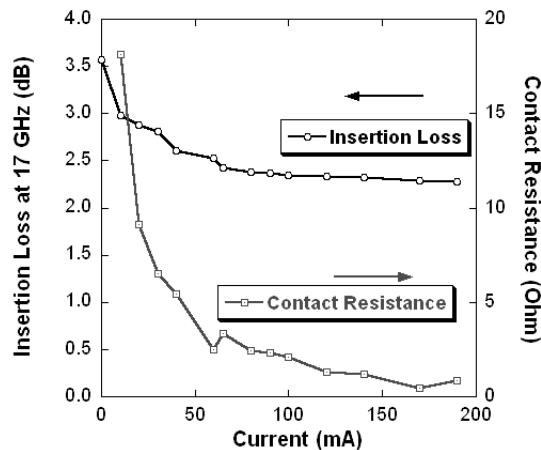

Figure 4.73: Contact resistance and insertion loss at 17 GHz for PZT SW5.2 device A06 having an actuator with an actuated length of 115 μm on a low resistivity substrate (Wafer 5165). The actuation voltage applied to the actuators is 9 volts.

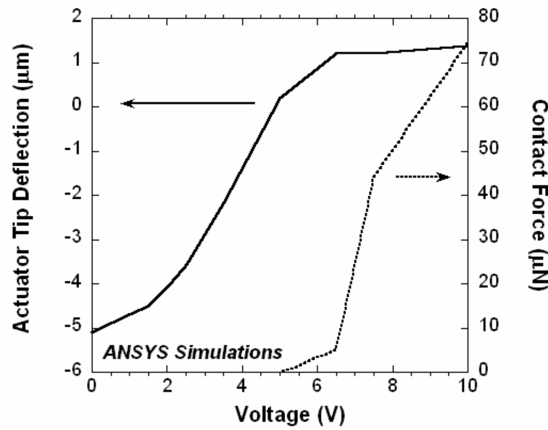

Figure 4.74: Contact force (µN) as a function of the actuation voltage for a PZT switch having an actuator with an actuated length of 90 µm. ANSYS simulations were completed by Jeffrey Pulskamp (US Army Research Laboratory).

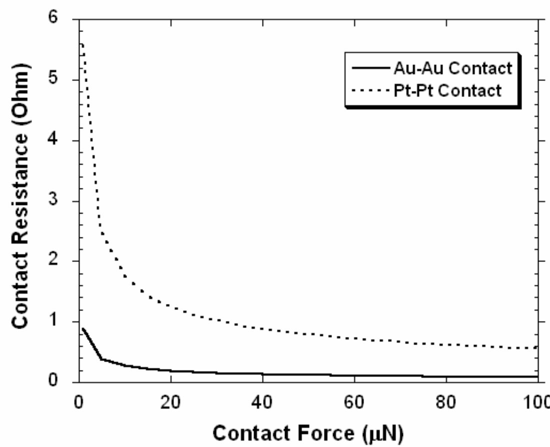

Figure 4.75: Contact resistance of contaminant free Pt-Pt and Au-Au contact pairs as a function of contact force. These plots should set the bounds for the PZT switch assuming a contaminant free Au-Pt contact pair.

It is important to note that higher contact resistances are linked with heat generation at the contacts. The heat generated (Q in Joules) at the contacts can be computed by Joule's Law (see Equation 4.11), where I is current, R is resistance, and t is time. The Joule heating of the PZT switch design SW5.1 was modeled by Jeffrey

Pulskamp (US Army Research Laboratory) with the results highlighted in Figure 4.77. This model for design A02 assumes full contact between all three sets of contact pairs on each side of the RF contact pad, (i.e. each of the 3 contact dimples located at the RF-in and RF-out cantilevers). Additionally, each side of the RF contact pad is assumed to have a resistance of 1 Ohm, which is an upper bound of the contact resistances that has been experimentally observed with 50 – 125 mA of current applied to the contacts. The results from this model for a current of 100 mA_{DC} indicates a temperature rise in the RF pad of nearly 20°C whereas the PZT actuators experience only a 4°C rise in temperature at the tip of the actuator.

$$Q = I^2 Rt \qquad \text{Equation 4.11}$$

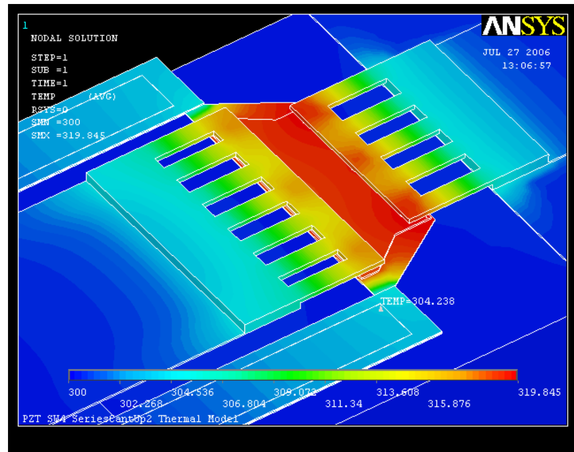

Figure 4.76: ANSYS model highlighting the Joule heating and the thermal conduction paths for the PZT SW5.1 (design A02). The model assumes contact at all 6 contacts and a 1 Ohm resistance per set of 3 contacts (i.e. RF-in or RF-out). For 100mA_{DC}, the temperature rise in the RF pad should be approximately 20ºC, whereas the PZT actuators should see a temperature increase of only 4ºC.

Experimentally, the temperature increase as a function of current was determined using a FLIR systems ThermoVision SC6000 MWIR camera with a 4X objective lens. In this test, a PZT switch (SW5.2 design A06) was wirebonded into a dual in-line package and mounted onto a printed circuit board underneath the camera. The applied

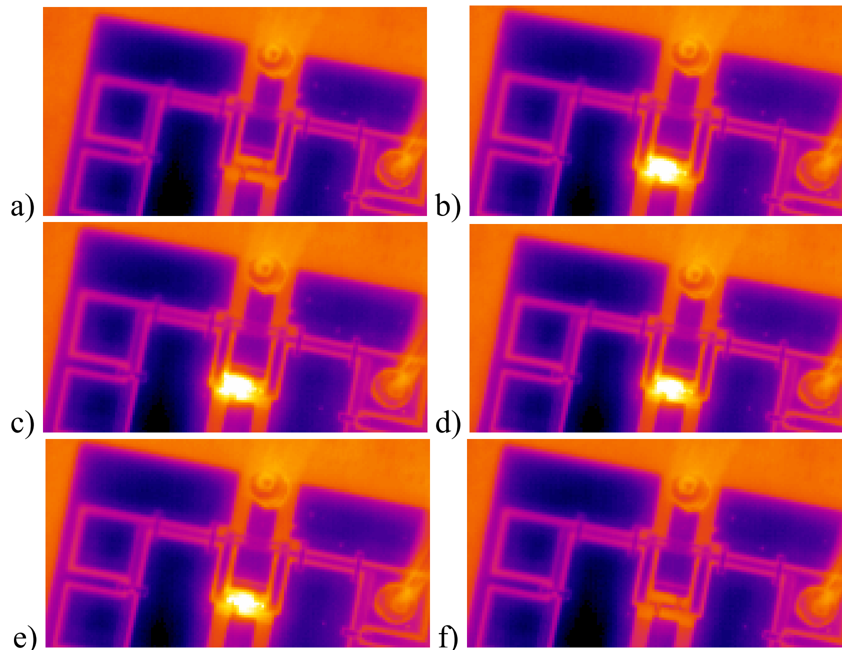

Figure 4.77: Thermal scans of a PZT SW5.2 (design A06) as a function of applied current: a) 0 mA_{DC}, b) 70 mA_{DC}, c) 100 mA_{DC}, d) 150 mA_{DC}, e) 200 mA_{DC}, f) 0 mA_{DC}. The hot zone is indicated by the white areas and is limited to the RF contact pad region.

current and contact resistances were recorded at set intervals up to a maximum of 200 mA_{DC}. For each current level, images of the device were recorded to map the temperature. The camera system was not calibrated for this test, so absolute magnitudes were not acquired. The results for each applied current are displayed in Figure 4.77. The hot zone indicated by the white areas is confined to the RF contact pad region, agreeing with the thermal model for the SW5.1 PZT switch design. Additionally, there is very little change in temperature at the ends of the PZT actuators. The temperature difference along the RF contact pad, RF-in and RF-out cantilevers, and the PZT actuators was recorded and is plotted along with the contact resistance in Figure 4.78. No temperature difference was visible at the first test current of 50 mA_{DC}. A maximum temperature increase of nearly 40ºC is observed for the RF contact pad at 70 mA_{DC} and then the temperature decreases with increasing current up to 200 mA_{DC}. The location of the maximum temperature agrees fairly well with the slope change on the contact resistance versus current plot and is a possible indication of the resistive contaminant film prior to

its breakdown. As the contact resistance decreases with increasing current, the heat generated at the contacts is reduced, at least for the current levels examined during this experiment. At higher current levels, the heat generated should begin to rise as the contact resistance no longer decreases.

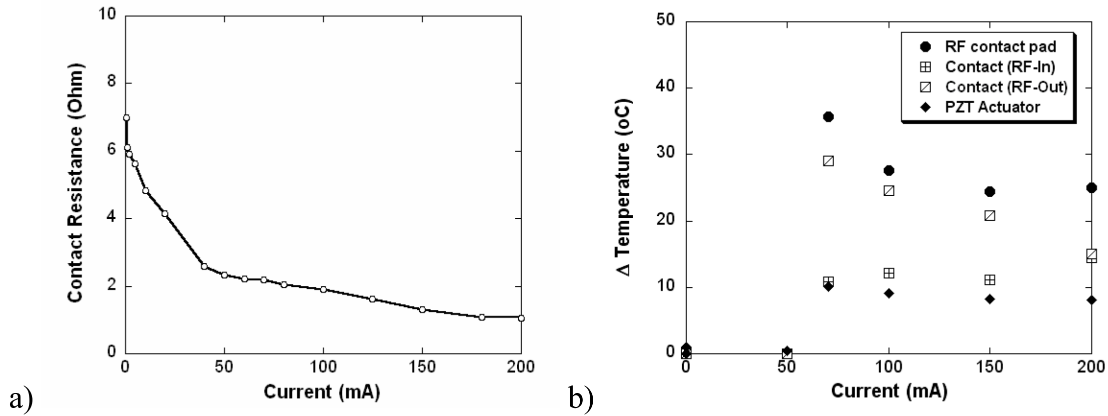

Figure 4.78: a) Contact resistance and b) temperature change of a PZT SW5.2 (design A06) as a function of DC current along the RF conductor as shown in Figure 4.77.

4.5.4 Influence of Contact Metal Choice on Current Handling

A change in the contact metals could be used to enhance the power handling capabilities of the switch. One potential way to improve this performance is by using a eutectic solder encapsulated with a refractory metal. The physical contact point for two contacting surfaces is a small number of asperities.[37,38] As such, a hypothesis of this thesis is that a low melting point eutectic solder used as part of the contact pair will allow mechanical deformation that improves the contact performance. In this scenario, the heat generated at the contact can soften the eutectic solder, potentially allowing it to increase the contact area by smoothing the asperities participating in the electrical path. The result should be a reduction in the contact resistance.

This hypothesis was tested by depositing four different metal combinations as the contact dimple on the RF contact pad. In all cases, the RF cantilever was a 2 μm thick gold contact. For this test, the choices of contacts are listed in Table 4.11. It is critical for this approach to contain the eutectic material with an overlay of a refractory metal to

prevent a softened or molten eutectic from flowing onto the contact pad and reducing the effective height of the contact dimple. Contact dimples of pure gold and platinum coated gold were used as controls. All metals were evaporated in one deposition process using multiple evaporation sources in which each layer was evaporated without removing the wafers from the vacuum chamber while the next material was loaded for deposition. This process ensures minimal interfacial contamination between the multiple metals. To minimize the influence of changes in contact force between PZT actuators, all four metals were deposited onto a single wafer. The wafer was divided into four quadrants using a ¾ shadow mask during the evaporation process. Following the fourth deposition, undesired metals and resist were removed using the lift-off technique described in Chapter 3.2.7.

Table 4.11: Evaporated contact metals used to examine current handling.

Contact Metals	Thickness (Å)
Au	5000
Au/Pt	4000 / 1000
Au/AuSn (80:20) /Au/Pt	500 / 3000 / 500 / 1000
Au/AuSn (80:20) /Au/Pt	2500 / 1000 / 500 / 1000

After fabrication, switches from each quadrant were tested as a function of applied DC current along the RF transmission line with the switches in the closed state. The results are summarized in Figure 4.80 for currents up to 200 mA_{DC}. As expected, there is a substantial difference among the initial contact resistances, with pure gold contact dimples providing a five to six times reduction in contact resistance relative to the platinum coated dimples. For clean gold contacts, one would expect very little change in contact resistance with current. However, several of the devices had high contact resistances for a gold-gold contact pair. These observations are further evidence of the presence of a resistive contaminant film between the contacts. Furthermore, after testing, several devices clearly exhibited a contaminant film present on or near the contacts. The image in Figure 4.79 highlights one of the more pronounced cases where large areas of

contamination were visible near the dimple at the center of the RF contact pad (which is not used in the modified switch).

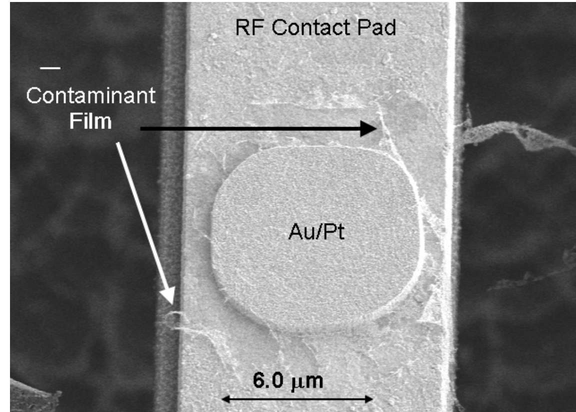

Figure 4.79: SEM image illustrating the presence of a contaminant film on the contact dimples of Wafer 5230.

In contrast to the initial resistance values, the contact resistance at 200 mA_{DC} is nearly identical (0.7 – 0.9 Ohm) for the different contact dimples. It should be noted that half of the switches with gold contact dimples failed (stuck closed) following the DC current test compared with only 2 of the other switches (one with Au/Pt and one with Au/0.3 μm AuSn/Au/Pt).

With a contact resistance of nearly 1.0 Ohm at 200 mA, the voltage drop across the contacts is 200 mV. This voltage level should exceed the softening voltage of both Au and AuSn (80:20) but is slightly less than that of Pt (see Table 4.12). The softening voltage of AuSn was computed based on experimentally observed softening in evaporated AuSn thin films at 150ºC (see Figure 4.81). The corresponding softening voltage and melting voltages for AuSn (80:20) can be computed based on the voltage temperature relationship in Equation 4.12, where L is the Lorenz constant (2.45 x 10^{-8} V^2K^{-2}), T_1 is the bulk temperature (assumed to 298K), and T_m is the contact temperature.[38]

$$V^2 = 4L(T_m^2 - T_1^2) \qquad \text{Equation 4.12}$$

This relationship holds as long as the Wiedemann-Franz Law ($\lambda\rho = LT$) is valid, assuming that both thermal conduction (λ) and electrical resistivity (ρ) arise from electronic transport within the metal.

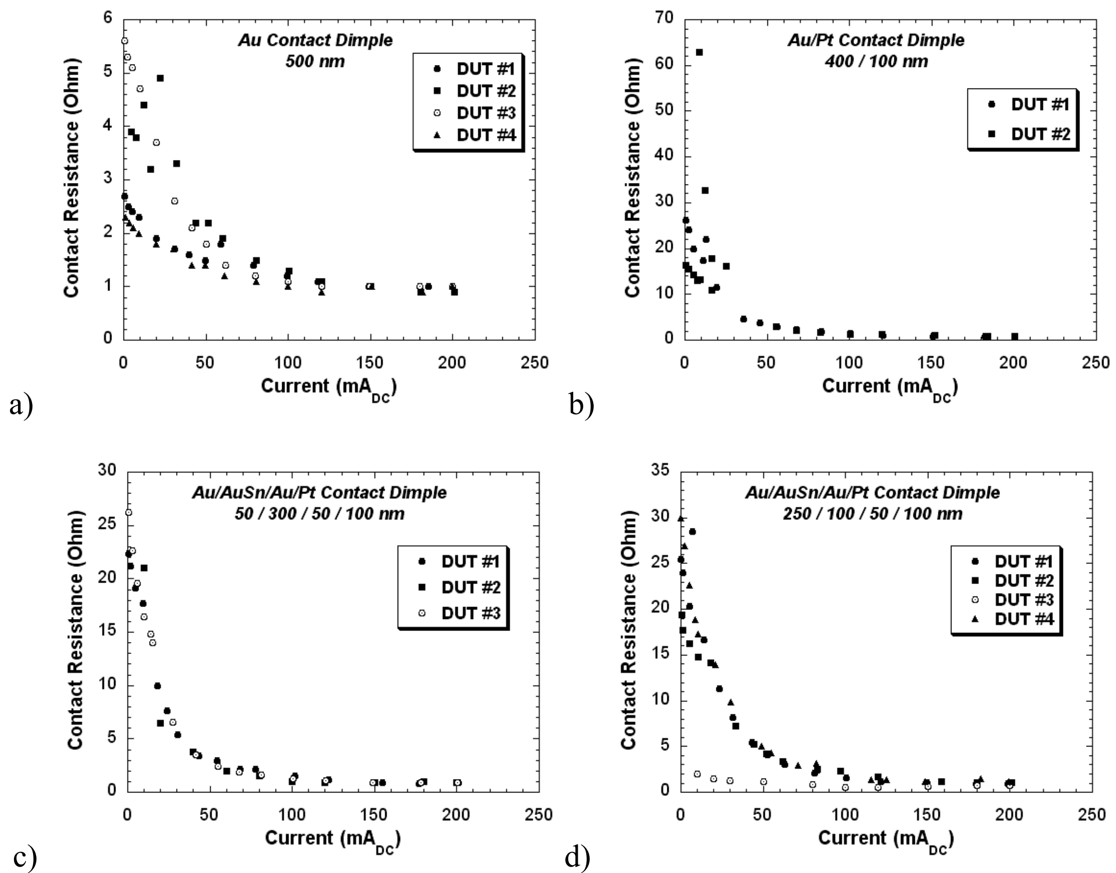

Figure 4.80: Summary of results for contact resistance on PZT switches with different contact metals: a) Au, b) Au/Pt, c) Au/0.3 µm AuSn/Au/Pt, d) Au/0.1 µm AuSn/Au/Pt.

As a result, changes in the contact resistance should begin to appear as the voltage drop increases past the softening voltage. As seen in the gold contact data, the contact resistance reaches its minimum of 1 Ohm near 80 mA, agreeing with expectations. However, the platinum and the resistive contaminant film appear to control the behavior in the AuSn contact dimple switches, even as the alloy melting temperature is approached. Examination of the contacts after the DC current tests failed to provide any

indication of softening and/or melting in any of the contacts (see Figure 4.82). One possible explanation for the lack of visible evidence of any changes in the contacts is that the majority of the voltage drop occurs in the platinum and therefore the Au and AuSn materials do not exceed their softening voltages. Another factor is that the contact resistance of the switch may be dictated by the RF contact pad rather than by the switch contacts. This possibility will be discussed further in the section on RF power handling.

Table 4.12: Voltage for softening (V_s) and melting (V_m) for the contact metals used with the PZT switch.[38] *Note that the values for AuSn have been calculated

Material	V_s (mV)	V_m (mV)
Au	80	430
Pt	250	650
AuSn (80:20)*	94	146

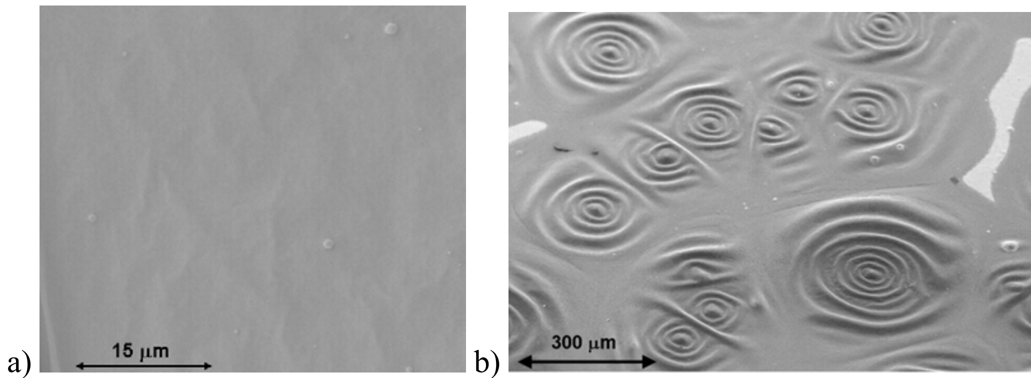

Figure 4.81: SEM image of a 1.0 μm thick evaporated AuSn (80:20) thin film coated with a 0.1 μm thick Au capping layer illustrating (a) softening at 150ºC highlighted by the soft texturing of the surface of the Au thin film and (b) melting of the AuSn after exposure to 300ºC for 2 minutes, highlighted by rippling of the surface gold coating.

The PZT SW5.2 design exhibited the ability to handle greater than 200 mA_{DC} without signs of significant contact damage. Contamination, most likely from remaining resist residues, limits the initial contact resistance. The contamination undergoes electrical breakdown with applied currents greater than 75 mA_{DC}. Softening of contacts containing AuSn is expected to occur as the voltage across the switch contacts exceeds 94 mV. However, no contact showed any signs of softening or melting at less than 200

mA_{DC}. A possible explanation for this will be discussed in the section on RF power handling.

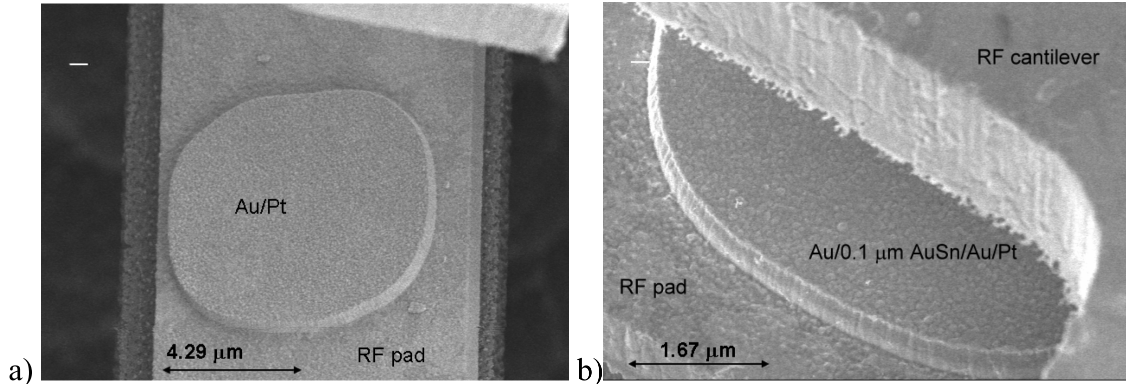

Figure 4.82: SEM image of a) Au/Pt and b) Au/0.1 μm AuSn/Au/Pt contacts after the DC current tests. The image of the AuSn/Au/Pt contacts is a view looking at the corner of the RF cantilever at the RF contact pad and dimple.

4.5.5 RF Power Handling

The RF power handling was determined using a scalar measurement of RF power delivered at the probe tip and the RF power output from the switch. The difference between these two values is equivalent to the isolation in the open state and the insertion loss in the closed state. As a result of calibration drift with time and power level, these values are accurate to +/- 0.25 dB. Is in the DC current tests, each of the four contact dimple metal stacks were examined as a function of RF power (see Figure 4.83). As expected from the DC analysis, the initial insertion loss of the Au contact dimple switch outperforms the others. Again, switches with platinum coated dimples have initial insertion loss values in the 1 – 2 dB range and quickly drop to the 0.25 dB level with increasing RF power. During the tests, it is observed that 500 – 750 mW_{RF} are required to permanently improve the insertion loss characteristics of the switch.

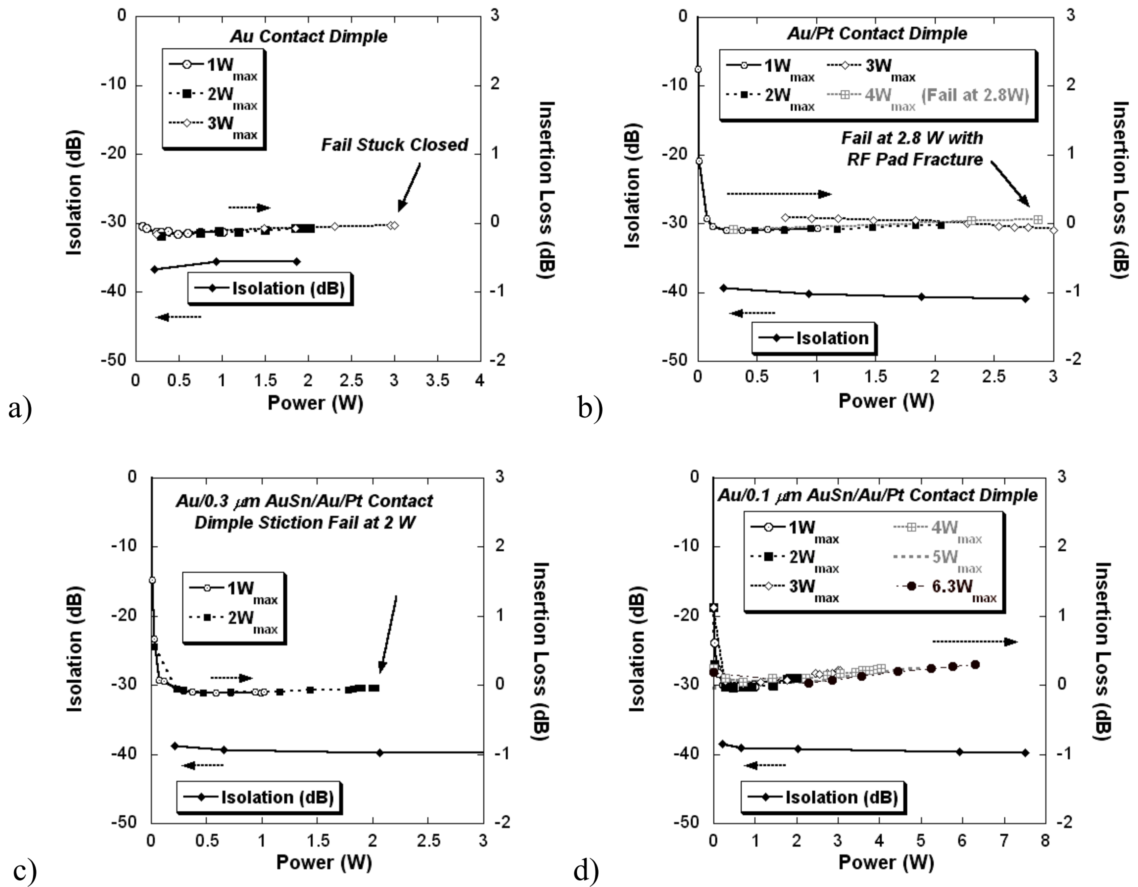

Figure 4.83: Examples of the RF power handling for each of the contact dimple metal combinations for PZT SW5.2 devices: a) Au, b) Au/Pt, c) Au/0.3 µm AuSn/Au/Pt, d) Au/0.1 µm AuSn/Au/Pt.

For each contact dimple type, several devices were tested, with sample size limited to less than 5 tests per dimple type. Although the dataset has limited statistical significance, there exist several noteworthy observations. Regardless of the contact type, the average power at failure is between 2 and 3 W_{RF}. The Au contact dimple switches exhibit the lowest power at failure. During the testing, digital images and video were captured to aid in isolating the failure event. The typical failure modes are outlined in a series of SEM images for each contact dimple type (see Figure 4.84, Figure 4.85, Figure 4.86, and Figure 4.87). The most common failure mode for the switches is a melting of the RF contact pad metallization near the center of the contact pad. The location of the failure coincides with the part of the contact pad farthest away from a thermal heat path to the substrate (i.e. along the RF cantilevers). Higher magnification images of the

melting failure, see Figure 4.88, resemble electromigration failures generated with an alternating current (AC) observed in CPW transmission lines (see Figure 4.89) and will be discussed below.[42] The other observed failure modes for the gold contact dimples are contact stiction and fracture at the RF contact pad connection with the PZT actuators. Arcing was observed for one of the AuSn contact dimples (see Figure 4.86c), although melting in the RF pad was the main failure mode for this sample.

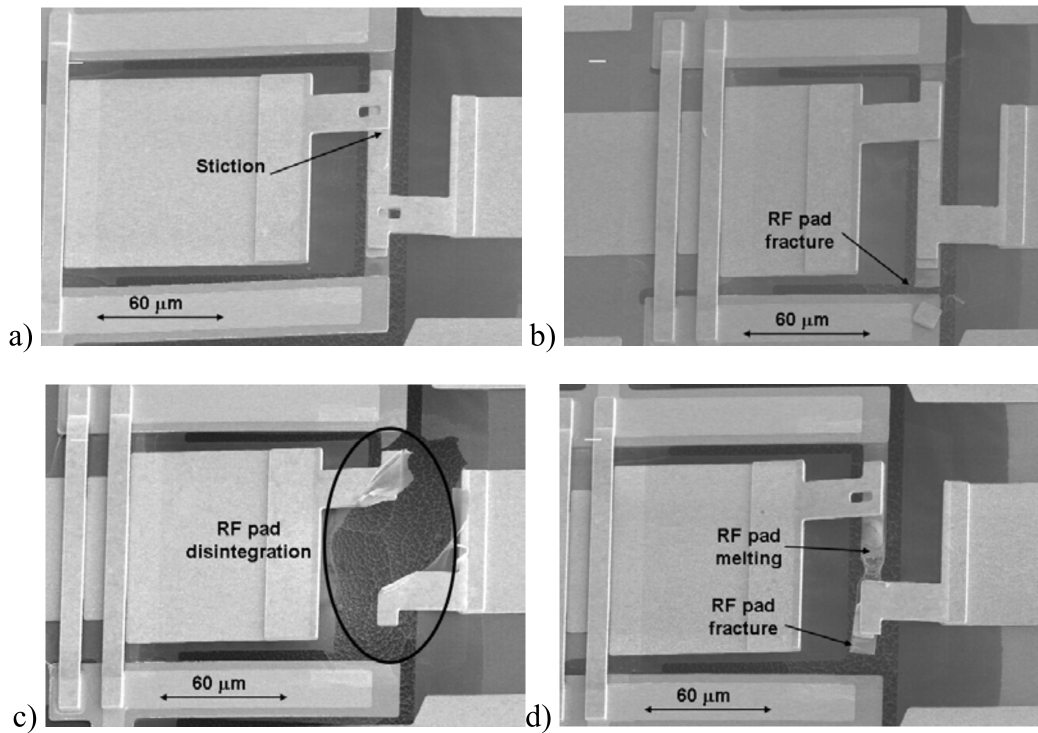

Figure 4.84: SEM images of the failures observed for Au contact dimples: a) stiction, RF pad fracture, RF pad disintegration, RF pad fracture and melting of the gold on the RF pad.

Electromigration in contacts can occur as atoms move toward the anode and vacancies accumulate inside the cathode.[38] As the vacancies accumulate, the electrical resistivity increases within this region.[38] In some instances, voids can be generated which lead to an increase in resistance or open circuit failures (see Figure 4.90). In the case of the PZT switch, electromigration type failures occur in the RF contact pad and not the contacts. A possible explanation for this phenomenon is that the contact resistance of

the switch is limited by the RF contact pad and not the contact dimples. Therefore the vacancies may be accumulating at the center of the contact pad and initiating the failure of the switch.

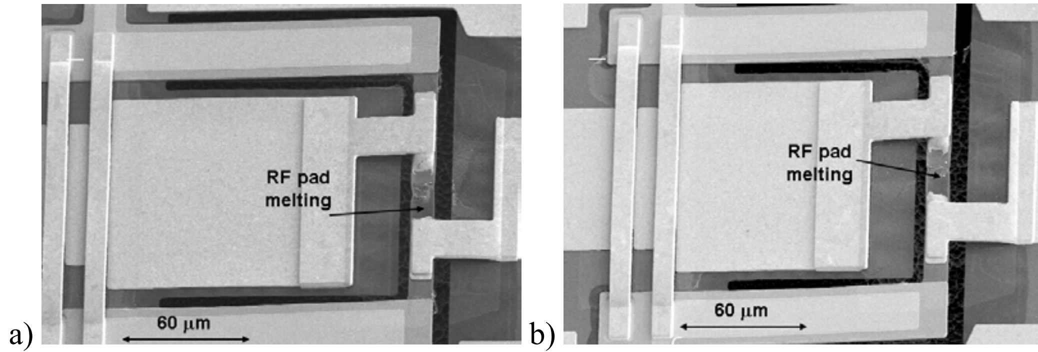

Figure 4.85: SEM images of the RF contact pad failures observed for Au/Pt contact dimples.

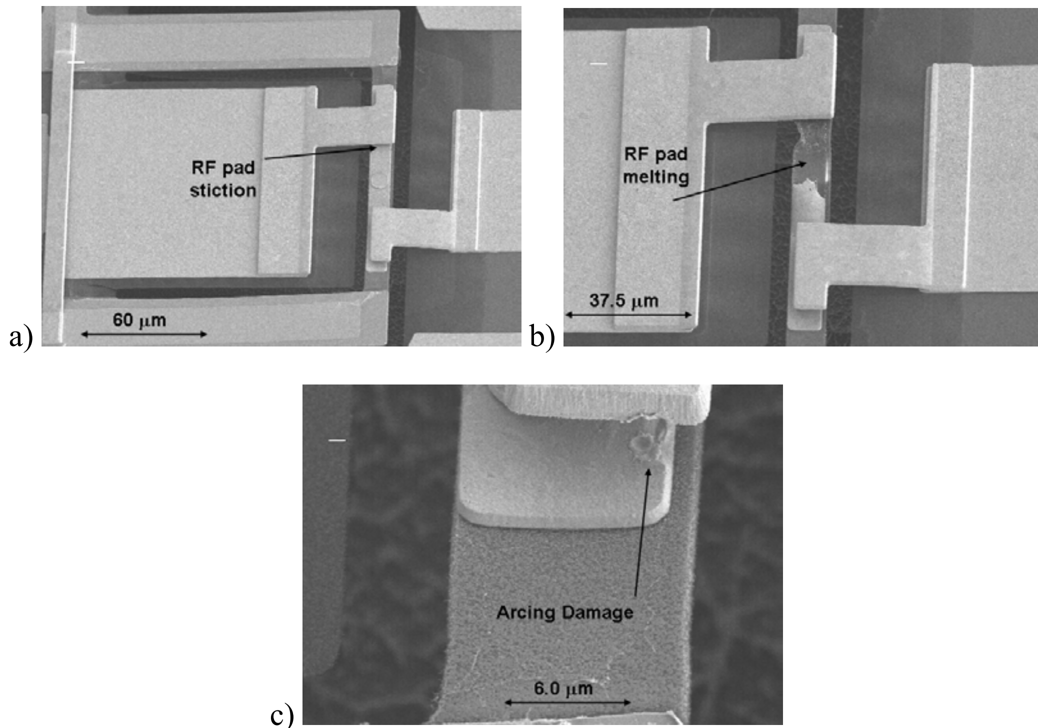

Figure 4.86: SEM images of the failures observed for Au/0.3 μm AuSn/Au/Pt contact dimples: a) stiction, b) melting of the gold on the RF pad, and c) arcing between the RF pad and RF cantilever.

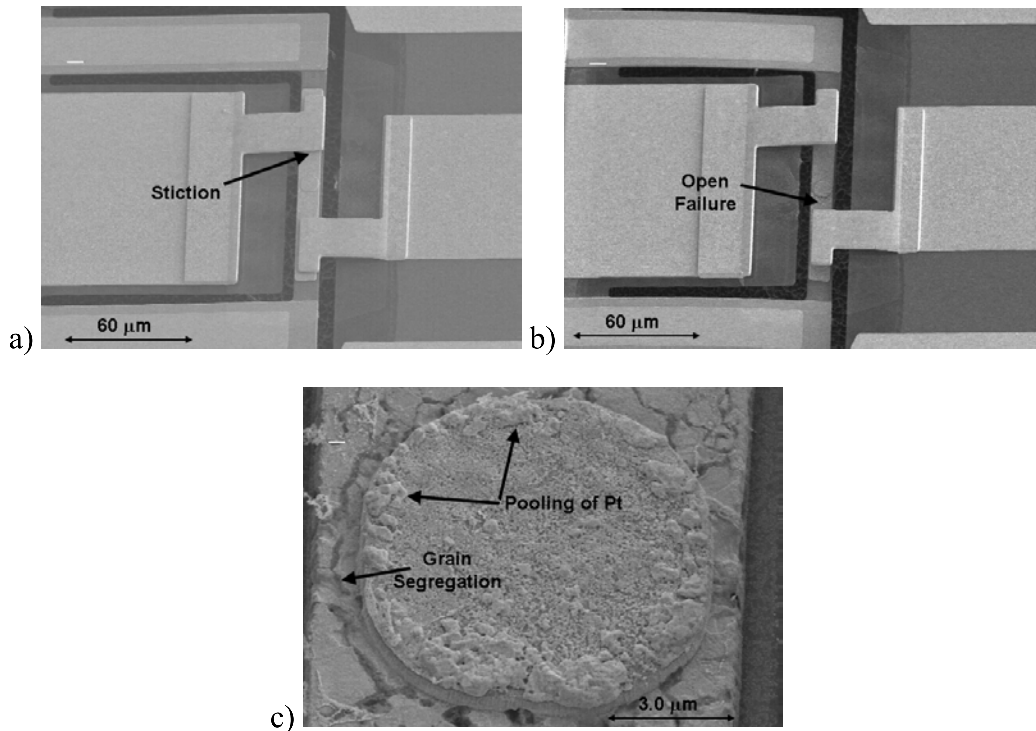

Figure 4.87: SEM images of the failures observed for Au/0.1 μm AuSn/Au/Pt contact dimples: a) stiction, b) open state failures, and c) grain segregation and melting of the AuSn thin films of the center dimple.

It is worth considering more carefully the RF power handling tests in the sample with Au/0.1 μm AuSn/Au/Pt contact dimples. Even though the average failure was 3.2 W_{RF}, several switches with this metal stack survived past 4 W_{RF}, with the highest value being 6.3 W_{RF} without complete failure. For a device that failed at 4 W_{RF}, the switch contacts would no longer properly close and make contact with both RF cantilevers (see Figure 4.87b). For the device still operating at 6.3 W_{RF}, the RF contact pad started to deteriorate and separate along grain boundaries (see Figure 4.87c). Closer examination of the contact dimple located at the center of the RF contact pad illustrates the possibility that localized melting occurred in the AuSn layer of the contact dimple. The bottom of the contact dimple remains intact even as the gold in the RF contact pad is separating. However, the AuSn layer appears to have melted, causing the Pt to pool along the edges of the contact. It is important to note that this contact dimple does not make contact with the RF cantilevers and thus is only affected by heat generated or transmitted along the contact pad. Additional examination of the contact dimples for this switch show that the

entire RF contact pad is riddled with evidence of thermal grain boundary grooving,[43] with the separation of the gold most likely occurring from the heat generated in the contact pad (see Figure 4.91). However, the edge dimples under the RF-in and RF-out cantilevers does not show any sign of melting of the AuSn layer. This is further indication that the resistance of the RF pad is either in the same range of or higher than that of the contact resistance of the two dimples. If the contact dimples had a larger resistance than the contact pad, the dimples would be expected to illustrate signs of melting especially for the AuSn containing dimples. On the other hand, if the contact pad resistance is greater than the contact dimples, the resistance would be expected to be the greatest at the center of the contact pad. Furthermore, the center of the pad would have the largest temperature change, as it has the longest thermal heat path to the substrate. Thus, the center of the pad would be the most likely failure point and the weakest link for RF power handling.

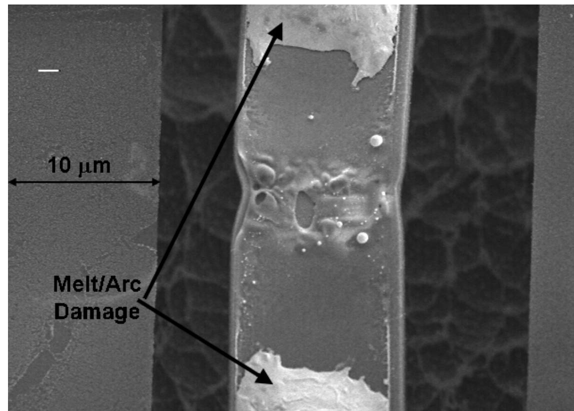

Figure 4.88: SEM image of an electromigration initiated failure along the center RF conductor. Necking of the elastic layer of the contact pad is indicative of electromigration failures.

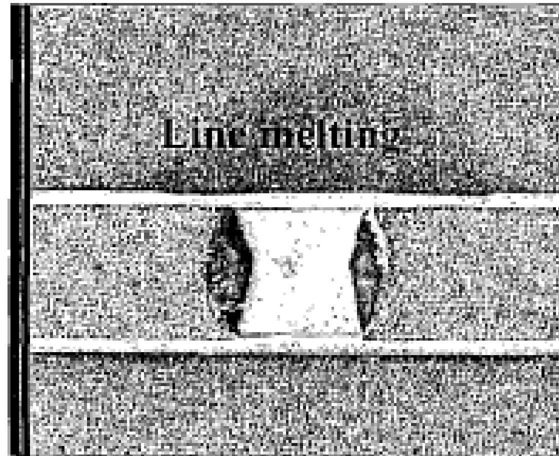

Figure 4.89: DC electromigration failure in a CPW transmission line (image from reference 42).

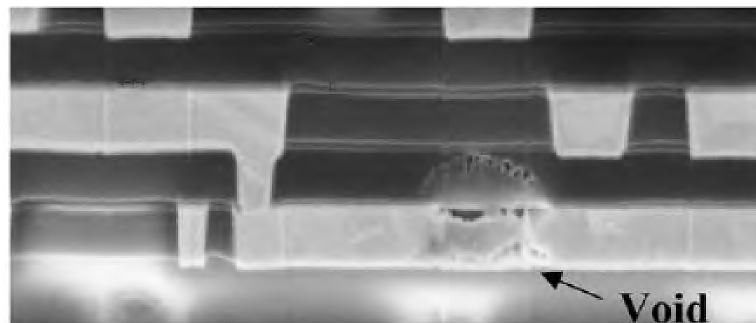

Figure 4.90: SEM image of DC electromigration failures in a copper interconnect (image from reference 43).

The RF power handling of PZT switch design SW5.2 can be summarized as having an average failure power of 2.6 W_{RF} limited by the resistance of the RF contact pad. The high resistance of the contact pad limited the ability to examine the influence of using an eutectic solder as part of the contact dimple. Increasing the width of the contact pad will lower the contact resistance, transferring the weak point of the switch from the contact pad to the contact dimples. This redesign of the switch will be left for future work.

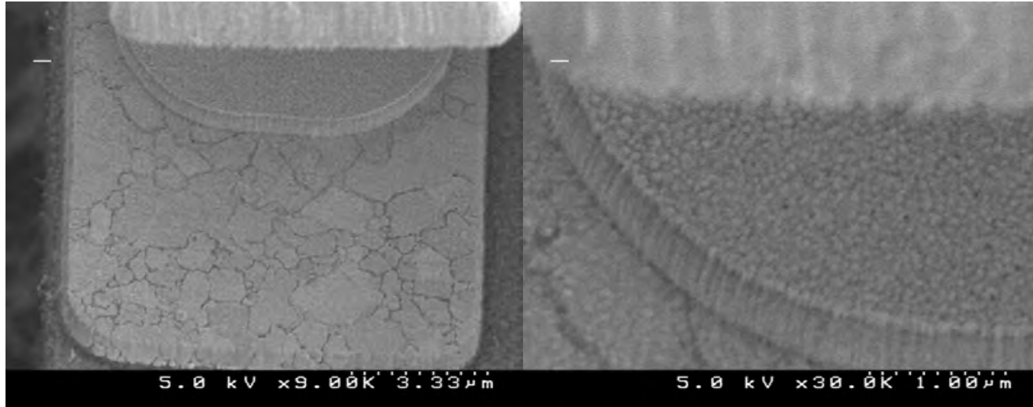

Figure 4.91: SEM images of the edge dimple (Au/0.1 μm AuSn/Au/Pt) near the RF-out cantilever for a switch that was successfully operated to 6.3 W_{RF}. The gold in the contact pad shows signs of grain grooving possibly from the heat generated during testing while the contact dimple shows no signs of softening or melting.

4.6 References

[1] M. Kohli, P. Muralt, and N. Setter, "Removal of 90º domain pinning in (100) $Pb(Zr_{0.15}Ti_{0.85})O_3$ thin films by pulsed operation," vol. 72, no. 24, Appl. Phys. Lett., pp. 3217 – 3219, 1998.

[2] W.L. Warren, D. Dimos, B.A. Tuttle, R. D. Nasby, and G.E. Pike, "Electronic domain pinning in $Pb(Zr,Ti)O_3$ thin films and its role in fatigue," vol. 65, no. 8, Appl. Phys. Lett., pp. 1018 – 1020, 1994.

[3] G.E. Pike, W.L. Warren, D. Dimos, B.A. Tuttle, R. Ramesh, J. Lee, V.G. Keramidas, and J.J.T. Evans, "Voltage offsets in $(Pb, La)(Zr,Ti)O_3$ thin films," Appl. Phys. Lett., vol. 66, pp. 484 – 486, 1995.

[4] D. Dimos, W.L. Warren, M.B. Sinclair, B.A. Tuttle, and R.W. Schwartz, "Photoinduced hysteresis changes and optical storage in $(Pb, La)(Zr,Ti)O_3$ thin films and ceramics," J. Appl. Phys., vol. 76, pp. 4305 – 4315, 1994.

[5] W.L. Warren, D. Dimos, B.A.Tuttle, G.E.Pike, R.W.Schwartz, P.J. Clews, and D.C. McIntyre, "Polarization suppression in $Pb(Zr,Ti)O_3$ thin films," J. Appl. Phys., vol. 77, 6695 – 6702, 1995.

[6] Y. Zhou, H.K. Chen, C.H. Lam, and F.G. Shin, "Mechanisms of imprint effect on ferroelectric thin films," J. Appl. Phys., vol. 98, pp. 024111-1 – 024111-9, 2005.

[7] A.L. Kholkin, S.O. Iakovlev, and J. L. Baptista, "Polarization control and domain manipulation in ferroelectric films with UV light," Integ. Ferro., vol. 37, pp. 195 – 204, 2001.

[8] K.-T. Lim, S.-M. Koo, K.-T. Kim, D.P. Kim, and C.-I. Kim, Improvement in ferroelectric properties of Pt/PZT/Pt capacitors etched as a function of Ar/O_2 gas mixing ratio into Cl_2/CF_4 plasma, Thin Solid Films, vol. 459, pp. 71 – 75, 2004.

[9] Q. Y. Jiang and L.E. Cross, "Effect of porosity on electric fatigue behavior in PLZT and PZT ceramics," J. Mater. Sci., vol. 28, pp. 4536 – 4543, 1993.

[10] Q.Y. Jiang, W. Cao, and L.E. Cross, "Electric fatigue in lead zirconate titanate ceramics," J. Amer. Ceram. Society, vol. 77, pp. 211 – 215, 1994.

[11] S. Chen and V. Lee, "Aging behavior and recovery of polarization in $Sr_{0.8}Bi_{2.4}Ta_2O_9$ thin films," J. Appl. Phys, vol. 87, 3050 – 3055, 2000.

[12] Joe Evans, Radiant Technologies, *private communication*.

[13] P. Muralt, IEEE Sensors Conference, Daegu, Korea (2006).

[14] S. Trolier-McKinstry and P. Muralt, "Thin Film Piezoelectrics for MEMS," J. Electroceramic, vol. 12, pp. 7 – 17, 2004.

[15] J.F. Shepard, P.J. Moses, and S. Trolier-McKinstry, "The wafer flexure technique for the determination of the transverse piezoelectric coefficient (d_{31}) of PZT thin films," Sens Act. A, vol. 71, pp. 133 – 138, 1998.

[16] M. Dubois and P. Muralt, "Measurement of the effective transverse piezoelectric coefficient $e_{31,f}$ of AlN and $Pb(Zr_xTi_{1-x})O_3$ thin films," Sens. Act. A, vol. 77, pp. 106 – 112, 1999.

[17] S. Trolier-McKinstry, N. Gharb, and D. Damjanovic, "Piezoelectric nonlinearity due to motion of 180º domain walls in ferroelectric materials at subcoercive fields: A dynamic poling model," Appl. Phys. Lett., vol. 88, pp. 202901-1 – 202901-3, 2006.

[18] K. Lefki and G.J.M. Dormans, "Measurement of piezoelectric coefficients of ferroelectric thin films," J. Appl. Phys., vol. 76, 1764 – 1767, 1994.

[19] S. Buhlmann, B. Dwir, J. Baborowski, and P. Muralt, "Size effect in mesoscopic epitaxial ferroelectric structures: Increase of the piezoelectric response with decreasing feature size," Appl. Phys. Lett., vol. 80, no 17, pp. 3195 – 3197, 2002.

[20] V. Nagarajan, A. Stanishevsky, L. Chen, T. Zhao, B.-T. Liu, J. Melngailis, A. L. Roytburd, R. Ramesh, J. Finder, Z. Yu, R. Droopad, and K. Eisenbeiser, "Realizing intrinsic piezoresponse in epitaxial submicron lead zirconate titanate capacitors on Si," Appl. Phys. Lett., vol. 81, no. 12, pp. 4215 – 4217, 2002.

[21] R. Blevins, *Formulas for Natural Frequency and Mode Shape*, Robert E. Kreiger Publishing, Malabar, FL, 1979, pp. 101 - 110.

[22] J. Gere & S. Timoshenko, Mechanics of Materials, Boston, MA, PWS Publishing, 1997, pp. 400-403.

[23] P. W. Rehrig, W. S. Hackenberger, S. E. Park, and T. R. Shrout, "Relaxor-based ferroelectric single crystals for electromechanical actuators," in *Piezoelectric Materials in Devices*, ed. by N. Setter, Ceramics Laboratory EPFL, Lausanne, Switzerland, pp. 433 - 454, 2002.

[24] G. Rebeiz, *RF MEMS Theory, Design, and Technology*, John Wiley & Sons, Hoboken, NJ, 2003.

[25] T. Watanabe, A. Menjoh, M. Ishikawa, and J. Kumagai, "Stacked $SiO_2/Si_3N_4/SiO_2$ dielectric layer for reliable memory capacitor," IEDM Tech. Digest, pp. 173 – 176, 1984.

[26] S. Nozaki and R. V. Giridhar, "Study of carrier trapping in stacked dielectrics," IEEE Elec. Dev. Lett., EDL-7, no. 8, pp. 486 – 489, 1986.

[27] W. Ting, J. Ahn, D.L. Kwong, “Charge trapping and interface state generation in ultrathin stacked Si_3N_4/SiO_2 gate dielectrics,” J. Appl. Phys, vol. 70, no. 7, pp. 3934-3936, 1991.

[28] A. J. Moulson and J.M Herbert, *Electroceramics*, Chapman and Hill, New York, 1990.

[29] K. Uchino & J. Giniewicz, Micromechatronics, New York, NY, Marcel Dekker, pp. 242-254, 2003.

[30] Polcawich, R.G. and Trolier-McKinstry S., “Piezoelectric and dielectric reliability of lead zirconate titanate thin films,” J. Mat. Res. 15, pp. 2505-2513, 2000.

[31] I. Demir, A.L. Olson, J.L. Skinner, C.D. Richards, R.F. Richards, and D.F. Bahr, “High strain behavior of composite thin film piezoelectric membranes,” Microelect. Eng., vol. 75, pp. 12-23, 2004.

[32] R.A. Coutu, P.E. Kladitis, K.D. Leedy, and R.L. Crane, “Selecting metal alloy electric contact materials for MEMS switches,” J. Micromech. Microeng., vol. 14, pp. 1157-1164, 2004.

[33] S. Majumber, N.E. McGruer, and G.G. Adams, “Study of contacts in an electrostatically actuated microswitch,” Sens. Act. A, vol. .93, no. 1, pp. 19-26, 2001.

[34] J. Schimkat, “Contact measurements providing basic design data for microrelay actuators,” Sens. Act. A., vol. 73, pp. 138-143, 1999.

[35] R.A. Coutu, P.E. Kladitis, R.E. Strawser, R.L. Crane, “Micro-switches and sputtered Au, AuPd, Au-on-AuPt, and AuPtCu alloy electric contacts,” IEEE Trans. Comp. Pack. Techn., vol. 29, no. 2, pp. 341 – 349, June 2006.

[36] N.E. McGruer, G.G. Adams, L. Chen, Z.J. Guo, and Y. Du, “Mechanical, Thermal, and Material Influences on Ohmic-Contact-Type MEMS Switch Operation,” Proc. MEMS 2006, pp. 230-3, 2006.

[37] R. Holm, *Electric Contacts: Theory and Application*, Springer-Verlag, New York, 1967.

[38] P. Slade, *Electrical Contacts: Principles and Applications*, Marcel Dekker, 1999.

[39] Ron Bradbury, AZ Electronic Materials, *private communication*.

[40] http://www.darpa.mil/mto/hermit/

[41] S. Majumder, J. Lampen, R. Morrison, and J. Maciel, “A packaged, high-lifetime ohmic MEMS RF switch,” 2003 IEEE MTT-S Int. Microw. Symp., Vol. 3, pp. 1935 – 1938, 2003.

[42] B. Ducarouge, D. Dubuc, F. Flourens, S. Melle, E. Ongareau, K. Grenier, A. Boukabache, V. Conedera, P. Pons, E. Perret, H. Aubert, and R. Plana, “Power capabilities of RF MEMS,” Proc. 24th Int. Conf. Microelectronics (MIEL 2004), vol. 1, pp. 65 – 70, 2004.

[43] W. Zhang and I. Gladwell, “Thermal grain boundary grooving with anisotropic surface free energy in three dimensions,” J. Crystal Growth, vol. 277, pp. 608 – 622, 2005.

Chapter 5

Conclusions & Future Work

The primary objective of this thesis was to design, fabricate, and demonstrate a robust, surface micromachined RF MEMS switch utilizing piezoelectric actuators. Creating such a switch has required interaction between materials and fabrication, mechanical design, and high frequency engineering. This chapter highlights the results of this thesis and provides a list of recommended topics for future research efforts.

5.1 Conclusions

This thesis describes the development of a high performance, RF MEMS ohmic contact series switch using low voltage piezoelectric actuators with a biasing architecture independent from the co-planar waveguide transmission line. The switches were designed such that the PZT actuators reside within the gap between the center conductor and the two ground planes. The location of the actuators allows them to be effectively absorbed within the ground planes such that very minimal amounts of RF energy are lost by capacitive coupling. The switch architecture relies on a two-contact point switch to complete the series connection. A RF contact pad mechanically linking the two actuators is used to complete the RF circuit.

The switches were fabricated using surface micromachining technologies relying on combinations of plasma deposition of insulating materials, sputtering and evaporation of metals, and mostly dry etching techniques. The PZT actuators consist of a silicon dioxide/silicon nitride/silicon dioxide elastic layer and a titanium/platinum/PZT/platinum piezoelectric stack. The elastic layer is specifically designed to result in a negative static deflection of the unbiased actuator. The RF components of the switch including the CPW transmission line, RF contact pad, and RF cantilevers are primarily comprised of gold to minimize high frequency conductive losses. The suspended gold cantilevers were created using a resist sacrificial layer that was removed using an oxygen plasma.

Patterning the CPW transmission line directly on the elastic layer resulted in a transmission line loss of 1.3 dB/mm at 40 GHz. This large line loss limits the

performance of the switch especially for use in large distributed circuits such as phase shifters. The loss is associated with the silicon nitride and/or silicon nitride/silicon dioxide interfaces. Electric charges can be trapped either at the interface or within the nitride layer, resulting in increased loss. A process modification to thin the elastic layer under as well as between the CPW transmission line to less than 800 Å in thickness while keeping the elastic layer intact under the PZT actuators and RF contact pad was implemented and successfully reduced the transmission line loss to 0.2 – 0.4 dB/mm at 40 GHz.

The fabrication process is reliable and successfully produced devices with better than 85% yield with an as-fabricated median actuation voltage of approximately 5 volts. Poling of the PZT actuators lowers the actuation voltage to a median of 3.8 volts, with a low of 2 volts being demonstrated. Additionally, holding the switch in the closed state for extended periods of time resulted in decreases in the actuation voltage as the PZT is continually poled during the test. In several instances, a slightly negative voltage was required to open the switch as the residual poling strain resulted in a change in the unbiased static deflection. Aging of the piezoelectric was shown to have a limited effect on the actuation voltage. The largest observed change in actuation voltage was less than 1.0 V.

The isolation characteristics for PZT SW5.1 are better than 20 dB up to 65 GHz and the insertion loss of the switch is less than 1 dB up to 40 GHz using a CPW transmission line on the elastic layer. The switch insertion loss improves to better than 0.5 dB for frequencies below 40 GHz for transmission lines patterned on a thinned elastic layer. This performance can be improved further with the addition of DC current or RF power. Each of these conditions improves the performance by breaking through a contamination layer on the contacts. This layer is believed to result from either a carbonization or oxidation of the sacrificial resist during the oxygen plasma process used to remove the resist. Lowering the RF power to reduce the temperature during the release process should reduce the contamination level.

Thermal stability measurements show no change in the isolation observed from 25ºC to 125ºC. However, the actuation voltage increased to 20V to maintain closure at 100ºC in Generation II switches. The length of the RF pad in the original design is the

key contributing factor that breaks the switch contact at elevated temperatures. To improve the thermal sensitivity, the switch design was modified to reduce the RF contact pad length. The modified switch was shown to exhibit no changes in the isolation characteristics and less than 0.1 dB change in the insertion loss (better than 0.3 db below 40 GHz) from -25ºC to 100ºC.

Cycle reliable was evaluated at 6 GHz using a cold switching waveform for device operation. During these tests, all devices fail in an open, high contact resistance failure mode. The mean cycle to failure is in the low millions of the cycles. The use of platinum to prevent stiction between two contacting gold surfaces is hampered by the generation of an organic material built up on rubbing contact surfaces, possibly from the polymerization of hydrocarbons, on the contacts with repeated cycle operation. The process is exacerbated by the presence of an organic contaminant from incomplete removal of the sacrificial resist.

The last switch parameter evaluated was DC current and RF power handling. Different combinations of contact metals including Au, Au/Pt, and Au/AuSn/Au/Pt were used to assess the power handling capability. As expected, the gold contacts exhibit initially low contact resistances, followed by decreases in the resistance with increasing DC current. Each of the other three contact metals performs with similar characteristics, including an initially large contact resistance. In all cases investigated, the resistance of the contacts decreases to 1 (±0.3) Ohm at 200 mA_{DC}. The DC current tests resulted in stiction failures for gold-gold contacts and little to no stiction failures for the remaining contact pairs.

For RF power handling, most devices failed to operate above 3 W_{RF}. A host of failure modes were observed including stiction, RF contact pad conductor failure, and fracture between the RF pad and PZT actuators. As with the DC current tests, the primary failure mode of the gold contact pair is stiction. Although stiction is observed for a few of the other contact metals, the primary mode of failure is melting of the gold RF pad. In all but one case, in which the switch survived to 6.3 W_{RF}, the contact dimples and the underside of the RF cantilevers did not exhibit any indication of wear, contamination build-up, or damage. The limitation on power handling for the PZT

SW5.2 switch designs is related to a high resistance of the RF contact pad resulting in failures resembling those from electromigration.

5.2 Recommendations for Future Work

During the process of completing the research for this thesis, several additional research areas have come to light as follow-on research. Summaries of these topics will be discussed in this section as a potential guide for these efforts. The three themes that will be discussed are investigating the ferroelectric degradation during switch fabrication, improving the cycle reliability, and investigating how the switch scales with miniaturization.

5.2.1 Investigating the Degradation of the Ferroelectric Properties During Switch Fabrication

As discussed in Section 4.1.1, the ferroelectric properties of the PZT thin films are far from ideal following the switch fabrication process. Improving the ferroelectric properties such that they are stable with the fabrication process is strongly desired so as to prevent degradation in the piezoelectric response. A limited investigation into the possibility of lead removal during extended solvent soaks has been undertaken. PZT – coated silicon substrates were subjected to 60 min soaks in PRS-3000, acetone, and de-ionized (DI) water (control sample). Afterwards, the solutions were analyzed with inductively coupled plasma mass spectroscopy and compared to unused samples of each solution. During the ICP-MS analysis, the constituent elements of the PZT thin film were analyzed. The initial ICP-MS results indicate the strong possibility of lead removal by Baker PRS-3000 resist stripper (see Table 5.1). This solution is comprised of several components including amines and has a pH of 10 – 11.[1,2] Unfortunately these initial results also showed a 0.026% removal of Pb from the film by de-ioized (DI) water. The mixed results from this initial test are troubling as the PZT thin films are not expected to leach in DI water. Without further testing to verify these results no conclusions can be made at this time.

A follow-on to the initial investigations would include additional ICP-MS experiments on PZT thin films. These tests would include repeating the initial tests as well as investigating samples that have undergone a portion of the fabrication process including ion-milling of the top Pt and PZT features and exposure to the oxygen plasmas prior to the solvent soaks. This data can provide further information on whether or not ion-mill or oxygen plasma induced surface damage of the PZT thin films influences the lead removal during the solvent soaks. In addition, it may be critical to investigate the solvent soaks in the order they occur during the fabrication. In other words, a wafer undergoes a PRS-3000 soak for an hour followed by an additional soak in PRS-3000 for an hour which is then followed by a soak in acetone for hour. The original test investigated three separate blanket films exposed to three different solvents. A wafer that undergoes a series of solvent soaks may experience even further degradation once the surface has been degraded by the initial soak. This may be especially important for highlighting the effect the acetone has on an already degraded PZT thin film.

Table 5.1: Results from ICP-MS analysis after soaking 0.5 μm thick PZT (52/48) thin films in various solutions for 60 min.

Solution	Pb (ppb)	Zr (ppb)	Ti (ppb)
DI H_2O	984.85	0.036	0.057
PRS-3000	1984.4	26.4	51.8
Acetone	0.2	0	0.2

One clear solution to this problem is changing solvents for resist stripping for metal liftoff. Without changing solution manufacturers, Malinkroft Baker does offer another solvent product for resist removal that has a lower pH. This product may provide a reasonable replacement for the PRS-3000. However, compatibility with existing resists as well as additional ICP-MS analysis of its effect on the PZT thin films will still be crucial to ensure its full compliance with the existing fabrication process.

Another possibility is to incorporate a barrier coating on the exposed PZT areas to protect them from chemical attack. The barrier coating must prevent chemical attack of the PZT by both solvents and exposure to oxygen plasmas. Another key attribute is the coating must be deposited with a conformal deposition process to ensure complete

sidewall coverage on the PZT actuators. Additionally, the coating has to have very good adhesion to each of the thin films within the composite actuator stack. A concern with this approach is added residual stress from a thin layer atop the actuators that can have a significant effect on the stress-induced tip deflection of the actuators.

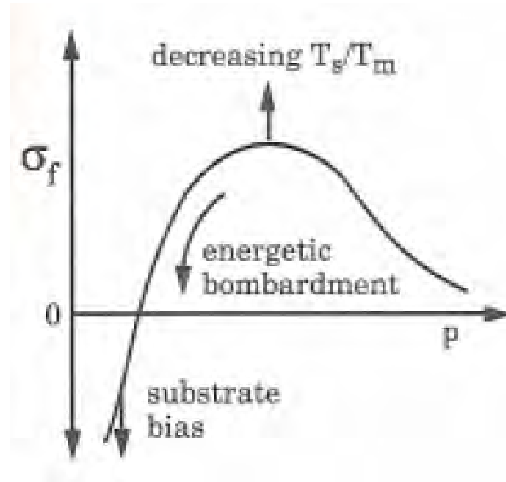

Figure 5.1: Behavior of thin film stress (σ_f) with sputtering conditions: pressure (p), substrate bias, energy bombardment, and the temperature of the substrate (T_s) and melting temperature (T_m) of the thin film (from Reference 5).

One likely candidate thin film is a sputtered coating of titanium dioxide.[3] Sputtered coatings are attractive both because of the reasonably conformal deposition as well as the fact that the growth conditions can be controlled to limit the processing temperature and residual stress. As discussed in Section 4.1.1, thermal processing temperatures must be kept below 350ºC to ensure a negative stress induced tip deflection. Amorphous and crystalline titanium dioxide thin films can be sputtered at temperatures as low as room temperature using reactive sputter deposition in oxygen containing plasmas and a titanium target.[4] Additionally, the residual stress of sputtered films can be controlled to a degree by manipulating either the DC or RF bias, depending on the sputtering configuration (see Figure 5.1).[5] Figure 5.2 illustrates how the PZT actuator beam curvature can be altered by a conformal titanium dioxide thin film of several different thicknesses and assuming a residual stress of 300 MPa (based on Reference 4). In conjunction with deposition controlled stress manipulation, the titanium dioxide thin films can be patterned to remove it from the top of the platinum top electrode, with

appropriate pattern offsets to account for lithography misalignment. With this patterning, the coating can still provide protection to the exposed PZT regions and the influence of the coating on the stress induced deflection can be minimized.

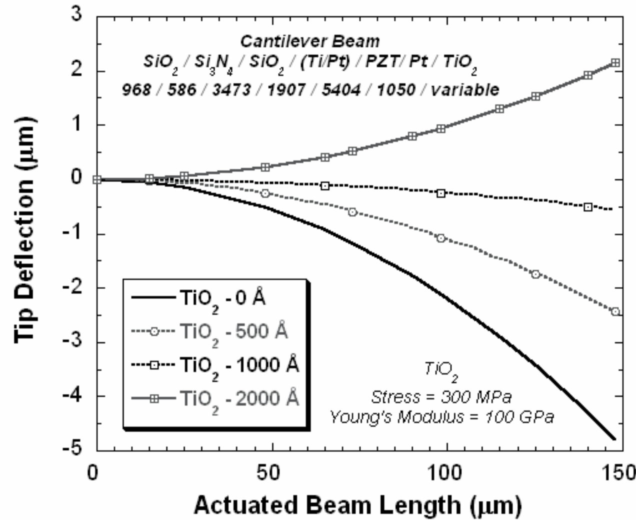

Figure 5.2: Modeled results comparing a PZT thin film cantilever comprised of $SiO_2/Si_3N_4/SiO_2$/Ti/Pt/PZT/Pt with and without a TiO_2 thin film coating on top of the beam of 500, 1000, or 2000 Å. Note, the residual film stress of the TiO_2 was assumed to be 300 MPa based on Reference 4.

5.2.2 Improving Cycle Reliability

A major limitation of the current PZT switch is cycle reliability. It is believed that the lifetime limiting factor is contaminants. Organics are present either because of incomplete removal of the sacrificial resist layer used in releasing parts of the switch or as a result of testing in a non-hermetically sealed environment. Discussions with engineers at AZ Electronic Materials highlighted concerns that the RF power used during the oxygen plasma resist ashing step (see Section 3.2.8) may be too high, such that the surface temperature of the resist rises resulting in a carbonization of the resist prior to its removal.[6] Reducing the RF power from 800 W to 400 W will reduce the wafer temperature during the ashing process. The lower temperature should prevent the resist from carbonizing before the oxygen ions have time to etch the resist.

Although the switches were tested in a wafer probe station in a dry nitrogen environment, the contact surfaces remain contaminated with a small degree of organics present within the enclosure. To achieve MEMS switch cycle reliabilities in excess of 10^9 cycles, an integrated wafer level package is absolutely required.[7,8,9] Wafer level packaging has received great interest in recent years with a large effort funded by DARPA focused on packaging of RF MEMS switches.[10] The primary motivation for the packaging program has been cycle reliability of RF MEMS switches. An additional benefit is reduced cost, as hermetic packaging can make up the majority of the overall cost for MEMS devices. Wafer level packaging approaches use several different technologies including epoxy seals, metal solder seals, anodic seals with glass, glass frit bonding, and thermocompression seals with soft metals. These techniques usually entail bonding multiple wafers. In the bonding process, the most routine packaging approach bonds a cap wafer with no functioning MEMS parts to the RF MEMS switch wafer. Alternatively, the MEMS switch fabrication can be completed as a result of the bonding process. In this approach, one wafer may have the RF transmission line, DC bias lines, and switch contacts and the second wafer has the movable switching structure with the gap between the wafers dictated by the bonding process.

Wafer bonding approaches have exhibited excellent performance. However, there are two major concerns with this type of packaging. One is the design of the RF feed-throughs, especially for metal sealing techniques. For metal seals, capacitive coupling to the cap wafer can create elevated losses at higher frequencies.[9,11] Proper design can mitigate these concerns, but it requires extensive modeling of the entire switch and package.[11] An additional concern is the surface profile of the package. Wafer bonding essentially doubles the thickness of the packaged RF component (see Figure 5.3).

An alternative approach is encapsulation packaging, which relies on the use of additional sacrificial layers to create a suspended dome above the switch. After the sacrificial layer is removed, a sealant is applied to the wafer to create a hermetic environment around the switch. Encapsulation processes result in very low profile packages, can be used to provide local packaging of individual switches on larger RF circuits such as phase shifters, and because of the use of a dielectric for the encapsulant can be applied to an existing switch technology with little degradation in RF

performance. This approach typically uses a dielectric such as silicon nitride that is several microns thick to provide a structure for the dome. An example of this technique is illustrated in Figure 5.4. To seal the cavity, several possibilities exist, including PECVD deposition of silicon dioxide and silicon nitride, spin-on glass, epoxy, and photodefineable organics.[9]

Figure 5.3: Image of the Radant MEMS packaged RF MEMS switch illustrating the height of the packaged relative to that of the RF substrate.[12]

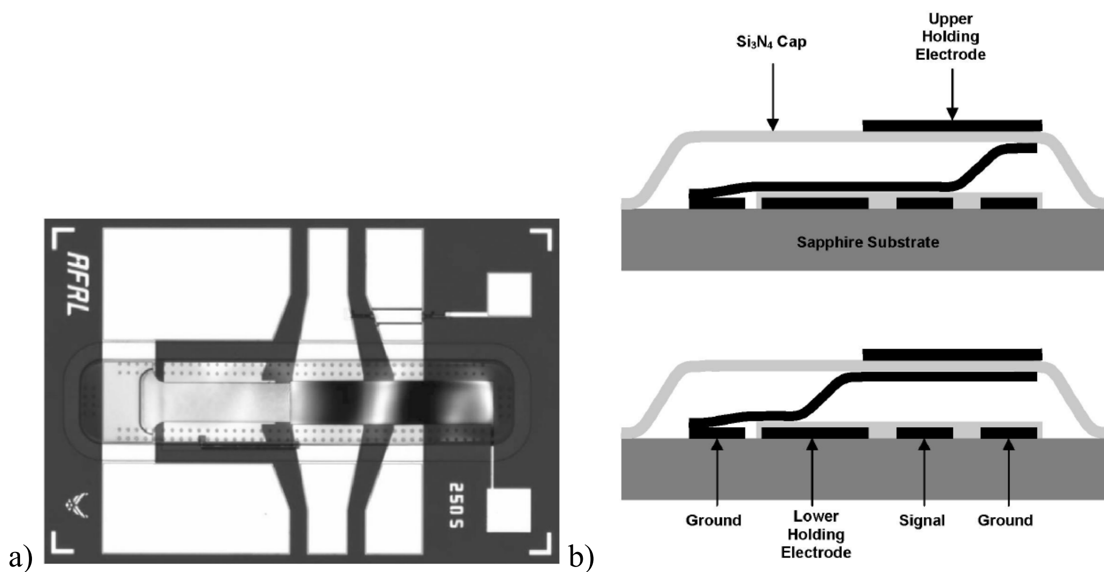

Figure 5.4: a) Optical image and b) schematic cross-section of an encapsulated RF MEMS switch.[13]

In reference to the existing switch process, an encapsulation technique is ideal. Within the past year, researchers at ARL have demonstrated an encapsulation process for an electrostatic switch.[14] As illustrated in Figure 5.5, a PECVD deposited cage is used as the foundation for the encapsulated package and has demonstrated less than a 0.044 dB increase in insertion loss. This process has yet to be demonstrated with the PZT switch fabrication process, but it should be compatible with the existing process flow. The suspended dielectric cage can be created with the inclusion of an additional sacrificial layer combined with a low temperature deposition of silicon nitride. One concern during the release process will be the robustness of the low temperature PECVD silicon nitride when exposed to the XeF_2 etchant used to release the PZT actuators. Following release, low temperature spin-on glass or thinned epoxy can be used to provide the sealant to the package. A concern with these types of sealants are the viscosity and the sealant surface tension as these properties will determine the hole spacing necessary to prevent the sealant from penetrating through the cage and destroying the switch contacts. Additionally, the environment within the package is important to overall switch operation. The pressure of the gas within the package will determine the damping characteristics of the switch contacts. Additionally, correct choice of the gas used within the package can aid in suppressing arcing damage from breakdown of air.[15,16]

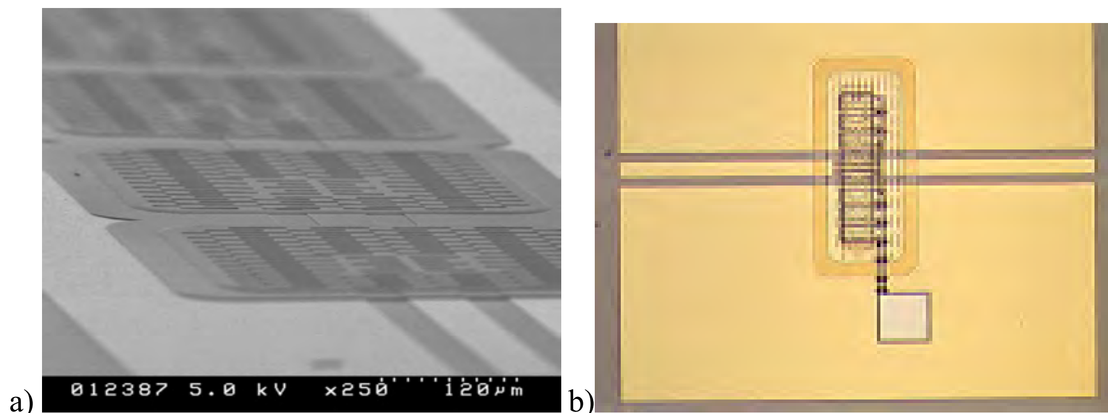

Figure 5.5: Images highlighting an ARL encapsulated electrostatic switch with a process thought to be compatible with the PZT switch process.

5.2.3 Switch Miniaturization

The increasing demand on computational power has resulted in a tremendous demand on the miniaturization of the transistor. The Moore's Law for microprocessors has a current demand in excess of 3 billion transistors per chip (see Figure 5.6).[17] To achieve this level of miniaturization, complementary-symmetry metal-oxide-semiconductor (CMOS) transistor designers are reducing the amount of dielectric material in the gate.[18] An adverse result of reducing the effective gate length is an increase in the leakage power for CMOS transistors.[18] Increases in leakage power result in a substantial increase in the heat generated in both the on and off states for the transistor. One of the leading solutions to the heat generation problem is switching to a high dielectric constant material for the gate dielectric.[19]

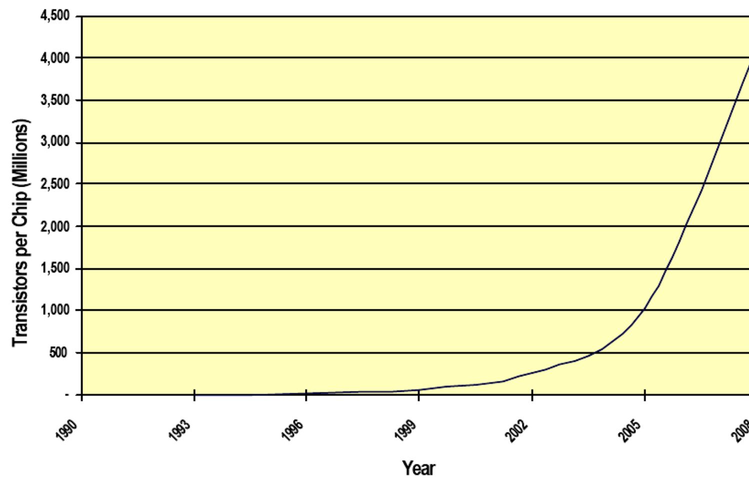

Figure 5.6: Moore's Law for microprocessors (Reference 17).

An alternative approach is to combine mechanical switches with the CMOS transistor.[20] A mechanical switch with near infinite isolation in the off state would reduce the off state leakage power drain for the CMOS transistor. Existing RF MEMS series switch technology, including that reported in this thesis, use switches with device areas several tens or hundreds of microns on a side with excellent characteristics at DC. For example, the PZT switch reported earlier (Section 4.4.3) has an effective device area of 250 x 250 μm with at isolation less than -60 dB at DC. However, this size is

significantly larger than a CMOS inverter (see Figure 5.7) comprised of two transistors with an area of approximately 6 x 6 μm using 90 nm gate technology.[21] With transistor technology currently at 65 nm and pushing rapidly toward 45nm and below, the size of the inverter also shrinks. Thus, an inverter using 65 nm technology will have an effective area of 2 x 2 μm. To be of greatest use, each mechanical switch would have to effectively fit into at most half of this area (because there are two transistors per inverter). More than likely, the mechanical switch would have lengths and gap distances in the sub-micron region. In addition to the size requirement, there are additional constraints on the mechanical switch, including drive voltages compatible with the transistor logic (one volt or less with existing technology), switching times on the order of a few nanoseconds or faster (a 4 ns period would enable approximately 250 MHz operation), and static power dissipation 5 – 10x better than the transistor alone. Furthermore, cycle lifetime requirements are expected to be 10^{18} cycles (an operating frequency of 1 GHz for 365 days generates 3.2 $x10^{16}$ cycles).

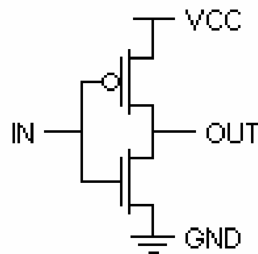

Figure 5.7: Image of a static CMOS inverter with VCC representing the control voltage (Reference 18).

The PZT MEMS switch is one candidate for this particular application, with actuation voltages already demonstrated as low as 2 volts and a static on state power draw of approximately 750 pW. However, scaling the existing PZT switch to meet the transistor demands poses a significant challenge. Scaling the switch consists of three main aspects. First, the constraints imposed by operating at RF frequencies can be removed, eliminating not only the ground planes but also the width requirement on the RF transmission line. A nano-electro-mechanical (NEMS) switch for a transistor does

not have a large power handling requirement, thus the electrical contact areas and electrical traces can be reduces significantly. Implementing these engineering changes can reduce the switch to essentially the dimensions of a single PZT cantilever along with a contact pad. However, the switch still has an approximate footprint of 40 x 200 μm.

The second aspect of switch miniaturization is scaling the switch using the existing fabrication constraints for film thickness and sacrificial layer thickness. The best procedure for this process is to use mechanical models to predict actuator tip deflections as a function of applied voltage and predicting switching speed as a function of voltage and contact gap. Using an actuator stack corresponding to that described in Section 3.1.3 with a $SiO_2/Si_3N_4/SiO_2$/Ti/Pt/PZT/Pt (1000 / 500 / 3500 / 200 / 850 / 5000 / 1050 Å) stack, it is expected that this process will result in a reduction in the actuator length to 50 μm to 75 μm based on analytical models.[22]

Further scaling will still be required to match a footprint compatible with a transistor. To achieve this goal, the switch must be scaled in three dimensions. Several questions arise, including how the piezoelectric coefficient will scale with reducing thickness and device area. Previous reports have demonstrated an increase in the piezoelectric coefficient for submicron PZT capacitors with the increase explained by from a reduced influence of substrate clamping on the piezoelectric coefficient.[23] However, in its current state the PZT actuator is released from the silicon substrate so the improvements in the piezoelectric coefficient with reductions in lateral dimensions should not hold true with scaling the PZT MEMS switch. Alternatively, sol-gel PZT thin film capacitors have previously been shown to have lower piezoelectric coefficients with reducing film thickness.[24] The piezoelectric coefficient is expected to drop significantly for film thicknesses less than 0.25 μm, which poses a significant challenge to achieve a one volt actuation. Even as the contact gap is scaled, achieving the necessary tip deflection for reasonable isolation and contact force with a 400 nm long actuator may be unattainable without a reasonably high transverse piezoelectric coefficient. If the PZT thickness is reduced to 100 nm and the elastic layer is scaled 10x, tip deflections on the order of a few nanometers are achievable with an actuation voltage of 1 volt (see Figure 5.8). Note, this prediction has several assumptions that may not hold true. For this model, the same effective piezoelectric coefficient as discussed in Section 4.1.2 was used

and as mentioned previously, the piezoelectric coefficient is expected to be lower for significantly thinner films. Additionally, the Bernoulli-Euler beam bending models used for these calculations may not valid for beams of these dimensions as these structures begin to approach plate and cube dimensions. Given these assumptions, this model gives an indication of the challenges with this proposed concept. At a contact gap of only a 1 - 10 nanometers, the electric field across the gap at 1 volt is 0.1 - 1.0 GV/m and can lead to breakdown phenomenon. At these gaps, field emission or tunneling are the predominant failure mechanisms with an air atmosphere.[25] A potential solution to preventing breakdown across the gap may be to include vacuum packaging to increase the breakdown resistance.

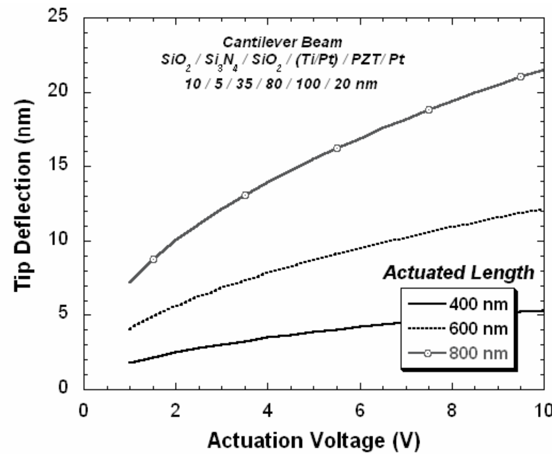

Figure 5.8: Predicted tip deflection for a scaled PZT actuator with three sub-micron lengths using film thicknesses as labeled. This prediction assumes the same effective $e_{31,f}$ as reported in Section 4.1.2 for the PZT MEMS actuators.

Current Mechanism	Gap Distance
Townsend Avalanche of gaseous ions	> 5 µm
Field Emission of electrons	5 nm to 5 µm
Tunneling of electrons	< 2 nm

Figure 5.9: Mechanisms of breakdown across a gap between two conductors.[25]

In addition to the aforementioned challenges, the fabrication process required for creating a PZT NEMS switch compatible with CMOS poses additional challenges. Ferroelectric random access memory (FRAM) using PZT thin films and CMOS has already been demonstrated.[26] However, the inclusion of sacrificial layers extra metallizations, and high piezoelectric coefficient PZT thin film add additional complexity to an already challenging fabrication process. It is envisioned that this program could use PZT film thicknesses on par with those used in FRAM either previously demonstrated or currently in production. However, the standard architectures and fabrication creates a PZT capacitor structure atop a metallization via that connects to the transistor. This architecture will have to be modified for the inclusion of a sacrificial material, preferably a material that could be dry etched without undo harm to any of the electronic structures. Possibilities include amorphous silicon, polycrystalline silicon, and metal masking layers such as chrome. The first two materials could be easily etched with XeF_2 as demonstrated with the PZT MEMS switch fabrication. The problems with the metal sacrificial layers are compatibility with temperature, stress, and compatibility with the release agent.

The task of combining mechanical switches to improve the leakage power of CMOS transistors is a challenge and if successful could revolutionize the IC industry. Of course, the obstacles in the path of success will ultimately determine how successful this concept will become.

5.3 References

---

[1] Kyle Dailey, Mallinckrodt Baker, *private communication*.
[2] Meghan Mooney, Doe & Ingalls, *private communication*.
[3] Joe Evans, Radiant Technologies, *private communication*.
[4] J. Klemberg-Sapieha, J. Oberste-Berghaus, L. Martinu, R. Blacker, I. Stevenson, G. Sadkin, D. Morton, S. McEldowney, R. Klinger, P. Martin, N. Court, S. Dligatch, M. Gross, and R. Netterfield, "Mechanical characteristics of optical coatings prepared by various techniques: a comparative study," Appl. Optics, vol. 43, pp. 2670 – 2679, 2004.

[5] D. L. Smith, *Thin-Film Deposition: Principles & Practice*, McGraw-Hill, Washington, D.C., 1995.
[6] Ron Bradbury, AZ Electronic Materials, *private communication.*
[7] T.A. Midford, J.J. Midford, and R. L. Sturdivant, "The evolution of packages for monolithic microwave and millimeter-wave circuits," IEEE Trans. Antennas Prop., vol. 43, pp. 983 – 991, 1995.
[8] Nick McGruer, Northeastern University, *private communication.*
[9] G. Rebeiz, *RF MEMS Theory, Design, and Technology*, John Wiley & Sons, Hoboken, NJ, 2003.
[10] DARPA Harsh Environment Robust MicroMechanical Transducers (HERMIT) Program, www.darpa.mil/mto/programs/
[11] B. Min and G. Rebeiz, "A low-loss silicon-on-silicon DC-110 GHz resonance-free package," IEEE Trans. Microw. Theory Techn., vol. 54, pp. 710 – 716, 2006.
[12] http://www.radantmems.com/
[13] J. L. Ebel, R. Cortez, K. D. Leedy, and R. E. Strawser, "A latching capacitive RF MEMS switch in a thin film package," IEEE MTT-S Internat. Microw. Symp. Digest, pp. 259 – 262, 2006
[14] R. G. Polcawich, J. Pulskamp, and D. Judy, US Army Research Laboratory, *unpublished results*.
[15] P. Slade, *Electrical Contacts: Principles and Applications*, Marcel Dekker, 1999.
[16] D. W. George and P. H. Richards, "Electrical field breakdown in sulphur hexafluoride," Brit. J. Appl. Phys. (J. Phys. D), Vol. 2, pp. 1470-1 , 1969.
[17] N. Tredennick, "The evolution of digital design," MEMS and Dynamic Logic, Sept 2001 (www……)
[18] http://en.wikipedia.org/wiki/CMOS_transistor
[19] G.D. Wilk, R.M. Wallace, and J. M Anthony, "High-k gate dielectrics: Current status and materials properties considerations," J. Appl. Phys., vol. 89, pp. 5243 – 5247, 2001.
[20] DARPA Nano Electro Mechanical Computers (NEMS), www.darpa.mil/mto/programs/
[21] Narain Arora, Cadence Design Systems, *private communication.*
[22] Jeffrey Pulskamp, US Army Research Laboratory, *private communication*.
[23] V. Nagarajan, A. Stanishevsky, L. Chen, T. Zhao, B.-T. Liu, J. Melngailis, A. L. Roytburd, R. Ramesh, J. Finder, Z. Yu, R. Droopad, and K. Eisenbeiser, "Realizing intrinsic piezoresponse in epitaxial submicron lead zirconate titanate capacitors on Si," Appl. Phys. Lett., vol. 81, no. 12, pp. 4215 – 4217, 2002.
[24] F. Chu, F. Xu, J. Shepard, and S. Trolier-McKinstry, "Thickness dependence of the electrical properties of sol-gel derived lead zirconate titanate thin films with (111) and (100) texture," Symp. Ferroelectric Thin Films VI, Boston, MA, pp. 409 – 414, 1998.
[25] A. Wallash and L. Levit, "Electrical breakdown and ESD phenomena for devices with nanometer-to-micron gaps," Reliability, Testing, and Characterization of MEMS/MOEMS II, Proc. SPIE, vol. 4890, pp. 87 - 96, 2003.
[26] Y. Arimoto and H. Ishiwara, "Current status of ferroelectric random access memory," MRS Bulletin, pp. 823 – 828, 2004.

Vita

Ronald G. Polcawich

Ronald Polcawich was born in Pittsburgh, PA in 1975. He received a Bachelor's of Science degree from Carnegie Mellon University in Pittsburgh, PA in Materials Science and Engineering in 1997. In 1999, Ronald obtained a Master's of Science degree in Materials from the Pennsylvania State University for work on piezoelectric and dielectric reliability of PZT thin films. In the fall of 1999, he joined General Technical Services as a research scientist contracted to the US Army Research Laboratory (ARL) to support their piezoelectric MEMS efforts. In addition, he began his doctoral research while on-site at the ARL. Ronald joined the US Army Research Laboratory in 2001 as a MEMS engineer and continued his doctoral research. His doctoral work involved the development of surface micromachined RF MEMS switches utilizing piezoelectric thin film actuators to realize a reliable, temperature stable, and low voltage switch. He is currently a engineer with the RF and Electronics Division of the US Army Research Laboratory and his research focuses on RF MEMS devices, electronic scanning antenna, PZT thin films, MEMS fabrication, and microrobotics.